MANCHESTER 1824

The University of Manchester

Assessing the single cell and tissue response to altering Her6 dynamics by protein destabilisation in the zebrafish telencephalon

A thesis submitted to the University of Manchester for the degree of

Doctor of Philosophy

in the Faculty of Biology, Medicine and Health

2022

Parnian Doostdar

Department of Developmental Biology and Medicine, School of Medical Sciences

wellcome

Contents

Word Count: 45767

List of figures

List of tables

Terms and abbreviations

AIS . . . . . anterior intraencephalic sulcus

ANB . . . . . Anterior neural boundary cells

AP . . . . . Anterioposterior

Ap . . . . . Alkaline phosphatase buffer

Ascl1 . . . . . Achaete-Scute Complex-Like 1

BAC . . . . . Bacterial artificial chromosome

bHLH . . . . . Basic helix-loop-helix

BMP . . . . . Bone morphogenic protein

bp . . . . . Base pairs

BSA . . . . . Bovine serum albumin

BSF . . . . . Biological Services Facility

caNotch . . . . . constitutively active form of Notch

CDKs . . . . . Cyclin dependent kinases

cDNA . . . . . Complementary DNA

CDS . . . . . Coding sequence

CHX . . . . . Cycloheximide

CNS . . . . . Central nervous system

CV . . . . . Coefficient of Variation

DBZ . . . . . Dibenzazepine

dEGFP . . . . . Destabilised EGFP

DIG . . . . . Digoxigenin

Dll1 . . . . . Delta-like 1

DNP . . . . . Dinitrophenol

dpf . . . . . Days post fertilisation

DUB . . . . . Deubiquitinating enzyme

DV . . . . . Dorsoventral

EMT . . . . . Epithelial to mesenchymal transition

EtOH . . . . . Ethanol

FA . . . . . Formaldehyde

FBS . . . . . Fetal bovine serum

FDAP . . . . . Fluorescnece decay after photo-switching/activation

FDR . . . . . False discovery rate

FGF . . . . . Fibroblast growth factor signaling

FISH . . . . . Fluorescent in-situ hybridisation

FITC . . . . . Fluorescein

GABA . . . . . Gamma-aminobutyric acid

GAVPO . . . . . Gal4 DNA binding domain and p65 activation domain

Grg . . . . . Groucho-related gene

HDR . . . . . Homology directed repair

Her . . . . . Hairy-related

HES . . . . . Hairy and Enhancer of split

Het . . . . . Heterozygous

Hh . . . . . Hedgehog

Hom . . . . . Homozygous

HP . . . . . Her6-PA GFP

hpf . . . . . Hours post fertilisation

HPP . . . . . Her6-PA GFP-PEST

HV Her6-Venus

HVP Her6-Venus-PEST

IF . . . . . Immunofluoresence

IPC . . . . . intermediate progenitor cells

ISH . . . . . In-situ hybridisation

IZ . . . . . Intervening zone

K . . . . . Lysine

K>R . . . . . Lysine to Arginine

kb . . . . . Kilo-bases

KD . . . . . Knock-down

kDa . . . . . Kilo Daltons

Keima . . . . . Histone 2B-Keima

KI . . . . . Knock-in

LHA . . . . . Left homology arm

LLR . . . . . Log likelihood ratio

LM . . . . . Low melting

LNAi . . . . . Locked nucleic acid inhibitor

LSM . . . . . Laser scanning microscopy

MAB . . . . . Maleic Acid buffer

MAML . . . . . Mastermind-like

MBS . . . . . miR-9 binding site

MeOH . . . . . Methanol

MHB . . . . . Midbrain/hindbrain boundary

miR-9 . . . . . microRNA 9

miRNA . . . . . micro RNA

MODC . . . . . Mouse ornithine decarboxylase

NEC . . . . . Neuroepithelial cells

Ngn1 . . . . . Neurogenin 1

Ngn2 . . . . . Neurogenin 2

NHEJ . . . . . Non-homologous end joining

NICD . . . . . Notch intracellular domain

non-osc . . . . . Non-oscillatory

NPCs . . . . . Neural progenitor cells

NVP . . . . . N-version programming

O/N . . . . . Over night

ODC . . . . . Ornithine decarboxylase

ORF . . . . . Open reading frame

osc . . . . . Oscillatory

PA . . . . . Photo-activatable

PA-GFP . . . . . Photo activatable green fluorescent protein

PBS . . . . . Phosphate Buffered Saline

PCR . . . . . Polymerase chain reaction

PEST . . . . . Proline, Glutamic acid, Serine and Threonine-rich

Ph3 . . . . . Phospho-Histone H3

PK . . . . . Proteinase K

PS . . . . . Photo-switchable

PSM . . . . . Presomitic mesoderm

qPCR . . . . . Quantitative polymerase chain reaction

RB . . . . . Rohon Beard neurons

RBP-j . . . . . Recombination signal-sequence binding protein

RGC . . . . . Radial glial cells

RHA . . . . . Right Homology arm

RT . . . . . Room temperature

RT-PCR . . . . . Reverse transcription PCR

SCLC . . . . . Small cell lung cancer

SD . . . . . Standard deviation

sgRNA . . . . . Single-guide RNA

SHH . . . . . Sonic-Hedgehog

siRNA . . . . . Small interfering RNA

smFISH . . . . . Single molecule fluorescent in situ hybridisation

SOP . . . . . Standard operating procedures

SoxB1 . . . . . SRY-box containing B1

SSA . . . . . Single strand anealing

ssDNA . . . . . Single strand DNA

SVZ . . . . . Sub-ventricular zone

TLE1-4 . . . . . Transducing-like E(spl)

TX-100 . . . . . Triton X-100

UI . . . . . Uninjected

Usp22 . . . . . Ubiquitin specific protease 22

UTR . . . . . Untranslated region

V-mt . . . . . Venus-Myc tag

VZ . . . . . Ventricular zone

WT . . . . . Wild type

ZLI . . . . . Zona Limitans interthalamica

Abstract

HES1 is an oscillatory transcriptional inhibitor whose expression dynamics are critical for its role in maintaining neural progenitors in mammalian Central nervous system (CNS) development. Here, I have taken advantage of the optical and developmental properties of the zebrafish telencephalon to study and functionally assess the dynamic expression of Her6 , a zebrafish orthologue of HES1, by combining single cell and tissue level analysis which had never been done for HES1.

her6 expression did not overlap with young *elavl3*-expressing neurons or early fate determination markers *ngn1* and *ascl1*, supporting its function as an early progenitor regulator. Following detailed characterisation, I used the Her6-Venus (HV) endogenous Knock-in (KI) line (Soto et al., 2020) to study Her6 protein dynamics between 20-30hpf. Her6 expression was heterogenous in tissue snapshots, explained by its short and long term temporal fluctuations in single cells. In 5-37% of cells, the short term fluctuations were oscillatory with 1.9 hour period and 1.4 fold-change. The long term trends in single cells were predominantly declining, consistent with Her6 down-regulation over time.

To understand the role of these dynamics, I compared Her6 behaviour in HV with Her6-Venus-PEST (HVP) KI line where Her6 was destabilised and expected to have altered dynamics. The levels of Her6 expression were lower in most HVP cells but unexpectedly, also more heterogenous, as some cells retained the ability to express normal Her6 levels. Also, the differences in Her6 expression levels between neighbouring cells were higher in HVP. Mathematical modelling of these observations showed that HVP traits could only be replicated in presence of cell coupling and Notch-like lateral inhibition. I propose that Her6 pattern in HVP can be explained by indirect strengthening of lateral inhibition as a result of weakened Her6 auto-inhibition due to its low levels. This highlights the importance of combined cell and tissue analysis in interpreting oscillator behaviour.

In HVP, Her6 oscillated in a larger proportion of cells (32.5-67.9%) with higher fold-change (1.9) but unaltered periodicity ($\sim$2.1 hours). But it was also expressed in fewer cells and downregulated slightly more rapidly. Even though the total number of proliferative cells in telencephalon was not affected, there was a presumptive shift in the mode of cell divisions in Her6^{+} cells from self-renewal towards asymmetric. This was consistent with prolonged or increased expression of differentiation genes in HVP. As a whole, these findings provide further support for the involvement of HES/Her oscillations in the transition between progenitor to neuronal commitment in the CNS.

Declaration of originality

I hereby confirm that no portion of the work referred to in the thesis has been submitted in support of an application for another degree or qualification of this or any other university or other institute of learning.

Copyright statement

i The author of this thesis (including any appendices and/or schedules to this thesis) owns certain copyright or related rights in it (the "Copyright") and s/he has given The University of Manchester certain rights to use such Copyright, including for administrative purposes.

ii Copies of this thesis, either in full or in extracts and whether in hard or electronic copy, may be made *only* in accordance with the Copyright, Designs and Patents Act 1988 (as amended) and regulations issued under it or, where appropriate, in accordance with licensing agreements which the University has from time to time. This page must form part of any such copies made.

iii The ownership of certain Copyright, patents, designs, trademarks and other intellectual property (the "Intellectual Property") and any reproductions of copyright works in the thesis, for example graphs and tables ("Reproductions"), which may be described in this thesis, may not be owned by the author and may be owned by third parties. Such Intellectual Property and Reproductions cannot and must not be made available for use without the prior written permission of the owner(s) of the relevant Intellectual Property and/or Reproductions.

iv Further information on the conditions under which disclosure, publication and commercialisation of this thesis, the Copyright and any Intellectual Property and/or Reproductions described in it may take place is available in the University IP Policy (see `http://documents.manchester.ac.uk/DocuInfo.aspx?DocID=24420`), in any relevant Thesis restriction declarations deposited in the University Library, The University Library's regulations (see `http://www.library.manchester.ac.uk/about/regulations/`) and in The University's policy on Presentation of Theses.

Acknowledgements

I am grateful to have been able to undertake this PhD, for which I would like to acknowledge and thank the joint financial support from the Wellcome Trust and the Faculty of Biology, Medicine and Health. Also, I would like to thank the amazing supporting staff at the university who have helped me immensely. I specially would like to thank Dr David Spiller from the Systems Microscopy Imaging Facility who provided huge amount of support in establishing my many microscopy set-ups. I would also like to thank the amazing David Barker, Vicky Taylor and Joseph Pennock from the university's Biological Services Facility for all their help with the fish in the past few years.

This experience was truly made most special by the many many wonderful and amazing people that I was surrounded with. I'm not even sure I would have enough space to thank everyone but I will try...

First and foremost, I would like to thank and acknowledge my incredible family. My beautiful parents **Homeyra** and **Hatef** are angels that sacrificed a great deal to get me to this stage. They sacrificed witnessing the past 10 years of my life first hand and resorted to sharing my pains and joys from a different continent only so I can have a better life. We have all suffered from this distance immensely but I am so very grateful that they are present and healthy. I am also grateful to have made the most of my opportunities that their sacrifice brought me to build a life that I am proud of. During my time in the UK, my sister **Nazanin** has been the only constant through all stages. We have been through so much together and grown with each other. It has been a huge source of comfort knowing that my loving sister is in my life and only one phone call away. So thank you for being my constant through tumultuous times, thank you for always being there.

Next, I'd like to acknowledge my amazing scientific family since I could not have asked for a better and more supportive team. **Nancy**, thank you for your invaluable guidance through this project but also allowing me to evolve as an independent scientist. I have learnt a great deal from you so it is difficult to name all. But the two most important ones were to remind me that despite all the fancy techniques we have access to, "observation" by the humble eye is still the most powerful tool for a biologist. In fact, the main findings presented in this thesis stem from this guidance from Nancy that led me to stare at my data for the first half of lockdown! The other lesson that has not only contributed to my scientific choices but also life choices is that "One can talk themselves out of any experiment; Sometimes you just have to do it and see what happens!". So thank you so much for being an incredible role model.

Ximena, your work was the foundation of this PhD and for that I am immensely grateful. I am grateful for hours and hours that you spent helping me with the grueling half-life experiments. But more importantly, thank you for passing on so much of your knowledge to me and setting the foundation for the scientist I am today. Without a doubt, you have been one of the most influential people in my life. It was from you that I learnt to think things through efficiently and not to rush things to guarantee high quality of work (with the exception of the times when we needed to do everything at the same time!). You once told me that I will be a different person at the end of my PhD, and you were absolutely right. I have grown so much and you have contributed to that greatly.

Veronica, thank you so much for always being eager to listen and help in any way possible. I am extremely proud of and grateful for the work we have accomplished in collaboration together. But most of all, I remember all the times that I was sad and down about [yet another] something that had gone wrong but you were always there to provide perspective and lighten the load. The one thing I will always remember is your acceptance of the fact that there is no such thing as perfect data, but lots of good ways to still use and learn from imperfect data.

Elli, you have been my fairy godmother during my PhD. Two of the most challenging aspects of my work (genotyoing and half-life measurements) were resolved with your magic touch, dedication and help. I am so very grateful that you took the time to help me, teach me many many things and most importantly be a friend when I really needed it. I'm so happy to have worked alongside you and to have gained your friendship.

Anzyyyyyy! You've contributed so much to my well-being and happiness as well as work in the past few years and for this I appreciate you immensely! Thank you for being such an advocate for balancing work and life especially during lockdown. I will always remember our Zoom and in person tea and Curly Wurly parties! Not to mention all the scientific things I have learnt from you like Cloning, qPCRing and plasmid designing! Just thank you so much for being who you are!

Tom (The Minch) Minchington, you were one of the first people to realise and speak to me about my struggles at the beginning of my PhD when I was thinking of quitting. Your intervention and friendship came at a time that I needed it the most and my gratitude is beyond words. Thank you for pushing me to be better (albeit sometimes purely by snarky comments and judgement) and helping me to be brave and undertake learning things that I didn't think I could. Thank you for always providing help with coding even when I was too shy to ask, for generating the code that made the analysis of all of the single cell data possible. But mostly thank you for being the uncensored source of humor and comedy for which I am yet to find a match!

I am of course extremely grateful to have works alongside and learnt many things from two legends in the Papalopulu lab, **Rob** and **Nitin**. **Rob**, you are the master of the In

situ hybridisation and I am so glad to have learnt from you. Thank you for all the help and support you have provided and all the [gazillion] questions you answered. But more importantly, thank you so much for always being up for a chat and/or laugh. **Nitin**, well, what can I say, you are like a Deity! The knower of all things (may the lord forgive me for this blasphemy)! You helped me a huge deal with the old Western Blot and I am blessed to have learnt from you.

I have also been blessed by the most incredible group of extended sisters. My strong and beautiful **Ece**, the crossing of our paths in life was so serendipitous that it can only have been fate! You are an incredible human being and friend and I appreciate you beyond words. I am so happy to have lived with you the past few years and can say without a doubt, it would not have been as joyful (and crazy!) with anyone else. **Catia**, you have been an inspiration for me as a scientist but most importantly as a woman. You were a very important part of my growth as a person in these past years and for that I am forever grateful. **Bahareh** and **Samira**, my Persian sisters, thank you so much for your friendship and companionship through this process, for checking up on me and always being up for hanging out for every reason or no reason at all!

And of course, my dear **Josh** (Hawley - just to prevent any confusion), when the whole world went into lockdown, I did not expect to come out of it with a partner. Especially not someone as unique and wonderful as you who would change my whole outlook on life! But thank you for not accepting when I said PhD life is not compatible with having a relationship and thank you for helping me see life and the world in a new light. Thank you for your continuous support in these final months of my PhD and for always providing a shoulder to cry on. I am extremely grateful for your calm and joyful presence in my life.

Finally, I'd like to also thank **myself** for being persistent and strong, for enduring all the visa applications, long hours of imaging, failures and setbacks. It certainly has been a difficult journey but I grew to see this PhD as an opportunity to learn about myself, people as well as science. And I am very proud of my growth and the person it has made me. I am proud to have pushed myself to learn new things like coding but also learning when it's time to stop pushing myself and taking care of myself instead. Now as 2022 Parnian, I welcome a post-PhD life of continuing to learn, grow but mostly ***live***.

Chapter 1

Introduction

1.1 Overview

Biological oscillators are important orchestrators of the temporal events in development, physiology and behaviour (Uriu, 2016; Laje et al., 2018). They are classified according to their periodicity. Infradian and circadian oscillations with periods longer than or around 24 hours, respectively, coordinate seasonal and daily physiological and behavioural changes (Laje et al., 2018). In the past two decades, it has become clear that subtle intracellular temporal patterns were masked due to the predominant use of bulk-cell techniques and averaging in molecular and cell biology (Levine et al., 2013). As advances in these fields enabled reliable examination of gene and protein expression in single cells, a new class of oscillators with periodicities much shorter than 24 hours were identified. These so called ultradian oscillators, have since been found to be involved in many cellular contexts including development, cell proliferation and DNA damage response (Isomura, Kageyama, 2014).

Some of the best characterised ultradian oscillators are Hairy and Enhancer of split (HES) transcriptional inhibitors which are Basic helix-loop-helix (bHLH) proteins that play key roles in vertebrate segmentation clock (Aulehla et al., 2008; Rohde et al., 2021), and in cell fate determination in the developing Central nervous system (CNS) (Shimojo et al., 2008; Imayoshi et al., 2013; Manning et al., 2019; Imayoshi et al., 2015). In the segmentation clock, *Hes* gene oscillations in the Presomitic mesoderm (PSM) are more or less synchronised in cells that are physically close to each other. This feature makes them detectable with less sensitive tools for visualising gene expression such as In-situ hybridisation (ISH) (Holley et al., 2000; Oates, Ho, 2002; Sieger et al., 2004; Shankaran et al., 2007). But since *Hes* oscillations in the CNS are often asynchronus between neighbouring cells, their detection and investigation has been only possible with the development of engineered reporters and knock-ins KI that enable real-time visualisation of expression dynamics in single cells. These tools have revealed the presence of HES oscillations in a range of CNS tissues.

The work of Shimojo et al. (2008) and Imayoshi et al. (2013) suggested that in mouse telencephalon slice and dissociation cultures, *Hes1* gene and HES1 protein were expressed in an oscillatory manner in all Neural progenitor cells (NPCs) (for gene/protein nomenclature guidelines used in this thesis please see 2.1). They also proposed that HES1 oscillations drive dynamic expression of proneural factors such as *Neurogenin 2 (Ngn2)*, *Delta-like 1 (Dll1)* (Shimojo et al., 2008) and Achaete-Scute Complex-Like 1 (Ascl1) (Imayoshi et al., 2013) which helped to maintain NPCs by preventing premature neural differentiation. In other CNS regions, HES oscillations were attributed to cell state transitions. For instance, Manning et al. (2019) showed that in mouse spinal cord slice cultures, the expression of HES5 (similar to HES1 in structure and function) was periodic or oscillatory in $\sim$40% of NPCs but more frequently observed in cells that are moving towards differentiation. Similarly, in the zebrafish hindbrain, Hairy-related 6 (Her6), the orthologue of HES1, was

reported to be aperiodically noisy in neural progenitors but oscillatory in cells transitioning towards differentiation (Soto et al., 2020).

Even though a complex picture of the involvement of *Hes* gene and HES protein oscillations in single cell behaviour and state transitions is emerging in different biological contexts, cell-population properties of these oscillators in the CNS have been mostly overlooked. Meanwhile, due to the fascination with high reproducibility of somitogenesis and almost synchronised oscillations despite intrinsic noise, a great deal of research has sought to uncover the collective properties of the segmentation clock in tissues (Horikawa et al., 2006). Cell coupling driven by Notch signalling has been found to be the main mechanism for noise cancellation and intercellular communication that underlies clock synchronisation (Jiang et al., 2000; Horikawa et al., 2006; Özbudak, Lewis, 2008; Lewis et al., 2009; Keskin et al., 2018). Notch signalling and oscillations of the Notch ligand Dll1 are also involved in the neural progenitors. But when it comes to how cell coupling affects the population, reports seldom go beyond describing the relationship between single cell oscillations in neighbouring cells which unlike the PSM, are anti-phase or out of phase (Shimojo et al., 2016; Kageyama et al., 2018).

Recently, Biga et al. (2021) have described previously unrecognised spatiotemporal pattern of HES5 expression in mouse spinal cord slice cultures. By computational assessment of this pattern, they proposed that different levels of cell-coupling can underlie different population-level patterns of HES5 in the neural tube which correspond to varying capacities for differentiation. This work highlights the relevance of examining cell-population behaviour in understanding aspects of CNS ultradian oscillators that are beyond the single cell. Zebrafish is a unique multi-cellular model where complex biological phenomena can be studied at various scales, from single cell to behaviour (Kozol et al., 2016). Therefore, it is an ideal system for studying and manipulating CNS oscillators at a single cells, cell population and systemic level which will ultimately provide better understanding of the nuances of neurodevelopment.

Much of the insight into single cell dynamics and oscillations have been achieved by a range of experimental methods that target different components of the oscillatory network. However, even though protein turnover is a key feature of these regulatory networks, its direct alterations have not been used as a tool to examine oscillatory behaviour in the neural context.

In this chapter, I aim to provide further detail of the HES oscillatory networks and outline some approaches that have been used for their manipulation. After an overview of protein turnover in cellular processes, I will review the literature that has revealed its importance in oscillatory networks. This is to highlight the potential of alterations in protein stability as a tool for manipulating and understanding expression dynamics including ultradian oscillations. I will continue by describing the developmental characteristics of zebrafish forebrain which make it suitable for observing and altering protein expression dynamics

in a neural context. This chapter will culminate in the research aims that have directed the work presented in my thesis.

1.2 HES1 structure and function

The mammalian HES factors are homologous to the Drosophila hairy and Enhancer of Split [E(Spl)] proteins. They are transcriptional inhibitors localised in the nucleus that can actively or passively repress the transcription of target genes (Kageyama et al., 2007). The structure of HES proteins which consists of three conserved bHLH, Orange and WRPW domains is shown schematically in figure 1.1,A (Akazawa et al., 1992; Sasai et al., 1992; Kageyama et al., 2007). The Basic helix-loop-helix (bHLH) domain can be divided to two functional regions: the basic region (b) that mediates DNA binding and the Helix-Loop-Helix (HLH) region which allows dimerisation. The Orange domain is involved in the selection of dimerisation partners (Kageyama et al., 2007; Kobayashi, Kageyama, 2014) while the WRPW domain is critical in recruiting co-repressor factors Transducing-like E(spl) (TLE1-4)/Groucho-related gene (Grg) for inhibiting the transcription of target genes (Fisher et al., 1996; Grbavec, Stifani, 1996). The WRPW domain is also involved in proteasomal degradation of HES proteins (Kang et al., 2005; Chen et al., 2017).

Some bHLH factors such as ASCL1 are transcriptional activators which often bind to an E box (CANNTG) consensus sequence, usually following heterodimerisation, like the ASCL1-E47/E12 heterodimer (Fig 1.1,B) (Johnson et al., 1992). But in the case of the HES factors that are transcriptional inhibitors, a single Proline residue in the basic domain weakens their interaction with the E box while allowing strong binding to an alternative consensus sequences the N box (CACNAG) or the class C site (CACG(C/A)G) (Akazawa et al., 1992; Sasai et al., 1992; Kageyama et al., 2007).

During neuronal development, HES1 is associated with promoting progenitor maintenance and self renewal by preventing premature neuronal differentiation. This was demonstrated by Nakamura et al. (2000) who analysed *Hes1*$^{-/-}$ mouse embryos in detail. Using a neurosphere formation assay, they showed that while neurospheres from *Hes1*$^{-/-}$ telencephalic cells (primary neurospheres) were the same size as those generated from Wild type (WT), they were far fewer. These primary neurospheres also did not reproduce as many secondary neurospheres after dissociation. Combined, these findings suggested that the absence of *Hes1* had reduced the self-renewal capacity of telencephalic NPCs. They further demonstrated that relative to WT, *Hes1*$^{-/-}$-derived primary neurospheres were more prone to generate neuronal-only clones in expense of clones with both neuronal and glial fates (Nakamura et al., 2000) suggesting a role for *Hes1* in keeping neuronal fates in check.

In line with this, it is known that HES1 inhibits transcription of genes that promote neural differentiation (i.e. proneural genes) and cell cycle exit. For instance, it can passively repress the function of proneural bHLH factor ASCL1 by directly forming a complex with

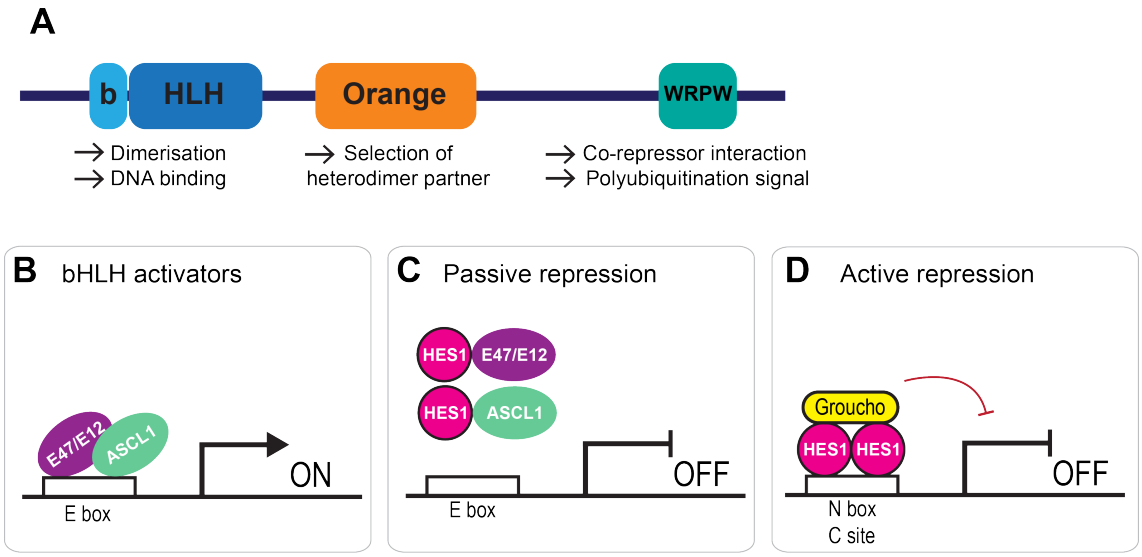

Figure 1.1: **HES protein structure and modes of function.** **(A)** HES factors share three conserved domains. The bHLH is involved in protein dimerisation and DNA binding. Orange domain mediates heterodimer partner selection. The WRPW domain enables co-repressor interaction and polyubiquitination of the protein. **(B)** bHLH activators like ASCL1 bind co-factors such as the E47/E12 protein and bind E box sequences of their target genes. **(C)** HES1 can passively repress some targets like ASCL1 by directly binding to the protein or its co-factor to prevent their binding to the E box. **(D)** HES1 can also actively repress genes by homodimerisation and forming a complex with Groucho. This complex can bind N box or C sites of target genes and actively repress their transcription. Adapted from Johnson et al. (1992); Kageyama et al. (2007); Kobayashi, Kageyama (2014)

ASCL1 or its heterodimerisation partner E47/E12 which prevents them from binding to the E box sequence of their target genes (Fig 1.1,C Passive repression) (Sasai et al., 1992; Johnson et al., 1992; Kageyama et al., 2007). This has been suggested as the cause of strong *Ascl1* upregulation in *Hes1*$^{-/-}$ mouse embryos (Ishibashi et al., 1995). Furthermore, HES1 can mediate active transcriptional repression of target genes by directly binding the N box in their promoter regions (Fig 1.1,D). Findings in Small cell lung cancer (SCLC) cells have shown that HES1 can directly bind ASCL1 promoter and prevent its expression (Chen et al., 1997).

Due to compensation between HES factors, even more drastic phenotypes are observed when *Hes1*, *Hes5* and *Hes3* are depleted simultaneously. Hatakeyama et al. (2004) reported significant upregulation of *Ascl1* and the proneural Notch ligand, *Dll1*, across the developing CNS of *Hes1;Hes5* double mutant mouse embryos. *Hes1;Hes5;Hes3* mutant mice had increased expression of another proneural factor, *Ngn2*, in dorsal telencephalon which accelerated neurogenesis in favour of Cajal-Retzius cells but to the detriment of the non-neuronal secretory Choroid plexus cells that normally develop in this region (Imayoshi et al., 2008). Additionally, HES1 directly inhibits the expression of the cyclin-dependant kinase inhibitor *p21* that promotes cell cycle exit upon neural differntiation (Castella et al., 2000). These findings consolidated the narrative of HES1 as a switch whose presence maintained mitotically active neural progenitors and prevented premature differentiation while its absence led to cell cycle exit and neuronal differentiation.

The work of Hirata et al. (2002) was first to show that both *Hes1* mRNA and HES1 protein are expressed in an oscillatory manner in a variety of *in vitro* contexts. In this study, oscillations were measured following Fetal bovine serum (referred to as serum from hereon) treatment in bulk synchronised cells using Northern and Western blotting which lacked single cell insight. More recent studies that utilised advanced imaging techniques to observe these dynamics at a single cell level demonstrated that HES1 function is indeed nuanced and dependant on its dynamics.

In the mouse telencephalon dissociation and slice cultures, *Hes1* gene expression was shown to be oscillatory which was observed with a *Hes1* promoter-Luciferase reporter (Shimojo et al., 2008). Shimojo et al. (2008) introduced constituitively active HES1 expression vector into mouse developing telencephalon by electroporation and later dissociated the telencephalon to analyse gene expression by microarray. They showed that persistent and high levels of HES1 induced marked down regulation of proneural genes including *Ascl1*, *Ngn2*, *Dll1* and *Neurod4* as well as regulators of cell cycle progression like *Cyclin D1*. The unexpected simultaneous down regulation of proneural and cell cycle progression genes in sustained presence of HES1 highlighted the importance of its oscillatory dynamics and showed that HES1 does not merely act as an on/off switch. At a single cell level, HES1 expression had inverse correlation with expression of proneural factors such as Ngn2 and Dll1 (Shimojo et al., 2008). Additionally, Shimojo et al. (2008) used Luciferase reporters under the regulation of *Ngn2* or *Dll1* promoters to show that the expression of these genes oscillated in cells that were negative for the neuronal marker Tuj1 whereas they were expressed in a sustained manner in differentiated Tuj1$^+$ cells (i.e. neurons).

These findings were further supported by Imayoshi et al. (2013). They generated Bacterial artificial chromosome (BAC) transgenic mice with protein reporters for HES1 or ASCL1 where the coding sequence for the protein was fused to Luciferase. Their examination of protein dynamics at single cell level in telencephalon slice cultures confirmed the HES1 oscillations that were reported by Hirata et al. (2002). Furthermore, Imayoshi et al. (2013) also showed that HES1 oscillations were anti-correlated with oscillations of ASCL1. In asymmetric divisions, ASCL1 accumulated in daughter neurons. However, in daughter neural precursors, both HES1 and ASCL1 oscillations continued (Imayoshi et al., 2013). Combined, these findings led to the proposal that neural progenitor state is defined by HES1 oscillations which drive dynamic expression of proneural factors such as *Ascl1* and *Ngn2* while differentiation is defined by sustained expression of one of these proneural factors (Fig 1.2).

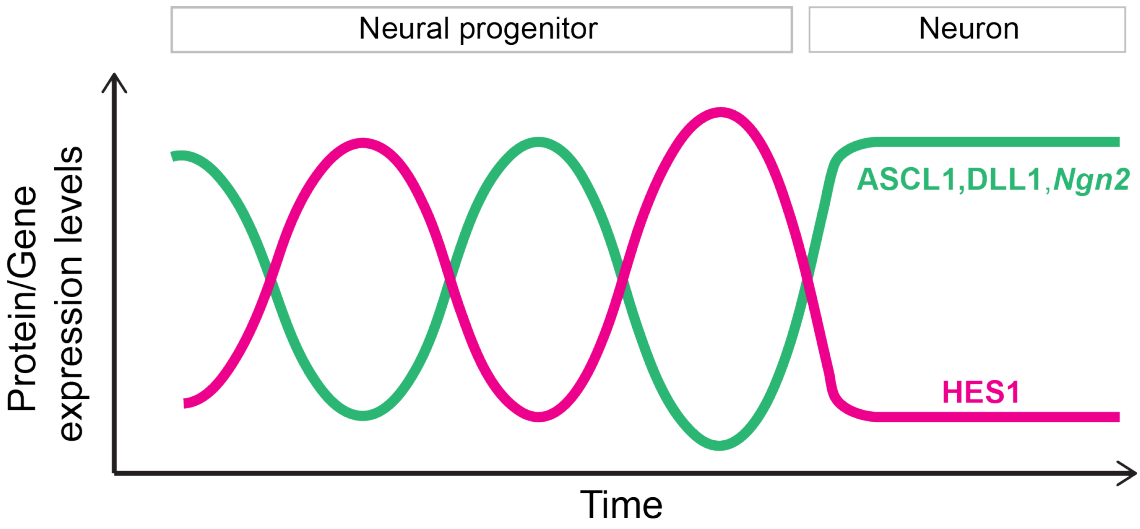

Figure 1.2: **Dynamic model purposed to distinguish progenitor and neuronal fates.** Based on this model which is predominantly based on mouse telencephalic cells, neural progenitors express *Hes1* and proneural genes like *Ascl1*, *Ngn2* and *Dll1* simultaneously in an oscillatory but anti-phase manner (i.e. when *Hes1* peaks, the proneural genes trough). In his model, neuronal differentiation occurs when *Hes1* is downregulated and proneural genes are expressed at high levels and sustained manner. Adapted from Kageyama et al. (2018)

Studies of other developmental contexts in the CNS have expanded on the role of HES oscillations at a single cell level. In the mouse spinal cord, HES5 expression displayed a range of dynamic fluctuations which in 41% of cells, were periodic oscillations with a declining trend. In this context, oscillatory HES5 expression was more prevalent in cells that displaced further from the ventricles and into the mantle zone where differentiation takes place (i.e. differentiating cells). This is while progenitors were more likely to display noisy but aperiodic fluctuations (Manning et al., 2019). Similar findings were reported in zebrafish hindbrain where Her6, the orthologue of HES1, was expressed in a noisy but aperiodic manner in early stages of hindbrain development and switched to a more oscillatory expression regime allowing the progenitors to undergo state transitions toward neural differentiation (Soto et al., 2020). In short, these findings have shown the involvement of HES oscillations in cell state transitions between progenitor and differentiated fates.

1.3 *Hes1* gene regulatory network

Hes1 expression dynamics are a result of the specific properties of its gene regulatory network that allows the mRNA and protein to be expressed in an oscillatory manner (Fig 1.3). Like many biological oscillators, a delayed auto-inhibitory feedback loop lies at the core of *Hes1* expression dynamics (Monk, 2003; Imayoshi, Kageyama, 2014). HES1 strongly binds to a consensus CACNAG or the N box sequence (Akazawa et al., 1992; Sasai et al., 1992) which is also present in the promoter region of the *Hes1* gene itself. This allow HES1 to bind this promoter and inhibit the transcription of its own gene (Takebayashi et al., 1994). Mathematical modelling of the *Hes1* network has also confirmed that the intrinsic

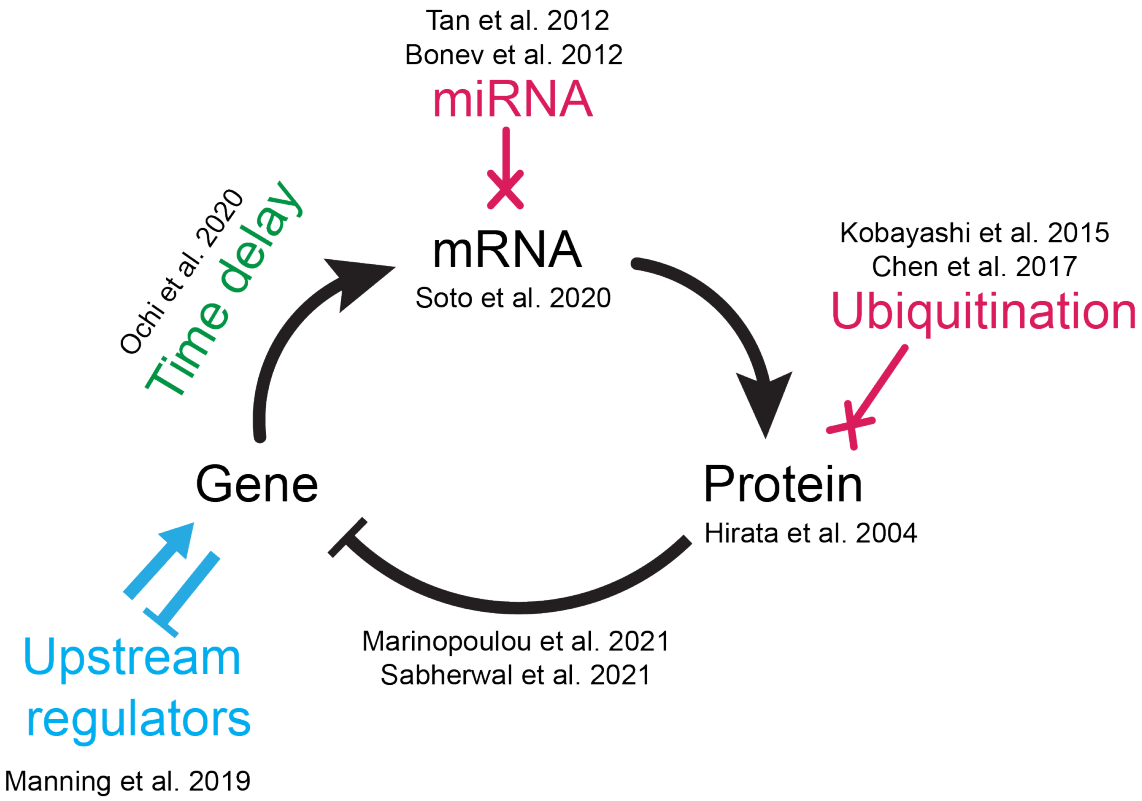

Figure 1.3: **Overview of a delayed auto-inhibitory feedback loop network** *Hes* genes have upstream regulators such as Notch. They are transcribed and result in the mRNA. This process is inherently associated with time delays. *Hes* mRNA is rapidly degraded which due to micro RNA (miRNA) function in case of *Hes1*. The mRNA is translated into the HES proteins which itself is short lived as it is degraded by ubiquitination. The HES protein is a transcriptional repressor which inhibits target genes but also its own gene forming an auto-inhibitory feedback loop. The citations refer to the literature that have targeted each part of this network (further described in section "Altering oscillations but manipulating different aspects of the oscillatory networks").

delay of transcription and translation is a critical component for generating oscillations (Monk, 2003).

In addition to the delayed auto-inhibitory feedback, generating ultradian oscillations also requires optimal kinetics of molecular turnover (Monk, 2003; Isomura, Kageyama, 2014). In biological systems, this is often reflected in mRNA and protein instability. Indeed, the mouse HES1 protein is short-lived with a half-life of ∼22.3 minutes since it is rapidly ubiquitinated and degraded (Hirata et al., 2002). *Hes1* mRNA also has a short half-life of ∼24.1 minutes (Hirata et al., 2002) under the control of microRNA 9 (miR-9) which binds to the *Hes1* 3'-UTR to mediate its degradation (Bonev et al., 2012; Tan et al., 2012). In theory, this prevents mRNA and protein accumulation in the cell, allows the system to be cleared in a timely manner and relieves the gene from its auto-inhibition. This, in turn, enables the re-expression of mRNA and protein and resetting the oscillatory cycle. Apart from these cell autonomous components, HES dynamics are also influenced by the upstream regulation of Notch which acts as a coupling mechanism and is further discussed in the next section.

1.4 Notch/*Hes*-mediated cell coupling

The Notch/*Hes* signalling that mediates intercellular communication was first identified in the context of lateral inhibition in Drosophila neurogenesis (Cabrera, 1990) (reviewed Hartenstein, Wodarz (2013)) and was later found to be conserved in vertebrates (Kageyama, Nakanishi, 1997). Notch is a cell surface receptor protein that consists of two fragments associated together as a functional heterodimer (Ohtsuka et al., 1999; Kageyama et al., 2007). The interaction of Notch with its ligand (e.g. Delta or Jagged) on the surface of a neighbouring cell triggers a series of successive proteolytic cleavages that culminate in the release of Notch intracellular domain (NICD) mediated by γ-Seratase enzymes (Kageyama et al., 2007). NICD translocates into the nucleus where it forms a ternary complex with Recombination signal-sequence binding protein (RBP-j) and Mastermind-like (MAML) proteins to activate transcription of downstream target genes (Kageyama et al., 2007; Kobayashi, Kageyama, 2014). This process is shown schematically in figure 1.4,A.

Hes1, *Hes5* and *Hes7* have RBP-j binding sites in their promoter regions and can thereby be expressed directly as a result of Notch activation (Jarriault et al., 1995; Bessho et al., 2001; Katoh, Katoh, 2007). This was supported by the findings of Ohtsuka et al. (1999) who infected cultured NPCs derived from embryonic mouse brains with retroviruses that express constitutively active form of Notch (caNotch). caNotch induced *Hes1* and *Hes5* expression in these cells. Furthermore, it prevented neuronal differentiation in cells derived from WT, $Hes1^{-/-}$ and $Hes5^{-/-}$ but not in $Hes1^{-/-}$- $Hes5^{-/-}$ double mutants (Ohtsuka et al., 1999). Based on these findings, Notch regulates *Hes1* and *Hes5* that in turn, prevent neuronal differentiation but can also compensate for each other.

The involvement of these *Hes* genes in the Notch signalling pathway in vertebrates fit well with the classical model of canonical Notch signalling and lateral inhibition which had been characterised earlier in *Drosophila* and C.elegans (Collier et al., 1996; Artavanis-Tsakonas et al., 1999). Based on this model, expression of the Notch ligand, Delta on one cell (Sender) would activate Notch and thereby the expression of *Hes* genes in its neighbouring cell (Receiver). In the Receiver cell, proneural bHLH factors along with Delta would be repressed, preventing Notch activation in the Sender and maintaining it in the progenitor state (Kageyama et al., 2007; Boareto, 2020) (Fig 1.4,A).

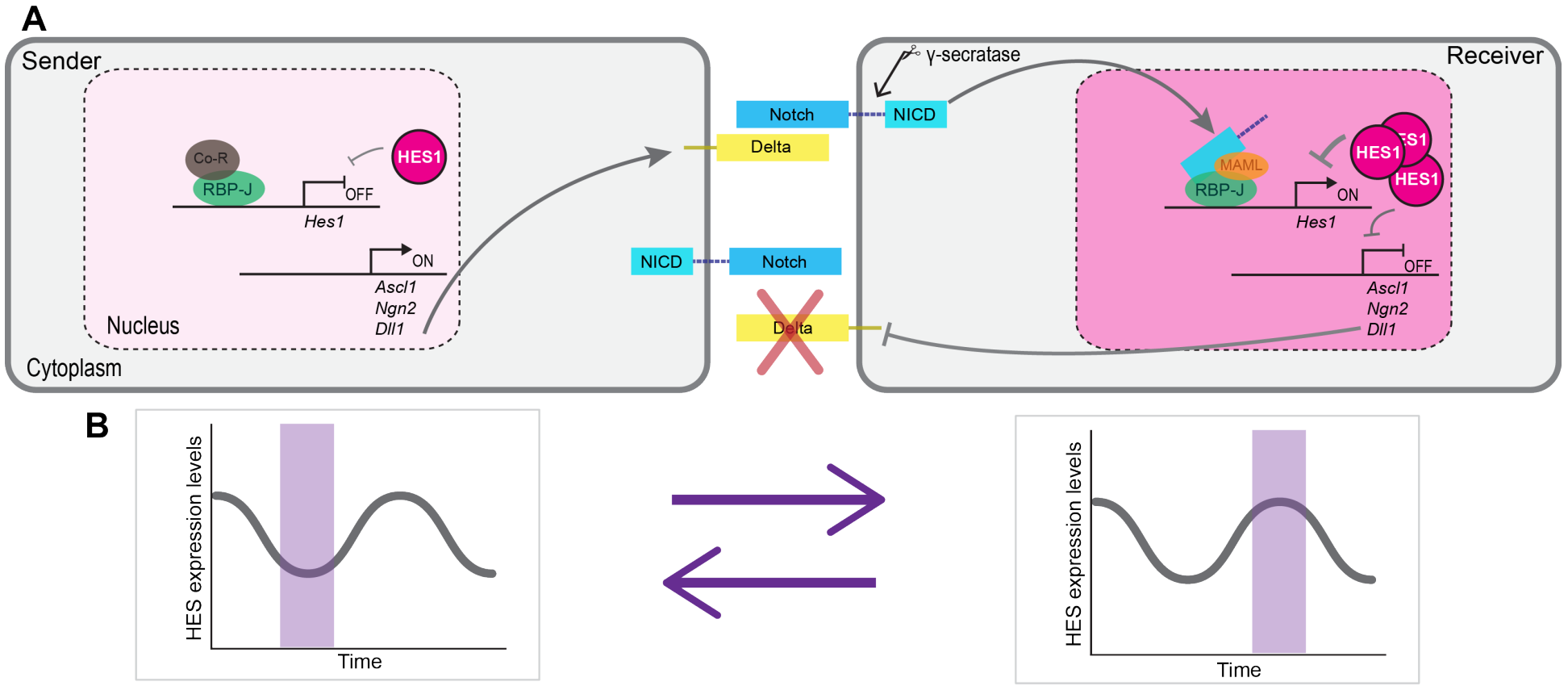

Figure 1.4: **Schematic diagram of Notch/HES mediated dynamic lateral inhibition. Caption on following page →**

Figure 1.4: **(A)** In the Sender cell Notch signalling is not active and RBP-J is bound to co-repressors that prevent it from activating *Hes1* gene. HES1 levels are low and *Hes1* and proneural genes like *Ascl1* and *Ngn2* are not strongly inhibited by HES1. The Notch ligand *Dll1* is also expressed and the protein is translocated to the cell membrane where it interacts with Notch in the Receiver cell. This activated a proteolytic cascade that culminates with cleavage of the Notch intracellular domain (NICD) by γ-secratase enzymes. NICD translocates to the nucleus where it binds with MAML and RBP-J to form an active complex that induces *Hes1* gene expression. The levels of HES1 protein increase and more strongly inhibits *Hes1* and proneural genes including *Dll1* which prevents Notch activation in Sender. **(B)** Rather than leading to static cell states, in the dynamic view of lateral inhibition, the Sender and Receiver states correspond to different oscillatory phases of HES protein over time in the progenitor state. The Sender state is at an HES1 expression trough while the Receiver is at a peak and they can dynamically switch over time. Adapted from Kageyama et al. (2007, 2018); Boareto (2020)

Fundamentally, the classical view of Notch-directed cell coupling in the developing CNS remains valid. However, as the dynamics of its components have been revealed, it has been adapted to a more dynamic view. This means that Sender and Receiver identities do not necessarily correspond to static states but different dynamic phases that can switch over time until cell fate decisions are made (Fig 1.4,A&B) (Kageyama et al., 2018). In addition to the *Hes* factors that exhibit oscillatory behaviour, *Dll1* gene and DLL1 protein are also known oscillators (Shimojo et al., 2008, 2016). Abolishing DLL1 oscillations by altering the length of its gene, did not affect its ability to activate Notch but did dampen *Hes1* oscillations. Hence, it became apparent that DLL1 and *Hes1* oscillations are interconnected. Using an optogenetic method, Isomura et al. (2017) addressed the question of intercellular transmission of oscillations by co-culturing a population of light-insensitive cells containing a *Hes1* reporter (Receivers) with cells that contained light-inducible *Dll1* (Senders). They succeeded to entrain the otherwise asynchronous oscillations of the *Hes1* reporter in the receiver cells by pulsing light and thereby controling *Dll1* oscillations in sender cells. This provided experimental evidence that the Notch/Dll control over oscillations of *Hes1* is transmissible between cells. In short, Notch/Dll and *Hes* networks enable dynamic coupling between neighbouring cells in the developing CNS.

1.5 Altering oscillations by manipulating different aspects of the oscillatory networks

Uncovering the dynamic nature of factors critical in neural development raised one important question: Are these oscillations encoding functional developmental signals or are they merely inevitable bi-products of the gene regulatory network? To answer this question, a wide range of experimental methods have been used to manipulate different aspects of the gene regulatory network and examine the functional consequences of altering the oscillatory dynamics (Fig 1.3). Some global approaches have targeted Notch, one important upstream regulators of the *Hes* cascade. For instance, Manning et al. (2019) treated mouse spinal cord slice cultures with the Notch inhibitor Dibenzazepine (DBZ). This shifted the type of dynamics exhibited by HES5 towards a predominantly oscillatory regime which

was often associated with cells transitioning towards neural differentiation.

The negative feedback aspect of the network has also been examined in HES1 regulation. This was achieved by the introduction of exogenous *Hes1* under the control of a ubiquitous Ubc promoter which unlike the endogenous *Hes1* promoter, cannot be inhibited by HES1 (Fig 1.3). This has been shown to override the endogenous HES1 oscillations in both MCF7 breast cancer cell line and dissociated mouse neural stem cells (Sabherwal et al., 2021; Marinopoulou et al., 2021). In MCF7 cells, abolishing HES1 oscillations impeded cell cycle progression, potentially by altering p21 expression dynamics during the cell cycle. This also affected fate determination in the cells based on the enrichment of $CD44^{High}/CD24^{low}$ cancer stem cells (Sabherwal et al., 2021). In neural stem cells, this manipulation revealed that HES1 oscillations are important in exit from quiescent state (Marinopoulou et al., 2021).

Changing gene length can alter the transcriptional time-delay and thereby dampen oscillations. Shimojo et al. (2016) generated two *Dll1* mutant mice with altered transcriptional delay. In one, *Dll1* introns were removed and in the other, the intron-less *Dll1* construct was added to the first exon of the WT *Dll1*, which elongated the gene. Both mutations quenched DLL1 oscillations in the PSM and neural progenitors, resulting in fusion of somites and reduced brain size in mouse embryos, respectively. Amplitude death in DLL1 oscillations also hindered *Hes1* oscillations in the neural progenitors (Shimojo et al., 2016). Removal of *Hes1* introns also reduced its transcriptional delay, dampened the amplitude of the oscillations to 37% of the WT. As a result of progenitor depletion and premature differentiation, mice with intron-less *Hes1* had premature upregulation of proneural genes and microcephalic phenotypes (Ochi et al., 2020).

Rapid mRNA turnover is another contributing factor in enabling oscillations. *Hes1* mRNA has a short half-life of $\sim$24 minutes (Hirata et al., 2002). The microRNA MiR-9 is responsible for modulating the stability of *Hes1* mRNA by binding its 3'UTR (Bonev et al., 2012). In support, inhibiting miR-9 in cerebellum derived neural stem cells (c17.2) using a Locked nucleic acid inhibitor (LNAi) increased levels of endogenous HES1 protein. Furthermore, luciferase reporter driven by *Hes1* promoter which included a mutated *Hes1* 3'UTR showed dampened *Hes1* oscillations in c17.2 cells in comparison to the WT 3'UTR (Bonev et al., 2012). This correlated with the fact that miR-9 depletion promoted maintenance of neural progenitors in Xenopus (Bonev et al., 2011) and mouse telencephalon (Tan et al., 2012). Bonev et al. (2011) also confirmed that these effects in Xenopus are related to the misregulation of *hairy1* (Xenopus orthologue of *Hes1*) and not other miR-9 targets. For this, they compared the phenotype induced by a target protector morpholino that blocks the *hairy1* miR-9 binding site (MBS) with miR-9 morpholino. They showed that in both cases, the expression of *N-Tubulin*, a marker of differentiated neurons is decreased, in line with the role of miR-9 in promoting neuronal differentiation (Bonev et al., 2011). In zebrafish hindbrain, when the endogenous MBS of *her6* (a *Hes1* orthologue)

was mutated, the Her6 protein was less likely to exhibit oscillatory down-regulation which is required for the transition towards differentiation (Soto et al., 2020).

Advances in optogenetics have lead to engineering of tools that allow precise control over the frequency of oscillations at the gene level (Isomura, Kageyama, 2014). One such system makes use of engineered protein Gal4 DNA binding domain and p65 activation domain (GAVPO) that when exposed to blue light illumination, forms a homo-dimer, binds UAS sequences and activates target gene expression (Wang et al., 2012) (Fig 1.5). The GAVPO-based system has been used to create a light-inducible ASCL1. Light-induced ASCL1 oscillations promoted proliferation in neural progenitors while light-induced sustained ASCL1 expression was permissive to neuronal differentiation (Imayoshi et al., 2013). A similar approach clarified that light-induced oscillations of DLL1 maintain neural progenitors while its sustained expression promotes differentiation, accompanied by upregulation of proneuronal gene *Ascl1* and cell cycle inhibitor *p21* (Shimojo et al., 2016). Additionally, using optogenetics, Isomura et al. (2017) have provided experimental evidence that the Notch/Dll control over oscillations of HES1 is transmissible between cells. These optogenetic systems have also been used as tools for measuring delays associated with transcriptional delay (Shimojo et al., 2016) and signaling transfer between coupled cells (Isomura et al., 2017).

Protein is the component of the oscillatory network that directly regulates the downstream genes and is therefore the functional hand of the network dynamics. As such, alterations directed at the protein are a useful way of interrogating the system. Furthermore, measuring protein stability is less technically demanding in comparison to some other features such as time delay. These features make protein degradation an appealing component to explore. In the following section, I will focus on this aspect of the gene network to highlight its potential for interrogating protein expression dynamics.

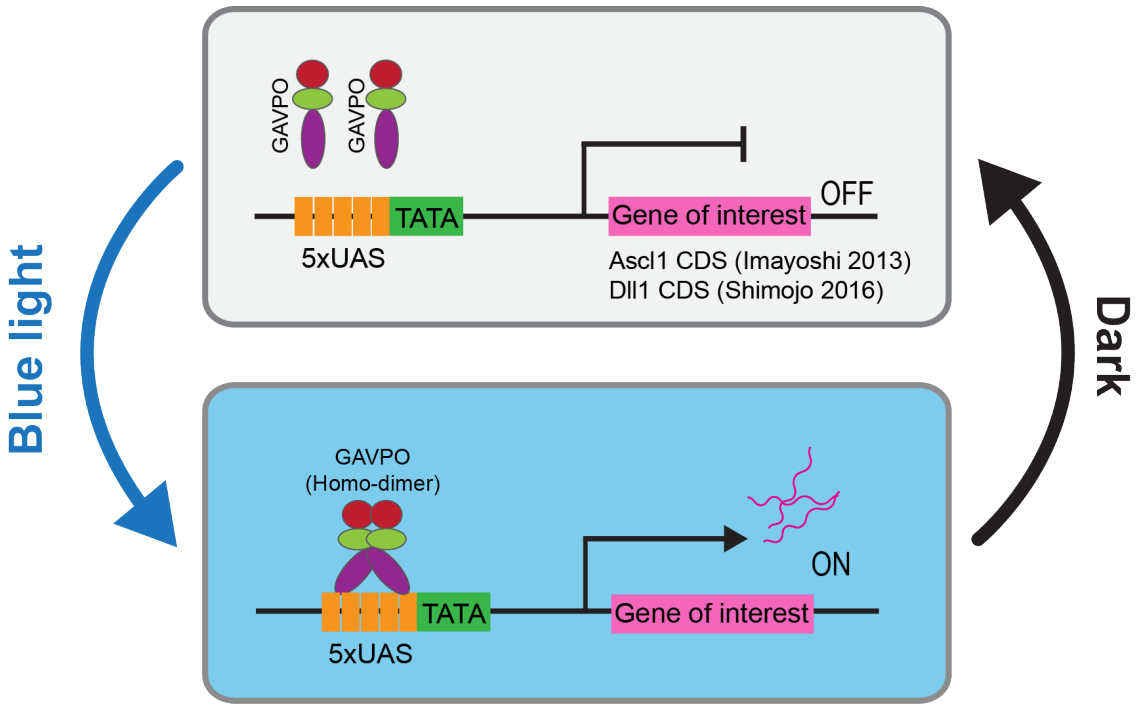

Figure 1.5: **Schematic diagram of the GAVPO light inducible system.** For using this system, the coding sequence for the gene of interest (*Ascl1* in Imayoshi et al. (2013) and *Dll1* in Shimojo et al. (2016)) is cloned downstream of 5 UAS sequences combined with a TATA sequence. In dark conditions, the Gal4 DNA binding domain and p65 activation domain (GAVPO) protein complex exists as a monomer which does not bind DNA. Upon exposure to blue light, GAVPO form Homo-dimer that can bind UAS sequences and activate expression of the gene of interest. Adapted from Wang et al. (2012)

1.6 Protein degradation and oscillations

Targeted protein degradation is an efficient method for regulating protein levels. Hence, proteolysis underlies all cellular processes that require cells to reprogram rapidly (Varshavsky, 1996; Zhou, 2004). It is therefore not surprising that ubiquitination directed proteolysis which is a mechanism for selective protein degradation (Hershko, Ciechanover, 1998) is a pivotal component of dynamic events such as the cell cycle (reviewed by King et al.), apoptosis (reviewed by Jesenberger, Jentsch (2002)) and ultradian oscillations (Hirata et al., 2002; Bessho et al., 2003).

1.6.1 Overview of ubiquitination-mediated protein degradation

Ubiquitination is a process whereby targeted proteins are covalently ligated to ubiquitin, a conserved small protein that marks them for proteolysis (Hershko, Ciechanover, 1998). This process requires the sequential action of three different types of enzymes, E1, E2 and E3. First, the ubiquitin is activated by specific activating enzymes (E1). This activated molecule binds the E1 enzyme and is then transferred to the active site of a ubiquitin-carrier enzyme (E2). In the third step, ubiquitin is added to a Lysine (K) residue in the target protein by a ubiquitin ligase (E3) enzyme. Proteins ligated to a polyubiquitin chain

are usually degraded by the 26S proteasome complex (Hershko, Ciechanover, 1998). E3 enzymes are the most important ones in determining the specificity of substrate selection for ubiquitination (Ravid, Hochstrasser, 2008).

Certain triggers for ubiquitination have been found in target proteins. For instance, Proline, Glutamate, Serine and Threonine rich sequences, also known as PEST domains, are observed in many rapidly degrading proteins (Rogers et al., 1986; Ghoda et al., 1989; Rechsteiner, Rogers, 1996). Phosphorylation can also act as a signal for ubiquitination and in some, but not all cases, the phosphorylated residues are within the PEST domains (Hershko, Ciechanover, 1998). The phosphorylation degradation signals or phosphodegrons are best characterised for their role in elimination of Cyclin dependent kinases (CDKs) during the cell cycle (Ravid, Hochstrasser, 2008). Another well characterised trigger for ubiquitination is known as the N-end rule where the residues at the N-terminus of the target protein mediate its ubiquitination and degradation (Varshavsky, 1996).

Eliminating ubiquitination of specific proteins is often a reliable way of confirming the importance of their turnover kinetics in cellular processes. Classically, this has been done by mutating the ubiquitin-targeted Lysine residues in the substrate (Treier et al., 1994; Xu, Jaffrey, 2013). A more recent method for impeding ubiquitination is to covalently fuse the catalytic domain of a Deubiquitinating enzyme (DUB) to the protein of interest (Stringer, Piper, 2011). DUBs are proteases that counteract ubiquitin ligases by removing ubiquitin from proteins and preventing their degradation (Nijman et al., 2005). The major advantage of using DUB catalytic domains is that it does not require precise knowledge of ubiquitination sites (Stringer, Piper, 2011). However, this alteration leads to complete stabilisation of the protein of interest and therefore mimics over expression (Stringer, Piper, 2011).

1.6.2 Alterations of HES oscillations by targeting protein stability

Rapid clearance of HES proteins from the cell is critical in relieving auto-inhibition and generating periodic expression. Consistent with this, both HES1 and HES7 proteins are ubiquitination targets. As a result, proteosome inhibition with MG132 stabilises both proteins and inhibits their oscillatory expression in serum-starved mouse fibroblast cells (C3H10T1/2) in response to serum (Hirata et al., 2002; Bessho et al., 2003).

This feature was further explored by Hirata et al. (2004) who used the classic method of targeting Lysine residues (Treier et al., 1994; Xu, Jaffrey, 2013) to directly manipulate the degradation of HES7 protein that oscillates in the PSM. For this, seven HES7 variants were generated, each with a single Lysine to Arginine (K>R) mutation. Their repressor activities were examined by co-transfection of Luciferase reporter under the control of an N-box containing promoter with WT or mutant *Hes7* vectors in C3H10T1/2 cells. They then measured the half-lives of the three HES7 mutants that retained their repressor activ-

ity by performing Cycloheximide (CHX) chase and Western Blot analysis in C3H10T1/2 cells. They further characterised the K14R mutation which partially stabilised the protein and increased its half-life from ∼22 minutes in WT to ∼30.3 minutes. HES7-K14R mutant KI mice exhibited WT gene expression during the generation of the first three to four somites. However, at later stages, HES7-K14R protein level was lower than WT and non-oscillatory. This suggested that an 8-minute increase in the protein half-life can dampen HES7 oscillations, consistent with in silico simulations of the WT protein and the stabilised version (Hirata et al., 2004).

More recently, some of the components of HES1 protein turnover have been identified and experimentally manipulated. Chen et al. (2017) discovered SCFFBXL14 as the ubiquitination complex that mediates the proteasomal degradation of HES1. Small interfering RNA (siRNA) Knock-down (KD) of RBX1, the Cullin-Ring E3 ligase of this complex in mouse-derived epithelial F9 cells, increased the HES1 half-life from approximately 50 to 110 minutes and prevented HES1 oscillations in response to serum by elevating its levels to a high steady state. Additionally, RBX1 KD in mouse embryonic stem cells also repressed proneural genes like *Ascl1* and *Dll1* as well as neuronal marker *Tuj1* (Chen et al., 2017). However, given that targeting the ubiquitin ligase completely stabilises its target proteins, there was a concern that the observed effects could be due to elevated levels of HES1 rather than its conversion from oscillatory to steady expression (Chen et al., 2017).

Deubiquitinating enzymes (DUBs) are also involved in oscillatory networks such as NFκ-B regulation (Wertz et al., 2004) and circadian networks (Oishi et al., 2003; Yang et al., 2012). DUBs that regulate HES1 have also been identified and targeted. The DUB Ubiquitin specific protease 22 (Usp22) has been reported to interact with mouse HES1 (Kobayashi et al., 2015). Indeed, *Usp22* KD in C3H10T1/2 cells using siRNAs, shortened HES1 half-life from 24.4 minutes to 19.3 or 15.9 minutes, depending on KD efficiency. Using Luciferase reporter under the control of *Hes1* promoter and single cell imaging in NIH3T3 fibroblasts, Kobayashi et al. (2015) showed that *Usp22* KD made the oscillatory period of *Hes1* expression more variable and increased the mean period from 151.2 minutes in control to 175.8 minutes. The authors suggested that this caused early desynchronisation of cells and abolished HES1 oscillations in response to serum at the population level in C3H10T1/2 cells. However, they provided no insight into how HES1 destabilisation affected the oscillations of the protein itself at a single cell level. Nonetheless, by electroporating *Usp22* siRNA into the embryonic mouse brain which resulted in premature neural differentiation, they showed that HES1 destabilisation causes developmental defects (Kobayashi et al., 2015).

The studies that were summarised in this section have provided the proof of concept that the kinetics of protein degradation can be altered to change the behaviour of the oscillatory network. However, due to the model systems that were used, these reports lack combined single cell and tissue level insight. This highlights the need for an alternative system for

further exploring the manipulations of protein stability as a tool for achieving altered protein expression dynamics and examining the impact in single cells and tissue environment simultaneously. Zebrafish presents an ideal model for this purpose where single cell, cell population and developmental response can be studied in the same context. To highlight its advantages, zebrafish neural development and the involvement of *Hes* genes in this process will be reviewed in the following sections.

1.7 Introduction to zebrafish as a suitable model for studying oscillatory dynamics

Zebrafish (Danio rerio) is in many respects a superior model organism for neurodevelopmental studies. Firstly, despite their distant evolutionary divergence from mammals, they are genetically comparable with higher organisms since approximately 71.4% of human genes have at least one orthologue in the zebrafish genome (Howe et al., 2013). Secondly, external fertilization makes the embryonic stages of zebrafish development accessible. Thirdly, the transparency of embryos is a huge optical advantage that allows live imaging at a single cell level (Schmidt et al., 2013; Kozol et al., 2016; Sakai et al., 2018). Lastly, zebrafish is amenable for genetic engineering and many methods have been developed for this purpose (Sassen, Köster, 2015; Rafferty, Quinn, 2018). These advantages, combined with the advances in gene editing technologies have made this organism a popular choice for real time explorations of oscillators in the segmentation clock (Özbudak, Lewis, 2008; Delaune et al., 2012; Soroldoni et al., 2014; Rohde et al., 2021) and more recently, the developing CNS (Soto et al., 2020).

1.8 Evolution of HES/Her bHLH factors in zebrafish

Based on their phylogenetic relationship and functional properties, bHLH factors have been divided to six higher-order groups of genes named A-F. Proneural bHLH factors are in group A, characterised by their binding to E box sequences in their target DNA. The HES/HEY factors are in group E which includes proteins characterised by preferential binding to the N box sequences as well as the presence of Orange and WRPW domain (Wang et al., 2009). Zhou et al. (2012) have proposed that all HES/HEY genes (group E bHLH factors) originated from one ancestral HEY gene in sponges which then diversified to four distinct groups: HEY1/HEY2/HEYL, DEC1/DEC2, HESL and HES1-7 which is the largest group. HES1-7 group of genes originated with the appearance of vertebrates (Zhou et al., 2012), allowing hundreds of millions of years of functional evolution.

19 of the 60 amino acids that form the bHLH domain are highly conserved between yeast to mammals (Wang et al., 2009). Using these 19 conserved amino acids of the bHLH domain,

Wang et al. (2009) identified 139 bHLH genes in zebrafish, 13 of which were HES1-7 genes in group E (HES/HEY). However, a later study which focused more specifically on identifying HEY/HEY factors in 17 species, found 22 HES/HEY genes belonging to the HES1-7 group in zebrafish which are often named Hairy-related (Her) genes (Zhou et al., 2012). This discrepancy may be explained by higher precision of the study by Zhou et al. (2012) for identifying HES/HEY factors by relying on not only one, but two conserved domains specific to this group, namely the Orange and bHLH domains (Zhou et al., 2012).

The presence of 22 HES1-7 homologous genes or Her genes in zebrafish in contrast to the 7 present in humans is due to combined influence of the whole genome duplication in fishes in addition to tandem duplication of specific HES/HEY genes (Zhou et al., 2012). For instance, the HES5 genes in zebrafish are distributed between chromosomes 11 and 23 (Zhou et al., 2012) which is perhaps the result of whole genome duplication. 5 of the 6 HES5 genes on ch23 are neighbour genes, supporting the hypothesis of tandem gene duplication events in certain gene clusters (Zhou et al., 2012). However, none of the zebrafish HES/HEY genes are zebrafish specific which is to say that they all correspond to one human orthologue (Zhou et al., 2012).

Figure 1.6 shows the expression of some of the *her* genes in 16-20hpf zebrafish embryos which highlights both their diversification and overlap predominantly using the data deposited by Thisse et al. (2001); Thisse, Thisse (2004); Thisse (2005) on the ZFIN database. Figure 1.7 includes all the 22 *her* genes identified by Zhou et al. (2012) and summarises the expression of those presented in figure 1.6. As it has been summarised by Dirian et al. (2014), all the *her* genes that have been studied in the developing CNS (e.g. *her4, her5, her6* and *her9*) are expressed exclusively in neural progenitors.

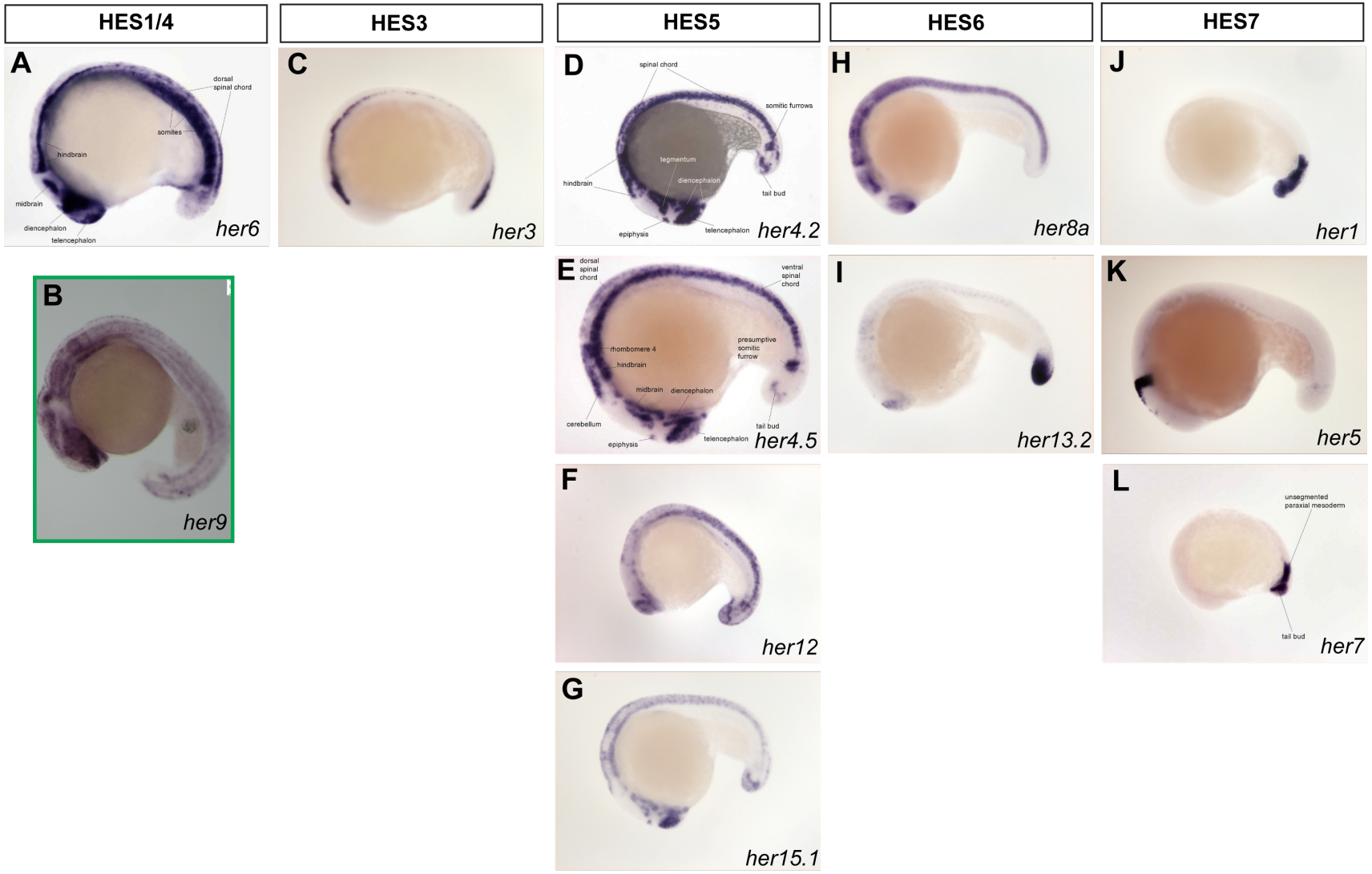

Figure 1.6: **mRNA expression of several *her* genes characterised using In-situ hybridisation (ISH) by Thisse et al. (2001); Thisse, Thisse (2004); Thisse (2005).** In all panels embryos are shown in lateral view, Anterior to the left. Each column corresponds to a human HES gene. Panel B outlined in green is my preliminary data (also seen in Appendix 8.10)

Human	ZF	Tel	Di	Mb	MHB	HB	CB	SC	SO	PAM	TB
HES1/4	her6										
	her9										
HES2	hes2.1										
	hes2.2										
HES3	her3										
HES5	her2										
	her4.1										
	her4.2			Tegmentum					Somitic furrows		
	her4.3										
	her4.4										
	her4.5								Somitic furrows		
	her12			ventral		ventral			caudal soomites		
	her15.1		ventral	ventral							
	her15.2										
HES6	her8a		Anterior								

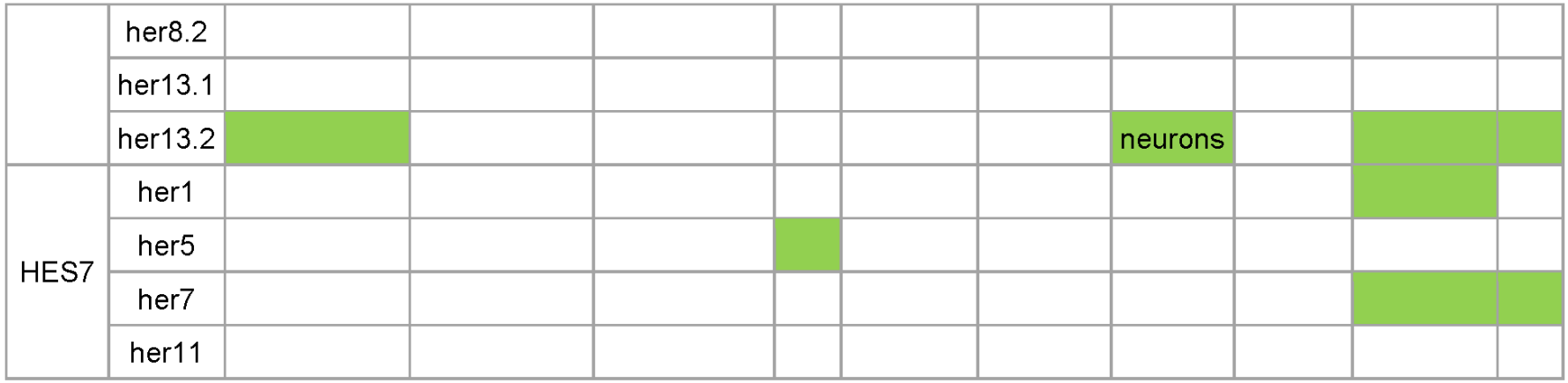

Figure 1.7: **All *her* genes identified in zebrafish by Zhou et al. (2012) and the summary of their expression based on figure 1.6.** Green shading refers to expression data based on figure 1.6. Dark green is based on images from Thisse et al. (2001); Thisse, Thisse (2004); Thisse (2005) and light green is based on my own data. No expression data was available for the 16-20hpf stage for *hes2.1, hes2.2, her2, her4.1, her4.3, her4.4, her15.2, her8.2, her13.1 and her11*. Tel: Telencephalon, Di: Diencephalon, Mb: Midbrain, MHB: Midbrain-hindbrain boundary, HB: Hindbrain, CB: Cerebellum, SC: Spinal cord, SO: Somites, PAM: Paraxial mesoderm, TB: Tail bud.

HES1 and HES4 are two closely related genes in the HES1-7 group that fit in one phylogenic clade (HES1/HES4) with three different tree generation methods (Neighbour-joining, Bayesian and Maximum-Evolution) (Zhou et al., 2012). Unlike some HES/HEY genes that have multiple copies in the zebrafish genome, this is not the case for HES1/HES4 as they directly correspond to Her6/Her9 in zebrafish. Despite their close phylogenetic relationship, while HES1 and HES4 have some overlapping functions in human development, they are not completely redundant. For instance, during human hematopoietic development, HES1 maintains hematopoietic progenitors in their quiescent stem cell state signified by CD34. Similarly, HES4 can prevent progression towards certain differentiated fates like natural killer and myeloid cells but it cannot repress B-cell development. Furthermore, HES4 can initiate T-cell development, a function it does not share with HES1 (De Decker et al., 2021).

To the best of my knowledge, no previous studies have compared the function of Her6 and Her9 in zebrafish CNS development. However, Soto et al. (2020) have shown that in 30-32hpf, while both *her6* and *her9* mRNAs are expressed in the developing CNS, their expression domains are not completely overlapping and at times are mutually exclusive. This was similar to my observations at earlier stages (16-20hpf) of *her9* mRNA expression using ISH in comparison to *her6* presented by Thisse et al. (2001). Specifically, at this early stage, *her9* was not expressed in the telencephalon while *her6* was extensively expressed in this region (Fig 1.6). Therefore, I suspect that Her6 and Her9 potentially have overlapping functions in the developing zebrafish CNS but these functions are not expected to be completely redundant.

As highlighted in previous sections, HES1 is one of the best characterised ultradian oscillators in the context of neural development. The wealth of knowledge on this gene, focused my attention on the zebrafish genes most closely related to HES1, Her6 and Her9, for studying HES/Her dynamics in this organism. Based on the reports of Soto et al. (2020), both *her6* and *her9* genes have binding sites for miR-9 which is an important factor in mediating oscillatory dynamics. But the miR-9 binding site (MBS) in *her6* is a better quality binding site (Soto et al., 2020). Therefore, *her6* was deemed more likely to exhibit detectable oscillatory dynamics. Hence, given these considerations and the focus of this thesis on such oscillatory dynamics, I decided to focus on *her6*.

1.9 Brief summary of neural induction and patterning of the zebrafish brain

Similar to other vertebrates, the specification of neural ectoderm is the initial stage of forming the nervous system in zebrafish. Neuroectoderm is induced at the onset of gastrulation by the complex interaction of extrinsic signals (BMP inhibition and FGF signalling) with the intrinsic transcription factor program including factors such as members of the

SRY-box containing B1 (SoxB1) family (Kimmel et al., 1995; Schmidt et al., 2013). In zebrafish, the neural tube does not directly result from folding of the neural plate. Instead, the folding of the neural plate at approximately 10 Hours post fertilisation (hpf) generates a condensed intermediate called the neural keel, which gives rise to the neural tube following cavitation (hollowing out) (Papan, Campos-Ortega, 1994; Kimmel et al., 1995).

The zebrafish brain acquires structural complexity in the early stages of its development which is schematically shown in figure 1.8. At 13hpf (Fig 1.8,A), the zebrafish brain lacks any morphological landmarks demarcating the different regions. However, they can be presumptively distinguished based on gene expression patterns (Bierkamp, Campos-Ortega, 1993). By 16hpf, the four prominent division of the brain namely the telencephalon and diencephalon in the forebrain, midbrain and hindbrain become readily distinguishable (Kimmel et al., 1995). Around 18hpf (Fig 1.8,B), the ventricles in the forebrain start to open, physically separating the telencephalon and diencephalon. Additionally, at this stage, the 7 segments of the hindbrain (rhombomeres) start to appear. By 24hpf (Fig 1.8,C), the morphological distinction of the telencephalon from the diencephalon is clearly visible. The hypothalamus, part of the diencephalon, is positioned ventral to the telencephalon. The ventricles in the midbrain become visible and this domain starts resembling the tectum. Posterior to the tectum, the developing cerebellum can be seen. By 30hpf (Fig 1.8,D), the optic stalk is positioned immediately ventral to the telencephalon while the hypothalamus moves posteriorly and folds underneath the rest of the diencephalon which includes the prethalamus and thalamus (Kimmel et al., 1995; Wilson, Houart, 2004).

1.10 The involvement of bHLH factors during zebrafish CNS development

Both proneural and inhibitory bHLH factors are extensively involved in zebrafish CNS development. In the posterior neuroectoderm, neurogenesis (here used to describe the process where some neural progenitors begin to move towards neural commitment and differentiation) starts with the expression of proneural genes such as *ascl1*, *ngn1* and *olig2* at $\sim$10hpf, towards the end of gastrulation (Allende, Weinberg, 1994; Blader et al., 1997; Park et al., 2002; Blader et al., 2003). These genes are expressed in proneural domains which are longitudinal stripes along the anterior-posterior axis of the dorsal ectoderm (Fig 1.9,A) (Allende, Weinberg, 1994; Park et al., 2002; Bae et al., 2006). At this stage, two *her* genes, *her3* and *her9*, are expressed in the space between these stripes known as interproneural domains, defining the boundaries of the proneural genes (Fig 1.9,B). In their combined absence, proneural genes become ubiquitously expressed in the neural plate (Bae et al., 2006). Hence, by actively inhibiting differentiation, these *her* genes maintain and expand the pool of cells (Schmidt et al., 2013). This is consistent with anti-neurogenic role of HES1 (Nakamura et al., 2000; Baek et al., 2006; Hatakeyama et al., 2004), the

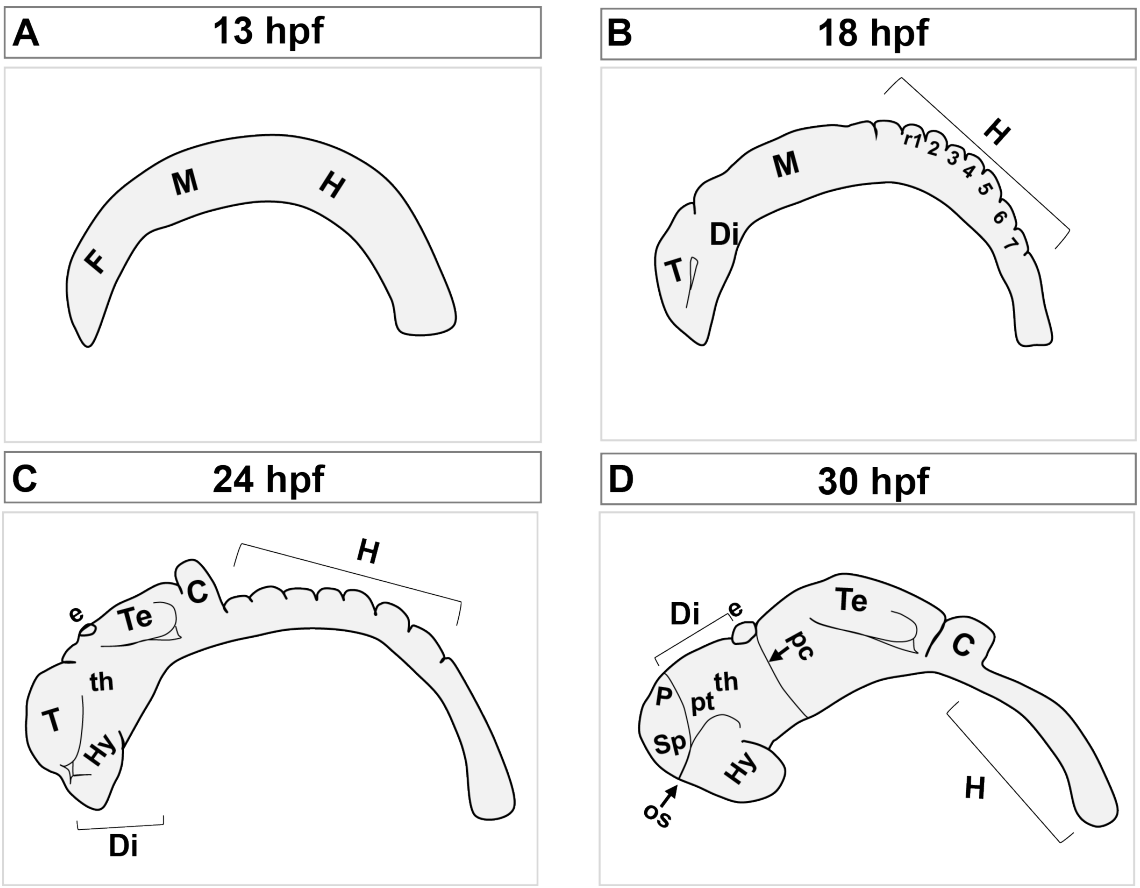

Figure 1.8: **Schematic diagram of anatomical features of the early brain development in zebrafish.** In all panels, embryos are shown without the yolk in a lateral view with anterior to the left. **(A)** In 13hpf embryo there are no morphological separation between different brain regions and are therefore labeled presumptively (Based on gene expression (Bierkamp, Campos-Ortega, 1993)). **(B)** By 18hpf, the telencephalon (T) and diencephalon (Di) can be distinguished. The midbrain (M) and the 7 rhombomeres (r) of the hindbrain (H) have also developed. **(C)** In the 24hpf embryo, the diencephalon expands to form the rudimentary hypothalamus (Hy) under the telencephalon (T). Thalamus (th) is located dorsal to the hypothalamus. Epiphysis (e) is seen at the dorsal roof of the diencephalon (Di). The tectum (Te) separates from the ventral midbrain. The cerebellum (C) becomes apparent between the midbrain and hindbrain (H). **(D)** Summary from different sources mainly Macdonald et al. (1994); Wilson, Houart (2004). The telencephalon consistes of pallium (P) dorsally and sub-pallium (Sp) ventrally with the optic stalk (os) immediately ventral to it. The Hypothalamus (Hy) folds and moves posteriorly to sit ventral to thalamus (th) and prethalamus (pt). The posterior commissure (pc) separates the diencephalon from the midbrain. F, forebrain; M, midbrain; H, hindbrain; T, telencephalon; Di, diencephalon; r, rhombomere; Hy, hypothalamus; th, thalamus; pt, prethalamus; Te, tectum; e, epiphysis; C, cerebellum; P, pallium; Sp, sub-pallium; os, optic stalk; pc, posterior commissure. Compiled based on Bierkamp, Campos-Ortega (1993); Macdonald et al. (1994); Barth, Wilson (1995); Kimmel et al. (1995); Wilson, Houart (2004)

mammalian orthologue of *her6/her9* (Wang et al., 2009; Coolen et al., 2012; Zhou et al., 2012). However, the expression of *her6* in these domains has not been described by Bae et al. (2006).

The earliest neurons in the posterior regions of zebrafish CNS appear between ∼14-16 hpf from the proneural domains. For instance, Rohon Beard neurons (RB) in the spinal cord which are primary sensory neurons involved in touch sensitivity, develop from the lateral expression stripes of *ngn1* (Fig 1.9,A) (Blader et al., 1997; Bae et al., 2006). This is while primary motoneurons involved in early movement, develop from the medial *ngn1* expression stripe (Fig 1.9,A) (Blader et al., 1997). *olig2* is also involved in development

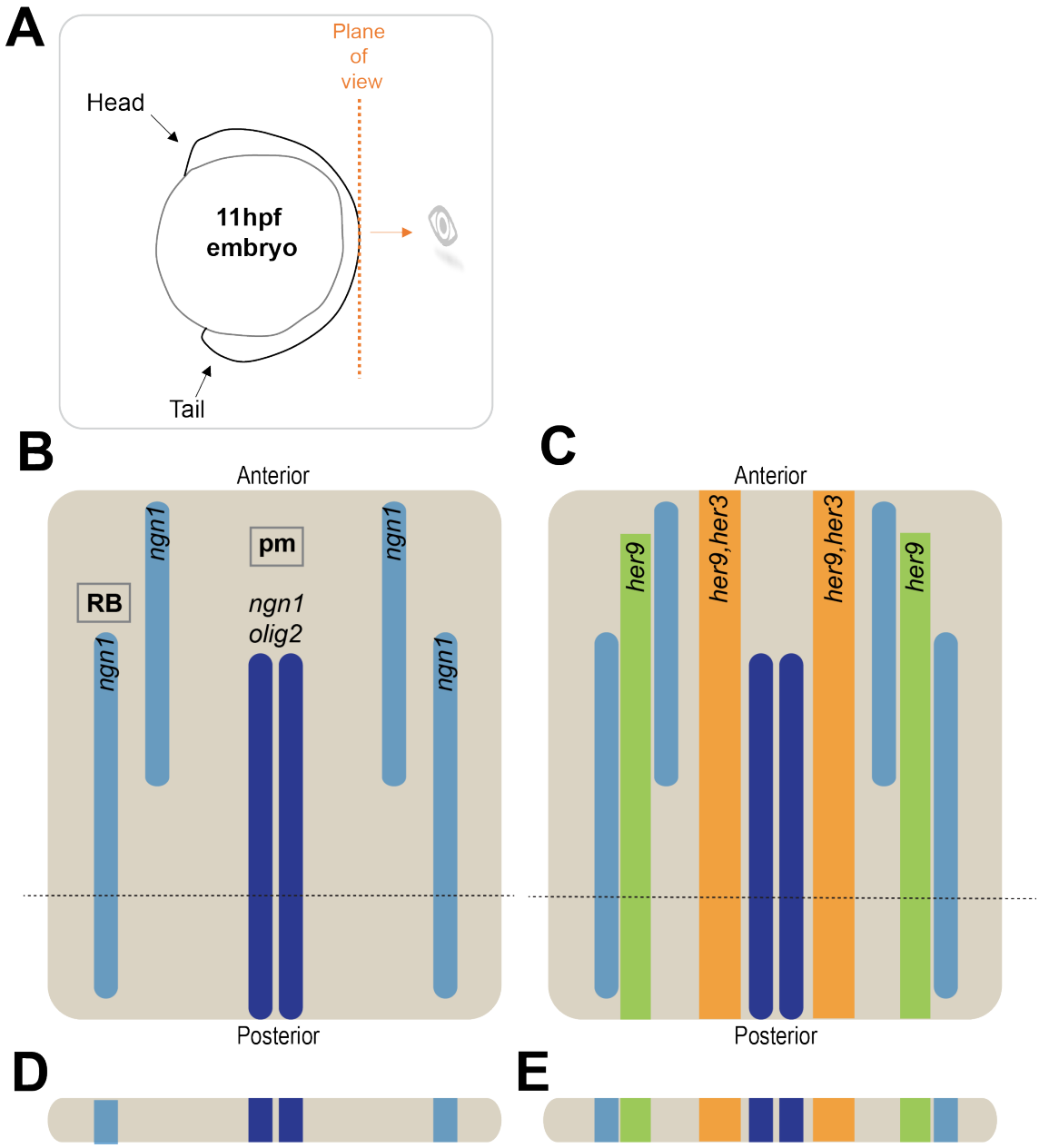

Figure 1.9: **Schematic diagram of the proneural and interproneural domains in posterior neuroectoderm. (A)** Schematic diagram showing an 11hpf embryo and the plane of view for observing the dorsal view of the hindbrain/spinal cord region. **(A)** Schematic position of the proneural domains based on expression of *ngn1* and *olig2* which proneural bHLH factors. *ngn1* is expressed in two medial stripes and four lateral stripes (two on each side of the embryo). *olig2* expression is more restricted and focused at the two medial lines. The medial proneural domains give rise to primary moroneurons (pm) and the lateral most domains give rise to Rohon Beard neurons (RB) neurons. **(B)** Schematic position of the expression of *her3* and *her9* in inter-proneural domains. *her3* is expressed between the medial and first lateral proneural domain (orange stripes). *her9* is expressed more extensively in all inter-proneural domains (orange and green). **(C & D)** Show the schematic cross section of A & B at the dotted line, respectively. Adapted from Bae et al. (2006)

of primary motoneuron as well as oligodendrocytes in the spinal cord (Park et al., 2002).

In the developing brain, *her5* (orthologous to HES7), is expressed in the Intervening zone (IZ), a non-differentiating region of the Midbrain/hindbrain boundary (MHB) from 3 somite stage (11hpf). This *her* gene appears to maintain the cells in this region at a highly proliferative state, potentially by inhibiting *p27Xic1-a*, and prevents their differentiation. Depletion of *her5* uncovers a pattern of differentiation that resembles the midbrain rostrally and the rhombomere 2 of the hindbrain caudally (Geling et al., 2003). This is consistent with the function of mouse HES1 in boundary regions like the isthmus, the mammalian MHB, and in the Zona Limitans interthalamica (ZLI), which separates dorsal and ventral thalamus (Baek et al., 2006).

her6 is also expressed in progenitor domains (Scholpp et al., 2009; Coolen et al., 2012; Schmidt et al., 2013; Dirian et al., 2014) and is extensively expressed during zebrafish brain development. Its transcripts appear just after 5hpf in the anterior neural plate and axis (Fig 1.10,A) (Thisse et al., 2001) and by 10hpf, it can be found prominently in the prospective forebrain (Fig 1.10,B) and thin transverse lines marking the developing hindbrain (Pasini et al., 2001). Between 10-24hpf, *her6* is expressed in rhombomeres in an anterior to posterior order (Pasini et al., 2001) while its expression in the forebrain persists up to 48hpf (Fig 1.10,C-J) (Thisse et al., 2001). Between 25-33hpf, *her6* is involved in patterning the thalamic structures by counteracting *ngn1* but promoting *ascl1* function (Scholpp et al., 2009). This *her* gene has also been implicated in DV patterning of the telencephalon as an inhibitor of *ngn1* (Yoshizawa et al., 2011).

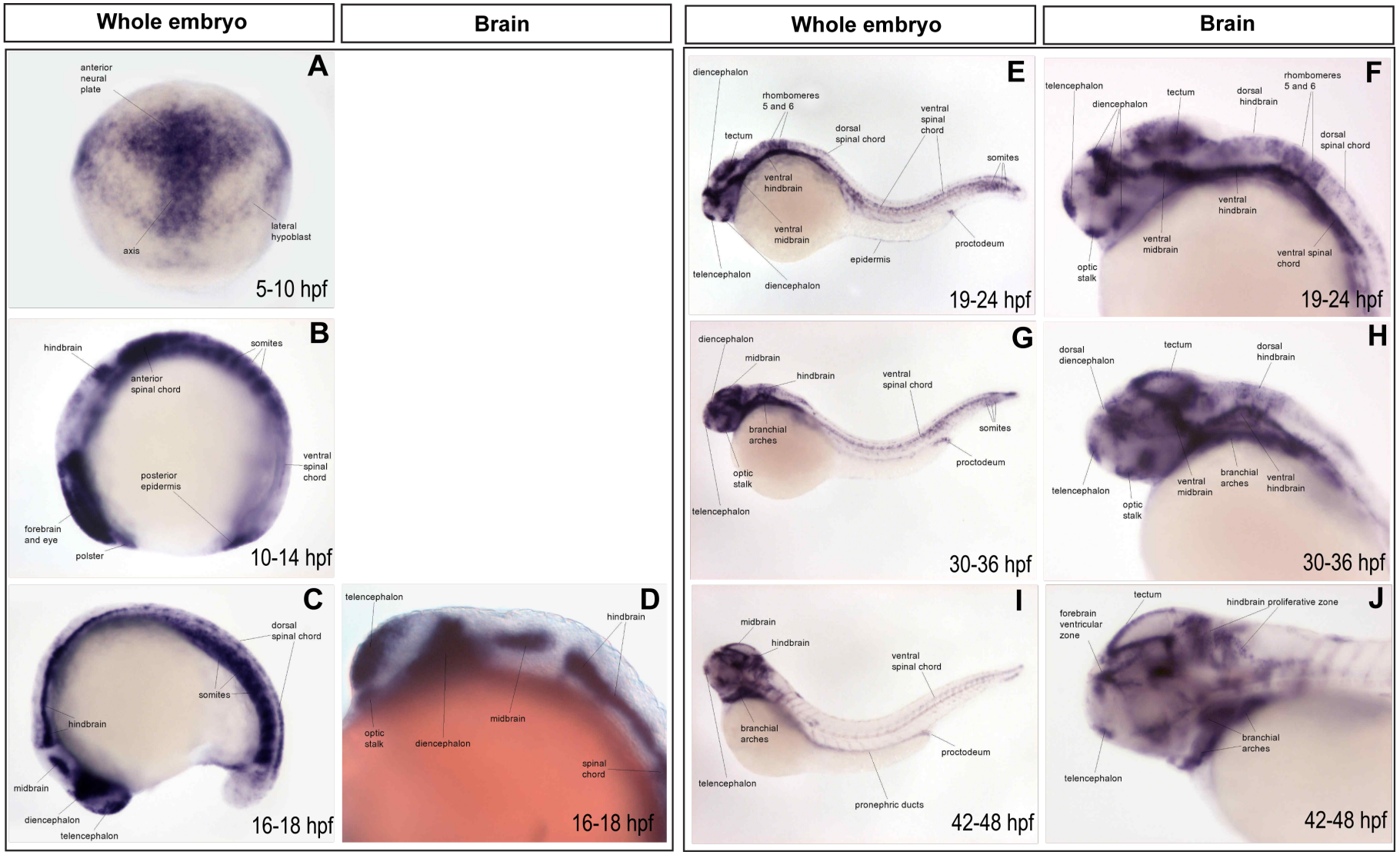

Figure 1.10: **Expression of *her6* mRNA characterised using In-situ hybridisation (ISH) by Thisse et al. (2001).** *A* Dorsal view, Anterior to the top, **B-J** Lateral view, Anterior to the left. The Diencephalic structures shown in C-F also include the embryonic thalamic structures.

1.11 Development of the zebrafish telencephalon

The telencephalon is the brain region that mediates higher functions like integrating the information from multiple sensory systems, motor control and memory (Turner et al., 2022) and is specified in the anterior neural plate. Anterioposterior (AP) patterning of the zebrafish CNS appears to follow a two-step model where the anterior neural tissue is induced (step one) and posterior regions of the developing CNS are subsequently posteriorised by transformer signals (step two) (Nieuwkoop, 1952). The zebrafish homeobox gene *dharma* (*bozozok, boz*) is involved in promoting neural induction (step one) by inhibiting *bmp2b/4*. It also maintains anterior neuroectoderm by inhibiting the posteriorisation signal, *wnt8* (Fekany-Lee et al., 2000). The importance of *dharma* becomes clear in its mutants which in the most severe cases, have complete loss of notochord, eyes and forebrain and reduced midbrain. This is while *krox20* expression that labels rhombomeres 3 and 5 was expanded in comparison to WT (Fekany et al., 1999). In line with this, over expression of *wnt* inhibitor *dkk1* in WT zebrafish led to enlargement of forebrain and eyes while it suppressed the defects of *dharma* mutant (Hashimoto et al., 2000).

In addition to the broad AP patterning in the CNS, localised signals further determine the regional identity of different brain domains. Within the boundaries of the forebrain itself, localised expression of a secreted frizzled-related Wnt antagonist, Tlc, by Anterior neural boundary cells (ANB) induces telencephalic fate and gene expression. Transplantation of ANB cells to more posterior regions of the neural plate leads to ectopic initiation of telencephalic programme (Houart et al., 2002).

Within the first two days of development, telencephalon is regionalised into the pallium (dorsal telencephalon) and sub-pallium (ventral telencephalon) (Wilson, Rubenstein, 2000; Danesin et al., 2009). This Dorsoventral (DV) patterning of the telencephalon is orchestrated by the interplay between *Wnt* and *Shh* signalling that determine the dorsal and ventral telencephalon, respectively (Wilson, Rubenstein, 2000; Danesin et al., 2009). *foxg1* is a transcriptional repressor expressed in telencephalic progenitors in many vertebrates and preforms the conserved role of controlling DV patterning (Danesin et al., 2009). Similar to mice, during zebrafish development, *foxg1* is expressed in a ventral to dorsal gradient in the whole telencephalon, only excluding the roof plate (Toresson et al., 1998; Danesin et al., 2009; Viktorin et al., 2009; Kumamoto, Hanashima, 2017). In short, *foxg1* acts downstream of *Shh* to promote ventral fates, it restricts Wnt/β-Catenin signaling dorsally to prevent the expansion of dorsal fates and also plays a role in maintaining the ventral boundary of the telencephalon with the hypothalamus (Danesin et al., 2009). Ultimately, this patterning leads to generation of distinct neuronal populations; glutamatergic neuronal fates in the dorsal telencephalon or pallium and GABAergic neuronal fates in the ventral telencephalon or sub-pallium (Martin et al., 1998; Viktorin et al., 2009).

1.11.1 Morphological characteristics of the developing zebrafish telencephalon

In most vertebrates, the adult telencephalon consists of two hollow hemispheres that surround the ventricles at their core which is known as an 'invaginated' morphology. In adult teleosts, however, the telencephalon is 'everted' where the hemispheres are two solid blocks of tissue that are separated medially by a T-shaped ventricle (Huesa et al., 2009; Folgueira et al., 2012). Dorsally, this ventricle is covered by the thin tela choridea membrane (Folgueira et al., 2012).

The classic view suggested eversion to be a result of the dorsal telencephalon (pallium) folding out laterally over the ventral telencephalon (sub-pallium) (Huesa et al., 2009; Folgueira et al., 2012). However, this model has been challenged more recently as it fails to completely explain the final organisation of domains in the adult zebrafish pallial regions (Mueller et al., 2011; Folgueira et al., 2012).

Folgueira et al. (2012) investigated the morphogenesis of zebrafish telencephalon between 1 to 5 Days post fertilisation (dpf) by live imaging. They characterised this period of development by two main events. First the anterior intraencephalic sulcus (AIS) forms between 18-22 hpf which opens the ventricle separating the telencephalon and the diencephalon. Next, between 2-5 dpf the pallial domain grows and is stretched along the AP axis resulting in the stretching of the roof of the AIS to form tela choridae. According to this model, the only mediolateral out-folding of tissue between 18hpf-5dpf occurs during the formation of the AIS at the telencephalic-diencephalic boundary. Folgueira et al. (2012) suggested that the final everted morphology of zebrafish telencephalon is the outcome of further refinement after day 5 of development. The most recent structural atlas of the developing zebrafish telencephalon shows that the refinement of telencephalon morphology is due to the expansive growth of different telencephalic regions after 5 dpf such as massive expansion of the pallium between 5-20dpf (Turner et al., 2022).

1.11.2 Neural progenitors of the telencephalon

In the context of mammalian cortex, after an initial expansion of the population by dorsal telencephalic Neuroepithelial cells (NECs), the NECs acquire glial morphology while maintaining their polarity and remaining as Neural progenitor cells (NPCs) often referred to as Radial glial cells (RGCs). RGCs divide asymmetrically at the apical side (adjecent to the ventricles, in the Ventricular zone (VZ)) with one daughter cell remaining a progenitor while the other differentiates into a neuron. Some of the progeny of these asymmetric divisions form a secondary group of progenitors known as the intermediate progenitor cells (IPCs) that migrate to reside in the Sub-ventricular zone (SVZ), a region immediately basal to the VZ. These cells are not polar but can divide once or twice to give expand the cortical population (Fernández et al., 2016).

To the best of my knowledge, no previous studies have characterised different types of neural progenitor specifically in the early embryonic zebrafish telencephalon (before 48hpf) and in relation to its sub-domains. But some characteristics of these cells can be inferred from the literature from later developmental stages and other brain regions. For instance, neural progenitors labeled by *her4* and/or PCNA (progenitor and proliferative cell markers respectively) have been shown to reside adjacent to the telencephalic ventricles in 48hpf zebrafish. Due to the everted morphology, this includes the midline between the two telencephalic lobes as well as the cells facing the tela choridea (Dirian et al., 2014; Furlan et al., 2017). Based on the findings of Dirian et al. (2014), the dorsomedial population of *her4* expressing progenitors in the 48hpf pallium are the origins of dorsomedial adult neural stem cells. This is while a lateral population of progenitors acquire *her4* expression in later stages that persist to form the lateral adult neural stem cell population. However, how these distinct progenitor pools are generated from early embryonic populations in the telencephalon (prior to 48hpf) is not yet known (Dirian et al., 2014).

By ventricle-targeted electroporation and single cell labeling in 22hpf embryos, Dong et al. (2012) showed that similar to RGCs, the forebrain embryonic neural progenitors also have a characteristic glial morphology and are also characterised by absence of early post-mitotic neural marker Elavl3. They also showed that the majority of these progenitor cells divided asymmetrically either to produce one neuron and a progenitor or to produce two deferentially fated progenitors (Dong et al., 2012). Even though the cells tracked by Dong et al. (2012) over time were predominantly from the diencephalon, it is possible that telencephalic progenitors share these features.

Between 24-72hpf, non-apical progenitors (perhaps similar to IPCs) have been observed in the developing zebrafish telencephalon. However, they form less than 10% of all of the progenitors in this domain and their molecular characteristics are not well understood (McIntosh et al., 2017). Regardless, some limited data suggests that each of these progenitors produces 2 neurons in the telencephalon which is similar to the role of IPCs in telencephalic expansion (McIntosh et al., 2017).

In short, the early steps in telencephalic determination (roughly before 17hpf) and it later characteristics (after 48hpf) have been more extensively studied. However, there are some gaps in the literature as to the specific molecular characteristics and different types of progenitors in this domain, particularly between 17-48hpf, that require further investigation.

1.11.3 Blurred line between primary and secondary neurogenesis

Historically, zebrafish neurogenesis has been described as two consecutive waves. The initial wave or primary neurogenesis takes place approximately between 10 to 48hpf (Kimmel et al., 1995) followed by secondary neurogenesis between 48 and 120hpf when the major brain areas become organised and differentiated. Secondary neurogenesis is characterised

by more refined proliferative domains that are mostly found surrounding the ventricles, also referred to as Ventricular zone (VZ) (Mueller, Wullimann, 2003). All neurogenesis in amniotes, genetically and temporally (in relative terms), correspond to the zebrafish secondary neurogenesis while there is no evidence of any process in amniotes comparable to the zebrafish primary neurogenesis (Wullimann, 2009).

In 24hpf embryos, the early neurons are organised in a simple network of well described tracts and commissures (Wilson et al., 1990; Ross et al., 1992). Between 24-48hpf, the number of axons increases by about one hundred fold. But during this time, only a few additional tracts and commisures are formed while the rest of the developing neurons mostly augment the initial tracts. Therefore, it has been suggested that the early neurons act as scaffolds to guide axons of later neurons (Wilson et al., 1990; Ross et al., 1992; Easter Jr et al., 1994). However, there is little evidence on how much these early tracts and commisures contribute to the adult CNS. In fact, some suggest that the majority of early neurons are transient and are replaced during secondary neurogenesis (Wullimann, 2009). This correlates with the number of apoptotic cells peaking between 36 and 48 hpf in many regions of the nervous system (Cole, Ross, 2001).

Certain neuronal populations do indeed undergo programmed cell death between primary and secondary neurogenesis. For instance, Rohon Beard neurons (RB) sensory neurons of the dorsal spinal chord gradually die between 1 day post fertilisation (dpf) to 7 dpf which co-incides with the development of the dorsal root ganglion neurons that structurally and functionally replace them (Reyes et al., 2004; Wullimann, 2009). The pioneer neurons of the olfactory system that guide axonogenesis of olfactory sensory neurons to the forebrain also undergo apoptosis between 30-48hpf (Cole, Ross, 2001).

However, to the best of my knowledge, there is no clear distinction between primary and secondary neurogenesis in the zebrafish forebrain. In fact, recent evidence clearly demonstrate that early telencephalic neurons can last well into the adult brain. Furlan et al. (2017) used a Tet-On-based genetic birth-dating strategy to label neural progenitors at different developmental stages. They show that neural progenitors as early as 14hpf contribute to the mature neuronal population of the central pallium as well as the sub-pallium in the 3 month old telencephalon. This implies that early or primary neurons are indeed relevant in the adult brain.

1.12 Concluding remarks

The extensive involvement of ultradian oscillators in development is not contested. In many aspects of CNS development, oscillations of HES factors are important in maintaining progenitor pools or at times, the transition towards neural differentiation (Shimojo et al., 2008; Manning et al., 2019). Much of the research to date has focused on the regulation and function of these dynamics in single cells (Shimojo et al., 2008; Manning et al.,

2019; Soto et al., 2020; Marinopoulou et al., 2021). However, only a few studies include the systemic properties of cell populations that express oscillatory and dynamic proteins (Biga et al., 2021). In this thesis, I have focused on HES1 as it is one of the best characterised oscillators in single cells, while its tissue level properties remain to be explored.

Zebrafish is a suitable model for studying the behaviour and developmental role of an oscillator at multiple scales, from single cells to tissue and systems level (Kozol et al., 2016). The primary neural network in zebrafish is in part transitory (Cole, Ross, 2001; Reyes et al., 2004; Wullimann, 2009). However, it is also simple and well characterised (Wilson et al., 1990; Ross et al., 1992). Furthermore, primary neurogenesis in some brain regions including the telencephalon generates regional patterning with distinct neuronal sub-types (Allende, Weinberg, 1994; Martin et al., 1998; Mione et al., 2001; Miyake et al., 2005; Viktorin et al., 2009; MacDonald et al., 2010; Yoshizawa et al., 2011; Yu et al., 2011) which also contribute to the adult brain (Furlan et al., 2017). Thus, the zebrafish telencephalon is an exciting model for fundamental questions in developmental neuroscience such as the dynamics of cell fate determination.

The expression of *Hes* orthologues (Hairy-related (Her) genes) is well characterised in snapshots of CNS development (Thisse et al., 2001; Geling et al., 2003; Bae et al., 2006). However, the studies of the real-time dynamics of these *Her* factors are scarce. Soto et al. (2020) have pioneered such dynamic studies in zebrafish using an endogenous Knock-in (KI) model that allows real-time visualisation of the HES1 orthologue, Her6. They have described the single cell dynamics of Her6 in the hindbrain and shown that these dynamics, including oscillations, are important in progression of neural differentiation in this brain region.

her6 is also expressed in the zebrafish telencephalon (Thisse et al., 2001) where it may be involved in DV regionalisation (Yoshizawa et al., 2011). However, Her6 function as a progenitor regulator, its expression dynamics and their potential involvement in neuronal fate determination in the telencephalon have not been explored. Based on the literature reviewed in this chapter, I hypothesised that Her6 is dynamically expressed in the neural progenitors of the telencephalon and that altering these dynamics by direct manipulation of protein stability will have developmental consequences in this region. In my thesis, I present the examination of this hypothesis using the following research aims:

1. How does *her6* mRNA expression in the telencephalon progress over development relative to neurogenesis?
2. What are the dynamics of Her6 protein expression in the telencephalon and does it exhibit oscillatory behaviour?
3. How are the dynamics of Her6 protein expression altered in single cells when protein stability, a cell-autonomous feature of the oscillatory network, is altered?

4. Does altering Her6 dynamics in single cells have any implications at the tissue level?
5. What are the implications of changing Her6 protein expression dynamics in neurogenesis?

Chapter 2

Materials and methods

2.1 Gene/protein nomenclature

In this thesis, I have endeavoured to adhere to the following guidelines for gene and protein nomenclature (2.1):

Table 2.1: Gene/protein nomenclature in mammals and zebrafish

Organism	Gene	mRNA	Protein
Mouse/Human	*Abc*	*Abc*	ABC
Zebrafish	*abc*	*abc*	Abc

2.2 Zebrafish husbandry and breeding

All animal work was in line with the Standard operating procedures (SOP) designed by the Biological Services Facility (BSF) guidelines, under a UK Home Office project licence. Animal handling was done by personal licence holders. Adult zebrafish were maintained at 28°C on a 12 hour light and dark cycle.

Zebrafish breeding was undertaken either by pairing selected fish in specialised breeding tanks or marbling whole tanks by marbling using the relevant BSF SOPs.

2.3 Anaesthetisation

Tricaine (Ethyl 3-aminobenzoate methanesulfonate) also known as MS222 stock solution was as followed: 0.4g of Tricaine powder (Sigma Aldrich E10521) was dissolved in 97.9ml of embryo water. To buffer, 2.1ml of 1M Tris buffer (pH 8.0) was added. The final pH was adjusted to 7 with NaOH and final volume made to 100ml. Stock solution was used at 50µl/ml of embryo water for anaesthetising embryos (final concentration 5%).

2.4 Genomic extraction

Genome extraction was performed on fin clippings from adult zebrafish (done based on the BSF SOP) or 2-4 Days post fertilisation (dpf) embryos using either Phire Animal Tissue Direct PCR Kit (Thermo Fisher - F140WH) or NP40/Proteinase K (PK) extraction method.

The Phire kit was used as per manufacturer instructions. In short, 15µl of the extraction buffer and 0.5µl of DNA release was used per fin clipping. Samples were incubated at Room temperature (RT) for 2-5 min and then enzyme was deactivated by 2-3 min incubation at 98°C in BIORAD T100 thermocycler.

NP40 lysis buffer was prepared to reach final concentrations as follows: 10µM Tris pH8,

1mM EDTA, 80mM KCL, 0.3% NP40 (Sigma Aldrich, AGEPAL CA-630 - I3021), 0.3% Tween 20 (Sigma - P9416). For this method of extraction, 25µl of PK (NEB - P8107S) /ml of NP40 lysis buffer was added to the samples (20µl for each adult fin clipping or 50µl for each embryo). Samples were incubated in BIORAD T100 thermocycler at 55°C for 3-4 hours. Following this incubation, enzyme was deactivated by 15 minute heat shock at 95°C.

All Genomic extracts were stored at 4°C.

2.5 Characterisation of the knock-ins by step-wise Polymerase chain reaction (PCR) and sequencing

All PCR reactions for characterising were done using the Phusion High-Fidelity DNA Polymerase kit (Thermo Fisher - F-530S) based on manufacturer instructions. dNTPs were prepared using dNTP Set 100mM (Bioline - BIO-39025). All reactions were run at the final volume of 10µl. Annealing temperature and extension times were adjusted based on the primers. The following primers (2.2) were used in this work and the numbers correspond to the numbers used in Chapters 3 and 4.

Table 2.2: List of PCR primers

Number	Zebrafish database number	Direction	Sequence (5'-3')
1	82 (182)	Forward	TCCAGTCTACGCAAACAATTCCAAC
2	83 (183)	Reverse	ACGCTGAACAAAGAAAACAAGTGTC
3	217	Forward	AAACTCCTCTTCTCCGGTCG
4	221	Forward	AGCCTAAGTTCAAAGCAGGT
5	391	Reverse	AGCCAACGCTATGTCCTGATAGC
6	396	Forward	TCTTGTCGATCAGGATGATCTGG
7	398	Reverse	TTTATCCGCCTCCATCCAGTC
8	259	Forward	ATTCATTAATGCAGCTGGCAC
9	196	Reverse	TCCTGAACTTTTGGCGCTGG
10	219	Reverse	ACTTACCGGTCATTTGTGCG

For sequencing, in some cases amplicons were either Topo cloned using Zero Blunt TOPO PCR cloning Kit (Invitrogen 45-0245). Transformation was done using XL10-Gold Ultracompetent cells by incubating plasmid in bacteria for 30 mins on ice, followed by 30s shock at 42°C. The bacteria were then incubated with 250µl of SOC medium (Thermo Fisher - 15544034) for 1 hour while shaking at 37°C. They were then plated and selected based on antibiotic resistance. Selected colonies were checked for inserion using EcoRI (NEB - R3101) restriction digest at 37°C for 1 hour and gel electrophoresis. Positive clones were sequenced using M13 primers included in the kit. In other cases amplicons were directly sequenced using the same primers used for amplification.

2.6 Fluorescent in-situ hybridisation (FISH) and In-situ hybridisation (ISH)

Embryos were dechorionated manually using forceps. They were anaesthetised and fixed at the desired stage in 4% Formaldehyde (FA) which was diluted from 16% stock (thermo scientific 28908) in 1xPhosphate Buffered Saline (PBS) (Sigma D1408). Fixation was done as samples were rocking for either 2 hours at Room temperature (RT) or Over night (O/N) at 4°C. The fixed embryos were dehydrated by a 15-minute wash in 100% Methanol (MeOH) at RT. MeOH wash was replaced with fresh 100% MeOH and embryos were stored for a minimum of 7 hours prior to use.

Probe preparation and FISH was carried out as described by Thisse et al. (2001) for whole mount ISH and modifications from Lea et al. (2012) for fluorescent labeling. *her6*-Digoxigenin (DIG), *her6*-Dinitrophenol (DNP), *Elavl3*-Fluorescein (FITC), *venus*-FITC, *ngn1*-Dig and *ascl1*-Dig probes were generated. Day 1: The embryos were rehydrated by incubation in PBT (1xPBS + 0.1% Tween-20 (Sigma P9416)), triethanolamine step was skipped. Embryos were then treated with PK for varied times based on age of embryo (10 mins for 29-30hpf, 5 mins for 22hpf and 2 mins for 17hpf), Day 2: Hyb- (50% formamide, 5xSSC, 0.01M citric acid, 0.1% Tween) replaces hybridization buffer. During the 60°washes, embryos were graduated from 100% Hyb- to 75%, 50% and 25% Hyb mixed with 2x SSC, finally reaching 100% 2x SSC (10 mins per wash). This was followed by 2x30min washes in xSSC before cooling at RT. Embryos were then graduated from 0.2xSSC to PBT with 25%, 50% and 75% PBT washes mixed with 0.2xSSC (10 mins per wash). Protocol was followed from step 7. Days 3 and 4 were skipped. Days 5 and 7: 250µl of amplification buffer was used. To complete the protocol after day 7, embryos were washed 3x with PBT and left in PBT ON. For membrane staining, embryos were incubated with 5µM Bodipy TR in PBS-0.1%Triton for 2 hours while mildly shaking. They were then washed 3 times for approximately 20 mins each.

Embryos were imaged using Upright LSM 880 Airyscan microscope in Fast Airyscan mode with a W Plan-Apochromat 20x/1.0 DIC (UV) VIS-IR M27 75mm lens. First step of processing was done using default Airyscan Processing setup in ZEN Black. Further analysis of domain sizes was done using Imaris 9.3.1 using Surfaces tool. The surface grain size was between 2-3µm and threshold were set manually for each gene in each embryo based on the signal.

Probes for ISH were prepared similar to FISH. Day 1 of the ISH protocol is identical to FISH. On Day 2, there is no H2O2 treatment and samples are moved directly to 2x5 min washes in Maleic Acid buffer (MAB). Samples are blocked and then incubated with Anti-Dig-AP antibody (Sigma Aldrich - 11093274910 - 1:2000). The antibody was washed off in MAB and samples were incubated in MAB rocking ON at 4°C. On Day 3, embryos were washed 3x5 mins in Alkaline phosphatase buffer (Ap) which was prepared as followed:

50ml Tris pH 9.5 1M, 25ml MgCl2 1M, 10ml NaCl 5M and 0.5ml Tween-20 = 500ml. Signal developing solution was prepared by adding 4.5µl of NBT (Merck - 11383213001) and 3.5µl of BCIP (Merck - 11383221001) per 1ml of AP. Embryos were transferred to 6 well plate and submerged with NBT/BCIP in AP solution and left rocking at RT for 30-60 minutes for signal to appear. After sufficient signal was achieved, the NBT/BCIP solution was removed and embryos were rinsed with PBST. Then they were washed 3x10 mins in PBST at RT and kept in PBST ON at 4°C. They were then fixed in 4% FA for 1-2 hours rocking at RT and then washed and in PBS (without Tween-20) and stored at 4°C.

For imaging, embryos were submerged in Glycerol in glass dishes, oriented to desired orientation and imaged using a Leica M165 FC Stereo microscope. All image processing and measurements from ISH were done using FIJI measurement tool.

All statistical analysis was performed using GraphPad Prism Version 9.3.1.

2.7 Whole-mount Immunofluoresence (IF)

Whole-mount IF was adapted from the protocol used by Mendieta-Serrano et al. (2013). Embryos were collected and fixed as with FISH. They were washed 2x10 mins in blocking solution (PBS, Bovine serum albumin (BSA) 0.1% (Sigma Aldrich - A7906) and Triton X-100 (TX-100) 1%) and 2x10 mins in PBS-TX while rocking at RT. For permeabalisation, embryos were treated with PK (10µg/ml in PBS) for 10 mins for 24Hours post fertilisation (hpf) embryos or 13.5 mins for 48hpf embryos and then washed 2x5 mins in PBS-TX. They were then blocked for 2 hours at RT while rocking. After blocking, embryos were incubated with chicken polyclonal anti-GFP antibody (abcam - ab13970, 1:300) and rabbit polyclonal anti-Phospho-Histone H3 (Ph3) antibody (Sigma Aldrich 06-570, 1:500) in blocking solution ON at 4°C.

Primary antibodies were washed off he following day by 1x20 min in blocking solution and further 5x10 min washes at RT while rocking. Following from this, they were incubated with Alexa Fluor 568 goat anti-rabbit antibody (Thermo Fisher - A11011, 1:500) and Alexa Fluor 488 donkey anti-chicken antibody (Jackson Immunoresearch - 703-545-155, 1:500) in blocking solution for 3 hours at RT while rocking. They were washed for 15 and then 10 mins in blocking solutions and a further 10 mins in PBS-TX.

For nuclear staining, embryos were incubated in DAPI (Thermo Fisher - 62248) at a final concentration of 5µg/ml at 4°C ON while rocking. On the following day, DAPI solution was removed and embryos were washed 3x10 mins with PBS-TX.

For imaging, embryos were mounted a 50mm glass bottom dish (MatTek Corporation, P50G-1.5-14-F) face-up for a transverse view in 1% Low melting (LM) agarose. After the agarose was set, they dish was filled with PBS. Embryos were imaged using Upright LSM 880 Airyscan in LSM mode with a W Plan-Apochromat 20x/1.0 DIC (UV) VIS-IR

M27 75mm lens. All processing was done using Imaris 9.3.1 Spots tool. Nuclei were identified semi-automatically using DAPI channel with 5µm spots at 24hpf and 4µspots at 48hpf. To determine GFP and Ph3 positive, mean intensity values of GFP and Ph3 channels were extracted and filtered based on a threshold that was determined based on intensity distribution and manually verified and altered when necessary.

All statistical analysis was performed using GraphPad Prism Version 9.3.1.

2.8 *in vitro* mRNA synthesis

10µg of plasmid DNA containing cDNA of the desired contruct was linearised with a restriction enzyme that would result in anti-sense exposure. All linearisation reactions were done ON. Linearised plasmids were purified using Phenol:Chloroform extraction. In short, Phenol:Chloroform was added in 1:1 ratio to the DNA mix and vortexted until milky. They were centrifuged (Eppendorf - 5424 R) for 15 mins at full speed (21000xg) and aqueous phase containing DNA was transferred to fresh tube. 100% Ethanol (EtOH) was added to the DNA mixture (2.5 times the volume of DNA retrieved) along with Sodium Acetate (0.1x times the volume of DNA retrieved. This mixture was combined well by pipetting and the incubated at -80°C for at least 1 hour or ON. Then this was centrifuged for 15 minutes at top speed at 4°C to retrieve the DNA and supernatant was removed carefully. The DNA pellet was washed with 500µl of 70% EtOH without disrupting the pellet and then centrifuged again at top speed for 10-15 mins. Liquid was removed and pellet was air dried before resuspension with Nuclease free water (Invitrogen - AM9937).

In vitro transcription was performed with the mMESSAGE mMACHINE™ SP6 Transcription Kit (Thermo Fisher - AM1340). Transcription reaction was incubated at 37°C for 2 hours. Then they were treated with TURBO DNase (Thermo Fisher - AM2238) for 15 minutes at 37°C. mRNA was purified with MEGAclear Transcription Clean-Up Kit (Thermo Fisher - AM1908) based on the manufacturer protocol. The optional precipitation with EtOH and Ammonium Acetate was also included. All mRNA were stored at -80°C.

2.9 Measuring protein half-life using PA GFP

PCS2-Her6-PA GFP-HA and PCS2-Her6-PA GFP-PEST-HA plasmids for these experiments were designed in collaboration with ***Dr Anzy Miller*** and custom made by GenScript. In both constructs, PA GFP was flanked by Eco-RI restriction enzyme binding sites and the desired cassette was inserted between BamHI and XbaI restriction sites.

To generate PCS2-PA GFP plasimd*, PCS2-Her6-PA GFP-HA and empty PCS2 were digested with EcoRI (NEB - R3101) at 37°C ON followed by 30min deactivation at 65°C.

The empty linear PCS2 was treated with Antarctic Phosphatase (NEB - M0289) to prevent their religation added directly to the digestion mix and incubated at 37°C for 30mins followed by 2min deactivation at 80°C. The ratios of vector to insert for ligation were calculated with NEBioCalculator tool. PCS2 vector and PA GFP insert were assembled using T4 DNA ligase (NEB - M0202) using the protocol recommended by the manufacturer and ON incubation at 16°C followed by 10min deactivation at 65°C on the following day. Transformation was done using XL10-Gold Ultracompetent cells as previously described in the section "Characterisation of the knock-ins by step-wise Polymerase chain reaction (PCR) and sequencing". Colonies were tested for successful ligation with Eco-RI restriction digest andgele electrophoresis. Positive clones were sequenced and the correct ones amplified with PureLin HiPure kit (Thermo Fisher - K210007).

**Note that the PA GFP was excised from PCS2-Her6-PA GFP-HA without a stop codon. This led to erroneous addition of 16 amino acids in frame with PA GFP rendering this PA GFP not functional.*

Her6-PA GFP-PEST (HPP), Her6-PA GFP-PEST (HPP) or PA GFP mRNAs were generated *in vitro* as described in section "*in vitro* mRNA synthesis". ∼120pg of mRNA was injected in each embryo along with 60pg of Caax-RFP mRNA to label membranes. Embryos were incubated at 28°C for about 3.5 hours and were then dechorionated and mounted in 50mm glass bottom dish (MatTek Corporation, P50G-1.5-14-F) in 1% LM agarose. Once set, plate was filled wth embryo water.

Imaging was done using Upright LSM 880 Airyscan microscope with W Plan-Apochromat 20x/1.0 DIC (UV) VIS-IR M27 75mm lens in Lambda scan mode with 488 laser covering a ∼30-40µm deep from the surface of the 4hpf embryo in 4-5 Z-sections. Imaging was done continuously. After 3-5 frames, imaging was paused and the selected embryo was exposed to 85-100% strength UV light from an HXP 120 V lighting unit (Zeiss) for 35s. Then imaging was continued for further 1-2 frames and then embryo was exposed to UV light for 20s. UV pulsing was continued until PA GFP activation was observed. This often took between 3-7 20s pulses and at times PA GFP activation was not seen. Upon activation, imaging was continued for 60-70 minutes to observe degradation. These were processed with linear unmixing using ZEN Black*.

**Note that some level of background PA GFP signal was also observed prior to activation, hence linear unmixing was not suitable for separating background from activated PA GFP as they shared spectra. But PA GFP was successfully separated from RFP.*

Further analysis was carried out using Imaris 9.3.1 Spots tool by measuring mean intensity of PA GFP in a group of cells at a time. Half-lives were calculated for each embryo in Excel by fitting an exponential trendline onto the data. The power of e in the equation for the

exponential decay (λ) was used in the formula

$$ln(2)/\lambda \tag{2.1}$$

.

2.10 Molecular cloning HV and HVP PCS2 constructs for Cycloheximide (CHX) chase in embryos

To generate PCS2-Her6-Venus-HA and PCS2-Her6-Venus-PEST-HA plasmids, Venus sequence was amplified from Her6-Venus (HV) CRISPR donor designed by Soto et al. (2020) using the following primers with inclusion of Eco-RI restriction sites (2.3):

Table 2.3: Primers used for amplifying Venus with addition of Eco-RI restriction sites

Name	Direction	Sequence (5'-3')
Venus F EcoRI	Forward	taggagGAATTCGTGAGCAAGGGCGAGGAGCT
Venus EcoRI R no stop NEW	Reverse	accgacGAATTCCTTGTACAGCTCGTCCATGCCG

The Venus-EcoRI amplicom was ran on 1% agarose gel from which it is was extracted using QIAquick Gel Extraction Kit (Qiagen - 28704) according to manufacturer protocol. The purified amplicon was cloned using Zero Blunt TOPO PCR cloning Kit (Invitrogen 45-0245) using manufacturer guidelines, transformed into XL10-Gold Ultracompetent cells (Agilant Technologies - 200315) as described in section "Characterisation of the knock-ins by step-wise Polymerase chain reaction (PCR) and sequencing". Selected colonies were minipreped with the QIAprep Spin Miniprep Kit (Qiagen - 27106) and checked for insertion using restriction enzyme digest with Eco-RI (NEB - R3101). Clones with successful insertion were sequenced (Eurofins, LIGHTRUN).

PA GFP was excised from PCS2-Her6-PA GFP-HA and PCS2-Her6-PA GFP-PEST-HA with Eco-RI digestion for about 3.5 hours or ON at 37°C. Eco-RI was deactivated by 30min incubation at 65°C for 30 mins. The digested DNA was resolved using agarose gel electrophoresis and the PCS2-Her6-HA and PCS2-Her6-PEST-HA were extracted from the gel with QIAquick Gel Extraction Kit. Vectors were treated with Antarctic Phosphatase (NEB - M0289) to prevent their religation. In some cases,this was done by adding 2.5µl of the phosphatase in the digestion mix after the 3.5 hour digestion and further incubating at 37°C for 30 mins followed by 2 min deactivation at 80°C. Alternatively, Antarctic Phosphatase treatment was done after vector purification for 30 mins 37°C, followed by 2 min deactivation at 80°C.

For assembly, the vector and insert ratios were calculated using NEBioCalculator tool. PCS2-Her6-HA and PCS2-Her6-PEST-HA vectors and Venus-EcoRI insert were assembled using T4 DNA ligase (NEB - M0202) using the protocol recommended by the man-

ufacturer and ON incubation at 16°C. Transformation was done using XL10-Gold Ultra-competent cells as previously described. The resulting colonies were examined by colony PCR using MyTaq Red mix (Meridian Bioscience - BIO-25043). Traces of single colonies were introduced in 10µl reactions of MyTaq based on manufacturer recommended protocol in presence of the following primers that amplify Venus (2.4):

Table 2.4: Primers used for amplifying Venus in colony PCR

Name	Direction	Sequence (5'-3')
Venus F	Forward	ACCCTGAAGCTGATCTGCAC
Venus R	Reverse	GGGTCTTGTAGTTGCCGTCGT

Colonies positive for presence of Venus were sequenced and the correct ones were Maxi prepped for use using PureLin HiPure kit (Thermo Fisher - K210007).

2.11 Cycloheximide (CHX) chase experiments in embryos

These experiments were adapted from Soto et al. (2020) by ***Dr Ximena Soto***. Injections, CHX treatment and protein extraction were done in collaboration with ***Dr Ximena Soto*** and Western blots were done by myself.

Wild type (WT) embryos were injected with either Her6-Venus (HV) of Her6-Venus-PEST (HVP) mRNA (40pg per embryo) along with Venus-myc tag (vGFP-mt) mRNA as injection control. They were incubated at 28°C for ∼2.5 hours to allow time for protein expression. Embryos were then dechorionated, and split into 7 pools of 20. They were then treated with Cycloheximide (CHX) (Prepared in 100%EtOH from powder - Sigma Aldrich - C7698 - Final concentration 200µg/ml or ∼700µM) for 0, 5, 10, 15, 20, 25 or 30 minutes. Uninjected (UI) embryos were used as negative control.

At designated time point, embryos were placed in eppendorf tube and CHX mix was removed from sample as much as possible. Deyolking buffer (Ginzburg Fish Ringer solution) was added 2µl per embryo. Yolk was disrupted by pipetting roughly 7 times. Embryos were pelleted by centrifugation for 1 min at 300g (Eppendorf - 5424 R) at 4°C. Supernatant was removed and 500µl of wash buffer was added and pellet wash washed by gently inverting the tube 3 times. Samples were centrifuged again for 1 min at 300g at 4°C. Second wash was done by repeating previous steps fallowing centrifugation. Supernatant was removed and 2µl/embryo of C^+ buffer (150mM NaCl, 50mM Tris pH 8.0, 1% NP40, 0.5% Deoxycholate, 0.5mM DMSF, 1mM C2Cl2, 1mM MgCl2 and 0.1% SDS diluted in H2O supplemented with protease inhibitors) was added and contents were mixed by pipetting roughly 7 times. These samples were incubated on ice for ∼1 hour. They were then resuspended with 6x SDS sample buffer (3ml of 1M Tris pH 6.8, 6ml Glycerol, 1.2g SDS, 0.93g DTT and 6mg bromphenol blue made to 10ml with H2O). Samples were then incubated at 95°C for 5 mins and stores at -80°C.

For Western Blot analysis, 20µl of each sample was loaded on 10% Mini-PROTEAN TGX Precast Protein Gels (BIO-RAD - 4561035) and run in 1x TGS buffer (BIO-RAD - 161-0772) using a 250V PowerPac HC (BIO-RAD - 1645052) for 1 hour at 50V and then at 150V for another ∼1 hour. Transfer was done using High MW setting on Trans-Blot Turbo Transfer system (BIO-RAD - 1704150) on Midi Format 0.2 µm Nitrocellulose transfer pack (BIO-RAD - 1704159). The membrane was blocked in 5% milk (Sigma Aldrich - 70166) in PBST for one hour and then incubated in anti-GFP mouse antibody (Merck - 11814460001, 1:1000 in 5% milk-PBST) ON shaking at 4°C. On the following day, blots were washed 3x10 mins in PBST and incubated with anti-α-Tubulin mouse antibody (Sigma Aldrich - T9026 , 1:1000 in 5% milk-PBST) for 1 hour rocking at RT and then washed 3x10 mins with PBST. Blots were incubated with Anti-mouse IgG, HRP-linked Antibody (Cell Signalling - 7076, 1:10000 in 5% milk-PBST) for 1 hour rocking at RT. Blots were developed using SuperSignal West Dura (Thermo Fisher - 34075) following manufacturer guidelines for 1 minute and were imaged using ChemiDoc XRS+ System (BIO-RAD - 1708265).

Data were exported using ImageLab software and quantification was done using the Measurement tool in FIJI. Fitting non-linear regression and half-life calculations were done using GraphPad Prism 9.3.1.

2.12 CHX chase experiments in MCF7 cells

This experiment was designed in collaboration with ***Dr Elli Marinopoulou***. Cell culture, imaging and cell tracking was performed by ***Dr Elli Marinopoulou***. Data processing and analysis was performed predominately by myself with assistance from ***Dr Elli Marinopoulou*** and ***Dr Anzy Miller***.

Human breast cancer MCF-7 cells were transfected with Lipofectamine 3000 (Invitrogen, L3000001) according to manufacturers instructions. 25K-35K cells were plated in one quarter of a 4-quarter glass bottom dish (Greiner, 627870) in DMEM media (Sigma Aldrich, D6429) supplemented with 10% fetal bovine serum (Gibco, 10270106). When cells reached 60-70% confluency (often after 24h) they were transfected with 500ng HV or HVP plasmid. 2-3days post transfection cells were treated with 5µg cycloheximide (Sigma-Aldrich, C4859) or DMSO (Sigma, D8418) and imaged straight after on Inverted LSM 880 Airy/FCS Multiphoton (NLO) microscope Plan-Apochromat 20x/0.8 M27 objective lens every 17 minutes using tile scanning for about 22 hours. Due to uncertaninty on how long CHX remains active, only the first 10 hours were analysed. Two separate detectors were used for high and low Venus levels.

Maximum intensity projections of all images were generated using FIJI and data was randomised by myself. Blind cell tracking on the randomised data was performed by ***Dr Marinopoulou*** in Imaris 9.3.1 using Spots tool with spot diameter of 11.9 µm. Venus in-

tensity mean from spots was extracted. If signal was saturated with detector at high levels, the mean intensity from the second detector was used.

The nonlinear regression analysis and half-life calculations were done in GraphPad Prism 9.3.1. Factor 2 polynomial fitting that was used to determine the trend in DMSO data and detrend DMSO and CHX data in R-4.1.3, where the trend-line was fitted with geom-smooth function and equation observed with Miscellaneous Extensions to ggplot2 3.3.5 (ggpmisc) package. A function was created based on the equation for DMSO trend-line which generated line values used to normalise the raw data by division.

2.13 Time-lapse imaging of live zebrafish embryos

Fast AiryScan microscopy allowed the desired balance between high signal to noise ratio and low laser power, resulting in high quality imaging with single cell resolution without extensive photobleaching over time.

All live imaging was done on the Zeiss Upright LSM880 Airyscan microscope in Fast Airyscan mode using a W Plan-Apochromat 20x/1.0 DIC (UV) VIS-IR M27 75mm lens. Embryos were mounted 1 hour prior to start of imaging in a 50mm glass bottom dish (MatTek Corporation, P50G-1.5-14-F) face-up for a transverse view in 1% LM agarose with MS222 (final concentration 160ng/ml). After allowing the agarose to set for 1 hour at RT, the dish was filled with embryo water supplemented with MS222 (final concentration 160ng/ml) and PTU (0.045% stock- Sigma Aldrich P7629). The chamber was maintained at 28°C and to prevent evaporation and changes in salt concentration, the water in the imaging dish was refreshed using a peristalsis pump (Harvard Apparatus 72-0001). The following lasers and fluorophore pairs were used for imaging: 514nm (between 6-13% for Venus), 458 (between 6-10% for mKeima) and 561 (between 2-10% for mRFP). It is important to note that the laser power in Fast Airyscan mode is equivalent to 10x of the power of the same laser in Laser scanning microscopy (LSM) mode (i.e. 10% in Fast mode=1% in LSM). Each channel was set up as a separate track and tracks was changed after every full Z-stack. Between 80-86 slices (0.47-0.54µm) were imaged (38.88-43.45µm total depth). For time-lapse imaging, timepoints were captured every 6 minutes for 6-12 hours. Line averaging was set at 4 and pixel dwell time was 0.54µs. The Airyscan files were processed using the automatic Airyscan processing provided on ZEN black.

2.14 Snapshot cell population live imaging analysis

This was done by utilising the Spots tool on Imaris 9.3.1 to automatically cells in the domain of interest based on the nuclear marker H2B-Keima. The automated detection was checked manually. Both Her6-Venus and H2B-Keima mean fluorescence intensity

A Data input for examining Venus vs Keima in HV

Table format: Grouped		Group A			Group B		
		Venus			Keima		
		A:1	A:2	A:3	B:1	B:2	B:3
1	1	60.48	60.97	60.80	34.43	34.66	30.38
2	20	68.56	64.31	72.31	32.35	31.20	31.35
3	40	76.56	83.00	88.20	24.37	30.09	31.19
4	60	84.41	105.95	90.62	22.71	28.86	29.98
5	80		136.05	100.42		32.57	29.42
6	100			115.26			30.81

B Global contribution of column and row factors to data variability

Fixed effects (type III)	P value	P value summary
Time	0.0442	*
Fluo	<0.0001	****
Time x Fluo	0.0002	***

C Venus and Keima examined at each time-point

Šídák's multiple comparisons test	Mean Diff.	95.00% CI of diff.	Below threshold?	Summary	Adjusted P
Venus - Keima					
1	27.59	13.09 to 42.10	Yes	*	0.0138
20	36.76	13.54 to 59.98	Yes	*	0.0195
40	54.04	32.03 to 76.05	Yes	**	0.0028
60	66.48	14.24 to 118.7	Yes	*	0.0281
80	87.24	-1168 to 1343	No	ns	0.5540
100	84.45				

Figure 2.1: **Example of mixed effect analysis.**

were extracted from these cells from selected time points, starting from the first frame of imaging and continuing at 2 hour intervals until the end of imaging.

The resulting data was processed using R-4.1.3. Main R packages used were readr 2.1.2, tibble 3.1.6, dplyr 1.0.8, tidyr 1.2.0, ggplot2 3.3.5 and tidyverse 1.3.1. All statistical analysis was done using GraphPad Prism Version 9.3.1.

For analysing data variability, multiple mixed-effects analyses were conducted (Fig 5.6). Mixed effect analysis is equivalent to 2way ANOVA when the replicates have varying lengths. In this case, different HV and HVP pairs were imaged for 6, 8 and 10 hours and they vary in length in time. These statistics were reported in Chapter 5 (Fig 5.6,C&D). As an example, for comparing Venus and Keima Coefficient of Variation (CV) in all cells in HV (Fig 5.6,C), data was input as shown in figure 2.1,A where the “Fluorophore” is the column factor and “Time” is the row factor. Next, with Mixed-effect analysis, the global effect of “Fluorophore” and “Time” to variability in CV values was examined showing that both contribute to the variation in CV values but Fluorophore contributes more (Fig 2.1,B). Venus and Keima CVs were also compared in each timepoint but these are not reported (Fig 2.1,C).

2.15 Single cell tracking and analysis

Imaris 9.3.1 was used for cell tracking. First, using the Imaris arithmetic tool, the mKeima signal (nuclear marker) was subtracted from the mRFP signal (membrane marker) to remove noise. The resulting channel was then subtracted from the Venus signal to segment it into distinguishable nuclei. We then used the 'Spots' (5µm in XY and Z diameter) and 'Track over time' functions to curate tracks of individual cells over time using a combination of automatic and manual tracking. In cases that automatic tracking was used, all final tracks were manually checked. We also generated background tracks to measure random fluctuations in fluorescence.

Firstly, in order to correct for any fluctuations in Her6-Venus that were caused by global changes in transcription and translation or technical issues during image acquisition, we normalised Her6-Venus to the H2B-mKeima signal. Secondly, since as described by Phillips et al. (2017) the analysis pipeline is most accurate in detecting oscillators in absence of long-term trends, we detrended the Her6-Venus and H2B-Keima from long-term trends over 4.5 hours (Lengthscale 4.5 hours) (Fig 2.2,A).

Peaks and troughs in the tracks were identified using Hilbert transform on detrended data (Fig 2.2,B, Bottom). Then, this information about the position of peaks and troughs was used to calculate fold-change (peak/trough) in the raw data (Fig 2.2,B, Top).

For dynamic analysis, we used a version of the method developed by Phillips et al. (2017) that has been adjusted for in vivo data from Zebrafish Soto et al. (2020). In summary, this method uses a basic model for gene expression combined with Locked nucleic acid inhibitor (LNAi) that approximates the dynamics as Gaussian processes. By adjusting the covariance function which is one of the defining factors in a Gaussian process model, the LNA can provide two theoretical models that correspond to either: 1- random aperiodic fluctuations (OU) or 2- intrinsically noisy oscillations (OUosc). During analysis, first the experimental time series data is fitted to both models separately and the probability of the data under each model is computed. The same is done for background tracks that are specified to the model to provide a measure of error in the raw fluorescence data that are caused by random fluorescent fluctuations. The confidence in the data being oscillatory is expressed as a Log likelihood ratio (LLR) of the probability of the data under the oscillatory model over the non-oscillatory model. To select the LLR threshold for classifying oscillators and controlling the False discovery rate (FDR), a set of synthetic data is generated from the OU model and its LLR score is calculated. By comparing the LLR score from the non-oscillatory synthetic data with LLR from the experimental data, we selected the LLR threshold suitable for our data with the stringent FDR of 1% (i.e. of 100 oscillators identified, 1 will be false positive). The results were also manually screened and short and duplicated tracks (due to cell division) were excluded from the data.

All track data were exported from Imaris 9.3.1. To connect dividing tracks, the data was

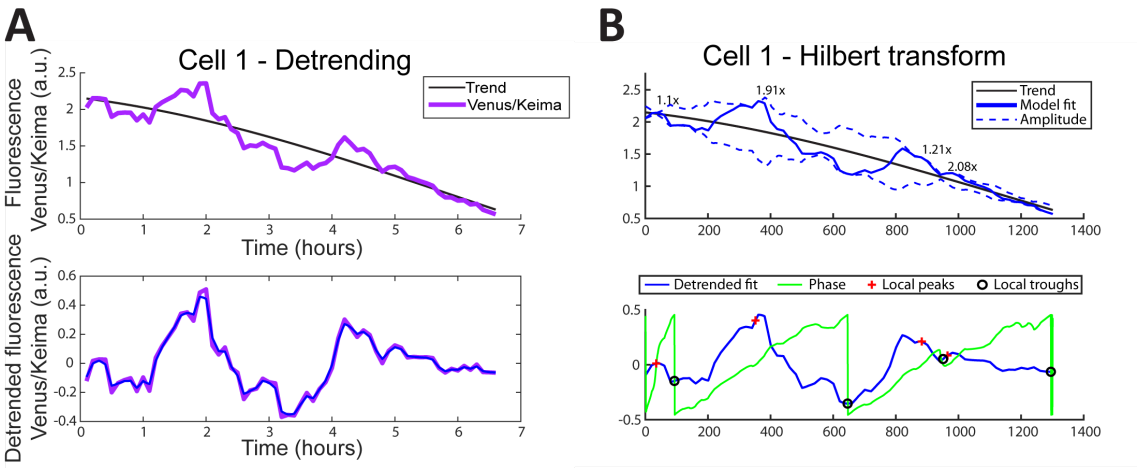

Figure 2.2: **Example of mixed effect analysis.**

processed with the Track Reconstruction (tRecs) Python script by ***Dr Thomas Minchington***. The code is publicly available on github (2020). The intensity mean data from tRecs output was processed using R-4.1.3. Main R packages used were readr 2.1.2, tibble 3.1.6, dplyr 1.0.8, tidyr 1.2.0, ggplot2 3.3.5 and tidyverse 1.3.1. All statistical analysis was done using GraphPad Prism Version 9.3.1.

2.16 Telencephalon dissection and RNA extraction

Petri dish was coated with 1% agarose in embryo water and once set, punctured with tip of a 10µl pipette tip to generate small holes. 24 or 48hpf embryos were anaesthetised with MS222 and placed stabilised in the small holes generated on the agarose plate. Embryos were visualised with intermediate contrast with stereo microscope and the telencephalon was dissected using a Gastromaster microdissection machine at the highest settings. The removed tissue was transferred using a 10µl pipette with low-melting (LM) agarose coated tip to prevent the tissue sticking to the plastic. Dissected tissue was directly transferred to either 5µl of Trizol and then snap frozen on dry ice or to 500µl of Trizol incubated on ice. 20 dissected telencephalons were pooled in each sample.

For RNA extraction, tissues were dissociated by pippetting. 100µl of chloroform was added to each sample and they were incubated at room temperature (RT) for 5 mins. Samples were centrifuged for 15 mins at full speed (21000xg) and supernatant was transferred to fresh tube. 0.5µl of Glycoblue (Invitrogen, AM9515) was added to facilitate RNA precipitation and colour the pellet along with 250µl of Isoproponol. Samples were incubated at -20 ON. The following day, they were centrifuged at top speed (21000xg) for 1 hour and supernatant was removed. Pellette was washed with 500µl of 70% EtOH and centrifuged for 5 mins at full speed (21000xg). Pallets were air dried for ∼5 mins at RT and resuspended in 7-10 µl of RNAse free water (Invitrogen, AM9932). RNA concentration was measured using Nanodrop.

2.17 Quantitative PCR

To remove any potential DNA contamination, RNA samples were treated with RQ1 RNase-Free DNase (Promega, M6101) system according to manufacturer protocol. cDNA was generated using SuperScript III Reverse Transcriptase kit (Invitrogen, 18080-044). In summary, between 350 ng of RNA was mixed with 1µl (50pmol) of Random Hexamers (Invitrogen, N8080127), 1µl of dNTPs (10mM) and made up to 13 µl with RNAse free water. The mix was incubated at 65°C for 5 mins followed by 1-2min incubation on ice. Then 4µl of First strand buffer, 1µl of0.1M DTT, 1µl RNasin Plus Ribonuclease Inhibitor and 1µl (Promega, N2611) SuperScript III RT were added. Reactions were incubated at 25C for 5 mins and then at 50C for 60 mins. Finally, reaction was inactivated by 15min incubation at 70C.

For qPCR reaction, the probes shown in table 2.5 were used with TaqMan Universal PCR Master Mix (Applied Biosystem, 4305719) or TaqMan Fast Advanced Master Mix (Applied Biosystems,4444964) were used according to manufacturer protocol. 5ng of cDNA was used in each 5µl reactions and each sample was run with 2 technical repeats. qPCR was carried out using a 96-well StepOnePlus Real-Time PCR System with quantitation (comparative CT) and TaqMan experimental setup either as a standard run when using TaqMan Universal PCR Master Mix or fast run for TaqMan Fast Advanced Master Mix.

Table 2.5: List of TaqMan qPCR Probes

Gene	Symbol	Thermo Fisher Assay ID
actin, beta 1	actb1	Dr03432610_m1
achaete-scute family bHLH transcription factor 1a	ascl1a	Dr03093273_g1
cyclin-dependent kinase inhibitor 1Bb	cdkn1bb (p27)	Dr03101118_m1
distal-less homeobox 5a	dlx5a	Dr03150313_m1
ELAV like neuron-specific RNA binding protein 3	elavl3	Dr03131531_m1
empty spiracles homeobox 3	emx3	Dr03086733_m1
forkhead box G1a	foxg1a	Dr03200829_s1
glutamate decarboxylase 1b	gad1b	Dr03080468_m1
glutamate decarboxylase 2	gad2	Dr03141402_g1
hairy-related 6	her6	Dr03176397_s1
neurogenin 1	neurog 1 (ngn1)	Dr03432616_g1
solute carrier family 17 member 6b	slc17a6b (vglut2a)	Dr03194447_s1
T-box brain transcription factor 1b	tbr1b	Dr03436735_m1
transmembrane protein 50A	tmem50a	Dr03108070_m1

CT values were analysed as follows: The technical repeats for each sample were checked to ensure there are no differences larger than 1 unit. The technical repeats were averaged for each gene with each sample. Based on report from Xu et al. (2016), classic housekeeping genes are not suitable for qPCR experiments in zebrafish. I selected Actinb1 as a

highly expressed classical control and Tmem50a which was one of the top recommended housekeeping genes for comparing zebrafish developmental stages according to Xu et al. (2016). The CT values for both housekeeping genes in each sample were averaged to give housekeeping CT. δCT was calculated by subtraction of houskeeping CT from the CT value of each gene of interest. $\delta\delta$CT was calculated as 2^{CT}.

All calculations were done on Excel and statistical tests were performed with GraphPad Prism 9.3.1.

2.18 Analysis of neighbouring cells

This analysis was performed by ***Dr Veronica Biga*** and the statistical analysis was done by myself.

The 3D coordinates of each detected nucleus in the cell population snapshot of selected timepoints were used to measure the inter-nuclear distance at approximately 2.3µm with no differences between HV (2.314 ±0.1326µm) and HVP (2.343 ±0.1388 µm). The closes neighbour to each each nucleus was identified based on minimal 3D Euclidean distance and the intensity levels of Venus and Keima were stored in paired datasets. In these datasets, the intensity on the x-axis showed the luorescence intensity in a selected nucelus while intensity on the y-axis was mean of fluorescence in its nearest neighbour. These datasets are referred to as cell-cell intensity distributions. Some signal variability was associated with Z depth due to imaging artefacts or other uncharacterised expression gradients. To circumvent their effect on the analysis, ratiometric analysis was performed where the ratio between mean fluorescence of each selected nucleus was calculated in relation to its nearest neighbour in each embryo. These were refered to as cell-cell intensity ratios.

Processing was done in MATLAB and all statistical analysis were performed using GraphPad Prism Version 9.3.1.

2.19 Mathematical modelling

All mathematical modelling was done by ***Joshua Hawley***, a doctoral candidate in Quantitative and Biophysical Biology. This methods section has been written by ***Joshua Hawley*** and edited by myself.

Model 1: Uncoupled cells with no protein auto-regulation

One of the simplest models that describes protein dynamics within a single cell is described by the equation

$$\frac{dp}{dt} = \alpha - \mu p, \tag{2.2}$$

where p is the abundance of protein as a function of time t, α is protein synthesis rate, and μ is the protein degradation rate. Regardless of the initial protein abundance, this model describes protein dynamics that will always evolve to a single steady state solution where the change in protein over time is zero. To find this steady state value, the equation can be solved analytically by setting the rate of change to $\frac{dp}{dt} = 0$ in equation (2.2) and rearranging to get

$$p^* = \frac{\alpha}{\mu}, \tag{2.3}$$

where p^* is the steady state protein abundance. The steady state value depends upon the ratio of the production rate and degradation rate. Mean expression for each cell will be determined by its production and degradation rates assuming each cell is at dynamic equilibrium (i.e. has had time to reach the mean expression level). If the assumption is made that mean Her6 levels in individual cells follow the condition in (5.1), predictions can be made for how the distribution of protein expression would change as degradation rate μ is increased.

To produce a distribution of protein expression levels with this model, the levels from a population of n-cells would need a range of $\frac{\alpha}{\mu}$ values, which is written as where $\vec{p^*}$ is a vector containing the steady state values of all cells.

$$\vec{p^*} = \begin{pmatrix} p_1^* \\ p_2^* \\ \vdots \\ p_n^* \end{pmatrix} = \begin{pmatrix} \alpha_1/\mu_1 \\ \alpha_2/\mu_2 \\ \vdots \\ \alpha_n/\mu_n \end{pmatrix}, \tag{2.4}$$

It could be the case that μ is the same in every cell, and only α varies across the population of cells, or vice versa, or that both μ and α vary between cells. It is not important for this analysis to assume any one of the three cases, but instead it is the ratio $\frac{\alpha}{\mu}$ that matters. If it can be shown that the cell-cell concentration difference always decreases in this model, then it can be ruled out as a model that sufficiently describes the distinct distribution of HVP data.

A population of cells with a range of steady state values (2.4) was considered in which

the degradation rate is increased by the same amount in all cells. The condition under which cell-cell concentration will always decrease is when high expressing cells reduce their protein abundance by the same amount or more than any given lower expressing cell. To express this condition mathematically, given any two cells i and j where i has the higher steady state protein abundance

$$p_i^*(\mu) > p_j^*(\mu), \tag{2.5}$$

then when μ is increased, cell i must have a larger negative change or reduction in abundance than cell j

$$\frac{dp_i^*(\mu)}{d\mu} \leq \frac{dp_j^*(\mu)}{d\mu}. \tag{2.6}$$

In the case of this simple model, condition (2.6) holds for any two steady state concentrations, because the steady state decreases faster for high steady state values than low steady state values, as can be seen by the exponentially decreasing curve in Figure 5.8,B (purple line). The gradient of this line which is given by

$$\frac{dp^*(\mu)}{d\mu} = -\frac{\alpha}{\mu^2}, \tag{2.7}$$

Model 2: Uncoupled cells with auto-inhibition

A well-established negative feedback loop model developed for Hes1 by Monk Monk (2003) is used here, but is reduced to only include protein abundance in order for easier analysis (shown in Figure 5.8D). The negative feedback is implemented by taking equation (2.2) and multiplying the translation rate α by an inhibitory Hill function to give the equation

$$\frac{dp}{dt} = \alpha \frac{1}{1 + (\frac{p}{p_0})^n} - \mu p, \tag{2.8}$$

where p_0 is the repression threshold, which defines the level of protein abundance at which the production rate will be 50% maximum. n is the Hill coefficient which defines the non-linearity of the transition from non-repressing to repressing the Hill function. High n-values provide sharper, more switch like transitions, and is often associated with protein cooperatively though this interpretation is context dependent Weiss (1997). It was assumed that like other bHLH factors, Her6 has to form dimers to be functional (Kageyama et al., 2007). Hence a Hill coefficient of 2 is a reasonable value (Santillán, 2008) assuming there is no additional regulation to Her6 transcription inhibition. The Hill function has a

value of 1 when there is no protein expressed and tends towards 0 with increasing protein expression, with the largest change occurring when protein abundance is equal to the p_0-value.

If the value of $n = 1$ is used in this model, then an analytical solution can be obtained, and this is found to only produce reduced cell-cell concentration differences with increased degradation. Analytic solutions for higher values of n are less straightforward, and so these are explored numerically. A range of p_0 versus $\frac{\mu}{\alpha}$, with $n = 2$ and $n = 8$ was explored. It is important to note that the Hill coefficient value being as high as $n = 8$ is extremely unlikely due to the high level of non-linearity produced by a relatively simple interaction Weiss (1997).

Model 3: Coupled 2-cell model with auto-inhibition

Here we implement a final layer of complexity into the modelling, which couples Her6 dynamics between 2 cells via lateral inhibition representative of Notch-Delta interactions. The lateral inhibition model used is adapted from Biga et al. (2021) and additionally to Model 2, includes time-delays, mRNA abundance, and lateral inhibition

$$\frac{dm_i(t)}{dt} = \alpha_m H_{auto}\Big(p_i(t-\tau_{auto})\Big) H_{LI}\Big(\overline{p}_i(t-\tau_{LI})\Big) - \mu_m m_i(t), \tag{2.9}$$

$$\frac{dp_i(t)}{dt} = \alpha_p m_i(t) - \mu_p p_i(t), \tag{2.10}$$

where $m_i(t)$ and $p_i(t)$ are the mRNA and protein abundance in cell i (as this is a two cell model, $i = 1, 2$). H_{auto} and H_{LI} are the autoinhibition, and lateral inhibition Hill functions which in full are

$$H_{auto}\Big(p_i(t-\tau_{auto})\Big) = \frac{1}{1 + \Big(p_i(t-\tau_{auto})/P_{0,auto}\Big)^{n_{auto}}}, \tag{2.11}$$

$$H_{LI}\Big(\overline{p}_i(t-\tau_{LI})\Big) = \frac{1}{1 + \Big(\overline{p}_i(t-\tau_{LI})/P_{0,LI}\Big)^{n_{LI}}}. \tag{2.12}$$

All parameters are defined in Table 1.

In a 2-cell model, if steady state values can be found for cell 1 and 2, then the cell-cell concentration difference at a given degradation rate is given by $\Delta p^*(\mu) = |p_1^*(\mu) - p_2^*(\mu)|$. Furthermore, if the degradation rate is increased by multiplying by a factor $d_f > 1$ then the difference between these two model outputs gives an error that indicates by how much the cell-cell concentration difference has changed

$$error = \Delta p^*(d_f \mu) - \Delta p^*(\mu). \tag{2.13}$$

Table 2.6: Model parameter values used Biga et al. (2021)

Symbol	Range explored	Biological definition
a_m	0.1-40 min^{-1}	Transcription rate
a_p	1-40 min^{-1}	Translation rate
u_m	$ln(2)/(2-30)$ min^{-1}	mRNA degradation rate
u_p	$ln(2)/(2-20)$ min^{-1}	Protein degradation rate
$P_{0,auto}$	100-25,000 proteins	HES5 autoinhibition repression threshold
$P_{0,LI}$	1-25,000 proteins	LI coupling repression threshold
n_{auto}	1-3	HES5 autoinhibition Hill coefficient
n_{LI}	1-4	Lateral inhibition Hill coefficient
τ_{auto}	0-20 mins	HES5 self-repression time delay
τ_{LI}	0-40 mins	Lateral inhibition time delay

To obtain this error by simulation, the model has to be run with the same parameter set twice, the first run with μ, and the second run with an increased degradation rate $d_f\mu$. Therefore, larger error values indicate that increased degradation rate has caused a larger increase in cell-cell concentration difference.

The MATLAB pattern search method is used as an efficient optimiser approach for its ability to explore non-smooth error spaces. Pattern search starts from a given point in parameter space, and then reads the output error from the model and subsequently tries to maximise the error value by moving to close-by parameter values with larger error, repeating the process until the error change is sufficiently low. The error used for this implementation of the optimiser is that in (5.2). Each run of pattern search returns one parameter set that it has found to have the maximum error. However it is unlikely that the optimiser will reach the same point in parameter space if started from a different initial parameter set. Therefore to map a wide region of parameter space, the pattern search algorithm is run many times from random initial points. The pattern search was not always be able to find large positive error values or produced highly oscillatory outputs, and so the outputs were filtered to only include $error > 1000$ and $coherence < 0.3$ (coherence measured in the same way as described in Phillips et al. (2016)).

Chapter 3

Characterisation of Her6 expression dynamics in the embryonic zebrafish telencephalon

3.1 Background

The telencephalon is the most complex structure of the vertebrate Central nervous system (CNS). By forming connections with many other neural structures like thalamus, hypothalamus, olfactory epithelium and the brain stem, it processes sensory input and ultimately mediates behavioural response (Wilson, Rubenstein, 2000). *Hes1* expression and HES1 protein oscillations are present in the developing mouse telencephalon where they are thought to maintain Neural progenitor cells (NPCs) (Shimojo et al., 2008; Imayoshi et al., 2013; Ochi et al., 2020).

The recent work by Biga et al. (2021) on a closely related protein, HES5, highlighted that the emergent tissue level pattern of HES5 expression mediated by Notch signalling is important in the pattern of neurogenesis in the mouse spinal cord. Like HES5, HES1 is a downstream target of Notch signalling (Ohtsuka et al., 1999) and the Notch/HES network mediates a dynamic interaction between telencephalic NPCs through oscillations of the Notch ligand, Delta-like 1 (Dll1) (Shimojo et al., 2016). However, despite the knowledge of this dynamic intercellular connection between telencephalic NPCs, no previous work has addressed the single cell and collective expression behaviour of HES1 in telencephalic progenitors in an *in vivo* tissue context. This, in part, could be attributed to the challenges associated with *in vivo* studies in mammalian embryos.

Zebrafish is an optically superior model for studying the behaviour of a dynamic protein in single cells and at tissue-level with single cell resolution. One zebrafish orthologue of *Hes1* is *her6* which is widely expressed during embryonic development including in the developing telencephalon (Thisse et al., 2001). The known function of *her6* in this domain is to negatively regulate the proneural gene *Neurogenin 1 (Ngn1)*. This was shown by *her6* over-expression which suppressed *ngn1* expression in Wild type (WT) telencephalon (Yoshizawa et al., 2011). Furthermore, Knock-down (KD) of *dmrta2* which is a proposed inhibitor of *her6*, led to the expansion of *her6* expression domain to the dorsal telencephalon and the inhibition of *ngn1* in this region (Yoshizawa et al., 2011) which gives rise to glutamatergic neurons later in development (Viktorin et al., 2009).

To the best of my knowledge, the work of Yoshizawa et al. (2011) which focuses on early telencephalon development between 14-19 Hours post fertilisation (hpf), is the only report to address the role of *her6* in this brain region. Hence, the studies of *her6* in the telencephalon are limited to its mRNA and predominantly consist of the descriptive analysis of its expression domain. As a result, unlike its mammalian counterpart, the role of *her6* as a progenitor regulator as well as the dynamics of its protein remain to be explored.

The expression pattern of *her6* had been previously described (Thisse et al., 2001). But to begin to better understand its role as a progenitor regulator, I first examined *her6* expression relative to *elavl3*, an early marker of post-mitotic neurons (Kim et al., 1996). Furthermore, I examined the expression domain of *her6* in relation to *ngn1* and *ascl1a*, dorsal and

ventral telencephalon fate determination markers, respectively (Allende, Weinberg, 1994; Miyake et al., 2017). It is important to note that by fate determination, I refer to when cells commit to a particular neuronal fate but prior to mitotic exit. This is based on the neurogenesis trajectory in embryonic thalamus (part of the diencephalon in the forebrain) proposed by Schmidt et al. (2013).

For assessing Her6 expression dynamics, I aimed to utilise the Her6-Venus (HV) CRISPR Knock-in (KI) line developed by Soto et al. (2020). In this zebrafish line, the coding sequence for the Venus fluorophore was inserted in frame with the endogenous *her6* to give rise to a fusion protein that allows detection of Her6 expression with single cell resolution. Soto et al. (2020) had characterised the genomic structure of the KI locus at the 5' end of the cassette to show in frame incorporation of Venus. However, the incorporation of the KI cassette at its 3' end was not characterised in detail. Hence, further characterisation of the KI locus and the expression of the HV fusion protein in the telencephalon was carried out to determine its suitability for studying Her6 expression dynamics in this tissue. In short, this chapter addresses the following aims:

1. To characterise *her6* expression in the telencephalon in relation to early post-mitotic marker *elavl3* as well as dorsal (*ngn1*) and ventral (*ascl1*) commitment genes;
2. To further characterise the HV KI locus predominantly focusing on the 3' end of the KI cassette;
3. Utilise the HV KI to describe Her6 dynamics in the telencephalon using *in vivo* imaging with single cell resolution.

3.2 Results

3.2.1 *her6* expression in the developing telencephalon relative to early neuronal marker and telencephalic sub-regions

As the first step in appreciating *her6* as a regulator of neural progenitor in the telencephalon, I wanted to investigate its endogenous expression. Since there are no suitable antibodies against endogenous Her6 protein, I characterised the expression pattern of its mRNA relative to the mRNA of early marker of post-mitotic neurons, *elavl3* (Kim et al., 1996) using Fluorescent in-situ hybridisation (FISH) in Wild type (WT) embryos. Embryos were imaged using a 10x objective lens in lateral position. The choice of orientation was to highlight the expression of these mRNAs across the anterior-posterior axis of the developing CNS.

As seen in Fig 3.1, *her6* was expressed in the anterior neural plate/presumptive forebrain as early as 11 Hours post fertilisation (hpf), prior to a clear physical separation between the

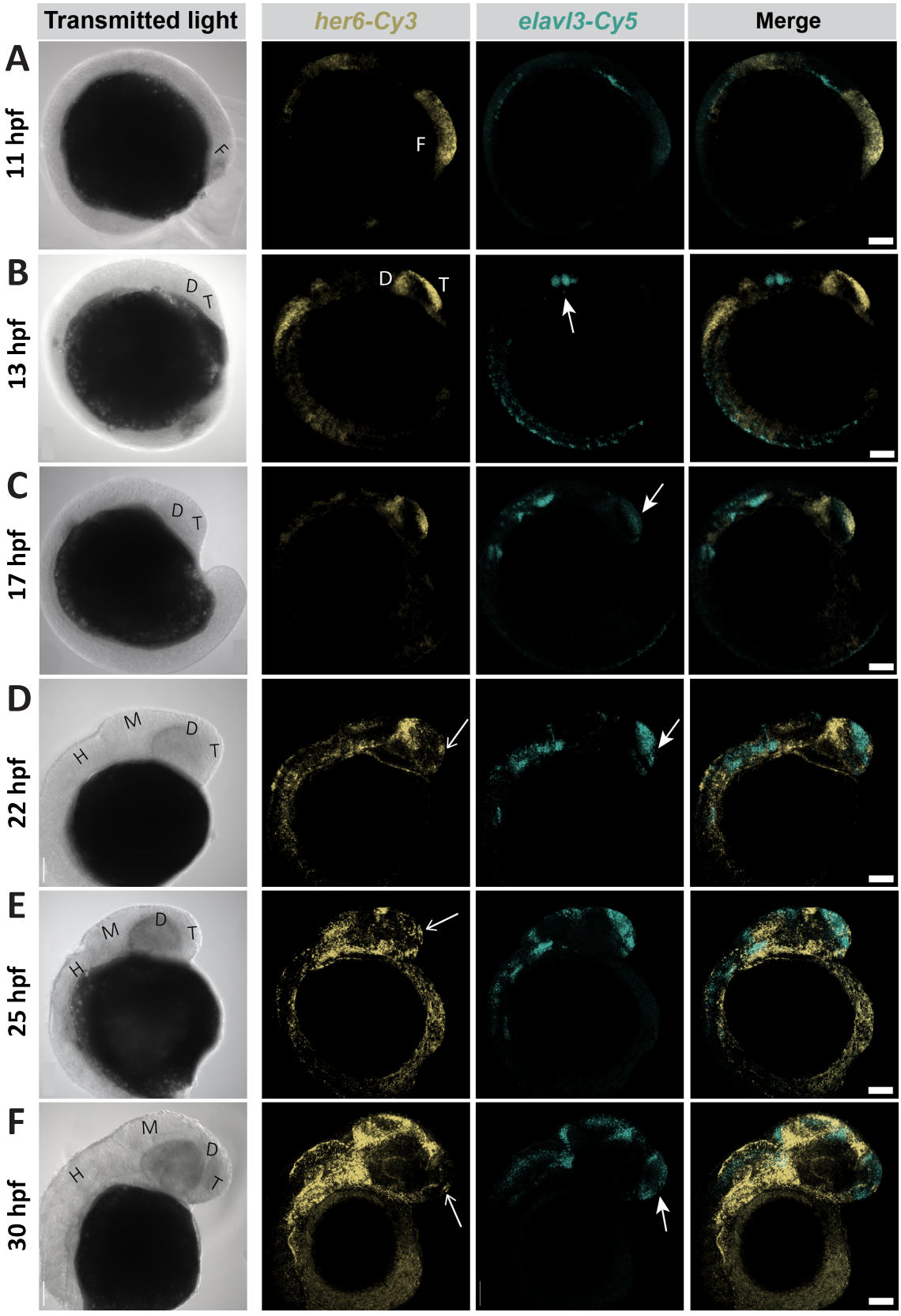

Figure 3.1: **Characterising the progression of *her6* expression in the telencaphalon using FISH. Caption on the following page →**

Figure 3.1: Characterising the progression of *her6* expression in the telencephalon using FISH. All images are displayed with rostral on the right and caudal on the left. All are maximum intensity projections of Z-stacks. **(A)** In 11 Hours post fertilisation (hpf) embryo the *her6* was expressed in presumptive forebrain where there was little to no *elavl3* expression. There was no morphological separation between D and T. **(B)** At 13hpf, D and T started to separate and *her6* was expressed in both. No *elavl3* expression was present in D or T but started to appear in more caudal regions (arrow). **(C)** At 17hpf, D and T had separated fully and *her6* continued to be expressed in both. *elavl3* started to appear at this stage in T (arrow) and strengthened in the more caudal regions. **(D)** By 22hpf, *her6* domain in T had reduced and was localised to the rostral tip (thin arrow) while *elavl3* expression strengthened in T but excluded the *her6* expression domain (arrow). **(E)** At 25hpf, *her6* in T was localised to the rostral tip (thin arrow) similar to 22hpf while *elavl3* was still strongly expressed in T. **(F)** By 30hpf, *her6* expression domain in T was very small (thin arrow) but still not overlapping with *elavl3* (arrow). F: Forebrain, D: Diencephalon, T: Telencephalon, M: Midbrain, H: Hindbrain. Scalebar = 100 μm.

telencephalon and the diencephalon. At this stage, no *elavl3* expression was detected (Fig 3.1,A). By 13hpf, *her6* was strongly expressed in the now distinct telencephalon and diencephalon (Fig 3.1,B). At this stage, *elavl3* expression was detected in caudal regions of the developing CNS but not in the forebrain (Fig 3.1,B, arrow) demonstrating that neural differentiation had commenced caudally. *her6* expression in the telencephalon continued at 17hpf when the onset of *elavl3* expression was also detected (Fig 3.1,C, arrow). By 22hpf, as *elavl3* expression strengthened, *her6* expression domain started to reduce in size and localise towards the ventral telencephalon (Fig 3.1 D, thin arrow). *elavl3* expression did not overlap with *her6* (Fig 3.1,D, arrow). At 30hpf, the expression of *elavl3* in the telencephalon appeared to be reduced which was consistent with its role as an early neuronal marker and therefore, transient nature. The *her6* domain persisted up to at least 30hpf, however it remained small (Fig 3.1,F, thin arrow) and mutually exclusive from *elavl3* (Fig 3.1 F, arrow). The lack of overlap between *her6* was also observed at a single cell level (Appendix 8.1). This suggested that cells downregulated *her6* prior to expressing *elavl3*.

Next, I sought to define the expression domain of endogenous *her6* with respect to the dorsal and ventral sub-divisions of the telencephalon (pallium and sub-pallium, respectively). Similar to before, due to lack of suitable antibody for labeling endogenous Her6 protein, I looked at the expression of mRNA. To this end, I performed FISH on 20, 24 and 28hpf embryos against *her6* combined with *ngn1* or *ascl1* which are the dorsal and ventral fate determination markers, respectively. The observations in all stages examined were similar, hence only 24hpf is shown.

The *her6* expression domain was placed anterior to the *ascl1* expression domain (Fig 3.2,A). In relation to the *ngn1* expression domain, *her6* was expressed ventrally. Due to the expression of *her6* mRNA in front of or anterior to *ascl1*, I determined the lateral orientation is best to display the spatial relationship between the expression of these mRNAs. No marked overlap between *her6* expression domain with either *ascl1* of *ngn1* was observed. This led to a basic model of telencephalon organisation including *her6* which is presented in figure 3.2,C. Based on this data, *her6* which was focused ventrally, was likely to be downregulated even prior to fate determination. In short, the data in this section suggested that *her6* may label early neural progenitors.

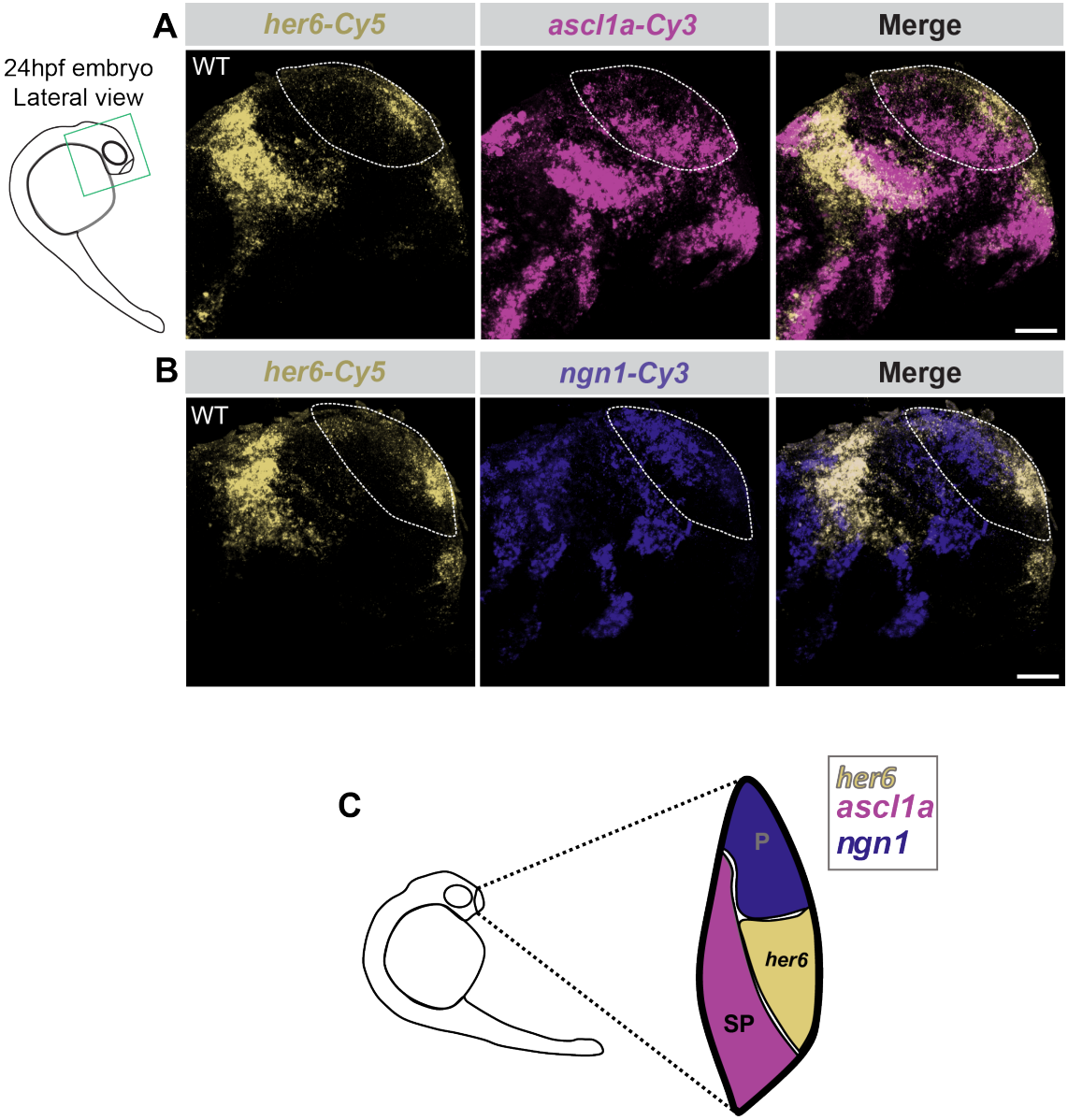

Figure 3.2: ***her6* is expressed anterior to *ascl1* and ventral to *ngn1*.** All embryos are 24hpf and WT, images at lateral view, with anterior to the right and posterior is to the left. A & B show area boxed in the schematic. **(A)** Maximum intensity projection of z-stacks. *her6* is expressed anterior or in front of the ventral region of the *ascl1* domain. **(B)** Maximum intensity projection of z-stacks. *her6* is expressed ventral to the *ngn1* domain. Scalebars = 40µm. **(C)** Schematic diagram of the the placement of *her6* expression domain relative to sub-divisions of the telencephalon. *her6* is more closely associated with the sub-pallium (SP) as it is located ventrally. P: Pallium, SP: Sub-pallium

3.2.2 Characterisation of the HV KI line

With a better understanding of WT *her6* expression in the telencephalon, I moved on to determine the suitability of the HV KI for studying Her6 dynamics. First I focused on a detailed characterisation of the KI locus. The original CRISPR design adapted from Soto et al. (2020) is shown in figure 3.3 (A, B and C). The endogenous *her6* locus comprises 4 exons. The Single-guide RNA (sgRNA) used for this CRISPR KI, targeted the fourth exon before the stop codon (Fig 3.3,A). Following a double-cut donor method (Zhang et al., 2018), binding sites for the same sgRNA were incorporated at extreme ends of the

homology arms in the donor plasmid to remove the backbone from the desired cassette upon injection into embryos (Fig 3.3,B). The KI cassette included exons 2 to 4 (minus the stop codon) connected to the coding sequence for Venus fluorescent protein at the C-terminus via a linker sequence (shown in purple). This cassette was expected to be incorporated in the endogenous locus in frame with the first exon following Homology directed repair (HDR) of the Left homology arm (LHA) and Right Homology arm (RHA) (Fig 3.3,C).

The characterisation done by Soto et al. (2020) confirmed that the 5' end of the KI cassette (i.e. the LHA) has incorporated correctly and in-frame with the endogenous first exon (all 5' and 3' directions are referring to the sense strand, from left to right). I used the primer combination they had used (primers 3-2; binding the genomic sequence before the LHA and the 5' end of the RHA after Venus, respectively) for Polymerase chain reaction (PCR) in HV genomic extracts to verify correct 5' incorporation of the LHA (Fig 3.3,D). This PCR resulted in a single band in presumptive Hom fish and a single smaller band in WT fish as expected. These bands at ∼2.8 and ∼1.9 Kilo-bases (kb) in HV KI and WT, respectively, were larger than the expected ∼1.9 and ∼1.2kb, which may be due to poor resolution of the DNA ladder. However, more importantly, the difference between HV KI and WT was ∼700 Base pairs (bp), which corresponded to the length of Venus coding sequence. This PCR in the donor plasmid (+C) resulted in a very large band (>3kb), which was likely due to erroneous binding of the primers (Fig 3.3,E). The Hom amplicon was sequenced and aligned to the expected sequence of the KI. This is shown in figure 3.3,F, where the arrows demarcated with a pink box are the sequencing results of the Hom amplicon. At its 5' end, this fragment spanned the junction between the 3' end of endogenous exon 1 and the 5' end of the LHA, demonstrating correct incorporation of the 5' end of the cassette (Fig 3.3,G). No aberrations were detected in the 3' end of this amplicon, which aligned correctly at the junction between Venus and the RHA with the stop codon intact (marked by the black box in Fig 3.3,H).

HV embryos could be presumptively categorised as Heterozygous (Het) and Homozygous (Hom) based on their Venus intensity (Fig 3.4,A). However, while optimising a more efficient PCR genotyping, indications of genomic aberrations were observed in the HV locus. Primers 1 and 2, which bind the 3' end of the LHA and the 5' end of the RHA respectively, were ideal for distinguishing between KI and WT. This pair was expected to amplify a 169bp fragment in WT genome and a 922bp fragment from the KI locus (Fig 3.4,B). PCR with 1-2 primers was expected to provide a clear distinction between Het and Hom DNA (Fig 3.4,C). However, in both Het and Hom HV genomic extracts, two bands were amplified that resembled the WT and KI bands expected in Het (Fig 3.4,D). This outcome replicated what had been previously observed and was suspected to be the outcome of erroneous incorporation of parts of the donor backbone (Soto, Unpublished work). Therefore, I examined the 3' end of the KI cassette which had not been previously done in detail.

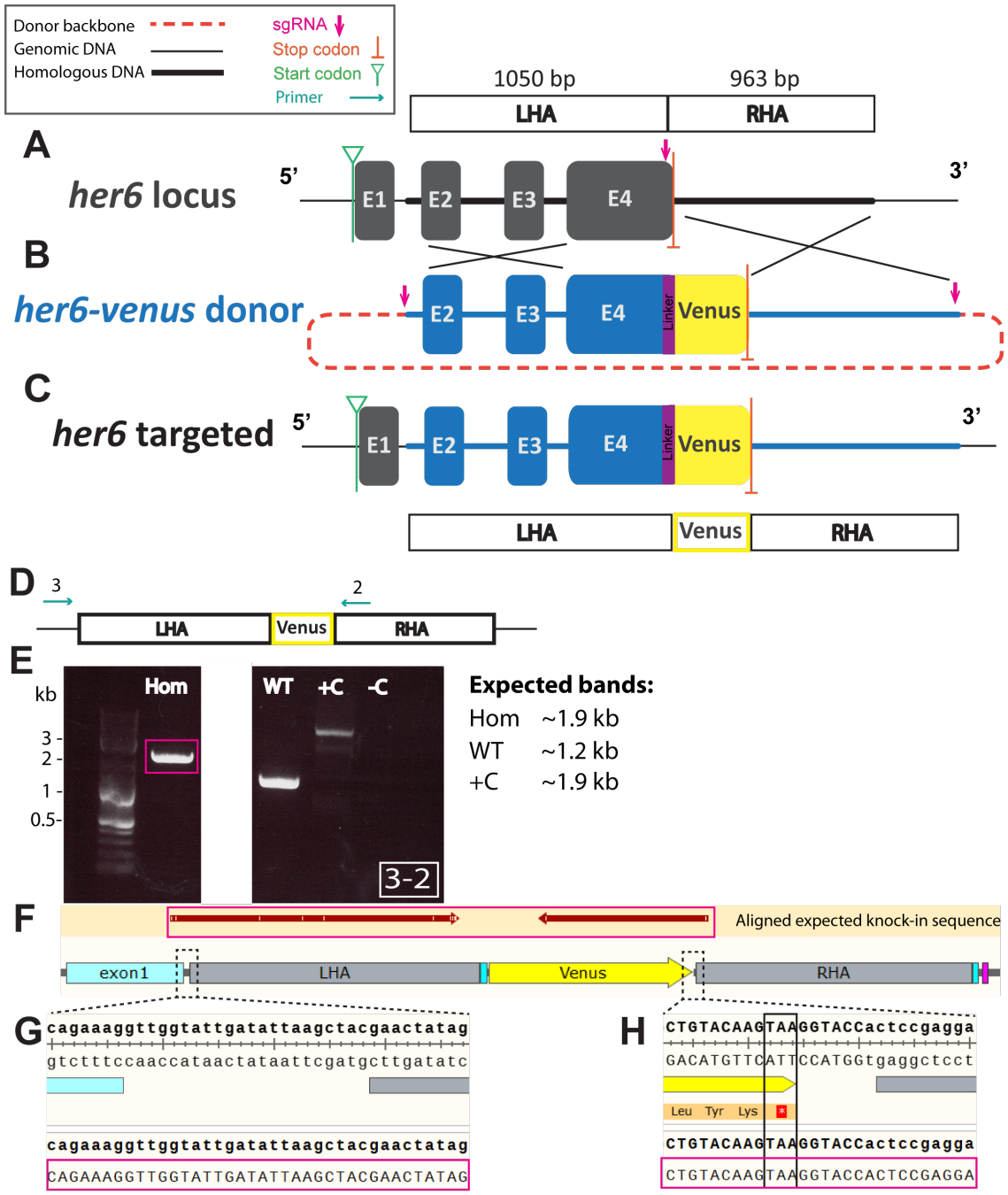

Figure 3.3: **Her6-Venus knock-in CRISPR design and detection of abarrations in the resulting genome. Caption on the following page →**

Figure 3.3: **(A)** Structure of the endogenous *her6* locus. sgRNA directed cleavage to the 3' end of exon 4, before the stop codon. **(B)** Structure of the *her6-Venus* CRISPR donor which excluded exon 1. Binding sites for the sgRNA were incorporated at either end of the KI cassette. **(C)** Shows the expected outcome of correct incorporation of the KI cassette in frame with endogenous start codon and exon 1. **(D)** Schematic diagram showing binding site of primers 3 and 2. **(E)** Image of gel electrophoresis following PCR amplification with primer pair 3-2 resulting in one ∼2.8kb band in Hom (outlined with pink box), one ∼1.9kb band in WT and a >3kb band in +C, which were larger than expected values. **(F)** The Hom amplicon outlined in pink box was sequenced. It aligned with expected KI sequence. **(G)** Alignment of Hom amplicon (pink box) with expected KI sequence; it showed correct incorporation at 5' end of LHA. **(H)** Alignment of Hom amplicon (pink box) with expected KI sequence showed that the stop codon (TAA) outlined in black box was intact at the end of *Venus* sequence.

For this, primers that bind the backbone sequence were utilised to check for amplification in genomic extracts from HV embryos (Fig 3.4,E). Pairing primer 4 which binds the 3' end of the RHA, and primer 5 which binds the 3' end of the NeoR/KanR gene, resulted in a ∼1.8kb amplicon from the KI genome. No WT sequences were amplified (Fig 3.4,F). The primer pair 6-7, both of which only bind to the donor backbone sequences, amplified a ∼1kb band in the Hom KI genomic extract while as before, no sequences were amplified from the WT DNA (Fig 3.4,G). These observations confirmed aberrant recombination at the 3' end of the KI cassette, leading to donor incorporation after the RHA.

The next step was to determine how much of the backbone has been incorporated. For this, primer 8 (binding the 3'-most section of the backbone and just before the LHA in the donor plasmid) and primer 9 (binding endogenous DNA expected immediately after the RHA) were used (Fig 3.4,H). In theory, if the donor had simply linearised and been inserted in the genome, the 8-9 primer pair would result in an amplicon of ∼400bp. Unexpectedly, this PCR reaction amplified a fragment close to 3kb (Fig 3.4,I). The amplicon was sequenced and aligned to the donor sequence showing the presence of an additional LHA and RHA without Venus coding sequence (Fig 3.4,J).

Taking the previous findings into consideration, a new model for the structure of the HV locus was hypothesised (Fig 3.5,A). In this model, there was correct incorporation of the LHA after the endogenous exon 1, which resulted in successful insertion of Venus in frame with the endogenous start codon. The stop codon at the end of Venus remained intact followed by the RHA. I estimate that a ∼6kb stretch of DNA including the whole donor backbone and duplicated LHA-RHA have been also incorporated in the genome. Since the duplicated LHA-RHA recapitulated most parts of the WT *her6*, it explained the outcome of PCR with primers 1 and 2 (Fig 3.4, C&D). In fact, the 8-9 amplicon sequence (Fig 3.4,H-J) aligned perfectly with WT *her6* genomic sequence (Fig 3.5,B). This included the WT TAG stop codon between the two arms (marked with black box in Fig 3.5,C). The presence of the WT stop codon (TAG) suggested the reconstruction of parts of the WT *her6* locus following the CRISPR reaction. To verify this model, I used primers 3-8-10 that were expected to amplify one ∼0.5kb band in WT and one ∼0.7kb band in donor (+C) but both bands in Hom HV. As shown in figure 3.5,D, both expected bands were observed in HV Hom, providing further support for the proposed model.

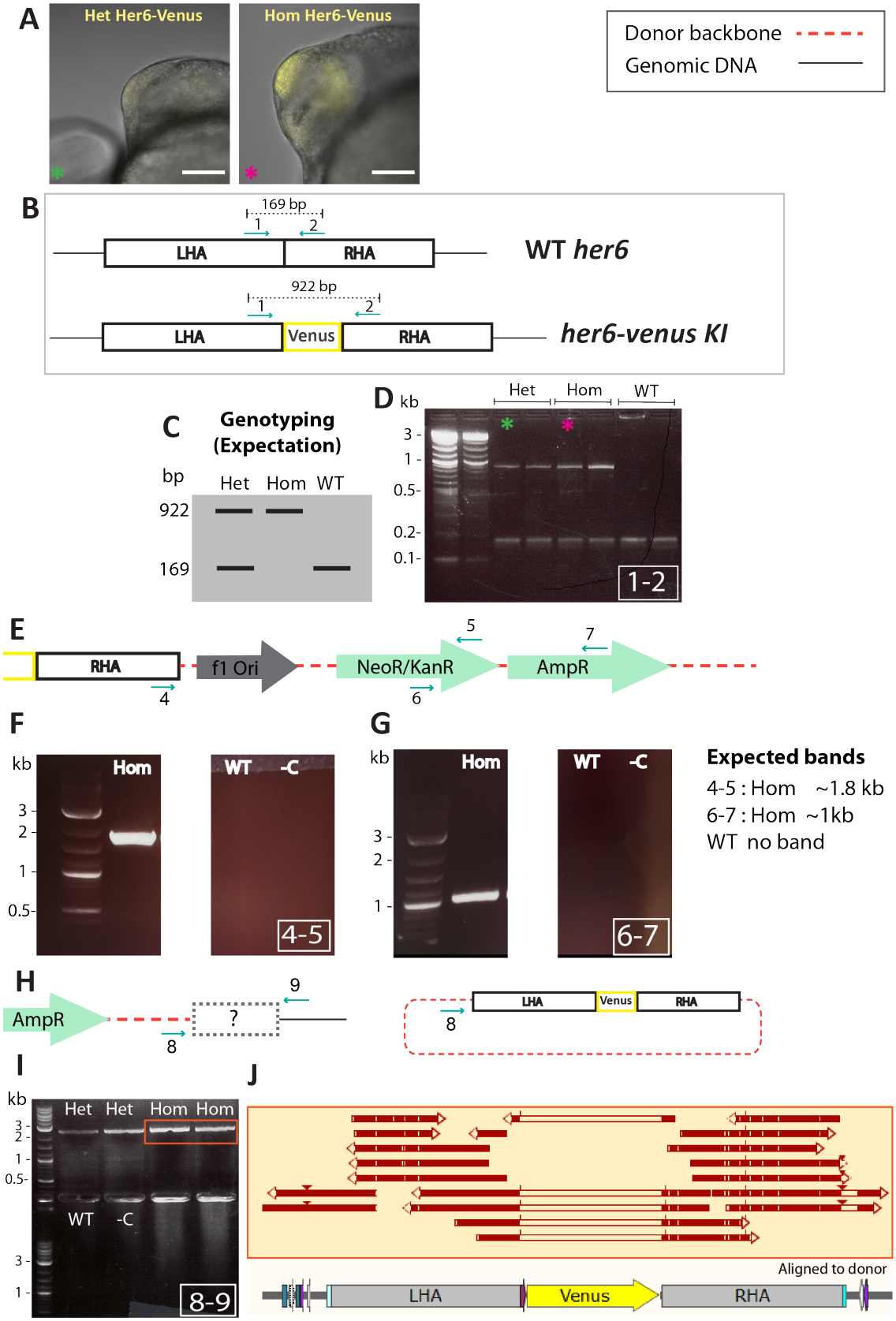

Figure 3.4: **Step-wise PCR for characterising 5' and 3' ends of the homologous recombination. Caption on the following page →**

Figure 3.4: **(A)** Confocal images of single Z plane from 17-18hpf embryos in lateral view. Rostral is on the left and caudal on the right. Using consistent confocal parameters for detecting HV expression, embryos could be separated into Het (left) and Hom (right) according to Venus intensity. Scalebar = 100µm. **(B)** Binding sites of primers 1 and 2 at the WT and KI *her6* locus which should result in a 169bp amplicon in WT and a 922bp amplicon in HV KI. **(C)** Schematic diagram of gel electrophoresis showing the prediction of PCR genotyping of HV with 1-2 primer pair. This was predicted to produce 169bp band in WT and 922bp band in Hom and both bands in Het. **(D)** Image of gel electrophoresis following PCR amplification with primer pair 1-2 which resulted in 2 bands in Het and Hom (∼1kb and ∼0.2kb) but only one band in WT (∼0.2kb). Green and pink asterisks refer to the Het and Hom imaged embryos from (A), respectively. **(E)** Schematic diagram of hypothetical KI locus structure where the donor backbone has inserted in the genome after the RHA. It also shows binding site of primers 4, 5, 6 and 7. **(F)** Image of gel electrophoresis using primers 4-5. This resulted in ∼2kb band in Hom and no bands in WT **(G)** Image of gel electrophoresis using primers 6-7 which resulted in ∼1.1kb band in Hom and no bands in WT. **(H)** On the left- schematic diagram of hypothetical KI locus structure where the donor backbone has inserted fully in the genome after the RHA and the gap between end of the donor with following genomic sequence. It also shows the binding site of primers 8 and 9. On the right - schematic diagram of the CRISPR donor and binding site of primer 8. **(I)** Image of gel electrophoresis using primers 8-9 that resulted in a ∼2.9kb band in Hom (outlined with orange box) and Het and no bands in WT **(J)** The Hom amplicon from J was aligned to the donor sequence. This amplicon aligned with the LHA and RHA but not with *Venus*.

The confirmation of the genomic structure proposed in figure 3.5,A raised the concern that in case of transcriptional read-through, unwanted open reading frames (ORFs) may be translated from the duplicate LHA-RHA which contains all of *her6* coding sequence excluding the first exon. I therefore checked the donor sequence for ORFs. As shown in figure 3.5,A, several ORFs were present in this sequence including those coding for antibiotic resistance (NeoR/KanR and AmpR). However, all of these ORFs culminated in a stop codon. Therefore, in case of transcriptional read through, I do not expect any part of the duplicated LHA-RHA to be translated, making ectopic expression of *her6* sequences extremely unlikely. Thus, the HV fusion protein is expected to be expressed in a manner that recapitulates WT *her6*, unhindered by the aberrant sequences that have been incorporated. This is summarised in figure 3.6 where in reality, only the expected and correct sequences for HV fusion protein are expressed.

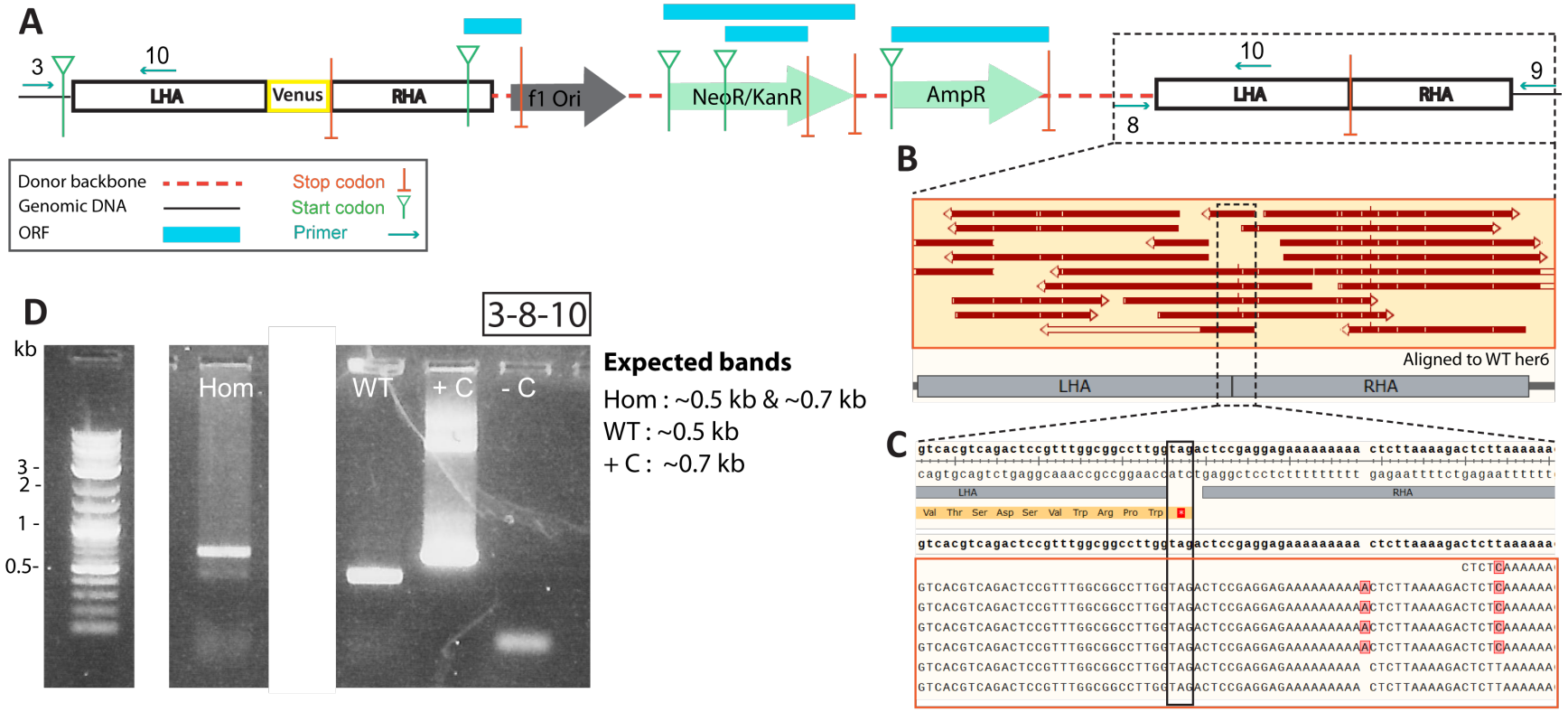

Figure 3.5: **A new model for the genetic architecture of Her6-Venus locus in the HV KI line.** **(A)** Schematic diagram of a proposed model for the structure of HV KI locus. In this model, the 5' end of the KI cassette had recombined correctly. The donor backbone had been fully inserted at the 3' end of the cassette, followed by duplicated WT LHA-RHA. It also shows the binding sites of primers 3, 8, 9 and 10 and the ORFs present in the donor sequence. **(B)** Sequence of 8-9 amplicon aligned with WT *her6* sequence showing the presence of duplicate of WT LHA-RHA. **(C)** The duplicated LHA-RHA contained the WT TAG stop codon (outlined in black box) **(D)** Image of gel electrophoresis using primers 3-8-10 that resulted in a ∼0.7kb and a ∼0.5kb band in Hom, a ∼0.7kb band in +C and a ∼0.5kb band in WT as hypothesised.

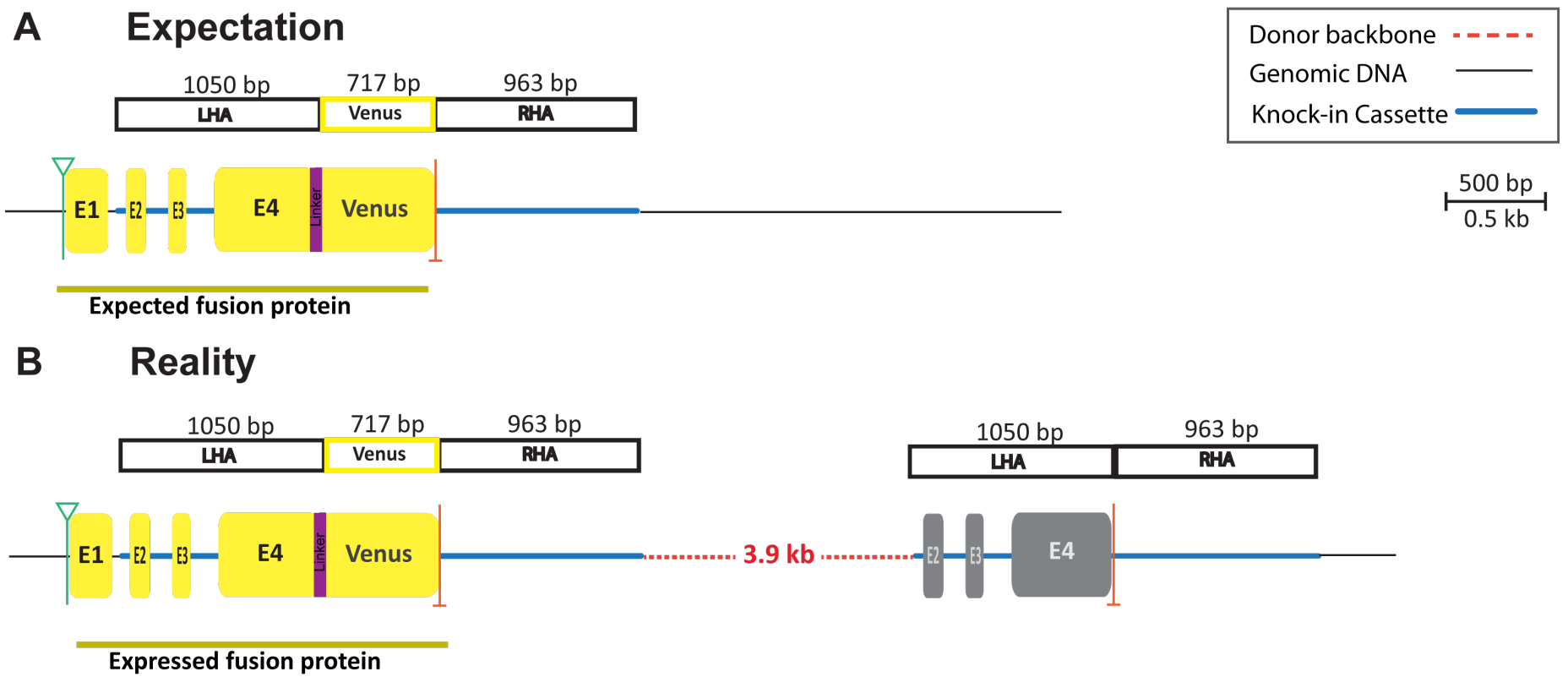

Figure 3.6: **HV KI locus summary: Expectation versus reality.** All structures are to scale except for the donor backbone which has been cut short in consideration of space. **(A)** The expected structure of the HV KI locus where the LHA-Venus-RHA are inserted in frame with Exon 1. The RHA is followed by genomic sequence. **(B)** The real structure of the HV KI locus where the correct expected sequence is present and expected to be expressed as such. The additional ∼6kb which include the donor backbone and Exons 2-4 are not expected to be expressed.

Indeed, Soto et al. (2020) had shown that HV expression is a faithful reporter for endogenous *her6*, both globally and specifically in the hindbrain. I further reaffirmed this finding focusing on the forebrain using FISH against endogenous *her6* on 17hpf WT embryos. To capture both the telencephalon (Te) and diencephalon (Di) where *her6* mRNA is expressed, I chose the lateral orientation. Imaging *her6* mRNA expression in both diencephalon and telencephalon as expected (Fig 3.7,B). The same expression pattern was seen at the protein level in a live HV embryo at a similar stage (Fig 3.7,C).

Next, I carried out FISH against *her6* and *Venus* on a mixture of Hom and Het HV embryos. The signal to noise ratio of the staining with the *Venus* probe was poor, particularly in heterozygous embryos. I did not carry out any co-localisation quantification between *her6* and *Venus* since the poor quality of *Venus* signal may have lead to low but misleading overlap levels. However, this data suggested that in both presumptive Hom and Het embryos, *her6* and *Venus* are expressed in comparable domains in the telencephalon (Fig 3.7,D&E). Most importantly, expression domain of *her6* was comparable between HV Hom, Het and WT demonstrating that the genomic aberrations resulting from the CRISPR process have not caused defected or ectopic *her6* expression.

3.2.3 Analysis of cell population heterogeneity and single cell variability in HV over time suggests that Her6 is dynamically expressed in the telencephalon

Having confirmed the HV line as a faithful reporter of Her6, Venus (representing Her6) expression in the telencephalon was imaged in live HV Hom embryos along with injected markers Caax-RFP and H2B-Keima which labeled cell membranes and nuclei, respectively. Time-courses ranged between 6-12 hours, starting from 19-20 hpf with 6 minute intervals. A total 4 embryos were imaged: Embryo 1 for 6 hours, embryo 2 for 8 hours, embryo 3 for 10 hours and embryo 4 for 12 hours.

To observe and quantify gene expression dynamics with single cell resolution, high quality imaging of maximum number of Her6 expressing cells was required. For this reason, I chose to conduct all live imaging at transversal orientation which enabled the observation of the almost the whole Her6 expression domain in both developing telencephalic lobes with limited interference from deep penetration into the tissue. This maximised both the number of cells imaged as well as the quality of imaging.

For a broad picture of the HV expression at the population level, snapshots at 2 hour intervals from these time-courses were analysed. As seen in a transversal snapshot of the telencephalon at 20hpf, the expression level of Venus varied from cell to cell and was heterogeneous in the domain of interest; this is outlined in the merge panel (Fig 3.8,A). To quantify this heterogeneity, telencephalic cell populations in embryos 1-3 were analysed. To this end, all nuclei (referred to as cells from hereon) were identified semi-automatically based on their H2B-Keima (referred to as Keima from hereon) fluorescence intensity (Chapter

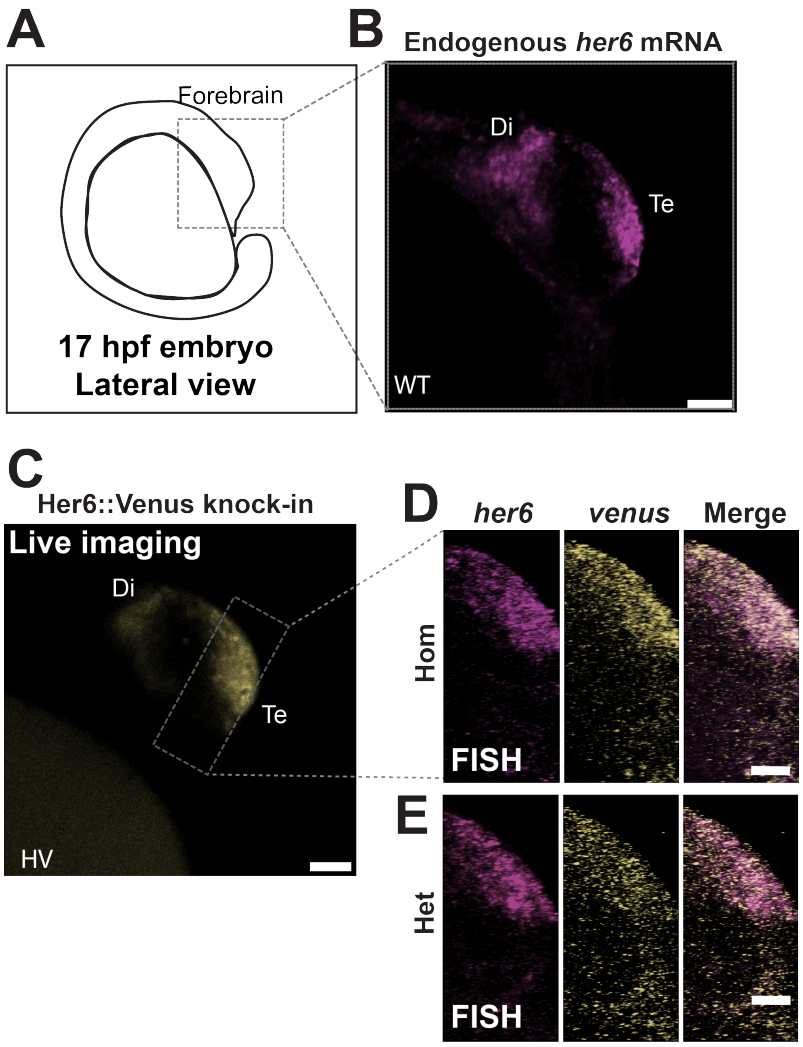

Figure 3.7: **The expression of Her6-Venus fusion protein recapitulates expression of endogenous *her6*.** **(A)** Schematic diagram of a 17hpf embryo in lateral view. **(B)** Maximum intensity projection image of FISH showing expression of *her6* mRNA in WT 17hpf embryo in Te and Di. **(C)** Confocal image from a single Z-plane of a live 17hpf Hom HV KI embryo showing expression HV in both Di and Te. **(D)** FISH showing co-localised expression of *her6* and *Venus* mRNA in the Te of Hom corresponding to the region outlined in C. **(E)** Maximum intensity projection image of FISH showing co-localised expression of *her6* and *Venus* mRNA in the Te of Het corresponding to the region outlined in C. Scale bars: B=50µm, C=50µm, D&E=20µm. Di: Diencephalon, Te: Telencephalon

2,"Snapshot cell population live imaging analysis"). Both Keima and Venus fluorescence intensities were extracted and their Coefficient of Variation (CV) was calculated for each time point in each embryo. CV which is calculated as standard deviation divided by the mean is a measure of variation in the data irrespective of mean levels. As shown in figure 3.8,B, in all embryos analysed (n=3), Venus CV was higher than Keima CV which increased over time. These differences were examined statistically with Mixed-effects analysis. The difference between Venus and Keima CVs were statistically significant at 20 (P=0.0138), 22 (P=0.0195), 24 (P=0.0028) and 26hpf (P=0.0281) but not at 28 (P=0.5540) and 30hpf (no P value was reported) which may be attributed to lower n numbers at these time points. At a global level, both developmental time (P=0.0442) and more so fluorophore (P<0.0001) significantly contributed to the difference seen in CV measurements. In short, these observations confirmed higher population heterogeneity in Venus expres-

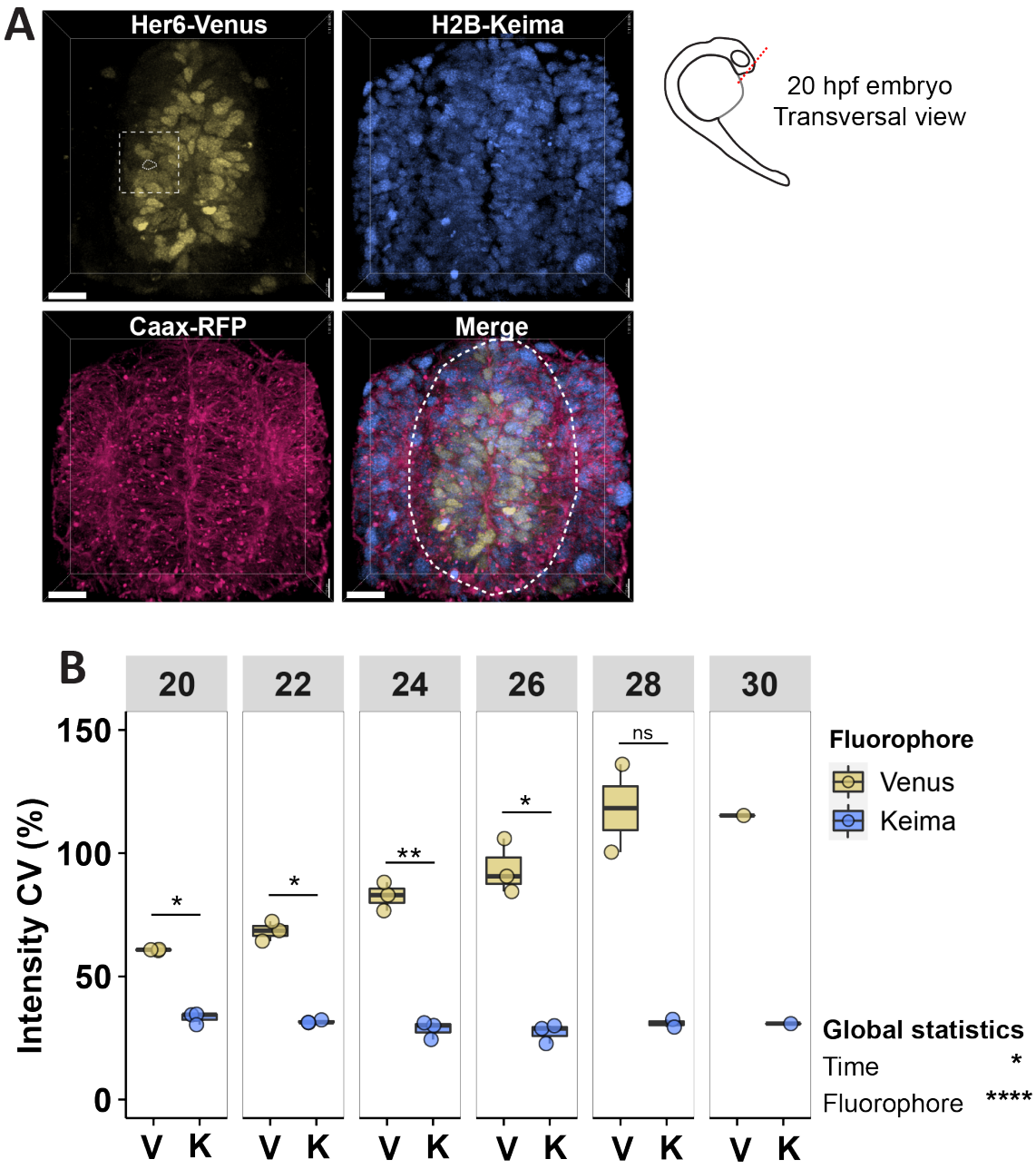

Figure 3.8: **Snapshot analysis of real-time imaging shows Venus expression in the telencephalon is heterogenous. (A)** 3D reconstruction of Z-stacks showing transversal snapshot of the telencephalon in a 20hpf Hom HV embryo injected with H2B-Keima and Caax-RFP mRNAs to label the nuclei and membranes respectively. The dotted outline in the Merge panel shows the visible boundaries of the telencephalon. Scalebars = 20µm. **(B)** Population CV calculated for all cells in selected time points (20-30hpf with 2 hour interval) from time-lapses of 3 embryos. CV of Venus expression was higher than Keima at all timepoint and this was statistically significant at 20 (*), 22 (*), 24 (**) and 26hpf (*). At a global level, both time (*) and more so fluorophore (****) significantly contributed to the variation in intensity CV. Mixed effect analysis, (ns): $P > 0.05$, (*): $P \leq 0.05$, (**): $P \leq 0.01$, (***): $P \leq 0.001$, (****): $P \leq 0.0001$

sion compared to Keima.

I next sought to determine if the population heterogeneity in Venus expression was a result fluctuations in its expression in single cells over time. For this, single cells were tracked over time and Venus and Keima variation from their mean expression was examined by calculating CV for each cell track (fig3.9,A). In all embryos analysed (n=4), single cell CV

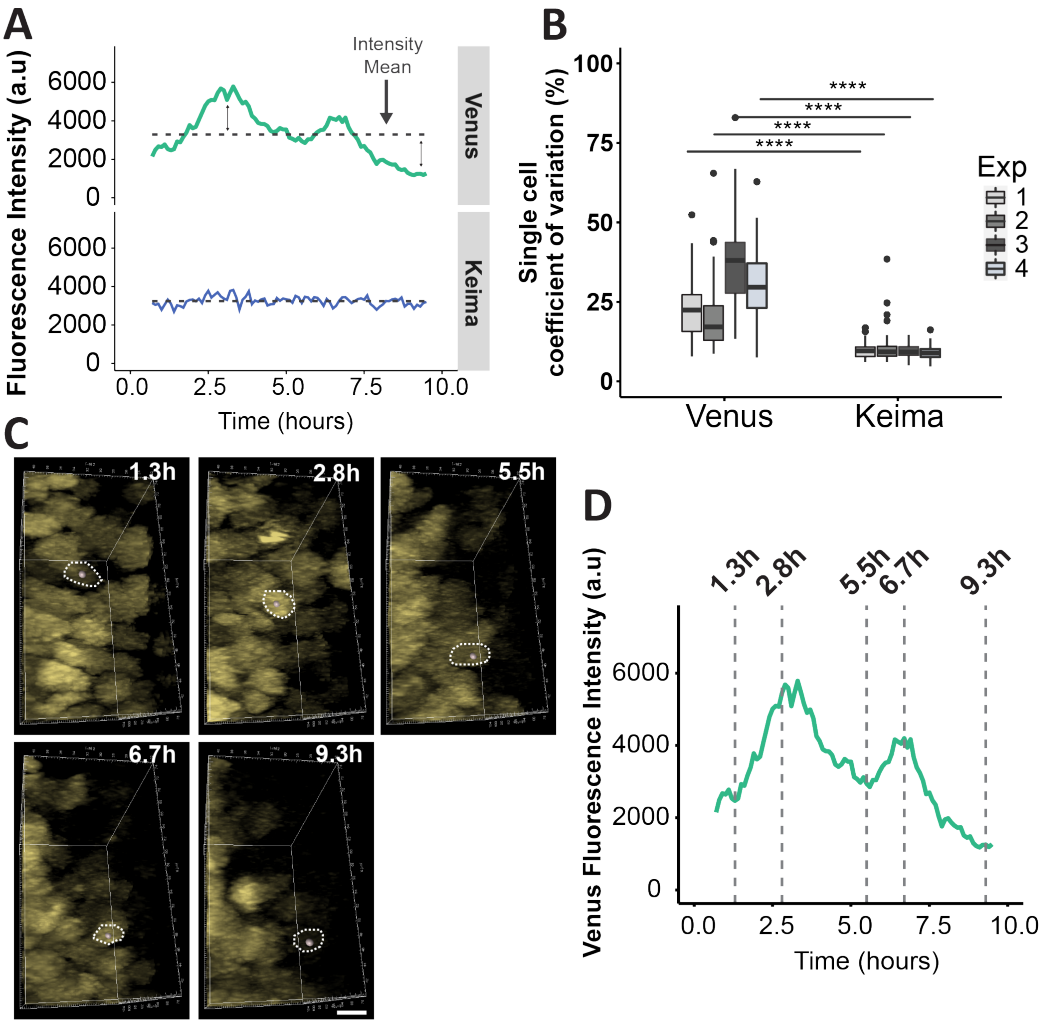

Figure 3.9: **Single cell tracking in real-time live imaging of embryos shows that Venus expression is dynamic at the single cell level.** Each experiment corresponds to a single embryo. **(A)** Example traces of Venus and Keima expression in a single cell over time. The dotted line shows the intensity mean of the corresponding signal and double ended arrows show the variation from the mean used to calculate standard deviation and single cell CV. **(B)** Single cell CV calculated for Venus and Keima in all single cell traces from 4 individual embryos. In all experiments, Venus CV was significantly higher than Keima CV (****). Wilcoxon matched-pairs signed rank test, (ns): $P > 0.05$, (*): $P \leq 0.05$, (**): $P \leq 0.01$, (***): $P \leq 0.001$, (****): $P \leq 0.0001$. **(C)** Shows 3D reconstruction image from z-stacks from the area outlined in 3.9,A. Venus expression followed in a single cell over time. Time-points correspond to expression peaks (2.8h &6.7h) and troughs (1.3h, 5.5h&6.7h). Scalebars = 5µm, h = hours. **(D)** The single cell trace of Venus expression the cell followed in C. The dashed lines correspond to expression peaks and troughs as shown in C.

in Venus traces was significantly higher than Keima (Wilcoxon matched-pairs signed rank test, p<0.0001), demonstrating that Venus expression fluctuated more than Keima over time and hence was more dynamic (Fig 3.9,B). Indeed, Venus level fluctuations could be visualised in single cells (Fig 3.9,C, from the region outlined in figure 3.8,A). In the example presented in figure 3.9,C, Venus fluorescence intensity periodically peaked at 2.8 and 6.7 hours after the start of imaging at 20hpf (Fig 3.9,C & D).

3.2.4 Examination of oscillatory behaviour in single cell time traces

To explore the single cell time-series in a statistical and unbiased manner, a computational pipeline first developed by Phillips et al. (2017) and later adapted for zebrafish cell traces by Soto et al. (2020) was utilised. In summary, this pipeline normalises the Venus intensities to Keima to alleviate any global imaging artefacts and next, removes the long-term trend from the data (detrending). Then, it separates stochastic single cell traces into aperiodic or periodic expression (Chapter 2, "Single cell tracking and analysis"). Both Oscillatory (osc) and fluctuating but Non-oscillatory (non-osc) Venus (i.e. Her6) expression were identified in the developing telencephalon. As expected, Keima expression was often categorised as non-oscillatory as is the case in the example traces shown in figure 3.10,A. More quantitatively, between 5-77% of HV traces (Median = 24%) passed as oscillatory while only 0-11% of Keima traces (Median = 5%) passed as oscillators. Even though Venus traces had a tendency for having more oscillators than Keima, the difference between proportion of oscillators between Venus and Keima traces was not statistically significant (Fig 3.10,B, "Original", 2way ANOVA, P = 0.2793).

The proportion of Venus oscillating cells was highly variable between experiments. For instance, in experiment 1, 5% of Venus traces passed as oscillatory, while in experiment 4, 77% of Venus traces passed as oscillatory. I hypothesised that this variability was at least partly technical and associated with the analysis pipeline. Two potential factors were identified to affect the proportion of oscillators: 1) the length of the time-course where longer time-courses had a tendency for higher percentage of oscillators and 2) paired or unpaired analysis of the data. To assess the contribution of these two factors, experiment 4 was used as an example. This embryo was imaged for the longest time (12 hours) and also as a single embryo, whereas experiments 1,2 and 3 were analysed in pairs with experimental embryos (Described in Chapter 5). To test this hypothesis, traces in experiment 4 were truncated to same length as experiment 2 (8 hours) and paired with the experimental embryo from experiment 2 (Chapter 5). This reduced the percentage of HV traces passing as oscillators in experiment 4 from 77% to 37% (close to the manual measurement at 39% - Data not shown) without altering the median (Fig 3.10, B, Venus, 2way ANOVA, P=0.9701). These alterations did not make a change in the Keima output (Fig 3.10, B, 2way ANOVA, P>0.9999) but reduced the P value for the difference between Venus and Keima (Fig 3.10, B,"Modified", 2way ANOVA, P=0.7164). Given the large variability in this data and the technical effects introduced by the analysis pipeline, it was not possible to report exact percentage of Venus oscillators in this system but rather a range between 5-37%.

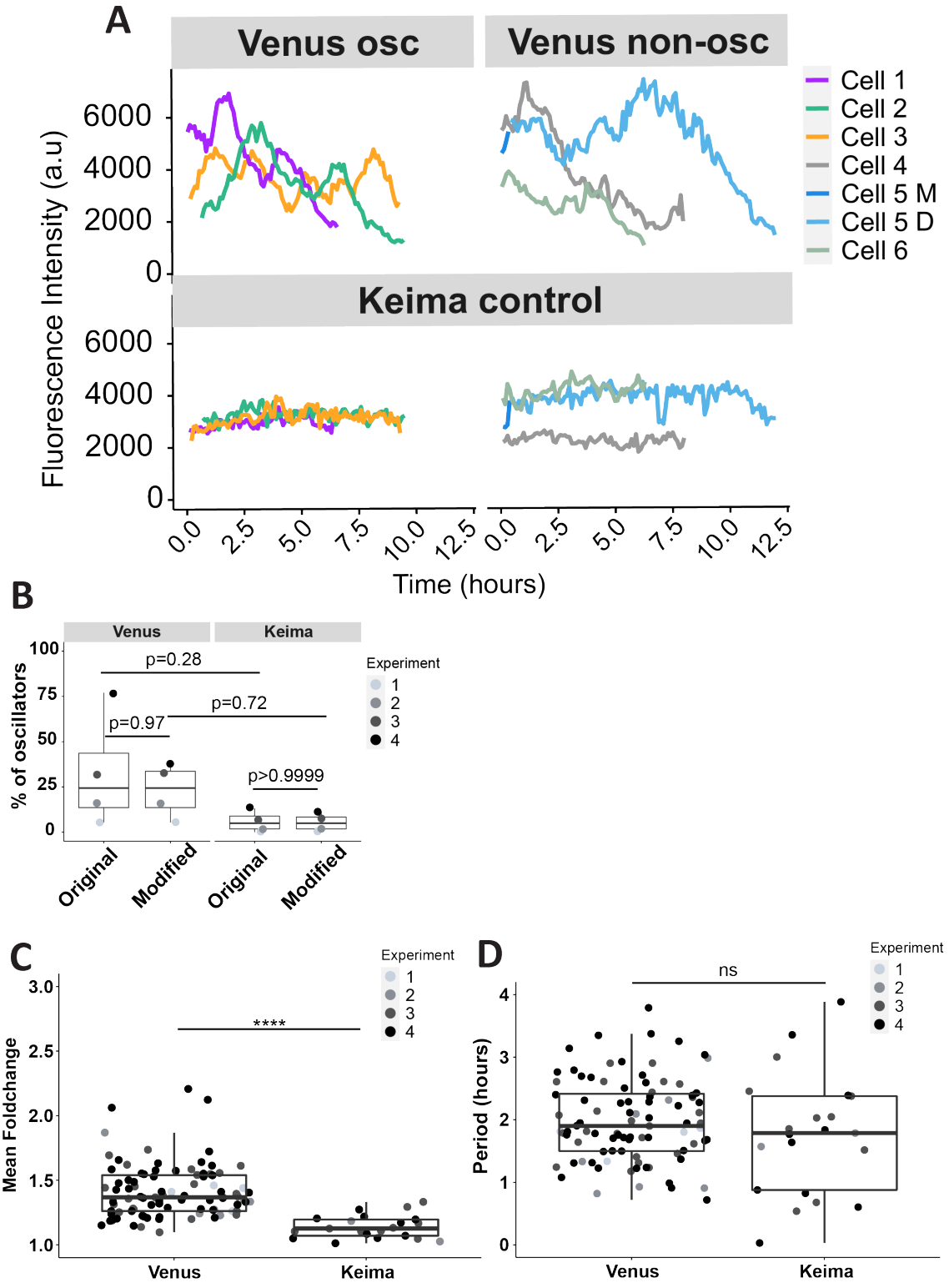

Figure 3.10: **Venus is expressed in an oscillatory manner in a subset of telencephalic progenitors.** Each experiment corresponds to a single embryo. **(A)** Examples of single cell traces computationally separated as oscillatory and non-oscillatory based on their Venus expression over time. Keima expression of each cell is also displayed as a negative control (i.e. non-oscillatory). **(B)** Percentage of oscillatory cells based on Venus and Keima traces. In "Original", all experiments were analysed for the full duration of the original time-course (Exp1 = 6 hours, Exp2 = 8 hours, Exp3 = 10 hours, Exp4 = 12 hours). In "Modified", exp4 was truncated to 8 hours and analysed as a pair with an experimental embryo from exp2. The proportion of Keima traces that passed as oscillatory (Median = 5%) was lower than Venus (Median = 24%) in both Original and Modified. These tendencies were not significant (ns). The modifications of Exp4 did not cause a significant change in percentage of oscillators in Venus or Keima (ns). 2way ANOVA, (ns): $P > 0.05$, (*): $P \leq 0.05$, (**): $P \leq 0.01$, (***): $P \leq 0.001$, (****): $P \leq 0.0001$. **Caption continued on the following page →**

Figure 3.10: **(C)** Mean fold-change measurement of cells that passed as oscillatory based on Venus or Keima signal. Each dot represents the mean of all fold-changes in one cell. Mean fold-change in Venus traces (Median = 1.4) was significantly higher than the mean fold-change in Keima (Median = 1.1) (Shapiro-Wilk test, Keima P=0.486 [Pass normality], Venus P<0.0001 [Does not pass normality], Mann-Whitney test, ****). **(D)** Period measurement for the cells that passed as oscillatory based on Venus or Keima (each dot represents a single cell). The period based on Venus had tighter distribution (median = 1.9), whereas the period based on Keima had a broader distribution (median = 1.8). There was no significant difference between Venus and Keima period (Shapiro-Wilk test, Keima P=0.7512 [Pass normality], Venus P=0.3177 [Pass normality], Welch's test, ns). ns): P > 0.05, (*): P ≤ 0.05, (**): P ≤ 0.01, (***): P ≤ 0.001, (****): P ≤ 0.0001

The mean peak/trough ratio (mean fold-change; average of all fold changes measured in each cell) of Venus traces that passed as oscillators (Median = 1.4) was significantly higher than the mean fold-change of Keima traces that passed (Median = 1.1) (Fig 3.10, C, Keima passed Shapiro-Wilk normality test but Venus did not, Mann-Whitney test, P<0.0001). This suggested that the Keima cells that passed the pipeline had low amplitude fluctuations that were most likely erroneously detected as periodic by the pipeline rather than being true oscillators. The median period of Venus oscillations was 1.9 hours and was consistent between all four experiments. The Keima traces that passed as oscillators had a median period of 1.8 hours (Fig 3.10,D, Both Venus and Keima passed Shapiro-Wilk normality test, Weltch's t test, P=0.3313). Even though measuring the proportion of oscillators was affected by track length and the analysis pipeline, it did not alter the period and fold-change measurements (Appendix 8.2).

3.3 Discussion

The work presented in this chapter aimed to shed light on Her6 as a regulator of neural progenitors in the zebrafish telencephalon and to characterise its expression dynamics. For this purpose, I first characterised the expression of WT *her6* relative to the early post-mitotic neural marker *elavl3* at the early stages of telencephalic development. The quality of the FISH got progressively lower between 22-30hpf with increasing levels of background. Therefore, further optimisation of the protocol is required to enhance signal to noise ratio at these later stages. Furthermore, based on my experience, this may be an embryo effect and imaging more embryos can help identify those with less background noise in the signal.

Nonetheless, I made several observations in this data that is worth noting. I showed that while *her6* is progressively expressed from 11hpf, its domain of expression got smaller and more ventral localised as development progressed and post-mitotic neurons began to emerge. This finding is consistent with the depletion of *her6* expressing progenitor pool in expense of differentiating neurons.

her6 expression was mutually exclusive from *elavl3* which was also seen at the single cell level with high resolution live imaging of HV::Tg(p*elavl3*:mCherry) double line (Ap-

pendix 8.1). This suggested that *her6* is downregulated prior to cell cycle exit and *elavl3* expression. Interestingly, this is in contrast with the observations of Soto et al. (2020) in the hindbrain where they described a transition zone between progenitors and young post-mitotic neurons in which *her6* and *elavl3* were co-expressed. Based on this difference, one may hypothesise that *her6* function may vary slightly between different parts of the developing brain. That is to say, in the hindbrain, *her6* may be associated with early and late progenitor states while in the forebrain, it is predominantly involved with earlier progenitor states.

This idea of *her6* involvement in early progenitors was also supported by the position of its expression domain relative to dorsal (pallium) or ventral (sub-pallium) fate markers, *ngn1* and *ascl1*, respectively. Previously, *her6* had only been described to negatively regulate *ngn1* expression in the dorsal domain (Yoshizawa et al., 2011). But it had never been examined relative to *ascl1* which is an early marker of ventral telencephalon (Allende, Weinberg, 1994; Miyake et al., 2017). Based on my observations, I concluded that in the 20-28hpf telencephalon, *her6* is at least in terms of position, more closely associated with the ventral telencephalon and hence *ascl1* expression. This is similar to *her6* expression in prethalamus and rostral thalamus which co-incides with *ascl1* expression in these domains but abuts *ngn1* expression in the more dorsally placed caudal thalamus (Scholpp et al., 2009). In contrast, while Scholpp et al. (2009) have reported an overlap between *her6* and *ascl1* in the thalamus, I did not observe marked overlapping expression between *her6* and *ngn1* or *ascl1*. However, unlike *elavl3*, I have not confirmed the mutually exclusive expression of *her6* relative to *ngn1* and *ascl1* at a single cell level.

Nonetheless, these observations of *her6* relative to other genes involved in telencephalon development supported its the role as a progenitor regulator and marker. Given the limited to no overlap between *her6* and the fate determination markers and post-mitotic marker *elavl3*, I propose that *her6* and Her6 expressing cells represent early neural progenitors (or neural stem cells) which move towards a cascade of fate determination and then mitotic exit.

A similar model has been proposed by Schmidt et al. (2013) for the development of the embryonic thalamus. In summary, they suggest that Her6 expressing cells represent embryonic neural stem cells (or early progenitors) with strong self-renewal capacity. Upon downregulation of early progenitor markers such as Her6, these cells become late progenitors which are still proliferative but express more specific markers like *ngn1* or *ascl1*, preliminary markers of glutamatergic and GABAergic fates, respectively (Scholpp et al., 2009). The cells that transition to become early post-mitotic neurons express markers such as *elavl3* and later give place to mature neuronal sub-types that express markers like *vglut* or *gad1* which are specific glutamatergic and GABAergic markers respectively (Schmidt et al., 2013). The implications of this model in the telencephalon poses intriguing questions regarding the movement of cells as they transition from early progenitors towards fate

determination, mitotic exist and maturation. Based on my data, this movement may be in a posterior-lateral direction but to the best of my knowledge, this has not been previously shown.

To study the expression dynamics of Her6, I first conducted a detailed characterisation of the HV KI line. I showed that the CRISPR donor backbone had been erroneously integrated in the HV KI genome. I suspect that this was, at least in part, due an active Non-homologous end joining (NHEJ) repair mechanism in zebrafish. Studies that have compared different modes of DNA repair following double stranded breaks in zebrafish embryos do confirm that NHEJ is the predominant mode of repair in comparison to homologous recombination and Single strand anealing (SSA) (Hagmann et al., 1998; Liu et al., 2012). Indeed, others have reported incidence of homology arm duplication which may be a suspected outcome of NHEJ taking place instead of HDR (Wierson et al., 2020). In the case of the HV line, it is likely that a combination of failed KI cassette release, multiple cleavages and NHEJ have contributed to this outcome since NHEJ alone cannot explain the presence of repeated LHA-RHA (Fig 3.5).

One can hypothesise that the use of a single sgRNA to cleave the endogenous target site as well as the donor plasmid may contribute to donor incorporation as it requires one sgRNA to cleave multiple sites. A potential way to avoid backbone integration could be by using distinct and efficient sgRNAs for releasing the KI cassette from its vector instead of same sgRNA that targets the endogenous target site. Indeed, universal CRISPR sgRNAs have been used for reproducible liberation of KI cassette from donor (Wierson et al., 2020). Furthermore, while some have reported higher success rates of HDR using donor plasmids (Zhang et al., 2018), others have shown more successful HDR in zebrafish using Single strand DNA (ssDNA) CRISPR donors (Bai et al., 2020).

Some have taken advantage of this propensity for NHEJ in zebrafish to KI linearised plasmids containing fluorophore coding sequence into a targeted locus. Kesavan et al. (2017) generated the Otx2::Venus reporter KI line using this method which incorporated the donor backbone into the genome. Most importantly, Kesavan et al. (2017) demonstrated that the KI loci can remain completely functional despite incorporation of the backbone. However, one important feature of the design by Kesavan et al. (2017) was that they directed plasmid incorporation to the non-coding sequences before the start codon of the target gene.

Nonetheless, even though the donor incorporation in the HV is at 3' end of the gene, Soto et al. (2020) showed that *her6* expression and embryo morphology are not affected in this KI. My work explains this by confirming that HDR at the 5' junction of the cassette has occurred without any issues placing Venus in frame with the endogenous ATG (start) codon. Also, the intact stop codon at the end of Venus makes aberrant protein translation after Venus unlikely. Another important consideration is that the *her6* 3' Untranslated region (UTR) that contains the miR-9 binding sites (MBS) was included in the RHA which was present in the correct position following Venus in the HV KI locus. This guarantees

correct post-transcriptional modification of *her6* mRNA which is critical in its dynamics (Soto et al., 2020).

However, even though I extensively examined the genomic composition of this KI domain, I have not examined the resulting mRNA that is expressed from this region. One may hypothesise that a long transcript is produced from this region that encompasses both the KI region and the duplicated LHA-RHA sequence (Fig 3.6,B). In this scenario, alternative splicing of the exons in the duplicated LHA (Exons 2-4) may result in mature mRNAs that lack Venus. This would lead to dilution of Venus signal at the protein level and could have implications in interpretation of live imaging as what is observed by Venus signal is not all the Her6 protein present in each cell in a homozygous context. This concern can be addressed by Reverse transcription PCR (RT-PCR) using a forward primer that targets either exon 1 or 2 and a reverse primer binding in the RHA. If only the desired mRNA is generated, I would expect a single amplicon while if alternative mRNAs are present, I would expect an additional amplicon that is $\sim$717bp smaller due to the absence of Venus.

In addition to genomic analysis, I used double FISH aiming to compare the expression of Venus-containing mRNAs with endogenous WT *her6* mRNA expression. Venus-containing mRNAs were indeed present in the anterior telencephalic domain comparable with the endogenous *her6* mRNA in WT and KI. However, the poor quality of the probe against Venus was a limiting factor to quantification. Furthermore, FISH does not provide single cell resolution which makes high resolution interpretation of gene expression challenging. Alternatively, an Single molecule fluorescent in situ hybridisation (smFISH) approach using probes against Venus and *her6* could provide both single cell resolution and quantitative quality and would be very suitable for confirming these findings.

Following the verification of HV as a suitable model, I imaged the Her6 expression domain of the telencephalon in live HV embryos. By analysing the cell population, I showed that Her6 expression in this domain was heterogenous, consistent with the expression of its mouse counterpart, HES1 (Shimojo et al., 2008; Imayoshi et al., 2013). According to Huang (2009), such heterogeneity can be an outcome of various single cell behaviour patterns over time such as set single cell levels, noisy but aperiodic expression but also periodic oscillations (Fig 3.11). By tracking Her6 expression in single cells over time, I showed that its levels fluctuate more than the control nuclear marker, H2B-Keima. This made set single cell levels an unlikely source of population heterogeneity. In 5-37% of cells, expression of Her6 oscillated periodically while in the rest, its fluctuations were aperiodic. However, unlike Soto et al. (2020), I did not perform any measurements of noise and hence cannot make conclusions on whether levels of noise is different between the oscillators and non-oscillators. Nevertheless, I can conclude that single cell fluctuations of Her6, including its oscillations are at least one of the sources of its heterogeneity in the population.

Several studies have linked population heterogeneity in the expression of bHLH transcrip-

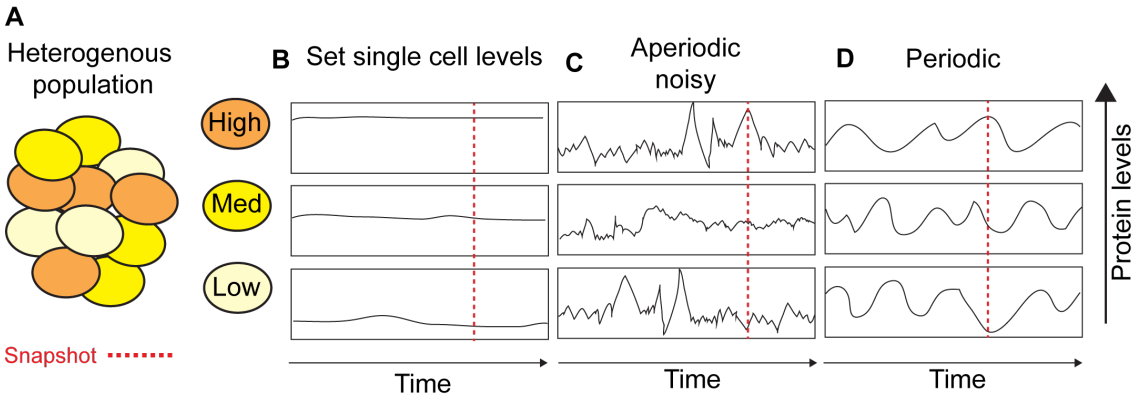

Figure 3.11: **Different sources of snapshot heterogeneity in a cell population.** **(A)** Schematic snapshot of a heterogenous population where some cells have high protein expression levels, some medium and some low. Various single cellular behaviours over time may give rise to such snapshot heterogeneity. **(B)** One scenario is "Set single cell levels" where cells have variable levels of protein expression which they retain over time. For instance, the High cell has steady high expression levels over time. At the snapshot time-point (red dotted line), these cells can reproduce the heterogenous population (A). **(C)** Another potential scenario to explain snapshot population heterogeneity is where individual cells exhibit noisy but aperiodic expression of the protein ("Aperiodic noisy"). At the snapshot time-point (red dotted line), these each cell would have certain level of protein depending on its noisy expression. For instance, one cell can be at a peak (top), another at intermediate levels (middle) and another may contain very little protein (bottom). Combined, all of these cells can reproduce the heterogenous population (A). **(D)** Another scenario that could explain snapshot population heterogeneity is if individual cells express the protein in a "Periodic" but asynchronous manner. In this case, at the snapshot time-point (red dotted line), the High cell is at the peak of an oscillation (top), the Medium cell is in the downward part of an oscillation (middle) while the Low cell is at an oscillatory trough (bottom). When these cells at different oscillatory phases are combined in a population, they can reproduce a heterogenous population (A).

tion regulators to their fluctuations at the single cell level including their ultradian oscillations (Shimojo et al., 2008; Kobayashi et al., 2009; Imayoshi et al., 2013, 2015; Manning et al., 2019; Soto et al., 2020). Shimojo et al. (2008) and Imayoshi et al. (2013) described *Hes1* oscillations in mouse telencephalon dissociation and slice cultures using *Hes1* promoter-Luciferase reporters. They claimed that all cells that expressed *Hes1*, did so in an oscillatory manner. However, consistent with my data, Manning et al. (2019) and Soto et al. (2020) who have reported on oscillations of HES5 and Her6 in mouse spinal cord and zebrafish hindbrain, respectively, show that in both of these systems, a combination of oscillators and fluctuating but aperiodic cells can be found. In more detail, HES5 expression oscillated in ∼41% of spinal cord cells (Manning et al., 2019) and Her6 was oscillatory in 40-80% of progenitor cells in zebrafish hindbrain (Soto et al., 2020).

The difference in the prevalence of oscillatory behaviour between different systems may be a reflection of differences in the functional role of oscillations. For instance, in mouse telencephalon, *Hes1* expression and oscillations are thought to maintain progenitors which would entail the necessity of oscillatory behaviour in all progenitors (Shimojo et al., 2008; Imayoshi et al., 2013). However, in mouse spinal cord (Manning et al., 2019) and zebrafish hindbrain (Soto et al., 2020), oscillatory expression of HES5 and Her6, respectively, are attributed to commitment of progenitors to move towards differentiation which does not necessarily occur in all cells simultaneously, resulting in lower proportion of oscillators

at any given time. Another potential contributing factor to these differences could be the methodology used to distinguish between oscillators and non-oscillators. Manning et al. (2019), Soto et al. (2020) and the work in this chapter used more thorough computational methods based on Phillips et al. (2017) which introduces specific criteria for classifying cells as oscillators. The stringency of these criteria may lead to fewer cells being classified as oscillators.

In support of the latter, I have shown that certain analysis conditions (individual vs paired) and the length of single cell tracks can indeed introduce an artefact in the number of cells that pass as oscillators. The exact cause of differences between individual and paired analysis are not yet clear. However, it is more intuitive to appreciate that longer cell tracks lead to higher likelihood of detecting periodicity. Indeed, Burton et al. (2021) have computationally shown that increasing the length of biological time-series data allows better parameter inference for an oscillator in comparison to increasing sampling frequency.

Using additional analysis methods may help bypass these technical artefacts and increase the robustness of the measured characteristics of the oscillator. For instance, MetaCycle is an R package that combines different methods of detecting periodicity (ARSER, JTK-CYCLE and Lomb-Scargle) to explore time-series data. By using N-version programming (NVP), it selects the best method for rhythm detection for the specific data and has been shown to perform well with time series where only one or two peaks are available (Wu et al., 2016). This can be particularly useful while analysing shorter time-series data.

3.4 Concluding remarks

In this chapter, I shed more light on Her6 as a regulator of neural progenitors in zebrafish telencephalon by studying its expression domain and dynamics. Using double FISH, I showed that *her6* mRNA is expressed extensively in the presumptive telencephalon but its domain shrinks as post-mitotic neurons that express *elavl3* begin to emerge. Furthermore, the *her6* and *elavl3* domains were not overlapping. In relation to the telencephalic sub-domains, *her6* was expressed ventrally and anterior to the sub-pallial markers, *ascl1* and ventral to the pallial marker *ngn1* in seemingly exclusive domain. When combined, this data supports the role of *her6* as a progenitor marker which, to the best of my knowledge, had not been directly described before.

To characterise Her6 expression dynamics with single cell resolution, I first characterised the HV KI locus in more detail. I confirmed that the Venus coding sequence has incorporated correctly and in frame at the endogenous *her6* locus, as was expected by the design. However, the CRISPR donor backbone has also been incorporated after the RHA, followed by aberrant duplication of the WT *her6* locus without a start codon (LHA-RHA). With a combination of ORF analysis, live imaging and double FISH, I confirmed that the expression of HV fusion protein recapitulated WT *her6* expression and therefore it is unlikely

that Her6 function has been affected. Live imaging of HV embryos demonstrated that Her6 expression in the telencephalon is heterogeneous which, at least in part, is explained by its dynamic expression at single cell level. These dynamics were classified as periodic oscillations in ∼5-37% of cells with a median period of 1.9 hours and median mean fold-change of 1.4. These findings raised the hypothesis that altering Her6 expression dynamics may provide insight into their regulation and function at single cell and population level which will be addressed in subsequent chapters.

Chapter 4

Characterisation of a model system for studying destabilised Her6 protein

4.1 Background

Rapid clearance of protein is an important feature of oscillatory networks as it assists the required resetting of the cycle (Monk, 2003; Isomura, Kageyama, 2014). Hence, ultradian oscillatory proteins are short-lived (Hirata et al., 2002; Bessho et al., 2003; Ay et al., 2013; Soto et al., 2020) and as highlighted by previous studies, changes in these protein degradation kinetics alter their oscillations. For instance, silencing components of the SCFFBXL14 ubiquitination complex that mediates the proteasomal degradation of HES1 using Small interfering RNA (siRNA), stabilised the protein and disrupted its oscillations in mouse-derived F9 cells (Chen et al., 2017). On the other hand, destabilising HES1 by siRNA Knock-down (KD) of its Deubiquitinating enzyme (DUB), Ubiquitin specific protease 22 (Usp22), shortened its half-life and abolished its oscillations in bulk serum-starved C3H10T1/2 cells (Kobayashi et al., 2015). In another report, Lysine to Arginine (K>R) mutations of HES7 ubiquitination sites increased its half-life from 22 to 30 minutes which disrupted the continuity of HES7 oscillations in mouse Presomitic mesoderm (PSM), leading to defects in later stages of somitogenesis (Hirata et al., 2004). Even though these reports highlighted the importance of protein turnover kinetics in oscillatory networks, they lacked combined single cell and *in vivo* insight and their methods were prone to unwanted effects.

Enzymes rarely have a single target and therefore, altering regulating enzymes for studying oscillations may also affect other target proteins. For instance, in addition to HES1, SCFFBXL14 ubiquitin ligase regulates the stability of other proteins such as MYC in glioma stem cells (Fang et al., 2017) and the Epithelial to mesenchymal transition (EMT) regulator, SNAIL1, in HEK293T cells (Viñas-Castells et al., 2010). Usp DUBs often contain protein-protein interaction domains that allow them to directly identify their targets rather than identifying them merely based on the presence of ubiquitin (Mevissen, Komander, 2017). However, Usps can still target more than one protein. As such, based on a large-scale ChIP-sequencing study in HeLa cells (human cervical cancer), the HES1 DUB, Usp22, has over 50 targets (Gong et al., 2018).

Even though K>R mutations are a more direct approach for hindering ubiquitination of the protein of interest, they have many disadvantages. Proteins often contain several Lysine (K) residues and it is possible for several of them to be ubiquitin targets. This not only makes this mutagenesis approach laborious (Xu, Jaffrey, 2013), but the combined effect of mutating several residues may also structurally affect protein folding and stability without impacting ubiquitination (Sokalingam et al., 2012). To add to the complexity, there is a level of flexibility in ubiquitin-targeted K residues since when the major ubiquitination sites are mutated, other residues can compensate for their absence (Hou et al., 1994; Bhat et al., 2010).

An alternative approach is protein destabilisation by direct fusion of a Proline, Glutamic

acid, Serine and Threonine-rich (PEST) sequence (Li et al., 1998). PEST sequences were proposed as signals that make proteins susceptible to rapid proteolysis by Rogers et al. (1986). Indeed, these sequences were enriched in short-lived proteins. That is to say, at least by 1991, only a small proportion of all proteins had PEST sequences but the majority of short-lived proteins contained these domains (Rechsteiner, Rogers, 1996). Furthermore, the truncation of PEST domains in such short-lived proteins, such as Ornithine decarboxylase (ODC) or IκBα, increased their half-lives (Ghoda et al., 1989; Whiteside et al., 1995). But most importantly, it was shown that when transplanted to stable proteins, PEST sequences could confer susceptibility to proteolysis (Rechsteiner, Rogers, 1996). As an example, when the PEST sequence from Mouse ornithine decarboxylase (MODC) was fused to a stable ODC from a protozoan parasite with a half-life of more than 4 hours, the resulting fusion protein had a half-life of ∼45 minutes (Ghoda et al., 1990). Even though the exact mechanism through which PEST sequences regulate protein stability is not well known, they most likely make proteins targets of the 26S proteosome pathway (Rechsteiner, Rogers, 1996).

The strong support for the "PEST hypothesis" first proposed by Rogers et al. (1986), has led to its wide acceptance and use in engineering short-lived proteins. This was pioneered by Li et al. (1998) who fused EGFP (with a half-life of much longer than 3 hours) to the PEST domain from mODC and generated Destabilised EGFP (dEGFP) with a 2-hour half-life. dEGFP with three Glutamic acid to Alanine mutations in residues 428, 430 and 431 of the mODC PEST sequence (E428A-E430A-E431A), had a half-life of ∼30 mins which was at least 6 times shorter than EGFP. Subsequently, PEST fusions have been extensively used to destabilise often stable fluorescent proteins in generation of reporters for studying dynamic processes in mice (Aulehla et al., 2008) and zebrafish (Yeo et al., 2007; Collery, Link, 2011; Ninov et al., 2012).

Based on this principle, the Her6-Venus-PEST (HVP) CRISPR Knock-in (KI) line was generated alongside Her6-Venus (HV), using the E428A-E430A-E431A variant of mODC PEST domain to circumvent potential stabilisation of Her6 by fusion to Venus (Both lines were generated by ***Dr Ximena Soto***). However, Soto et al. (2020) compared the half-life of HV with HA-Her6, representing Wild type (WT) Her6 (11 and 12 min, respectively), showing that fusion of Venus has not significantly stabilised Her6 in HV. This raised the hypothesis that HVP represents a destabilised form of Her6 and therefore, a potential model for altered Her6 dynamics. This hypothesis led me to characterise the HVP KI line in preparation for a comparative study of dynamics with HV, first by examining the incorporation of the KI cassette in the HVP genome.

In addition, for interpreting potential dynamic changes resulting from Her6 destabilisation, an estimate of the magnitude of change in protein half-life was required. The previous studies that had utilised the modified mODC PEST domain were not focused on precise changes of protein stability. Therefore, they had not provided any measurements of the

half-life changes induced by the addition of this PEST sequence in mouse (Aulehla et al., 2008) or zebrafish models (Ninov et al., 2012). Therefore, little was known about the magnitude of change it imposes in different organisms and model systems and whether it was relative to the initial half-life of the protein. As a result, estimating HVP half-life based on the HV half-life measured by Soto et al. (2020) was not possible. Hence, as the next characterisation step, I sought to measure and compare HV and HVP protein half-lives.

A number of techniques have been developed for measuring protein half-life. One common approach is Cycloheximide (CHX) chase experiments (Patrick et al., 1998; Kao et al., 2015). CHX blocks translation elongation and thereby inhibits protein synthesis (Kao et al., 2015). This allows the detection of protein degradation with either Western Blot or microscopy and measurement of protein half-life without the influence of newly synthesised protein. However, CHX treatment can lead to drastic and global changes in cellular metabolism (Schimke, Doyle, 1970; Zhang et al., 2007; Rogers et al., 2015).

To circumvent these shortcomings, I first used a more recent and alternative method based on irreversible Photo-switchable (PS) or Photo-activatable (PA) proteins (Zhang et al., 2007; Müller et al., 2012; Rogers et al., 2015). I will refer to this method as Fluorescnece decay after photo-switching/activation (FDAP), an expansion of the term proposed by Rogers et al. (2015). For FDAP, the protein of interest is fused to a PS or PA and upon exposure to the suitable switching/activation wavelength, a subset of the fusion protein becomes permanently distinguishable from newly synthesised proteins. In theory, and in absence of photo-bleaching, fluorescence decay is equivalent to protein degradation which can be used to measure half-life. The PS, Dendra2, switches from green to red emission upon exposure to violet or blue light and is predominantly the fluorophore of choice for FDAP (Zhang et al., 2007; Rogers et al., 2015). But PAs such as Photo activatable green fluorescent protein (PA-GFP) have also been used for this purpose (Plachta et al., 2011). This fluorophore is normally in low fluorescence conformation (Off) but when exposed to UV light, its fluorescence increases by $\sim$100-fold (On) (Patterson, Lippincott-Schwartz, 2002).

To use FDAP for measuring the effects of PEST domain on Her6 half-life, I opted for PA GFP as it is more closely related to Venus. Another advantage was that PA GFP reportedly matures faster than Dendra2 (Wang et al., 2014). This was desirable for measuring half-life of Her6-PEST as, in theory, the protein was short-lived. My attempt in FDAP was in part successful, but due to some challenges in its optimisation, reliable and consistent measurements of Her6 and Her6-PEST half-lives could not be made. Hence, I also conducted CHX chase experiments using HV and HVP over expression and Western blotting in zebrafish embryos (adapted from Soto et al. (2020)). Similar to the FDAP approach, this method also did not result in consistent results.

I speculated that the difference between HV and HVP is small and therefore difficult to measure in zebrafish. It has been established that to a great extent, protein half-life is

determined by the cellular context rather than protein sequence (Matsuda et al., 2020). In agreement with this, mouse HES7 degrades more slowly when examined in human cells (Matsuda et al., 2020). Using this principle, I made the assumption that HV and HVP would also adapt and degrade slower in human cells, which could amplify their difference and facilitate half-life measurement. This was tested by conducting CHX chase in human cells transfected with HV and HVP followed by live imaging.

In summary, the following points are addressed in this chapter:

1. Characterisation of the HVP KI locus;
2. Attempted use of FDAP for measuring protein half-life with Her6 and Her6-PEST fused to PA GFP;
3. Attempted use of CHX chase and Western blotting for measuring HV and HVP half-lives in a zebrafish over expression system;
4. Attempted use of CHX chase and live imaging to estimate the difference between HV and HVP half-lives using transient over-expression in human cells.

4.2 Results

4.2.1 Characterisation of the HVP KI locus genomic structure

The HVP KI line was designed and generated by ***Dr Ximena Soto***. For this, the endogenous Wild type (WT) *her6* locus was targeted with a Single-guide RNA (sgRNA) directed to the 3' end of exon 4, before the stop codon (fig4.1,A). To release the KI cassette from its vector (donor backbone), the KI cassette in the CRISPR donor was flanked by binding sites for the same sgRNA targeting the endogenous target sequence. This cassette consisted of the sequences of exons 2, 3 and 4 without the stop codon, forming the Left homology arm (LHA). The LHA was connected in frame via a linker sequence (shown in purple) to the coding sequence for Venus and a PEST domain, ending with a stop codon. 963 Base pairs (bp) of genomic DNA after the *her6* locus was included after this stop codon, serving as the Right Homology arm (RHA). The donor plasmid excluded the first exon and its start codon (fig4.1,B) and the KI locus was expected to contain the KI cassette inserted in frame with the endogenous exon 1 (fig4.1,C).

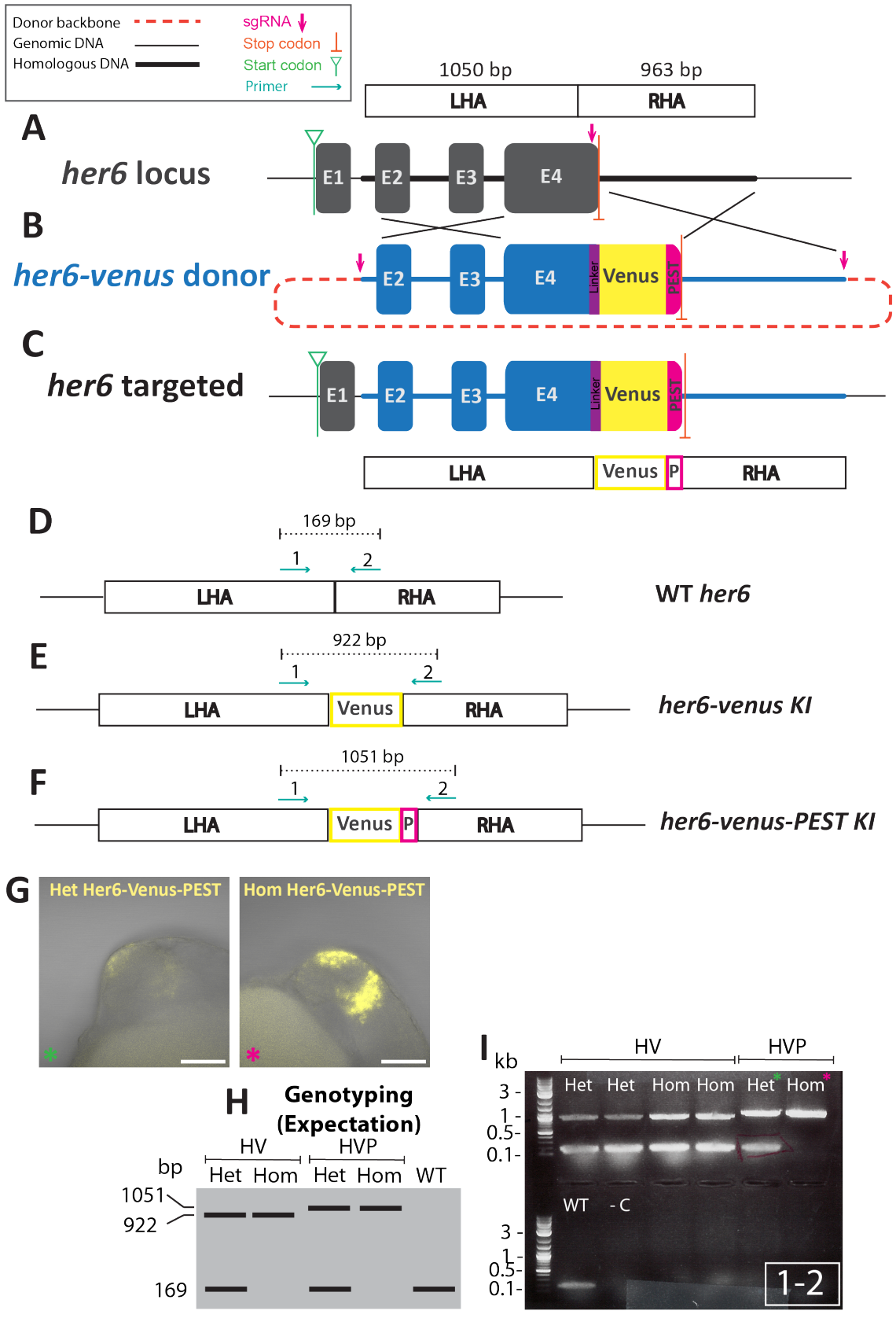

Figure 4.1: **Her6-Venus-PEST knock-in CRISPR design and genotyping.** **(A)** Structure of the endogenous *her6* locus. sgRNA directed cleavage to the 3' end of exon 4, before the stop codon. **(B)** Structure of the *her6-venus-PEST* CRISPR donor which excluded exon 1, but included exons 2, 3 & 4 that form the LHA. Genomic sequences after the *her6* exon 4 were included in the donor as the RHA. Binding sites for the sgRNA were incorporated at either end of the KI cassette to allow cassette release. **Caption continued on the following page →**

Figure 4.1: **(C)** The expected outcome of correct incorporation of the HVP KI cassette in frame with endogenous start codon and exon 1. **(D, E & F)** Binding sites of primers 1 and 2 at the WT *her6*, HV KI and HVP KI loci, which should respectively amplify a 169bp, 922bp and 1051bp amplicon. **(G)** Confocal images of single Z plane from 17-18hpf embryos in lateral view. Rostral is on the left and caudal on the right. Using consistent confocal parameters for detecting Venus expression, embryos could be separated into Het (left) and Hom (right) according to Venus intensity. Scalebar = 100µm. **(H)** Schematic diagram of gel electrophoresis showing the prediction of PCR genotyping of HV and HVP with 1-2 primer pair. This was predicted to produce 169bp band in WT, 922bp band in HV Hom, 1051bp band in HVP Hom and both WT and the corresponding KI band in Het. **(I)** Image of gel electrophoresis following PCR amplification with primer pair 1-2 resulted in 2 bands in Het and Hom HV embryos, 2 bands in HVP Het but only one band in HVP Hom (∼1 Kilo-bases (kb) and ∼0.2kb) and one band in WT (∼0.2kb). Green and pink asterisks refer to the Het and Hom imaged embryos from G respectively.

To determine if HDR has occurred successfully in the HVP KI locus and to compare it with HV, PCR amplification from genomic extracts of HV and HVP embryos was done in parallel. Primers 1 and 2, which bind the 3' end of the LHA and the 5' end of the RHA, respectively, were ideal for distinguishing between KI and WT as they spanned the junction between LHA and RHA. This pair was expected to amplify a 169bp fragment in WT genome, a 922bp fragment from the HV locus and a 1051 bp fragment from the HVP KI locus (Fig 4.1, D, E & F respectively). Similar to HV, HVP embryos could be presumptively categorised as Het and Hom based on Venus intensity (Fig 4.1,G). Therefore, a clear distinction between WT, Het and Hom was expected by amplifying HVP genomic extracts with primers 1-2 (Fig 4.1,H). While this PCR did not distinguish between Het and Hom HV embryos, it resulted in the expected amplicons in HVP, clearly genotyping Het and Hom (Fig 4.1,I).

Successful genotyping of HVP embryos was an indication of successful HDR following CRISPR. To confirm this, the junctions of the HVP KI cassette with the endogenous DNA surrounding the *her6* locus were further characterised with the same approach that was used for HV (Soto et al. (2020), see chapter 3). Successful incorporation of the 5' end of HVP KI cassette had been confirmed by ***Dr Soto*** previously. I verified this by pairing primer 3 that binds before the LHA with primer 2 (Fig 4.2,A). As expected, this reaction produced a single band in HVP Hom DNA which was slightly larger than the single band from HV, due to the presence of the PEST sequence (Fig 4.2,B). This band was expected to be ∼2kb but appeared bigger on the gel which could be a technical artefact because of poor resolution of the DNA ladder. The sequence of the HVP amplicon aligned with the expected HVP KI sequence (Fig 4.2,C). This fragment aligned with the junction between the endogenous exon 1 and the LHA, confirming correct HDR at the 5' end of the HVP KI (Fig 4.2,D). Furthermore, this confirmed the presence of the intended stop codon at the end of the PEST sequence (Fig 4.2, E).

Since this CRISPR design had led to donor incorporation at the 3' junction of the HV KI cassette (explained in chapter 3), this was also a concern for the HVP line. Therefore, primer combinations that target the donor backbone and had been used to characterise the HV line were used on HVP genomic extracts. Primers 4 and 5, which bind the 3' end of RHA and 3' end of the NeoR/KanR gene in the donor backbone, respectively (Fig 4.2,F),

amplified a ∼1.8kb band in HVP, as in HV (Fig 4.2,G). Similarly, primers 6 and 7, both of which bind only in the donor backbone sequence, amplified a ∼1kb band in HVP, as they did in HV (Fig 4.2,H). This confirmed that like HV, the donor backbone has also been integrated in the HVP genome.

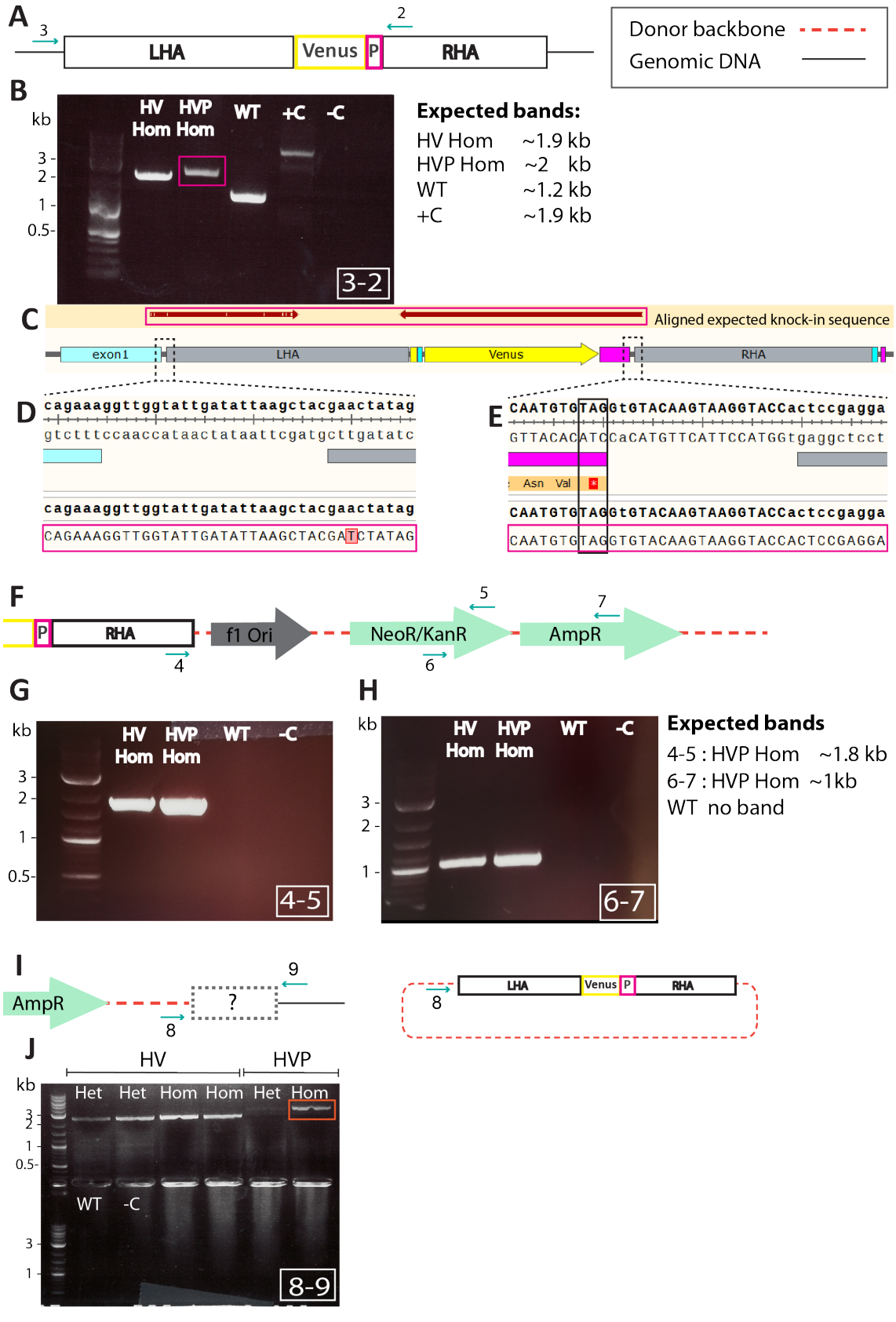

Figure 4.2: **Step-wise PCR for characterising 5' and 3' ends of the HVP KI locus. Caption on the following page →**

Figure 4.2: **(A)** Schematic diagram showing binding site of primers 3 and 2 in HVP KI. **(B)** Image of gel electrophoresis following PCR amplification with primer pair 3-2 in HV and HVP. This pair amplified one ∼2.8kb band in HV Hom and one ∼3kb band in HVP Hom (outlined with pink box), one ∼1.9kb band in WT and a >3kb band in +C, which were larger than expected values. **(C)** The HVP Hom amplicon outlined in pink box was sequenced. It aligned with expected KI sequence. **(D)** Alignment of HVP Hom amplicon (pink box) with expected HVP KI sequence showed correct incorporation at the 5' end of LHA. **(E)** Alignment of HVP Hom amplicon (pink box) with expected KI sequence showed that the stop codon (TAG) outlined in black box was intact at the end of the PEST sequence. **(F)** Schematic diagram of hypothetical HVP KI locus structure where the donor backbone has inserted in the genome after the RHA. It also shows binding site of primers 4, 5, 6 and 7. **(G)** Image of gel electrophoresis using primers 4-5. This amplified ∼2kb sequence in both HV and HVP Hom and no sequences in WT **(H)** Image of gel electrophoresis using primers 6-7, which resulted in ∼1.1kb band in both HV and HVP Hom, while no sequences were amplified in WT. **(I)** On the left - schematic diagram of HVP KI locus with unknown length of donor backbone insertion followed by endogenous sequences. It also shows the binding site of primers 8 and 9. On the right - schematic diagram of the HVP CRISPR donor and binding site of primer 8. **(J)** Image of gel electrophoresis using primers 8-9 that amplified a ∼2.9kb sequence in HV Het and Hom and a ∼4kb band in HVP Het and Hom (outlined with orange box), while no sequences were amplified in WT.

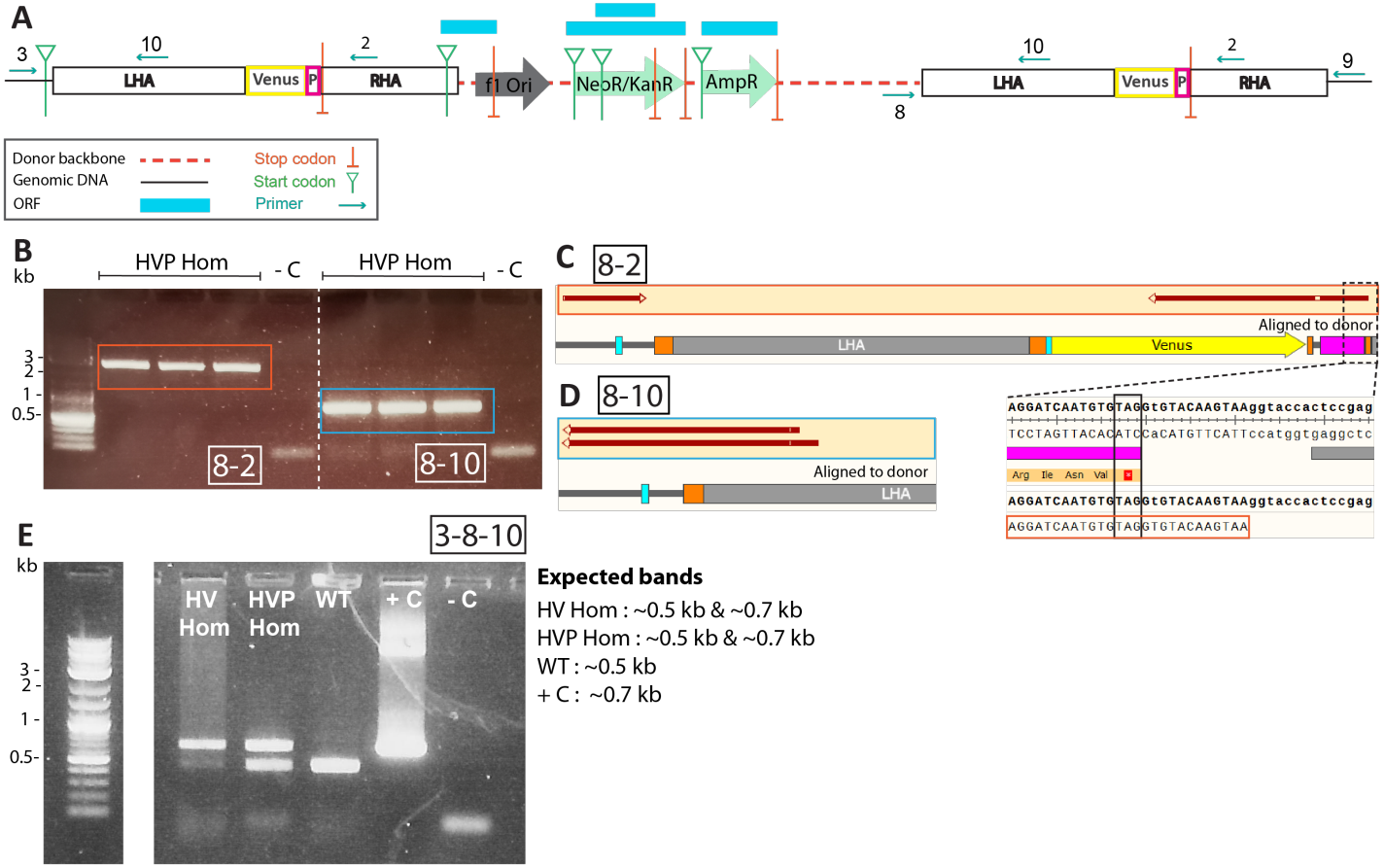

Figure 4.3: **A new model for the genomic architecture of the HVP KI locus. (A)** Schematic diagram of a proposed model for the structure of HVP KI locus. In this model, the 5' end of the KI cassette had inserted correctly. The donor backbone had been fully inserted at the 3' end of the cassette, followed by duplicated insertion of the KI cassette. It also shows the binding sites of primers 2, 3, 8, 9 and 10 and the ORFs present in the donor sequence. **(B)** Image of gel electrophoresis following PCR amplification with primer pairs 8-2 (left) and 8-10 (right). 8-2 pair amplified a ∼3kb sequence in HVP Hom genomic extracts. The 8-10 primer pair resulted in a ∼0.7kb amplicon in HVP Hom. **(C)** The 5' end of the 8-2 amplicon sequence aligned with the backbone sequence before the LHA while its 3' end aligned with Venus and PEST coding regions. This sequence also showed presence of TAG stop codon a the end of PEST (outlined in black box). **(D)** The sequence of the 8-10 amplicon spanned the junction between donor backbone and LHA. **(E)** Image of gel electrophoresis using primers 3-8-10 which amplified a ∼0.7kb and a ∼0.5kb band in HV and HVP Hom, a ∼0.7kb band in +C and a ∼0.5kb band in WT.

To determine the sequences following the donor backbone insertion in the HVP, primer 8, which binds the backbone immediately before the LHA was used in conjunction with primer 9, which binds the predicted endogenous sequence following the KI cassette. Theoretically, if the donor had linearised and been inserted in the genome, the 8-9 primer pair would result in an amplicon of ∼400bp. However, this PCR amplified a >3kb band in HVP, which was larger than the band amplified from HV DNA (Fig 4.2,J). I was unable to clone and sequence this amplicon, possibly due to its size. Nevertheless, its amplification implied that similar to HV, a duplication event had occurred in HVP.

Based on the PCR results described above and the final structure proposed for HV (shown in chapter 3), a new model for the structure of the HVP KI locus was hypothesised. In this model, the 5' end of the KI cassette had incorporated correctly and in frame with the endogenous first exon. At the 3' end of the KI cassette, the donor backbone had been inserted into the genome in full, followed by a full duplication of the HVP KI cassette (Fig 4.3,A). To confirm this in absence of the sequence from the 8-9 amplicon, alternative primer combinations were used. Primer 8 paired with primer 2 spanned most of the sequence between primers 8 and 9. This pair amplified a ∼3kb band in HVP Hom, while primers 8 and 10 amplified a ∼0.7kb band in HVP Hom (Fig 4.3,B). Alignment of the sequence of the 8-2 amplicon with the backbone confirmed the presence of a duplicated Venus and PEST domain including its TAG stop codon (Fig 4.3,C). Both 8-2 and 8-10 amplicons aligned perfectly with the junction between the donor backbone and LHA, confirming the absence of a duplicated exon 1 (Fig 4.3,C & D). These findings were further consolidated with the combination of 3-8-10 primers, which were expected to amplify two ∼0.7kb and ∼0.5kb bands in HVP and HV. This reaction resulted in the two expected bands (Fig 4.3,E), which supported the proposed model in figure 4.3,A.

To alleviate the concern for ectopic expression of the unwanted sequences in the HVP line, ORFs were detected in the aberrantly inserted sequences. The ORFs in the HVP donor were identical to the ones identified in HV. All of these identified ORFs culminated in a stop codon. Therefore, it is not expected for any part of the duplicated LHA-Venus-PEST-RHA sequence to be translated, even if they get transcribed as a result of read-through by the transcription machinery. Thus, the HVP fusion protein is expected to be expressed in a manner that is similar to WT *her6*, unhindered by the aberrant sequences that have been incorporated. This is summarised in figure 4.4 where in reality, only the expected and correct sequences for HVP fusion protein are expressed.

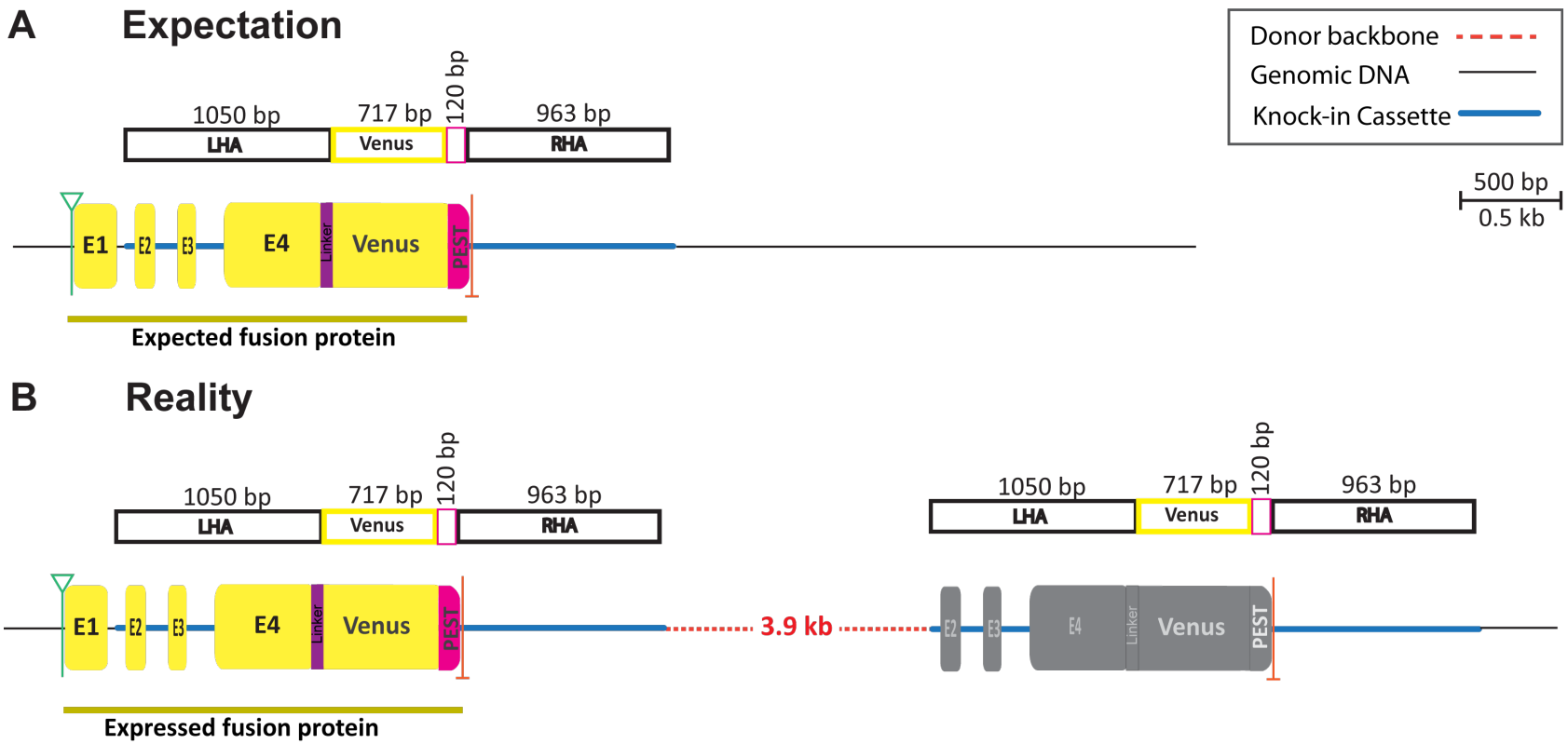

Figure 4.4: **HVP KI locus summary: Expectation versus reality.** All structures are to scale except for the donor backbone which has been cut short in consideration of space. **(A)** The expected structure of the HVP KI locus where the LHA-Venus-RHA are inserted in frame with Exon 1. The RHA is followed by genomic sequence. **(B)** The real structure of the HVP KI locus where the correct expected sequence is present and expected to be expressed as such. The additional ∼6.8kb which includes the donor backbone, Exons 2-4, Venus and PEST are not expected to be expressed.

4.2.2 Fluorescent in-situ hybridisation (FISH) and live imaging confirmed the absence of ectopic Venus expression in HVP

Prior to using the HVP line for a comparative study of Her6 dynamics alongside HV, I wanted to examine its expression pattern relative to WT and HV. This was to ensure that the duplication of LHA-Venus-PEST-RHA after the KI cassette had not led to any unwanted expression of Her6 or Venus sequences. For this, I used a combination of live imaging of Her6-Venus and Her6-Venus-PEST fusion proteins and FISH against the endogenous *her6* mRNA and *venus* containing mRNA on 18-19 Hours post fertilisation (hpf) embryos (Fig 4.5,A). The use of FISH to observe mRNA expression instead of immunostaining to observe protein was due to the lack of suitable antibody against endogenous Her6 protein. These embryos were imaged in a lateral position to highlight Her6 expression in both the telencephalon and diencephalon.

At this stage, endogenous *her6* was expressed in both the telencephalon and diencephalon of WT embryos (Fig 4.5,B). This matched the expression of both HV and HVP fusion proteins in live embryos at a similar stage (Fig 4.5,C&D). Importantly, Venus expression in the HVP did not appear brighter than in the HV, implying that the additional Venus sequence is not expressed. In fact, Venus expression in HVP appeared fainter than Venus expression in HV and this observation will be discussed further in chapter 5.

Double FISH showed that *her6* and *venus* mRNAs occupied similar domains of the telencephalon in HV and HVP embryos and no aberrant expression was detected. However, the domain of *venus* expression appeared slightly narrower than *her6*. I suspect that this is a likely outcome of the poor quality of the *venus* probe that fails to capture lower expression levels posteriorly. Due to the poor quality of *venus* probe, I did not carry out any further quantification on these images as it may have resulted in a misleading low overlap measurement.

4.2.3 Measuring the effect of PEST domain on Her6 protein half-life using over-expression of PA GFP fusion proteins in zebrafish embryos

Having established the correct expression of HVP fusion protein, I sought to determine whether the PEST domain had induced the expected destabilisation effect on Her6. For this, I first attempted to compare the degradation rates of Her6 and Her6-PEST using the FDAP approach. Since generating endogenous KIs of FDAP fusion proteins was time-consuming and more prone to errors, I opted for over-expressing the fusion proteins exogenously. To this end, Her6-PA GFP (HP) and Her6-PA GFP-PEST (HPP) plasmids were designed with assistance from ***Dr Anzy Miller***. In these plasmids, the *her6* Coding sequence (CDS) was fused with the CDS for PA GFP via a linker. In the case of HPP, the E428A-E430A-E431A variant of mODC PEST sequence (Li et al., 1998) was also fused

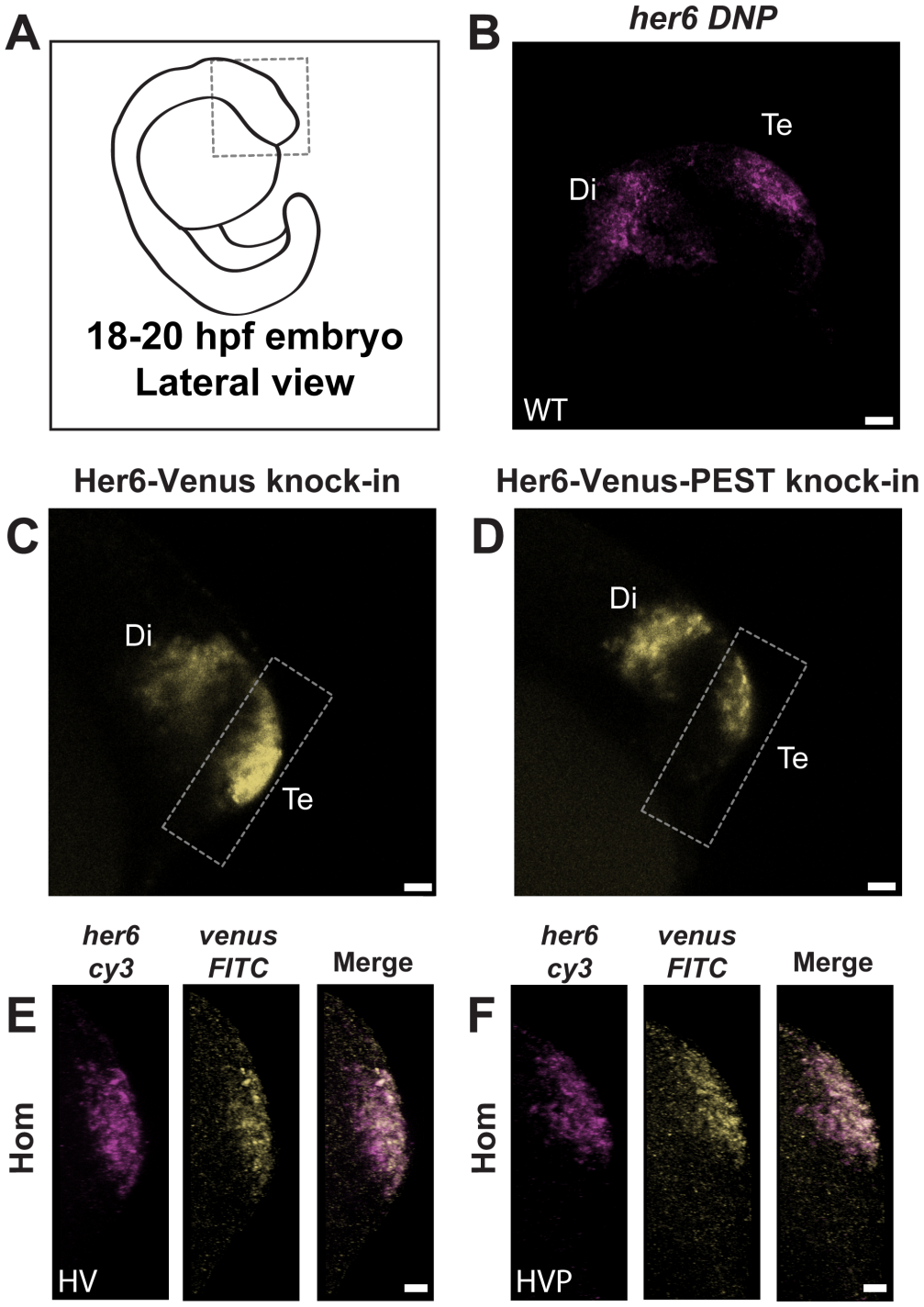

Figure 4.5: **The expression domain of the HVP fusion protein is comparable to expression WT *her6* and HV fusion protein** In all images, rostral is right and caudal is left. **(A)** Schematic diagram of a 18-19hpf embryo in lateral view. **(B)** Maximum intensity projection image of FISH showing expression of *her6* mRNA in WT 20hpf embryo in Te and Di. **(C&D)** Confocal images from a single Z plane of live 17-18hpf Hom HV and Hom HVP KI embryos showing expression of Venus in both Di and Te. **(E)** Maximum intensity projection image of FISH showing co-localised expression of *her6* and *venus* mRNA in the Te of HV 20hpf Hom embryos with no ectopic expression, roughly corresponding to the region outlined in C. **(F)** Maximum intensity projection image of FISH showing co-localised expression of *her6* and *venus* mRNA in the Te of 20hpf HVP Hom embryos with no ectopic expression, roughly corresponding to the region outlined in D. Scale bars: B,C&D=30µm, E&F=20µm. Di: Diencephalon, Te: Telencephalon

in frame at the end of PA GFP. Both constructs contained an HA tag after the PA GFP CDS (Fig 4.6,A). HP and HPP mRNAs were synthesised *in vitro*. Either HP or HPP was co-injected into 1 cell stage WT embryos with Caax-RFP mRNA to label cell membranes. 4hpf embryos were used for imaging (Fig 4.6,B).

PA GFP fusion proteins were successfully activated by exposure to four or five 20-30s UV pulses. The decay of the signal was imaged for ∼60 mins. Figure 4.6,C shows examples of ∼4hpf embryos injected with either HP and HPP. Panel 1 is before activation, panel 2 is after activation and panel 3 is the end of the time-course after protein decay. The raw PA GFP intensity from these embryos are plotted and marked in figure 4.6,D. The resulting decay traces from all embryos analysed were quite variable without a clear distinction between HP and HPP (Fig 4.6,E). The decay between 2 and 3 from each trace was fitted with an exponential curve and the half-life was calculated using the curve equation. Median half-life of HP was 34 minutes while the median half-life of HPP was 27 minutes, suggesting a small but statistically insignificant tendency for shorter half-life in HPP (Mann-Whitney test, P=0.8393, Fig 4.6,F).

I next introduced an estimated cutoff at 14 minutes to separate the activation signal from the decay signal. Then the decay signal from all embryos of each group were averaged and fitted with non-linear regression curves. Both HP and HPP were best fitted with "plateau followed by one phase decay" models. But the HP and HPP curves were significantly different (Extra sum-of-squares F test, P<0.0001) with estimated half-lives of 24.9 and 57.8 minutes, respectively (Fig 4.6,G). I suspected that these unexpected measurements could have been due to large variability between the embryos in each group, partly caused by varying levels of photo-bleaching.

To ensure that this decay is due to protein degradation and not caused by photo-bleaching, mRNA encoding only for PA GFP was injected in WT embryos. The activation of PA GFP on its own was more variable. In some cases, weak cytoplasmic expression could be detected (Fig 4.6,H), while in most cases PA GFP could not be activated (Fig 4.6,I). As a result, measuring any potential photo-bleaching to serve as control was not possible. Furthermore, exposure of embryos to UV light was associated with embryo death, the onset of which also affected PA GFP intensity measurements. The combination of these issues with the variability between embryos made this approach unreliable for making precise conclusions about the changes in Her6 half-life after the addition of a PEST domain.

4.2.4 Measuring HV and HVP protein half-lives by their over-expression in zebrafish embryos, CHX chase and Western Blot

Using the FDAP approach, a great deal of variability was observed between embryos that exogenously expressed either HP or HPP. Furthermore, due to issues with the negative control, I was unable to eliminate the potential effect of photo-bleaching. To circumvent

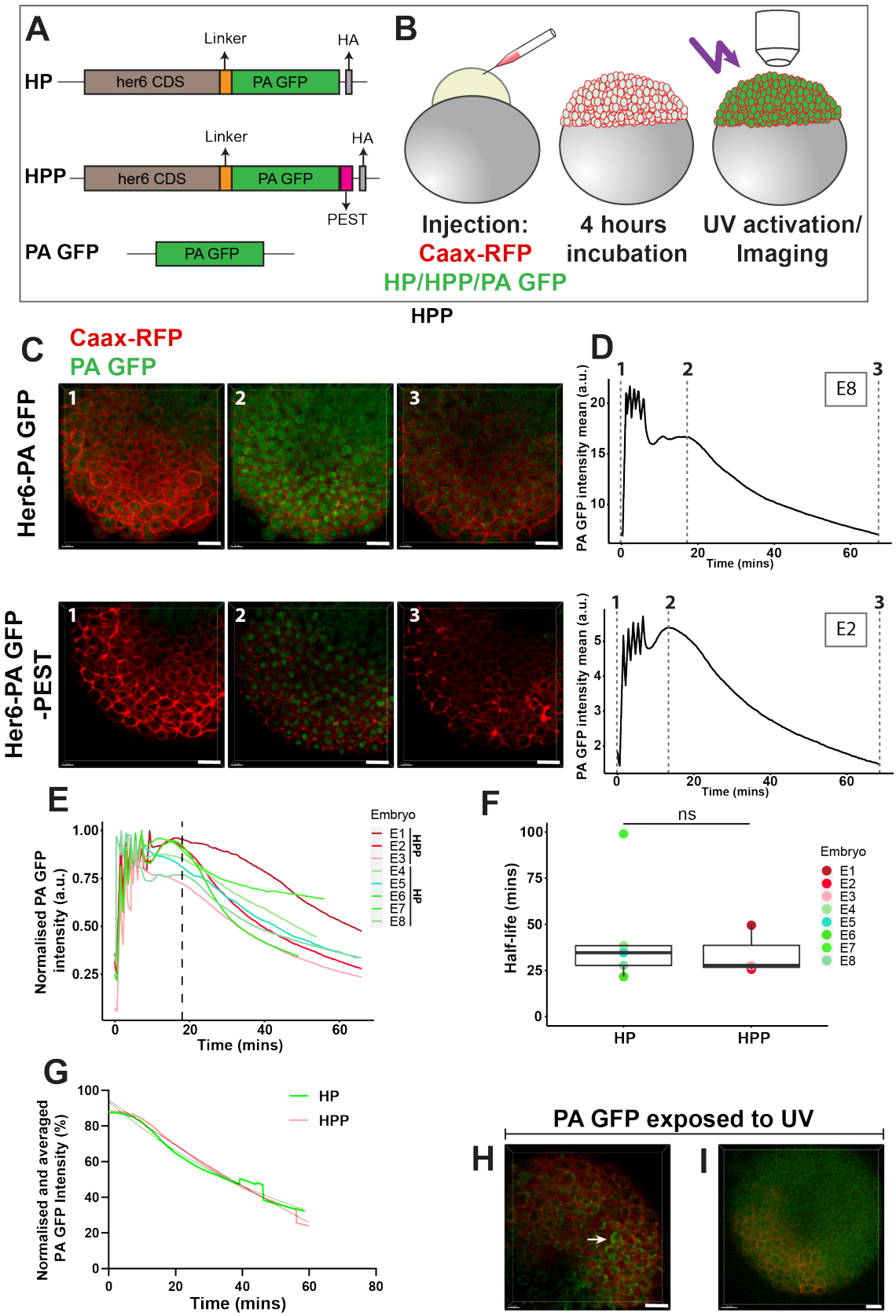

Figure 4.6: **Measuring the change in Her6 protein half-life by adding a PEST domain using PA GFP fusion proteins. Caption on following page →**

Figure 4.6: **(A)** Schematic diagram of the *her6-pagfp-HA*, *her6-pagfp-pest-HA* and *pa gfp* constructs. All were cloned in a PCS2+ vector. **(B)** Schematic diagram showing the experimental pipeline for measuring protein half-life using PA GFP fusion proteins. Embryos were injected with Caax-RFP which labels cell membranes and one of the PA GFP constructs at one cell stage. They were then incubated for 4 hours, allowing for sufficient mRNA translation. In 4-5hpf embryos, PAGFP was activated using UV light and imaged over time. **(C)** 3D reconstructed images from Z-stacks. Example of embryos injected with HP or HPP before UV activation (1), after UV activation (2) and after signal decay (3). **(D)** Raw PA GFP fluorescence intensity from all cells of corresponding embryos presented in C. These embryos are E8 and E2 in E and F. The intensity spikes between 1 and 2 were the UV pulses used for activation. Half-life was calculated roughly between 2 and 3. **(E)** Normalised PA GFP fluorescence intensity where each trace was normalised to the maximum value in that trace. **(F)** Half-life measurements from individual embryos. Median half-life in HP was 34 mins and median half-life in HPP was 27 mins. There was no significant difference between HP and HPP (Mann-Whitney, ns). **(G)** The PA GFP traces from all embryos in HP or HPP were combine together by averaging. They were fit with "plateau followed by one phase decay" non-linear regression models that were significantly different between HP and HPP (Extra sum-of-squares F test, ****). Based on these curves, the estimated half-lives for HP and HPP were 24.9 and 57.8 minutes, respectively. **(H&I)** 3D reconstructed images from Z-stacks of example embryos injected with control PA GFP mRNA and exposed to UV pulses. Faint activation of cytoplasmic PA GFP was detected in G (arrow) while there was no activation in H. Scale bars = 40μm. (ns): $P > 0.05$, (*): $P \leq 0.05$, (**): $P \leq 0.01$, (***): $P \leq 0.001$, (****): $P \leq 0.0001$

these issues, I turned to an alternative approach using exogenous HV or HVP expression, CHX treatment of pools of embryos and measuring protein decay with Western blot. To this end, the half-life measurement protocol from Soto et al. (2020) was adapted for this purpose by ***Dr Ximena Soto***. Injections, CHX treatment and protein extraction were done in collaboration with ***Dr Ximena Soto*** and Western blots and analysis were done by myself.

HV-HA and HVP-HA plasmids were generated by replacing PA GFP with Venus in HP-HA and HPP-HA constructs. HV-HA and HVP-HA mRNAs were synthesised *in vitro* and injected into 1 cell stage WT embryos with Venus-Myc tag (V-mt) mRNA which served as an injection control. Embryos were incubated for 2.5-3h to allow mRNA expression. Then, embryos were treated with CHX for 0-30 minutes and samples were collected in 5 min intervals (20 embryos per time point). Total protein extracts from these embryos were evaluated by Western Blot using anti GFP and anti α-Tub antibodies (Fig 4.7,A).

HV band was approximately 63 Kilo Daltons (kDa) as predicted. α-Tub was used as the loading control and the band was at the expected 50kDa. Based on the plasmid sequence, the V-mt protein was expected to be ∼33 kDa but appeared at ∼42kDa on the blots. However, this band was not due to nonspecific antibody binding as it did nor appear in the Uninjected (UI) control (Fig 4.7, B&C). Furthermore, V-mt was not affected by CHX in this timescale, suggesting that it did serve as a suitable control for injection variability (Appendix 8.3). Degradation of HV and HVP was quantified from Western Blots after normalisation to V-mt and α-Tub.

All values in each experiments were normalised to the maximum which was set as 100%. HV and HVP decay was observed in all experiments but the decay trends were variable across experiments (Fig 4.7, D&E). Interestingly, in HVP experiments 4, 5 and 6, a sharp decrease was detected between 10-15 minutes. This suggested that HVP decay could have occurred in the short 5-minute interval between these two time-points (Fig 4.7, E). For

each experiment, the best model fit was selected between simple “One-phase decay” and “Plateau followed by one phase decay”. The estimated half-life value from the best suited model for each experiment were plotted. The variability in the decay trends resulted in inconsistent half-life measurements for both HV and HVP which were not significantly different (Mann-Whitney test, P=0.4000, Fig 4.7,F). I also combined traces from different HV and HVP experiments by averaging and fitted with non-linear regression curves. HV decay was fit by a “One phase decay” model whereas HVP was best fit with “Plateau followed by one phase decay” model with estimated half-lives of 257 and 19.5 hours, respectively. Even though this was in line with the expected lower half-life in HVP, half-life measurements in the range of hours were much longer than expected for these proteins. I suspected that this was caused by inconsistent and variable decay trends between separate experiments.

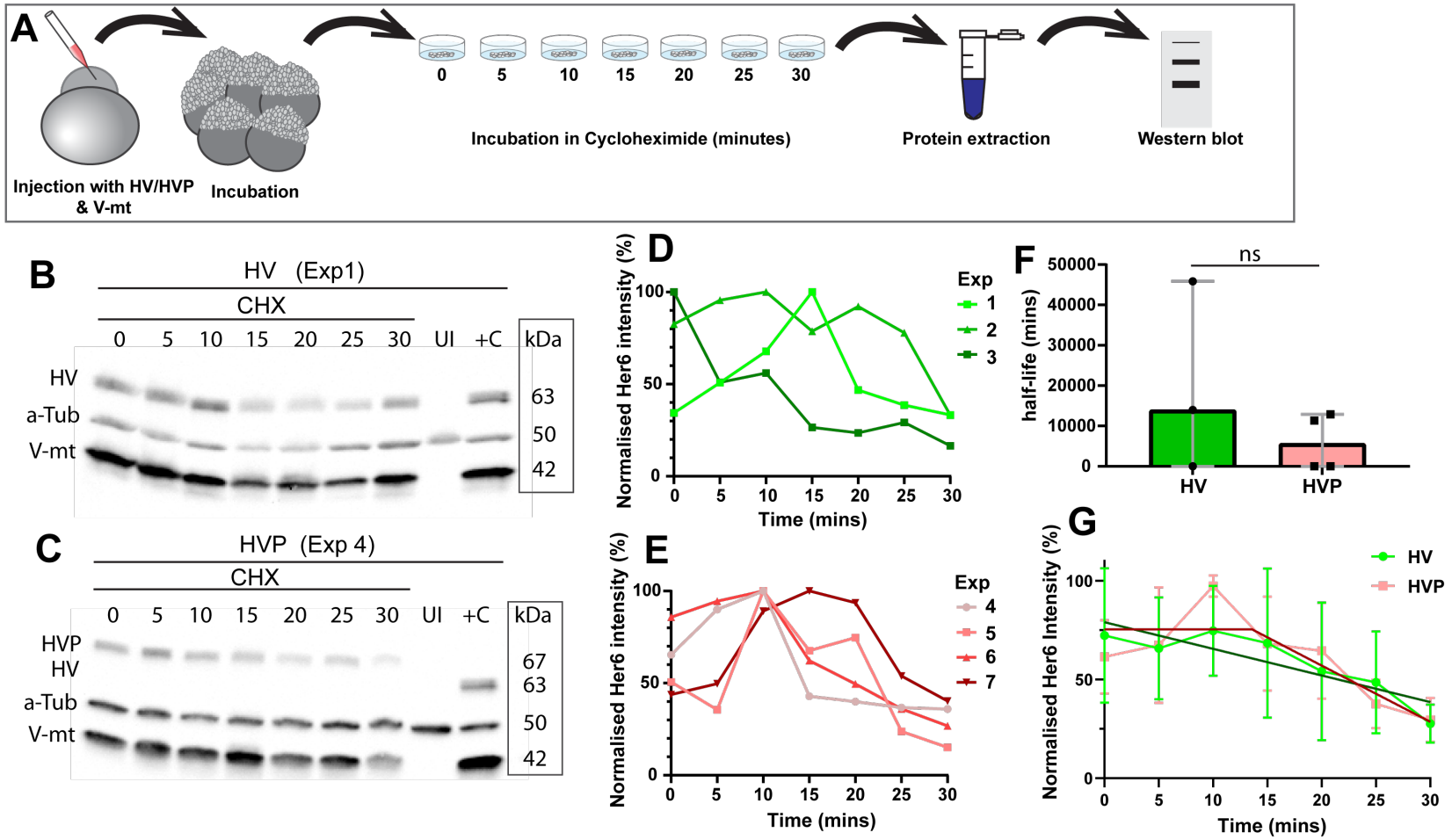

Figure 4.7: **Measuring HV and HVP protein half-lives by their over-expression in zebrafish embryos, CHX chase and Western Blot. Caption on the following page →**

Figure 4.7: **(A)** Schematic diagram of the experimental pipeline. WT embryos were injected with either HV or HVP mRNA. V-mt mRNA was included in both conditions as injection control. Injected embryos were incubated for 2.5-3 hours and pooled in groups of 20 that were treated with CHX for 0-30 minutes with 5 min intervals. Total protein was extracted from embryos in each time point and assessed by Western Blot. **(B&C)** Example Western blots from embryos injected with V-mt and HV or HVP mRNA. HV band was ∼63kDa while HVP band was slightly larger at ∼67kDa. α-Tub was 50kDa. The V-mt protein was expected to be ∼33 kDa but appeared at ∼42. HV, HVP and V-mt were absent in the UI. **(D&E)** Intensity of HV and HVP bands from Western Blots normalised to the maximum in each time-course set as 100%. HV decay trends were variable. The HVP decay trend was more reproducible and three out of four experiments shows rapid decline between 10 and 15 minutes. **(F)** The estimated half-life values from the best suited non-linear decay model fit to each experiment ("One phase decay" or "Plateau followed by one phase decay"). There was no significant difference between HV and HVP half-lives (Mann-Whitney test, ns). **(G)** Normalised Her6 intensity values were averaged between experiments and fit with non-linear regression models, comparing "One phase decay" model with "Plateau followed by one phase decay". HV was best fit with "One phase decay" while "Plateau followed by one phase decay" was best suited for HVP. These model curves are shown as solid darker lines. The estimated half-lives based on these models were 15407 minutes (257 hours) for HV and 1174 minutes (19.5 hours) for HVP. UI = Uninjected

4.2.5 Estimating HV and HVP protein half-lives by over-expression in MCF7 cells, CHX chase and live imaging

Following CHX chase in embryos, I speculated that HV and HVP half-lives and their difference may be too small relative to the temporal resolution and sensitivity of Western blotting. It was hypothesised that under the regulation of the mammalian proteosome, both HV and HVP could have longer half-lives which could amplify their difference to an extent that facilitates measurement. The generation of this hypothesis and the design of the following experiment was done collaboration with ***Dr Elli Marinopoulou***. Cell culture, imaging and cell tracking was performed by ***Dr Elli Marinopoulou***. Data processing and analysis were performed predominately by myself with assistance from ***Dr Elli Marinopoulou*** and ***Dr Anzy Miller***.

CHX chase experiments were conducted in MCF7 cells (human breast cancer cell line (Horwitz et al., 1975)) that were transiently co-transfected with PCS2-HV-HA or PCS2-HVP-HA plasmids with empty PCS2 vector plasmid. Two days post transfection, they were treated with either CHX or DMSO and Venus fluorescence was imaged for 22 hours (Fig 4.8, A). Due to the uncertainty of CHX effectiveness over a long time range, only the first 10 hours of the data were used for analysis.

The predicted effect was to monitor protein levels over time in DMSO treated cells and protein decay in CHX treated cells. Venus intensity in CHX and DMSO treated cells decreased over time in both HV and HVP, but perhaps more drastically in CHX treated cells (Fig 4.8,B). To understand the response at a population level, for each treatment group, single cell traces from four biological repeats were combined and the average trace was plotted with Standard deviation (SD) (Fig 4.8, C-F). For both CHX and DMSO traces, the fit of simple "One-phase decay" and "Plateau followed by one-phase decay" models were statistically compared. For CHX, the simple "One-phase decay" model was most suited while DMSO traces were best fit with the "Plateau followed by one phase decay" model,

which highlighted different modes of signal reduction between CHX and DMSO. After model selection, extra sum-of-squares F test was used to determine if in each condition, HV and HVP could be fit by the same curve. In the CHX treatment group, the curves fit to HV and HVP were significantly different with faster decay in HVP (Fig 4.8,C, HV half-life = 2.3 hours, HVP half-life = 2 hours, Extra sum-of-squares F test, P<0.0001). However, unexpectedly, the fluorescence decline that was observed in the DMSO treated traces from HV and HVP were also fit with significantly different curves despite the fact that the means and SDs were largely overlapping during the decline phase (Fig 4.8,D, Extra sum-of-squares F test, P<0.0001).

The underlying cause for the decline of Venus levels in DMSO treated cells was unclear. In an attempt to alleviate the influence of these unknown factor/s, a factor 2 polynomial curve was fit to the DMSO trends. All data were de-trended by removing this polynomial trend seen in DMSO. The resulting de-trended CHX traces were still significantly different between HV and HVP (Extra sum-of-squares F test, P<0.0001), while after de-trending, there was no significant difference between HV and HVP in the DMSO treatment group (Extra sum-of-squares F test, P=0.7876). This supported the prediction that Her6 is destabilised by the addition of the PEST domain.

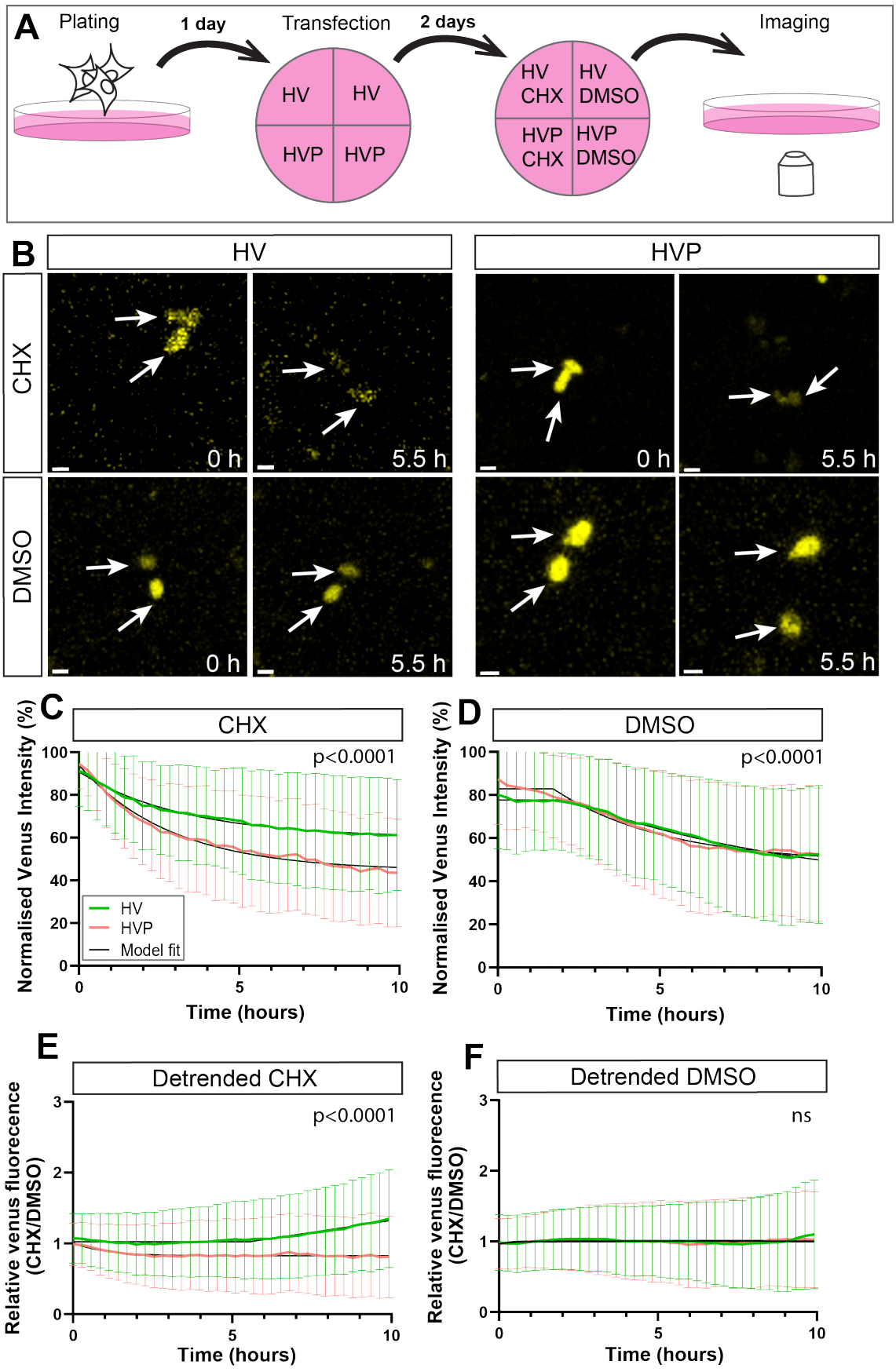

Figure 4.8: **Estimating HV and HVP protein half-lives by over-expression in MCF7 cells, CHX chase and live imaging. Caption on the following page →**

Figure 4.8: **(A)** The experimental pipeline for CHX chase in MCF7 cells. MCF7 cells were plated and incubated for one day. They were then transfected with empty PCS2 vector with either HV or HVP plasmids. Two days after transfection, they were treated with CHX or DMSO and imaged. **(B)** Maximum intensity projection images of example cells transfected with HV or HVP and treated with either CHX or DMSO at time 0 and 5.5h after treatment. Scalebars = 10µm. **(C)** Mean and SD of Venus intensity from all single cells treated with CHX. Both HV and HVP were fitted with a statistically preferred "One-phase decay" model and HVP intensities declined more rapidly (Extra sum-of-squares F test, ****). **(D)** Mean and SD of Venus intensity from all single cells treated with DMSO. Both HV and HVP were fitted with a statistically preferred "Plateau followed by one-phase decay" model. The decay trend of HV and HVP were similar but were statistically represented by two significantly different curves (Extra sum-of-squares F test, ****).**(E)** Mean and SD of CHX traces de-trended using a factor 2 polynomial trend fit on the mean DMSO traces. **(F)** Mean and SD of DMSO treatment group de-trended using a factor 2 polynomial trend fitted on itself. Here, HV and HVP were not significantly different (ns). (ns): $P > 0.05$, (*): $P \leq 0.05$, (**): $P \leq 0.01$, (***): $P \leq 0.001$, (****): $P \leq 0.0001$

4.3 Discussion

The availability of the HVP line presented a unique opportunity for studying altered Her6 dynamics through direct manipulation of protein stability. However, this KI line had not been fully characterised. For a better understanding of the HVP locus, I analysed the CRISPR junctions using PCR. Given that HVP was generated using the same CRISPR design as the HV line (Chapter 3), it was not surprising to find donor backbone integration in HVP as well. As discussed for the HV line in Chapter 3, this aberration can at least in part, be attributed to Non-homologous end joining (NHEJ) which is the predominant repair mechanism for double-strand DNA breaks in young zebrafish embryos (Hagmann et al., 1998; Liu et al., 2012). That is to say, it is likely that following a double strand break in the endogenous locus but prior to the complete release of the KI cassette from the donor, the linearised plasmid was incorporated in the endogenous locus through NHEJ, instead of Homology directed repair (HDR).

However, there were some differences between the HV and HVP loci. In HV, only the LHA-RHA sequence had been duplicated following donor backbone insertion, forming a region resembling the WT Her6 sequence. However, I suspect that two KI events have taken place in HVP. In theory, during the CRISPR reaction, HVP locus could have assumed an intermediate structure identical to the HV with duplication of LHA-RHA. But this aberrant duplication also reconstructed the sgRNA binding site, allowing a second cleavage and KI event at the duplicated site. This explained correct genotyping of the HVP embryos by using primers 1-2, which was not possible in HV. Therefore, I conclude that the combined effect of failed KI cassette release, multiple cleavages and NHEJ have contributed to this outcome.

Despite the presence of a duplicated KI cassette, I have shown that there is little concern around aberrant protein production. This is because all ORFs in the aberrant sequences culminated in a stop codon and were therefore not likely to generate aberrant fusion proteins with the duplicated Her6 and Venus sequences. Given the differences between HV and HVP loci, ectopic expression would have presented differently at the mRNA level in

both lines. In HV, *her6* was duplicated without *venus* and therefore only ectopic *her6* expression would have been expected. On the other hand, in HVP, both *her6* and *venus* would have been expected to be expressed ectopically as they were both duplicated. However, in this chapter, I have shown that neither *her6* nor *venus* appear to be ectopically expressed in HV or HVP. Additionally, Venus fluorescence was detected in the same regions as WT (i.e. telencephalon and diencephalon) in the developing zebrafish forebrain of both HV and HVP embryos. These observations implied that much like HV, the HVP locus is unlikely to have lost its functionality due to the CRISPR process (Soto et al., 2020).

However, it was observed that the expression domain of *venus*-containing mRNAs was slightly thinner than *her6* mRNA in both HV and HVP. In certain conditions, for example, in the presence of multiple mature mRNA species in the homozygous (described in Chapter 3-Discussion), this observation may be explained by changes in mRNA stability in presence of Venus. That is to say, if the hypothetical alternatively spliced mRNA species that lack Venus have a longer half-life, then these mRNAs would linger longer in the posterior regions where WT *her6* transcription does not linger as long as the anterior parts (Fig 3.1). This would result in a thicker *her6* expression domain in comparison to *venus*. However, it is unlikely that this is due to the presence of the PEST domain as it affects both HV and HVP. It is perhaps more likely that this effect is an artefact resulting from poor quality of the *venus* probes that do not capture lower expression posteriorly, resulting in a seemingly thinner expression domain.

As discussed in Chapter 3 for the HV KI line, despite extensive genomic characterisation of the HVP locus, I have not examined the mRNAs expressed from this region. Reverse transcription PCR (RT-PCR) can be used to check for the presence of alternatively spliced mRNA species which would further clarify these observations. Additionally, using more quantitative and high resolution techniques such as Single molecule fluorescent in situ hybridisation (smFISH) using probes against *venus* and *her6* can provide a better view of the expression of these mRNAs at a single cell level.

In theory, HVP was expected to have a shorter half-life than HV. However, this had not been measured. First, I used an FDAP-inspired approach by generating the HP and HPP fusions (Zhang et al., 2007; Müller et al., 2012; Rogers et al., 2015). Given the limited use of PA GFP fused proteins in zebrafish, there was little knowledge on PA GFP activation in this model. For instance, PA GFP is activated by exposure to 400-nm light (Patterson, Lippincott-Schwartz, 2002) and cell culture-based literature have reported successful activation of PA GFP using 405-nm lasers (Wang et al., 2014; Durisic et al., 2014). I was also able to successfully activate PA GFP in HEK cells transfected with HP or HPP by 1-2 seconds of 405-nm exposure (data not shown). However, in 4-5hpf zebrafish embryos, HP and HPP were not activated by exposure to 405-nm light and could only be activated with a total of approximately 90s of exposure to 85-100% UV, resulting in embryo death during or following imaging. Others have also pointed to photo-toxicity as one of the main short-

comings of using UV activated fluorescent proteins (Gurskaya et al., 2006; Zhang et al., 2007).

Furthermore, based on my experience, signal to noise (i.e. pre-activation fluorescence) ratio in embryos was lower than the previously reported ∼100-fold (Patterson, Lippincott-Schwartz, 2002). This low signal to noise ratio could have contributed to the over-estimation of HP and HPP half-lives as noise/background fluorescence potentially obscured the later parts of the decay curve for accurate measurement. An additional downside to my FDAP approach was the absence of a reliable negative control to eliminate the potential effects of photo-bleaching. This was most likely the result of a mistake in cloning the PA GFP construct where PA GFP was inserted in the vector without a stop codon, leading to an addition of 16 amino acids at the C-terminus of the protein. Therefore, while this method has advantages such as allowing direct half-life measurements of the protein of interest with single cell resolution, it requires further optimisation for reliable and accurate results.

The alternative approach of CHX chase in embryos had several important advantages relative to FDAP. These CHX chase experiments could be done using Venus, they eliminated the issue of photo-bleaching and more importantly, they were expected to be more reproducible due to the pooling of embryos in each time point. However, this technique also led to inconsistent results. I suspect that many factors contributed to this inconsistency. One was the temporal resolution in the experimental design. Ay et al. (2013) used CHX chase to measure the half-life of Her7, a closely related protein to Her6. They monitored Her7 degradation following CHX treatment of transgenic zebrafish with heat-shock inducible HA-Her7. They showed that this protein was extremely short-lived with a half-life of 3.5 minutes. The duration of their CHX chase experiments was 15 minutes, sampling at 2.5 minute intervals. It is likely that HV and HVP half-lives are similarly short, suggesting that the 5 minute sampling did not have suitable temporal resolution. This is supported by the rapid HVP degradation that was observed between the 10 and 15 minute time points. Another consideration is that the practical aspects of these experiments, such as the requirement for injecting a large number embryos and using early stage embryos, made them laborious. This hindered examining HV and HVP in parallel with the same embryo batches and the addition of further controls such as CHX-negative to the experimental design. These practical elements may have also contributed to the results being non-reproducible.

As it was speculated, in MCF7 cells, HV and HVP did degrade slower than in zebrafish, with half-lives measured at 2.3 and 2 hours, respectively. Even though this was a disadvantage for making exact half-life measurements, it allowed HV and HVP half-lives to be estimated. Assuming a linear scaling of protein half-lives between zebrafish and human cells, if HV half-life was ∼11 mins (Soto et al., 2020), HVP half-life could be estimated at ∼8.7 mins. The results from the CHX chase in MCF7 cells were somewhat overshadowed by the unexpected reduction in Venus intensity in the DMSO control group. I speculated

that it was caused by either a decline in overall protein levels between 48 to 96 hours after transient transfection or photo-bleaching. Nonetheless, all conditions were expected to be affected equally. This effect was alleviated by de-trending all data to the DMSO control, still leaving HV and HVP decay trends significantly different. Thus, using MCF7 cells did confirm that HVP has a shorter half-life than HV. Furthermore, it indirectly showed that the difference between HV and HVP half-lives is likely to be small. In the future, additional controls such as Venus-only transfected cells that are treated with CHX could alleviate the concern of differences between HV and HVP in the DMSO treatment, further improving the design.

An alternative method for measuring half-life would be to combine different methods presented in this chapter. That is to say, using young zebrafish embryos (4-5hpf) that have been injected with very specific volumes of HV or HVP mRNA followed by CHX treatment and imaging instead of WB. In this case, novel mRNA tagging methods such as fluorescent bioorthogonal Poly-A tail tags can be used to also allow mRNA visualisation (Westerich et al., 2020). These tags have been shown to not interfere with translation (Westerich et al., 2020). The main advantage of this setup is enabling mRNA half-life measurement. Since there is no endogenous expression of *her6* mRNA between 4-5hpf (Thisse et al., 2001), the pool of injected mRNA would be finite and its depletion could be associated with mRNA half-life. This would enable the calculation of mRNA half-life along with the protein (labeled by Venus) which can verify that the PEST sequence only affects protein stability and not that of the mRNA.

However, one shared shortcoming of all the half-life measurement methods tested here was the reliance on ubiquitous over expression of the protein. It has been observed that cellular context can affect the turnover rate of the same protein (Dörrbaum et al., 2018). Thus, it is ideal to measure HV and HVP degradation rates in the relevant context of the zebrafish telencephalon. Initially, I considered direct CHX treatment of HV and HVP KI embryos and measuring the decay of the endogenous Venus fluorescence. However, due to concerns around sufficient CHX penetration into the brain tissue, this was not carried out. However, others have reported successful CHX chase in 15-24hpf whole embryos (Ay et al., 2013; Jeffery et al., 2015), showing that CHX can enter tissues and inhibit translation. In conclusion, even though the MCF7 cell experiments have shown that HVP is more rapidly degraded than HV, CHX chase focused on the telencephalon of KI embryos at the desired stages may allow for more precise measurements.

4.4 Concluding remarks

In this chapter, I have introduced a previously uncharacterised KI line where Her6-Venus is fused to a destabilising PEST domain. I show that similar to the HV, the donor backbone has incorporated in the HVP genome during the CRISPR process. In addition, two KI

events have taken place in this line, meaning that an additional KI cassette is also present. However, using ORF search, FISH analysis and live imaging, I have shown that the duplicated region is not likely to be expressed or affect Her6 expression. To show that HVP does in fact represent a destabilised form of Her6, I have used FDAP, CHX chase in zebrafish embryos and CHX chase in MCF7 cells. FDAP and CHX chase in embryos presented many challenges that hindered reliable half-life measurements. However, CHX chase in MCF7 cells transfected with HV and HVP, showed that HVP is indeed degraded faster than HV, supporting the initial hypothesis about Her6 destabilisation in the presence of a PEST domain. The effects of this destabilisation on Her6 expression dynamics will be described in the following chapter.

Chapter 5

Examining the single cell and tissue-level outcome of altering Her6 expression dynamics by its destabilisation

5.1 Background

Many previous studies of Central nervous system (CNS) ultradian oscillators have observed that the levels of the oscillatory proteins in tissues are heterogeneous, which is a characteristic feature of the cell populations (Shimojo et al., 2008; Imayoshi et al., 2013; Soto et al., 2020). However, the multi-cellular aspects of protein oscillations in neural tissues are largely understudied. This is because much of the previous work has been done *in vitro* (Shimojo et al., 2008; Imayoshi et al., 2013; Marinopoulou et al., 2021) which does not recapitulate all aspects of the tissue structure. In others where *ex vivo* slice cultures or intact embryos such as in zebrafish had been utilised, the focus had predominantly been on detailed characterisation of single cell dynamics (Shimojo et al., 2008; Soto et al., 2020).

The studies where protein stability of an oscillator has been altered are also not exempt from this shortcoming. Much of the insight of how oscillatory cells respond to changes in protein stability come from indirect manipulations of this feature *in vitro* where the impact has been measured in bulk cells. Chen et al. (2017) used Small interfering RNA (siRNA) to Knock-down (KD) RBX1, one of the components of the E3 Ubiquitin ligase complex that targets HES1 in mouse derived F9 fibroblast cells. As a result, HES1 half-life increased from 50 to 110 minutes. This increased the levels of HES1 and dampened its oscillations. In another study, HES1 was destabilised by siRNA KD of *Usp22*, the main Deubiquitinating enzyme (DUB) that targets ubiquitinated HES1 in C3H10T1/2 mouse fibroblast cells. This shortened the half-life of endogenous HES1 from 24.4 minutes to 19.3 or 15.9 minutes, depending on the efficiency of the siRNA used. Even though HES1 destabilisation did not affect its transcription and translation rates, it did reduce the protein levels and dampened its oscillations which was measured by Western Blot in synchronised serum stimulated cells (Kobayashi et al., 2015). In this case, single cell reporters were used to show that the period of *Hes1* oscillations had increased by 25 minutes and become more variable. The authors believed this to be the cause of the delayed and dampened *Hes1* and HES1 oscillations, respectively in bulk cultured and synchronised cells.

In contrast to the indirect and *in vitro* studies, Hirata et al. (2004) generated a stabilised HES7 by Lysine to Arginine (K>R) mutation of K14 which was thought to be a ubiquitination site. HES7 K14R had a $\sim$30 minute half-life which was 8 minutes longer than the Wild type (WT). HES7 K14R exhibited dampened oscillations in the Presomitic mesoderm (PSM) of mutant mice which affected the progression of late somitogenesis. However, Hirata et al. (2004) utilised the synchronous nature of HES7 oscillations to infer the oscillations by snapshot detection of the mRNA using in situ hybridisation with intronic probes. Hence, even though this was done in the *in vivo* context with direct manipulation of the protein, there was a lack of single cell information. Furthermore, even though the PSM and CNS oscillators share some characteristics like the presence of an auto-inhibitory feedback loop, they differ in one important feature which is the interaction between neighbouring cells. Notch mediated cell coupling enables synchronised or in-phase oscillations

in cells that are spatially close to each other in the PSM (Özbudak, Lewis, 2008). This is in contrast to the CNS where neighbouring cells often show out of phase or anti-phase oscillations (Kageyama et al., 2018). Therefore, not all insights from oscillating populations in PSM are relevant in the CNS.

One recent report has provided a novel insight into the relationship between single cell HES dynamics and the multi-cellular behaviour and patterning. Biga et al. (2021) have described the presence of dynamic HES5 microclusters using single cell resolution live imaging of endogenously labeled HES5 in mouse spinal cord slice cultures. To determine how the population can give rise to these small HES5 clusters where cells are similar in protein levels and dynamics, they developed a multi-cellular computational model that incorporates single cell oscillations with cell-cell coupling. They particularly focused on exploring coupling strength which is defined as the HES5 levels required in one cell to reduce HES5 expression in its neighbouring cells by half. Using this model, they showed that changing the coupling strength altered the global pattern of HES5 in the simulated tissue. The model also predicted that increase in cell coupling which gives rise to an alternating high-low pattern of HES5 expression in neighbouring cells may be associated with increased probability of differentiation. In support of this, they showed that the motorneuron domain which has high differentiation rates at embryonic day 10.5 has an alternating high-low HES5 pattern between neighbouring cells, inferring that cells in this region are more strongly coupled.

The work by Biga et al. (2021) is a novel and detailed description of the relationship between a neural oscillator and patterning in a tissue context. It highlighted that combining single cell and cell population information can provide valuable insight into the interactions between the cells which affect developmental output, revealing the nuances of dynamic behaviour in tissues. However, the focus of this work was mainly on intercellular interactions and Notch alterations. Hence, the system response to altering an intracellular feature of the oscillatory gene regulatory network remains to be elucidated.

In chapter 3, the expression dynamics of Her6 were characterised in the zebrafish telencephalon using the Her6-Venus (HV) Knock-in (KI) and in chapter 4, I introduced the Her6-Venus-PEST (HVP) where Her6 is destabilised. In this chapter, I have conducted a comparative study between HV and HVP to understand how the single cells and cell population in the telencephalon respond to Her6 destabilisation and what that response may reveal about cell-cell interactions.

The following aims will be addressed in this chapter:

1- Determine the impact if Her6 destabilisation at the single cell level;

2- Describe the effects of Her6 destabilisation at the population level;

3- Characterise the potential implications of these single cell and cell-population changes

on patterning;

4- Use mathematical modelling to understand the tissue response.

5.2 Results

5.2.1 Investigating the effects of Her6 destabilisation on single cell expression dynamics in HVP

In the previous chapter, I showed that HVP represents a destabilised version of HV. Given the importance of targeted protein degradation in generating ultradian oscillations and cell state transitions, I hypothesised that Her6 destabilisation would alter its expression dynamics in single cells. This hypothesis was addressed by real-time single cell resolution imaging. Homozygous (Hom) HV and HVP embryos were injected with Caax-RFP and Histone 2B-Keima (Keima) for detection of cell membranes and nuclei, respectively, and imaged from 20 Hours post fertilisation (hpf) at a transversal view of the Her6 expression domain in the telencephalon for 6-10 hours. The transversal orientation maximised quality of imaging by limiting the depth of tissue and captured the majority of Her6 expressing cells in both telencephalic lobes. 20hpf embryos and the plane of imaging is schematically shown in Fig 5.1,A. Stage-matched 19-20hpf pairs of HV and HVP embryos were imaged simultaneously to ensure Venus fluorescence intensity is comparable. Fig 5.1,B shows an example 3D reconstruction of Z-stacks from of the first live imaging frame (Images of a single Z-plane are presented in Appendix 8.7).

Single cells were tracked over time and the fluorescence intensity of both Venus (readout of Her6) and Keima (readout of H2B) were plotted. Examples of single cell traces are shown in figure Fig 5.2,A. For better understanding of single cell behaviour, the characteristics of these traces were further analysed starting with mean intensity. The mean intensity of Keima in single cells was variable between embryos and experiments as a result of variability in injections. In experiment 1, the single cell mean intensities of Venus were similar in HV and HVP. However, in experiments 2 and 3, Venus mean intensities in single cells from HVP were lower than in HV (Fig 5.2,B). For statistical analysis, the average of mean intensities of all cells in each embryo was calculated. There was no overall difference in average Keima mean intensities between HV and HVP (Mann-Whitney test, $P>0.9999$). Average Venus mean intensities in HVP single cells had a tendency to be lower than HV, which however, was not statistically significant (Mann-Whitney test, $P=0.7000$) (Fig 5.2,C). The raw fluorescence intensities of different fluorophores are not directly comparable. Furthermore, in these embryos, Venus is expressed endogenously whereas Keima is injected. Hence, the sources of variability in their intensities are different. Therefore, no comparisons are reported between mean Venus and Keima intensities.

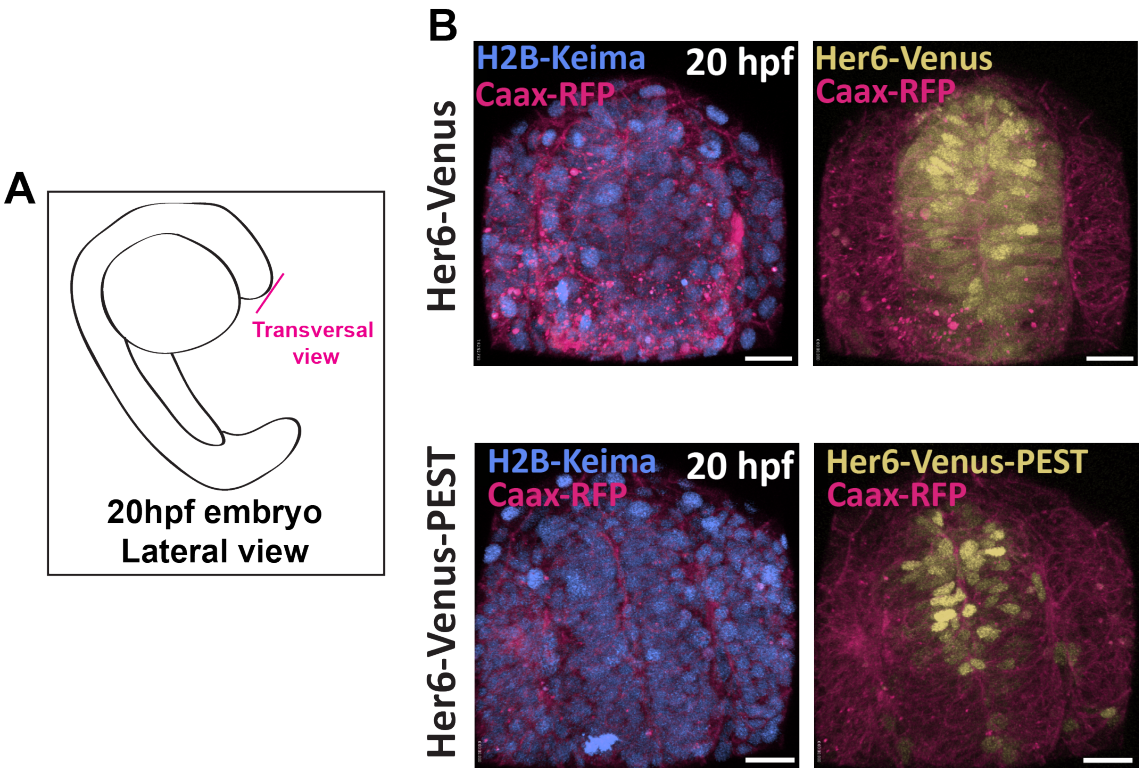

Figure 5.1: **Example of the starting point of HV and HVP paired live imaging with a traneversal view of the Her6 expression domain in the telencephalon**. **(A)** Schematic diagram of the lateral view of a 20hpf embryo. The pink line denotes the transversal plane for live imaging. **(B)** 3D reconstruction of Z-stacks from a pair of 20hpf HV (top) and HVP (bottom) embryos. They were injected with H2B-Keima to label the cell nuclei and Caax-RFF for labeling cell membranes.

Venus expression visibly fluctuated more than Keima expression over time, implying that Venus was more dynamic in HV and HVP. Additionally, Venus fluctuations appeared larger in HVP than in HV (Fig 5.2,A). To quantify these observations, Coefficient of Variation (CV) was calculated in each cell, measuring the variations around the intensity mean of that cell over time. In all three experiments, Venus CV in single cells was higher than Keima, demonstrating that Venus was more dynamic. Additionally, Venus CV in HVP was higher than HV in all embryo pairs analysed (Fig 5.2,D). The average of single cell CVs for each embryo was used for statistical analysis using 2way ANOVA with multiple comparisons (Fig 5.2,E). Venus variation around the mean was significantly higher than Keima in HV traces (P=0.0223) and more so in HVP traces (P=0.0003). Additionally, even though there was no significant difference in Keima variations between HV and HVP (P>0.9999), variations of Venus in single cells were significantly higher in HVP than in HV (P=0.0221). These observations suggested that the fluctuations in Venus expression is a result of Her6 expression dynamics which are absent in Keima expression. They also supported the hypothesis that Her6 dynamics have been altered in HVP.

Next, I assessed the oscillatory dynamics and long-term trends in single cells as two potential sources of Venus fluctuations that could have been altered in HVP. Venus (i.e. Her6) oscillations were examined by comparing the proportion of oscillators, fold-change and periodicity between HV and HVP. For this, Venus and Keima traces from HV and HVP were

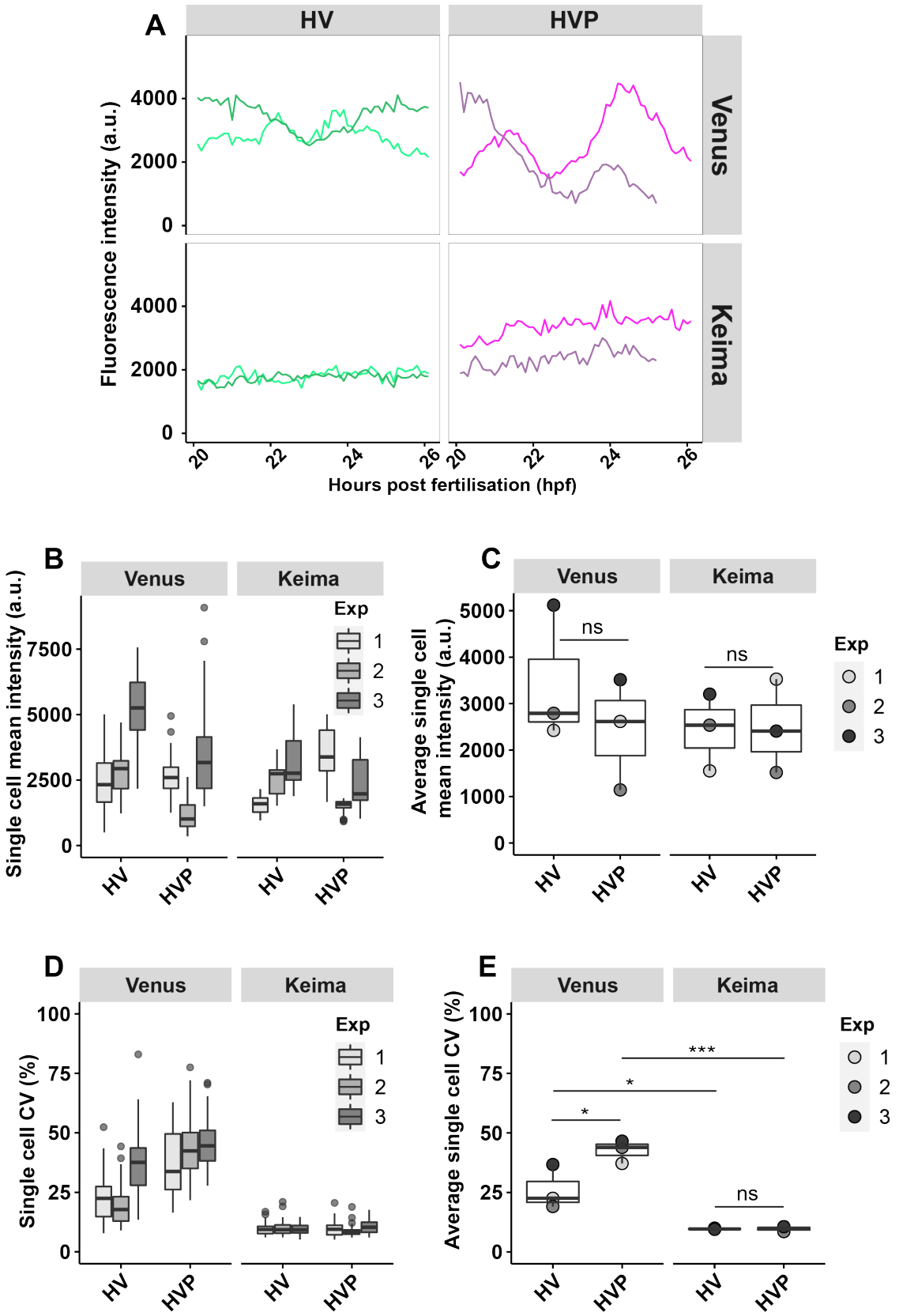

Figure 5.2: **Comparing mean intensity and temporal variations in single HV and HVP cells over time.(A)** Example Venus and Keima single cell traces from HV and HVP. **(B)** The mean intensity values for each cell were calculated. In experiment 1, mean intensities of Venus traces were not different in HV and HVP. In experiments 2 and 3, mean intensities Venus in HVP traces were lower than HV. Due to injection variability, Keima mean intensity values were variable. **Caption continued on the following page →**

Figure 5.2: **(C)** The average mean intensity of all single cells in each embryo was calculated and Mann-Whitney test was used for statistical analysis. HVP had a tendency for lower Venus intensities than HV but the difference was not significant (ns). There was no tendency and no difference between HV and HVP mean Keima intensities (ns). **(D)** Single cell CV was calculated as a measure of temporal variations around the mean intensity for Venus and Keima. In Venus traces, HVP CV was higher than HV CV in all experimental pairs. Keima CVs in both HV and HVP were low and comparable between HV and HVP. **(E)** All single cell CV values in each embryo were averaged and 2way ANOVA with multiple comparisons was used for statistical analysis. Venus CV for HV (19-37%) was higher than its corresponding Keima CV (9.7-10.1%) (*). The same was true for Venus HVP CVs (37-46%) relative to its Keima CVs (8.7-10.6%) with higher degree of significance (***). Average single cell CV was significantly higher in HVP than HV (*). There was no difference between Keima CVs in HV and HVP (ns). (ns): $P > 0.05$, (*): $P \leq 0.05$, (**): $P \leq 0.01$, (***): $P \leq 0.001$, (****): $P \leq 0.0001$

analysed using a computational method that separates periodic oscillators from aperiodic fluctuations (See "Single cell tracking and analysis" in Chapter 2, same method that was used in Chapter 3). Both Oscillatory (osc) and Non-oscillatory (non-osc) Venus expression were detected in HV and in HVP while Keima traces often did not pass as oscillatory (Fig 5.3,A). The percentage of oscillators was statistically assessed by 2way ANOVA. The proportion of Keima traces that passed as oscillators was not significantly different between HV and HVP (0-7.5% versus 0-7.5% , respectively, P>0.9999). But there were significantly more oscillating Venus traces in HVP than in HV (32.5-67.9% versus 5.2-32.5%, respectively, P=0.0397). In agreement with this, in HVP, a significantly larger proportion of Venus traces passed as oscillatory compared to Keima traces (P=0.0050). This is while in HV, there was a tendency for more oscillators in Venus traces than in Keima but this was not statistically significant (P=0.6570) (Fig 5.3,B). In Chapter 3, I showed that analysis parameters and track length can affect measuring the percentage of oscillators. However, the increased percentage of oscillators in HVP was seen with a range of analysis parameters and was not associated with differences in track length between HV and HVP (Appendix 8.4).

The peak to trough ratio (fold-change) of all oscillations in each single trace were measured and an average fold-change was calculated for each one. The mean of average fold-changes (referred to as fold-changes from hereon) in each embryo was used for statistical analysis using 2way ANOVA (Fig 5.3,C, single cell data is presented in Appendix 8.5,A). The smallest fold-change possible was 1 which meant that the peak and trough were equal and effectively no oscillations were identified. The fold-change of Keima traces that passed as oscillators was between 1-1.2 in HV and 1.1 in HVP. This implied that these Keima traces only have small amplitude fluctuations that erroneously pass as oscillators in this analysis pipeline. There was no difference in Keima fold-change between HV and HVP (P>0.9999). The fold-change of Venus traces in all experiments was significantly higher than Keima in HV (P=0.0408) and more so in HVP (P=0.0002). Furthermore, the fold-change of Venus oscillators in HVP which was between 1.8-2, was significantly larger than HV with a fold-change of 1.4 (P=0.0017).

The mean period (Fig 5.3,D) of HV Venus traces ranged between 1.7-2 hours while HVP Venus traces had mean periods of 2-2.1 hours (single cell data is presented in Appendix

8.5,B). Even though there was a small tendency for longer period of oscillations in HVP, this was not significantly different from HV (P=0.2821). There was no significant difference between the mean periods in Venus and Keima (HV-P= 0.9993 & HVP-P=0.0559). However, given the low percentage and fold-change of Keima oscillators, it is unlikely that the Keima period values point to actual periodic expression.

Next, I used a simple metric to examine the long-term dynamics of Venus expression in single cells. This was done by dividing the last intensity value of every single cell trace by its first intensity value, resulting in relative trend. This simple metric measured whether expression was upregulated (relative trend > 1), downregulated (relative trend < 1) or maintained around the mean over the time course (relative trend = 1). CV calculation for this metric showed that relative trends of Venus expression over time in HVP were significantly more variable than Keima (2way ANOVA, P=0.0001) and also compared to Venus relative trends in HV (2way ANOVA, P=0.0010). The relative trends of Venus in HV were slightly but insignificantly higher than Keima (2way ANOVA, P=0.1543). This is while there was no difference between Keima relative trends in HV and HVP (P>0.9999) (Fig 5.4,A).

The distribution of relative trends was examined by pooling all three experiments (the contribution of each experiment to these histograms is presented in Appendix 8.6). Relative trends of Keima expression were normally distributed around 1 in HV and HVP showing that this protein did not have a strong tendency for up or down regulation over time and was more likely to be maintained around the mean (i.e. stable) (Fig 5.4,B&C). The relative trend for Venus expression in HV was shifted to the left, showing that most cells have a declining trend with the peak of distribution at 0.4 (Fig 5.4,B). 13.6% of cells showed maintained or upregulated trend (signified by relative trends of 1 or higher) and only 17% of these cells were oscillators (Fig 5.4,B). This is while the relative trend of Venus expression in HVP was shifted more towards the left with the peak relative trend at 0.2, implying slightly more rapid decline in Venus (i.e. Her6) expression in HVP cells compared to HV (Fig 5.4,C). In HVP, around 10% of cells had relative trend of 1 or higher and $\sim$64% of them were oscillators (Fig 5.4,C). In short, relative to HV, HVP cells exhibited more variable long term Her6 expression trends, slight tendency for more drastic Her6 down regulation and increased contribution of Her6 oscillators to stable or up regulating cells.

5.2.2 Comparing Her6 expression domain in HV and HVP reveals global differences at the cell population level

Next, I set out to reveal the characteristics in the Her6 expression domain and the implications of altering single cell dynamics on the cell population. I first compared live Hom HV and HVP embryos at 18-19 hpf (Fig 5.5, A). Relative to HV, the Her6 expression domain in HVP appeared reduced ventrally with lower Venus fluorescence intensity (Fig 5.5,B).

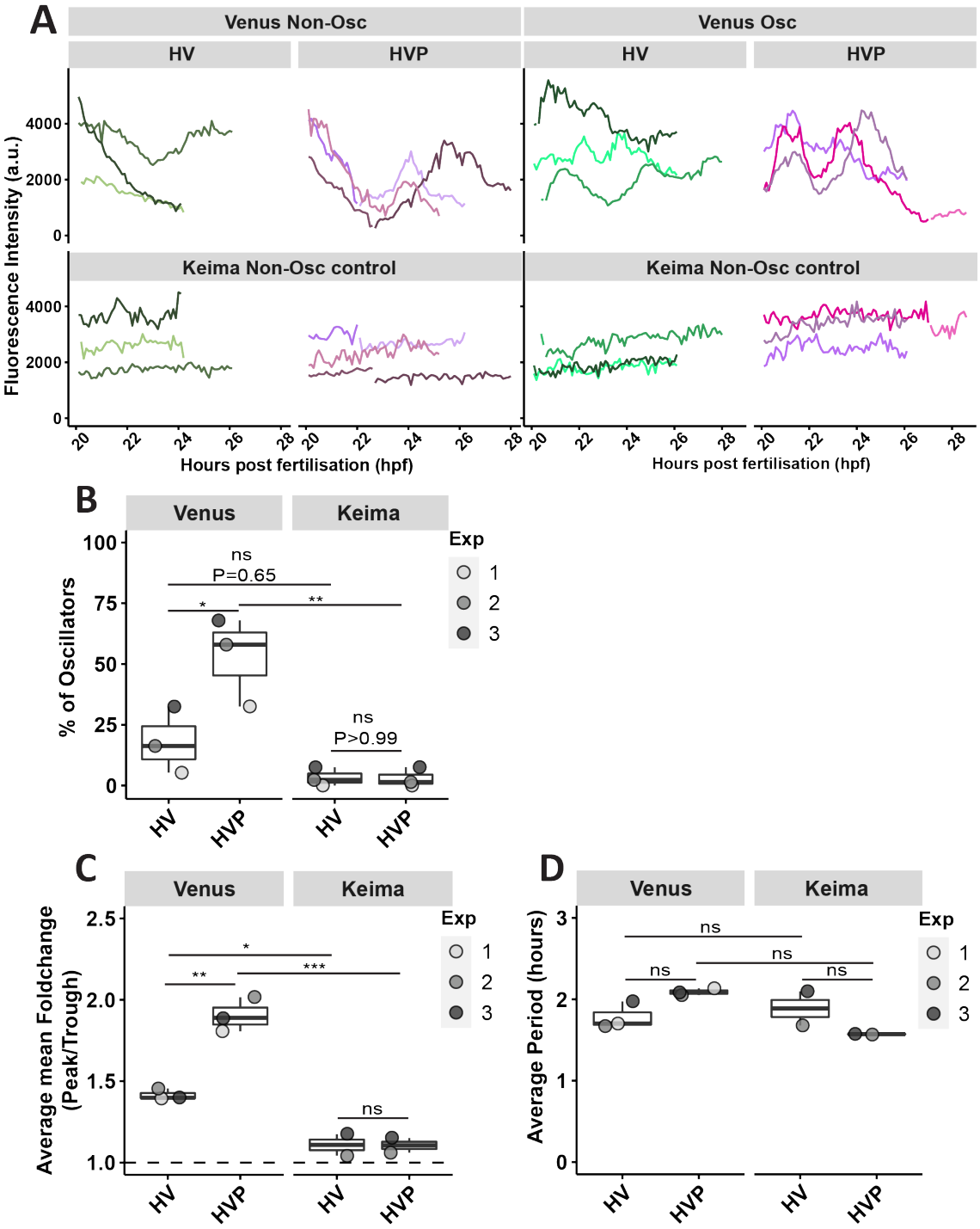

Figure 5.3: **HVP cells are more oscillatory than HV and their oscillations have bigger fold-change.** **(A)** Examples of oscillatory and non-oscillatory single cell traces from HV and HVP. The Keima traces are presented as control and these examples did not pass as periodic oscillators. **(B)** In HV, between 5.2-32.5% of Venus traces were oscillatory while 0-7.5% of Keima traces passed as oscillatory. The difference between Venus and Keima was not statistically significant (ns). In HVP, 32.5-67.9% of Venus traces were oscillatory in contrast to 0-7.5% of Keima traces that passed (**). Significantly higher proportion of oscillators were detected in HVP Venus traces than in HV (*). There was no tendency or significant difference between proportion of Keima traces passing as oscillators between HV and HVP (ns). **(C)** For each single cell that passes as an oscillator, the mean of all fold-changes over time was calculated. The average of mean fold-changes from all cells in each embryo was calculated for statistical analysis. In Keima, average mean foldchanges were close to 1 in both HV and HVP (1-1.2). The average mean fold-change in HV oscillators ($\sim$1.4) were significantly higher than Keima (*). The same was true for average mean fold-change in Venus HVP (1.8-2) relative to its Keima counterpart with higher degree of significance (***). Average Venus fold-changes in HVP were significantly larger in HVP (**). **Caption continued on the following page →**

Figure 5.3: **(D)** The average period for all oscillating cells in each embryo were measured and statistically assessed. Relative to HV Venus traces (1.7-2 hours), HVP had a small tendency for longer periods (2-2.1 hours). This difference was not statistically significant (ns). The average period detected in Keima traces that pass as oscillators range between 1.7-2 hours in HV and 1.6 hours in HVP. Their difference was not significant (ns). There was also no statistical difference between Venus and Keima average periods in neither HV or HVP (ns). 2way ANOVA with multiple comparisons. (ns): $P > 0.05$, (*): $P \leq 0.05$, (**): $P \leq 0.01$, (***): $P \leq 0.001$, (****): $P \leq 0.0001$.

For better insight, snapshots from the paired live imaging experiments were analysed in detail at two hour intervals. The live imaging plane with respect to the Her6 expression domain is shown as dotted line in Fig 5.5,B. Fig 5.5,C is a side by side comparison of the 3D reconstructed Z-stacks from an HV and HVP pair over time. Here, the fluorescence intensities have been adjusted in each embryo to optimise for visualisation. Unaltered images of Venus expression in this pair of embryos can be found in Appendix 8.7.

Both HV and HVP expression domains gradually decreased in size between 20-28hpf. But one gets the impression that relative to HV, the HVP expression domain was reduced ventrally and laterally, particularly between 20-24hpf. However, no conclusions were made about the dorsal part of the domain as this angle of imaging was not optimal for full visualisation of the dorsal boundaries of the Her6 expression domain and telencephalon over time (Fig 5.5,C). A distinction could be made between the patterning of HV and HVP expression. Cells in the HV expressing population appeared more uniform in intensity, while in the HVP expressing population, more contrast was observed between cells (Fig 5.5,C).

To quantify these differences between HV and HVP at the population level, the nuclear marker H2B-Keima (Keima) was used to identify all cell nuclei in the visible domains of the telencephalon regardless of their Venus expression. The distribution of fluorescence intensities of Keima was close to normal in each individual embryo but the width of the normal distribution varied between embryos showing injection variability. However, there was little change in the shape of the distribution in each embryo over time (Fig 5.5,D). HV expression at the earliest time point (20hpf) was normally distributed in the population. Over time, the number of cells with intensities close to zero increased and the number of higher intensities decreased, gradually shifting the distribution to the left (Fig 5.5,E). In contrast, in HVP, there was a high occurrence of Venus fluorescence intensities close to zero from 20hpf, leading to a shifted distribution from this early stage. Similar to HV, the number of low intensity cells in HVP increased over time while higher intensities gradually diminished, further exaggerating the left shift in the distribution (Fig 5.5,E). This was replicated in three separate pairs of HV and HVP embryos and the data for two other replicates are provided in Appendix 8.8.

In each embryo, $Venus^{+}$ and $Venus^{-}$ cells were separated using a threshold value. The threshold selection was guided by the median value of background intensity in each individual embryo and manual detection of lowest visible intensity values. For an overall

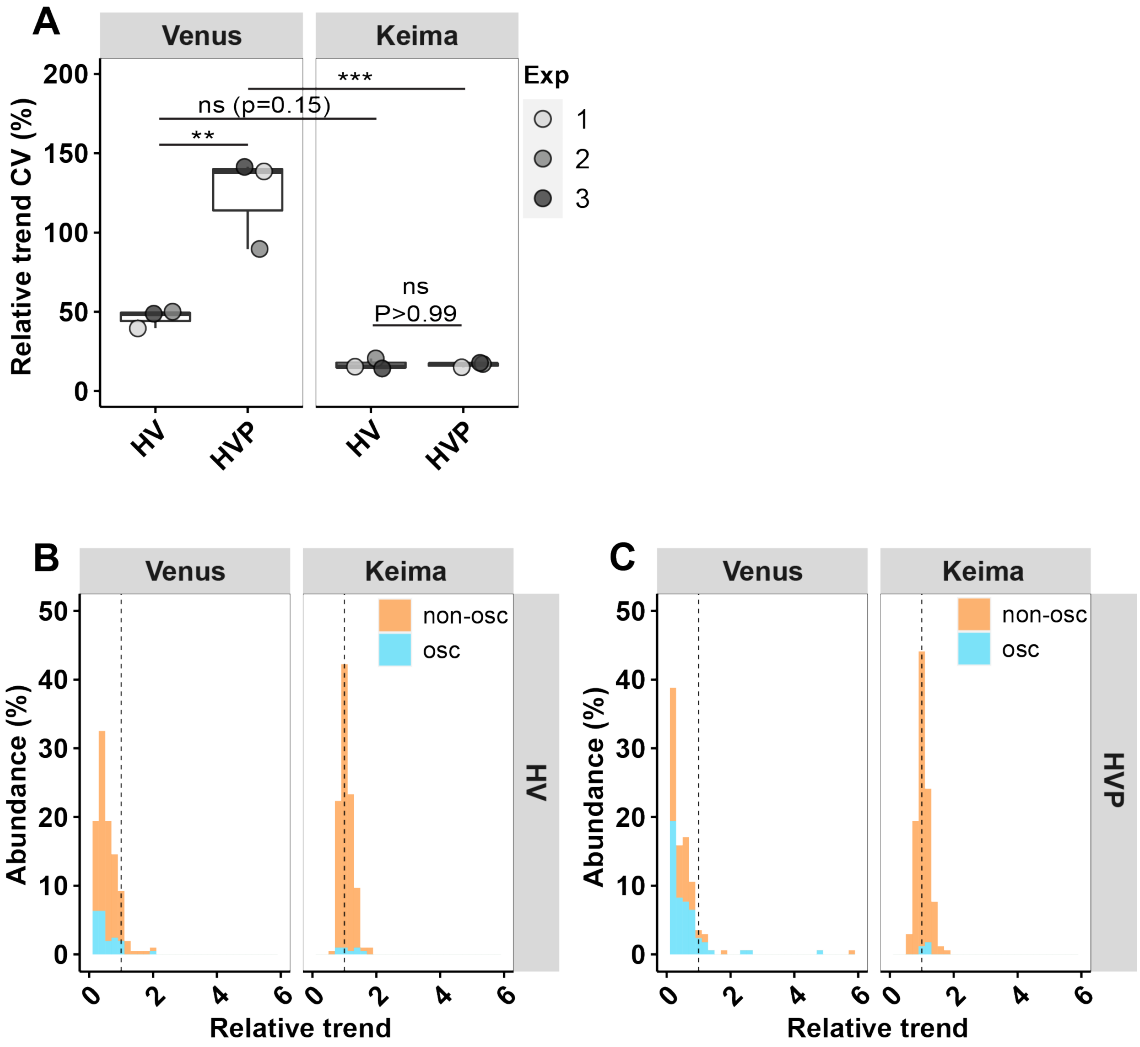

Figure 5.4: **Long term trends in Venus expression are altered in HVP**. **(A)** CV for relative trends of all cells in each embryo were calculated and analysed using 2way ANOVA with multiple comparisons. Variation in Keima relative trends were low and similar between HV (14.3-20.4%) and in HVP (14.9-17.7%) (ns). Variation in HV Venus relative trends was slightly but not significantly higher than its Keima counterpart (ns). Venus relative trend CVs in HVP were significantly higher than Keima (***) and Venus relative trend CVs in HV (**). **(B)** Proportional distribution of Venus and Keima relative trends in 3 HV embryos combined. They are presented as stacked histograms (bin width = 0.2), coloured with oscillatory state. Relative trends in Keima were normally distributed around peak of 1 (dotted line) denoting stable expression over time. Distribution of Venus relative trends was shifted to the left with peak abundance at 0.4. Abundance of oscillators in the whole population was low. 13.6% of cells were positioned at or above 1 and 17% of them are oscillators. **(C)** Proportional distribution of Venus and Keima relative trends in 3 HVP embryos combined. They are presented as stacked histograms (bin width = 0.2), coloured with oscillatory state. Similar to HV, relative trends in Keima were normally distributed around peak of 1 (dotted line) denoting stable expression over time. In comparison to HV, distribution of Venus relative trends in HVP was shifted more to the left with peak abundance at 0.2. Abundance of oscillators in the whole population was high. 10% of cells were positioned at or above 1 and 64% of them were oscillators. (ns): $P > 0.05$, (*): $P \leq 0.05$, (**): $P \leq 0.01$, (***): $P \leq 0.001$, (****): $P \leq 0.0001$.

representation of the whole population over time, cells detected in two-hour intervals were combined. The total number of cells in HVP was equal to HV in experiment 1, but slightly more in experiment 2 and slightly less in experiment 3 (Fig 5.5,F). Therefore, there was no consistent change in the total number of cells detected between HV and HVP. However, the total number of Venus$^+$ cells was consistently lower in HVP than its paired HV (Fig 5.5,F). Proportionally, in all three HV embryos tested, between 80-94% of cells were Venus$^+$ at 20hpf while only 35-55% of cells were Venus$^+$ in HVP at this stage (Fig 5.5,G). The proportion of Venus$^+$ cells reduced over time in both HV and HVP, dropping to 42-78% in HV and 17-30% in HVP at 26hpf which is the last shared stage between all three experiments (Fig 5.5,G). This decline of Venus$^+$ cells in HV and HVP was consistent with the tendency for declining trends at the single cell level (Fig 5.4,B&C)

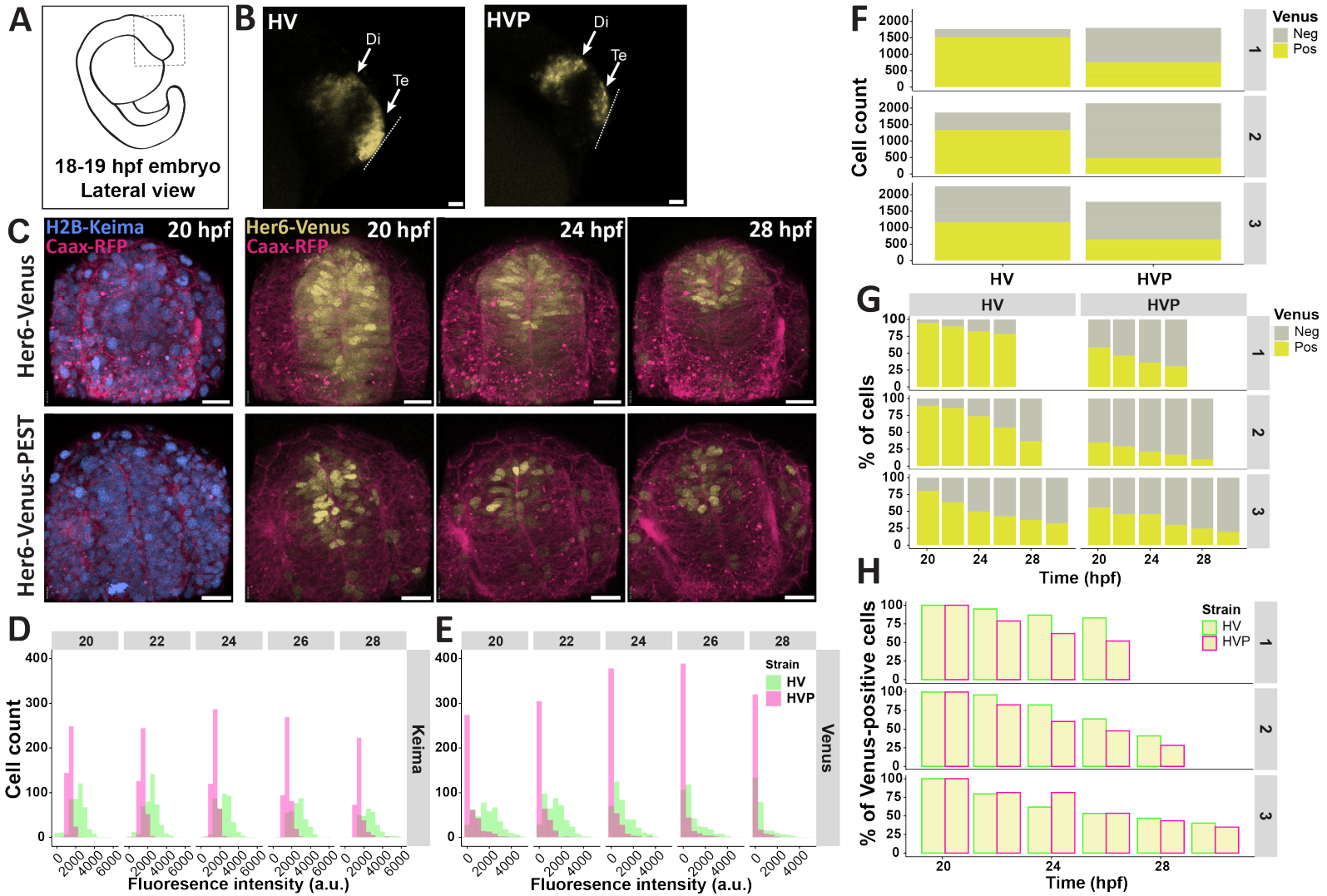

Figure 5.5: **There is a higher prevalence of Venus⁻ cells in HVP telencephalon. Caption on the following page →**

Figure 5.5: **(A)** Schematic diagram of an 18-19hpf embryo in lateral view. The boxed region is shown in B. **(B)** Venus is expressed in the telencephalon and diencephalon of 18-19hpf HV and HVP embryos. Its expression domain in the telencephalon is smaller and and dimmer in HVP. The dotted line shows transversal plane used for live imaging shown in C. Scalebar = 30µm.**(C)** 3D reconstruction Z-stack snapshots of live 20 hpf HV and HVP embryos injected with H2B-Keima and Caax-RFP (left). The progression of Venus expression in the ventral telencephalon between 20-28hpf (right). In HV, Venus was expressed in a broad domain which gradually decreased over time. In HVP, fewer cells expressed Venus and they also decreased over time. Scalebar = 20µm.**(D)** Keima intensity values in HV and HVP from all detected telencephalic cells were plotted in overlapping histograms. Distribution of Keima intensities in both HV and HVP populations were close to normal. The width of the distribution differed correlating with the quality of injection. **(E)** Venus intensity values in HV and HVP from all detected telencephalic cells were plotted in overlapping histograms. In 20hpf HV, Venus intensities were normally distributed. Over time, the distribution shifted towards lower values, peaking close to 0. In 20hpf HVP, the distribution of Venus intensities was shifted to the left with high count of cells with intensity values close to 0. The left-ward shift became more pronounced over time and higher intensities were depleted. **(F)** Total cell count from selected time points (2 hour interval) from three pairs of HV and HVP embryos. The colours represent Venus expression. Total numbers in HVP were comparable, more or less than HV in experiments 1, 2 & 3 respectively. But the number of Venus$^+$ cells in HVP were always lower than HV. **(G)** The percentage of Venus$^+$ and negative cells in three HV and HVP pairs over time. The percentage of Venus$^+$ cells in 20hpf HV ranged between 80-94% and it was lower in HVP 35-55%. Percentage of Venus$^+$ cells declined over time in HV and HVP reaching 42-78% and 17-30%, respectively. **(H)** The percentage of Venus$^+$ cells in HV and HVP relative to the initial state (20hpf). In experiments 1 and 2, Venus$^+$ cells in HVP declined faster than in HV. In experiment 3, the percentage of Venus$^+$ cells in both followed a similar trend over time apart from 24hpf where HV had proportionally fewer Venus$^+$ cells. Di: Diencephalon, Te: Telencephalon.

The rate of the depletion of Venus$^+$ cells was assessed by normalising the number of Venus$^+$ cells to the first time point in each embryo. In experiments 2 and 3, Venus$^+$ cells in HVP declined slightly faster than HV over time. This was in agreement with the slight tendency for more drastic down regulation trend in HVP single cells (Fig 5.4,C). However, this was not the case in experiment 3. Hence, it is likely that in HVP, the Venus$^+$ pool was depleted faster than in HV, but this was not seen in all HVP embryos (Fig 5.5,H).

5.2.3 The population changes in Her6 expression in HVP embryos is more complex than global reduction of Her6 expression levels

The drastic reduction of Venus$^+$ cells in the HVP could have been cause by a global reduction of Her6 expression levels across the population due to protein destabilisation. To address this possibility, I assessed the Venus fluorescence intensity in the cell population in both HV and HVP over time. In both HV and HVP, Venus intensity decreased over time, emphasising the observations of intensity distribution over time (Fig 5.5,D). However, in all stages, Venus intensity in HVP was lower than HV (Fig 5.6,A). However, this could have been partly due to the presence of more Venus$^-$ cells in HVP. Therefore, I removed these cells to examine the Venus$^+$ cells alone. In the Venus$^+$ cells, there was more overlap between Venus intensities in HV and HVP and both decreased over time but plateaued between 22-24hpf. Nonetheless, the majority of Venus$^+$ cells in HVP still had lower intensity levels than Venus$^+$ cells in HV (Fig 5.6,B). This reflected the slight tendency for lower Venus intensity means in single HVP cells over time (Fig 5.2,D&E). However, the upper limits of Venus intensity in all three HV and HVP pairs were comparable. That

is to say, the HVP cells with highest Venus expression matched and at times surpassed the highest Venus expression levels in HV Venus$^+$ cells (Fig 5.6,B). This observation suggested that in HVP, rather than global reduction of Her6 expression levels, the variability of its expression levels has increased.

Hence, the global variability of Venus expression in HV and HVP was quantified by calculating the Coefficient of Variation (CV) of Venus and Keima intensities for all cells in selected time points in each embryo. All statistical comparisons were made using multiple Mixed-effects analyses and only some of the global statistics are reported rather than the comparisons of individual time points (further detail on these analyses is provided in Chapter 2, "Snapshot cell population live imaging analysis", Fig 2.1).

At a global level, CV of Keima intensities was consistently $\sim$30% in both HV and HVP (P=0.7660). Venus CV was significantly higher than Keima in HV and HVP (P<0.0001 & P=0.0017, respectively). In all stages, Venus CV in HVP was higher than in HV and this difference between HV and HVP CVs was statistically significant at a global level (P=0.0122). The difference between Venus and Keima CV in HV was significantly influenced by passage of time (P=0.0442) while this was not the case in HVP (P=0.1656). In short, this meant that when considering all cells, Venus (i.e. Her6) expression was more variable than Keima (H2B-Keima) in HV and HVP but its variability in HVP was higher than HV. In addition, Venus expression variability in HV increased more drastically than HVP over time.

Next, I examined expression variability in Venus$^+$ cells. In comparison to the whole population (Fig 5.6,C), Venus CV was lower in both HV and HVP in Venus$^+$ cells (Fig 5.6,D). Furthermore, the effect of time on the difference between Venus and Keima CVs was also reduced in this population in HV and HVP (P=0.7362 & P=0.6072 respectively). These observations suggested that the Venus$^-$ cells are a major contributors to Her6 heterogeneity in the whole population and implied that the increasing gap between Venus and Keima CVs over time can be attributed to increasing numbers of Venus$^-$ cells or Venus (i.e. Her6) downregulation (Fig 5.6,C).

However, this was not the only cause for heterogeneity in Venus expression, as Venus CVs were still significantly higher than Keima in the Venus$^+$ population in HV (P=0.0388) and more so in HVP (P=0.0033). The variability of Venus expression in HVP still had the tendency to be higher than HV in the Venus$^+$ cells (P=0.1190). Even though this difference was not statistically significant, it was larger than the difference of Keima variability between HV and HVP (P=0.7680). In summary, in the Venus$^+$ cells, variability of Venus expression was still higher than Keima in HV and even more so in HVP. These observations supported the predictions from figure 5.6,B and confirmed that not only Her6 expression is more variable than Keima, it is also more heterogenous in HVP relative to HV.

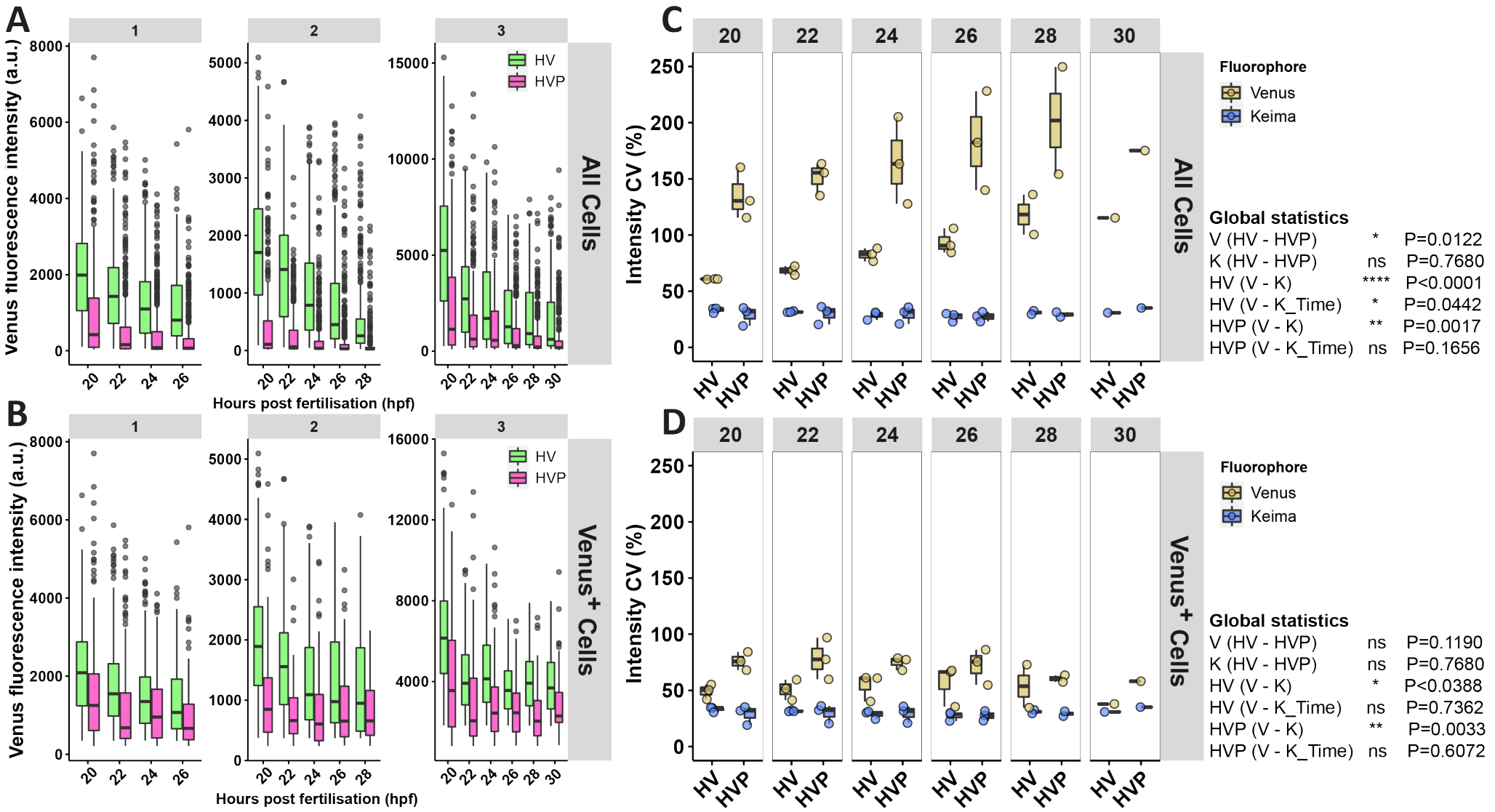

Figure 5.6: **HVP cell populations exhibit lower Venus expression levels but retain the ability for HV-level expression, increasing Venus heterogeneity. Caption on the following page →**

Figure 5.6: **(A)** Global Venus fluorescence intensity from all individual cells detected at 2-hour intervals was plotted for three pairs of HV and HVP embryos. In all pairs, Venus intensity in the population gradually reduced over time in HV and HVP but was lower in HVP in all time points.**(B)** Venus$^-$ cells were removed from the population and Venus fluorescence intensity from all individual Venus$^+$ cells was plotted. In all HV and HVP pairs, Venus intensity declined between 20-22 hpf but plateaued after this stage. In the Venus$^+$ population, the lower 75% of Venus intensities were lower than HV at all time points. But the top 25% of intensities were comparable or at times higher than HV (e.g. 20hpf in experiment 1 or 30hpf in experiment 3). **(C)** For each embryo, CV of Venus and Keima intensity values was calculated as a measure of heterogeneity at each time point. Three repeats were combined for statistical assessment. In the global population, Venus heterogeneity was higher than Keima heterogeneity in HV (****) and HVP (**). In both, Venus heterogeneity diverged more from Keima over time but this effect of time on heterogeneity was only significant in HV (*). Venus heterogeneity was higher in HVP in all time points and this difference was globally significant (*) whereas there was no difference in Keima heterogeneity between HV and HVP. **(D)** Venus$^-$ were removed from the population and CV of Venus and Keima intensities was calculated as a measure of heterogeneity in the Venus$^+$ cells at each time point. Three repeats were combined for statistical assessment. In the Venus$^+$ population, Venus heterogeneity remained higher than Keima heterogeneity in HV (*) and HVP (**). Heterogeneity in Venus$^+$ cells did change consistently over time. HVP retained its tendency for higher Venus heterogeneity relative to HV in all time points. This difference was no longer globally significant (ns). V: Venus, K: Keima. Mixed-effects analysis, (ns): $P > 0.05$, (*): $P \leq 0.05$, (**): $P \leq 0.01$, (***): $P \leq 0.001$, (****): $P \leq 0.0001$.

5.2.4 Assessing the implication of the changes in Her6 dynamics on its expression in neighbouring cells in HVP

Single cell and population level comparison of HV and HVP demonstrated altered Venus (i.e. Her6) regulation in HVP. The implications of this altered regulation in the pattern of Venus expression in the tissue was assessed by analysing neighbouring cells (This analysis was performed by ***Dr Veronica Biga***, Statistical analysis was done by myself). To this end, the closest neighbour to each cell was identified based on minimal 3D Euclidean distance. The intensity levels of Venus and Keima were used as paired data sets where intensity on the x-axis represents the fluorescence intensity of a selected cell and intensity on the y-axis represents the fluorescence intensity of its closest neighbouring cell.

The pattern of Venus expression in neighbouring cells was different between HV and HVP (Fig 5.7,A shows examples from only one experiment). In 20hpf HV, Venus expression intensity in each cell was more likely to positively correlate with its neighbouring cell. That is to say, an HV cell exhibited similar Venus expression levels to its neighbour. Even though the absolute expression values decreased by 28hpf, the positive correlation of Venus intensities between neighbouring cells was maintained (Fig 5.7,A, Top). In the 20hpf HVP, however, Venus intensity in neighboring cells was more prone to an inverse relationship which became more pronounced by 28hpf. This meant that an HVP cell expressing high levels of Venus was more likely to be close to a low expressing cell. The same analysis was performed for Keima that produced more random scattering of values and no significant difference between HV and HVP (Appendix 8.9). The correlation coefficients for Venus intensities in neighbouring cells from three pairs of HV and HVP embryos were analysed and statistically tested using Mixed-effects analysis. Neighbouring cells in HV had significantly stronger correlation than HVP (P=0.0186) but this did not significantly

change over time (P=0.2255) (Fig 5.7,B).

Since Keima was injected and Venus was expressed endogenously, the sources of variability in cell-cell intensities for Keima was different than Venus. To use Keima as a control and to circumvent variability of intensities due to Z-axis depth and different imaging parameters between different experiments, a ratiometric analysis was performed. For this, the ratio between fluorescence intensity in a selected cell and its neighbour was calculated in each embryo and mean cell-cell ratios were plotted. Cell-cell ratios in HVP were significantly higher than HV (P<0.0001) but this did not change significantly over time (P=0.2274, Fig 5.7,C). Cell-Cell ratios of Venus were close to Keima in HV but significantly higher (P=0.0041) (Fig 5.7,D). In the case of HVP, the mean ratios of neighbouring cells were also significantly higher than Keima but with higher degree of significance than HV (P<0.0001, Fig 5.7,E). This showed that relative to HV, the neighbouring cells in HVP have larger differences in Venus (i.e. Her6) expression.

5.2.5 Mathematical modelling presents cell-cell coupling as a potential mechanism for the altered patterning in HVP

Experimental evidence demonstrated that changing Her6 protein stability resulted in increased heterogeneity in its expression. That is to say, even though most HVP cells expressed Her6 at lower levels when compared to HV, some retained the ability to express Her6 at HV levels. This was accompanied with differences in the pattern of Her6 expression in neighbouring cells between HV and HVP. The observed effects were surprising and counter-intuitive as one would expect all cells to be affected in the same way by Her6 destabilisation and for patterning to remain unaffected. To understand the source of these differences between HV and HVP that could explain the counter-intuitive observations, we turned to mathematical modelling. To do so, three mathematical models with different levels of complexity were explored, with predominant focus on replicating the larger differences in protein expression between neighbouring cells that were seen in HVP (All mathematical modelling was performed by ***Joshua Hawley***).

Model 1: Uncoupled cells with no protein auto-inhibition

First, we considered the possibility where a single cell expressed Her6 autonomously and no communication or coupling between cells affected Her6 expression (i.e. uncoupled). This model also did not include Her6 auto-regulation and simply described the regulation of protein levels in a single cell with three parameters: p referring to protein abundance, α denoting protein synthesis (translation) rate and μ representing protein degradation rate. Under the assumption that the steady state protein concentration in a cell does not change over time, the steady state protein abundance was described as p^*, determined by the ratio

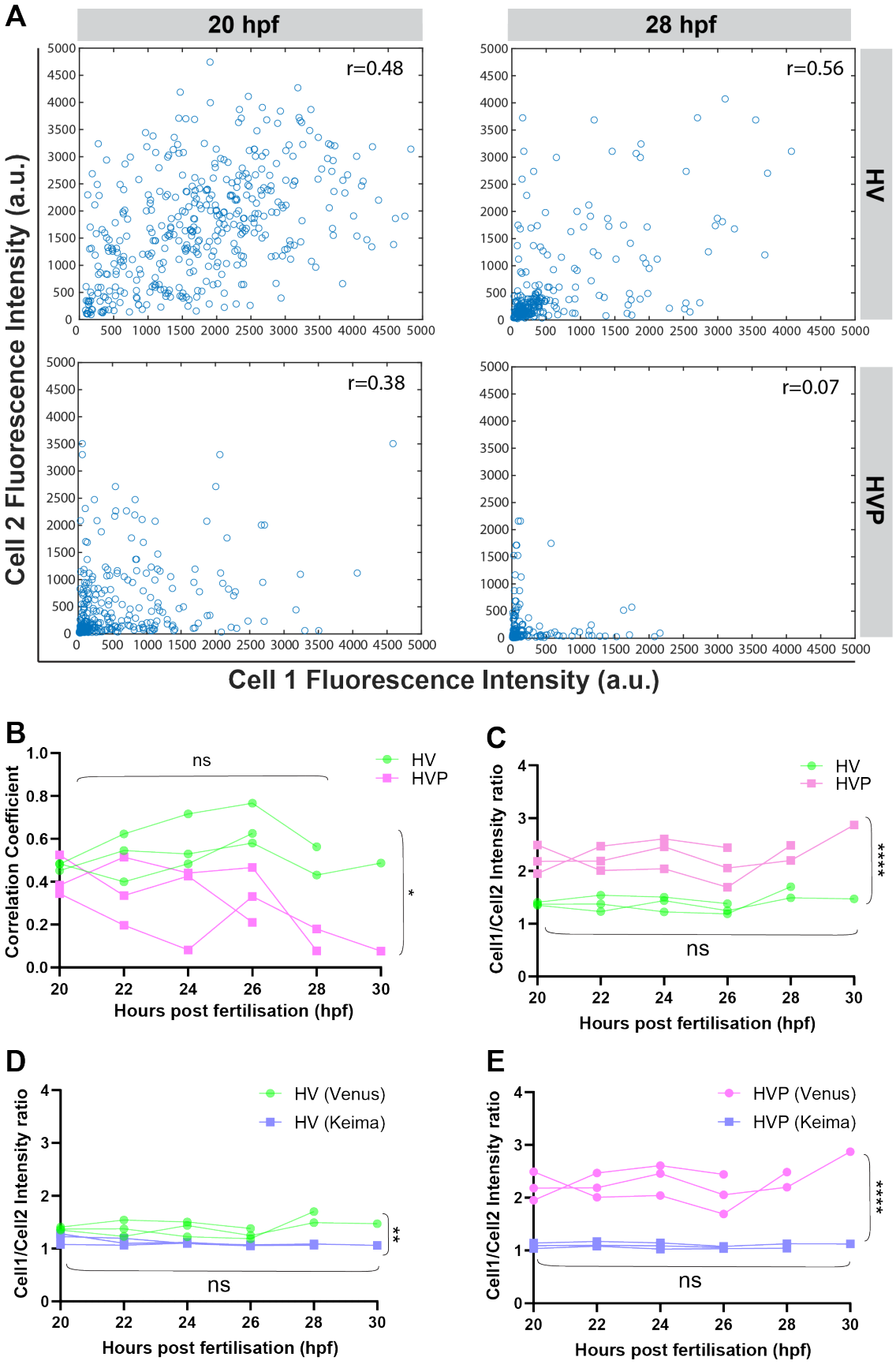

Figure 5.7: **Neighbouring cells have similar Venus expression levels in HV but more polarised Venus expression levels in HVP.Caption on the following page →**

Figure 5.7: **(A)** Example time points from only one experiment is shown (experiment 2). For each cell, the closest neighbour was identified and the intensity levels of Venus were plotted as paired sets with Venus intensity of a selected cell (cell 1) on the x-axis and its neighbouring cell (cell 2) on the y-axis. In HV, cell 1 and cell 2 intensities were similar, giving rise to a weak correlation at 20hpf (r=0.48). This correlation strengthened toward moderate by 28hpf (r=0.56). In HVP, cell 1 and cell 2 intensities had a tendency to diverge and at 20hpf had a weaker correlation than stage-matched HV (r=0.38). The correlation weakened over time since by 28hpf, there was no correlation between cell 1 and cell 2 intensities (r=0.07). **(B)** The correlation coefficient (r) from three HV and HVP pairs was shown over time. Correlation was significantly higher in HV than HVP (*) but there was no significant imposed by time (ns). **(C)** Intensity ratio was calculated for each pair of cells and the mean intensity ratio for each embryo at the selected stage were plotted. For Keima, the mean intensity ratio was maintained around 1. Venus mean intensity ratios were significantly higher than Keima (**). **(D)** The mean of intensity ratios were calculated for Venus and Keima from three HVP embryos. For Keima, the mean intensity ratios were maintained $\sim$1. Venus mean intensity ratios were significantly higher than Keima (****). **(D)** The mean of Venus intensity ratios from HVP embryos were significantly higher than HV (****). Mixed-effects analysis, (ns): P > 0.05, (*): P ≤ 0.05, (**): P ≤ 0.01, (***): P ≤ 0.001, (****): P ≤ 0.0001.

of protein production over its degradation

$$p^* = \frac{\alpha}{\mu}, \tag{5.1}$$

Cells in the HV telencephalon expressed a range of Her6 levels. It was assumed that the expression level in each cell at any given time point was the result of its production and degradation rates, following (5.1). Based on these assumptions, the changes in protein level distribution when the degradation rate (μ) is increased were predicted. For this, the degradation rate represented by normalised μ ($\frac{\mu}{\alpha}$ where α =1, referred to as μ from hereon) was changed by the same degree in two simulated cells with different p^* levels. The cells with higher starting p^* had a bigger decline in levels than the cells with lower starting p^* giving rise to an exponential curve (Fig 5.8,B Purple line). The gradient of this line always increased with μ (Fig 5.8,B Orange line).

If this model held true, all cells in a population would have a decline in expression levels, regardless of the starting p^*. To show how the experimental distribution would change under this modelling assumption, the distribution of HV values from the first time point of live imaging (20hpf, experiment 1) was tested under this model. Intensity values for each cell was multiplied by $\frac{1}{d_f}$, where d_f is a degradation factor indicating the amount of change in μ relative to its starting value. This showed that with increasing μ, all the values decreased, making the distribution narrower and shifting it completely to the left with no high expressing cells remaining (Fig 5.8,C). In short, under the assumptions of Model 1, with increase in μ, all cells in the population would be affected equally. That is to say, the Her6 levels in all of the cells and the differences in intensity between cells would always decrease. This was contrary to the HVP where Her6 levels decreased in most but not all cells and the differences between cells increased. Therefore, the simple model was not sufficient to explain the observations in HVP.

Model 2: Uncoupled cells with auto-inhibition

Model 1, based on simple mechanism of protein production and degradation, was not capable of producing higher cell-cell concentration differences with increasing degradation rate. Hence, a more complex model (Model 2) was devised by incorporating an auto-inhibition feedback loop into Model 1 (Fig 5.8,D). Addition of auto-inhibition was justified by its well known involvement in HES1 regulation and oscillation (Takebayashi et al., 1994; Hirata et al., 2002; Monk, 2003). This was done by multiplying the translation rate (α) by an inhibitory Hill function. p_0 represents the repression threshold, denoting the protein abundance that reduces protein production rate by 50% of the maximum. n is the Hill coefficient and high n-values increase the effect of protein on its production, leading to sharp and switch like transitions of protein abundance. It was assumed that like HES1, Her6 dimerisation is required for it to bind target DNA sequences and inhibit gene transcription, including the auto-inhibition of its own gene. Thus, Hill coefficient of 2 (referring to dimerisation) was deemed reasonable value for examining Model 2.

First, a range of p_0 versus μ was explored with $n = 2$ (Fig Fig 5.8,E**i**). Similar to Model 1, with increasing μ, the steady state concentration exponentially decreased for each p_0 value. In line with this, the gradient of this exponential decline also maintained the same shape as Model 1 and always increased with increasing μ (Fig 5.8,E**ii**). Interestingly when higher Hill coefficient values were used ($n = 8$), the gradient of the steady state abundance was no longer constantly increasing. This implied the possibility of protein abundance in high expressing cells declining at a slower rate than the lower expressing cells which in theory, could have resulted in higher cell-cell differences. However, based on previous literature (Weiss, 1997), such high n values were not deemed realistic and were therefore not further considered. Hence, within the realistic bounds of the Hill coefficient (i.e. $n = 2$), Model 2 also failed to generate high cell-cell differences in the population and hence, could not represent the HVP data.

Model 3: Coupled two-cell model with auto-inhibition

Given the inadequacy of simple single cell models to explain the HVP behaviour, one may hypothesis that interactions between cells play a role in this system and can impact the population response. To examine this hypothesis, another layer of complexity was applied to the model by linking two cells with Notch/Delta-like lateral inhibition, resulting in Model 3 (Fig 5.8,G). Given sufficient coupling between cells, if a small difference in the initial protein concentrations existed, the difference would be amplified due to lateral inhibition, increasing cell-cell difference.

In addition to the Hill function describing the auto-inhibition (H_{auto}), Model 3 included coupling strength which represented another Hill function for lateral inhibition, determining the amount of protein required in one cell to inhibit expression in the neighbouring cell

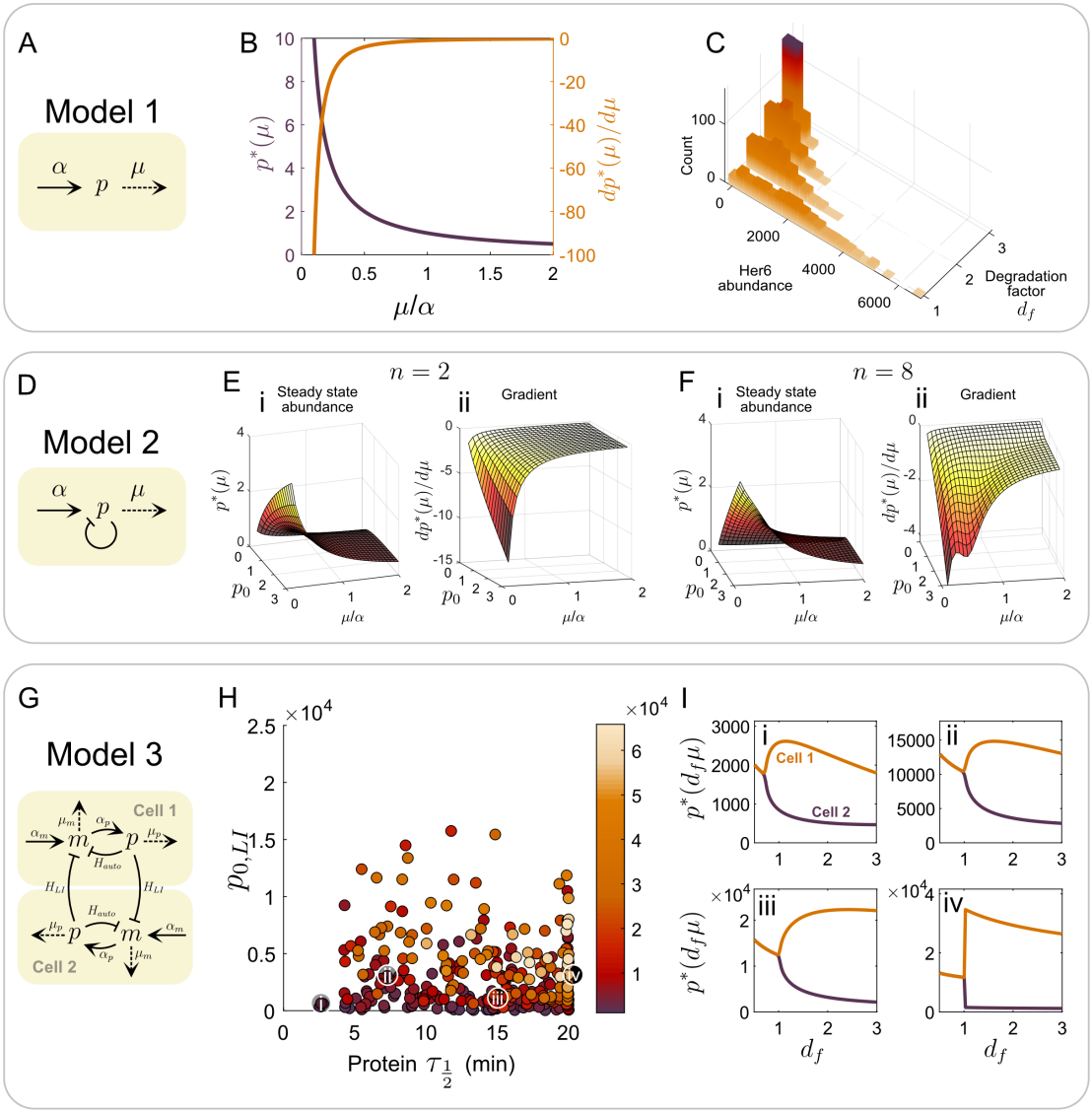

Figure 5.8: **Explorations of three mathematical models with varying levels of complexity point to cell coupling as potential source for HVP phenotype.** (**A**), (**D**), and (**G**) show the parameters and interactions in each model. (**B**) shows the steady state concentration $p^*(\mu)$ generated by equation (5.1) in purple (left axis), and the gradient of the steady state concentration is plotted as an orange line (right axis). (**C**) Shows experiment 1 data plotted at $d_f = 1$ and higher d_f values show the data multiplied by $\frac{1}{d_f}$. (**E i**) Shows steady state values generated from Model 2 using a Hill coefficient value $n = 2$ over a range of p_0 and $\frac{\mu}{\alpha}$ values. **ii** is the gradient of the steady state taken with respect to the $\frac{\mu}{\alpha}$ axis. (**F i**) and **ii** show similar plots as in **E**, using a Hill coefficient $n = 8$. (**H**) shows optimiser outputs plotted as 2D parameter space for protein half-life and coupling strength $p_{0,LI}$. Out of the 6340 runs of the optimiser, the data was filtered down to 291 plotted results that satisfy $error > 1000$ and $coherence < 0.3$. The colour bar refers to the error value ((5.2)). (**I**) Shows the change in the steady state of two cells with degradation factor d_f for four points in parameter space. (**i-iv** map to the same-numbered white circles in **H**)

.

by 50% (H_{LI}). Higher coupling strengths meant that low protein levels in one cell could have a large impact on protein levels in the neighbouring cell. In addition to these two parameters, Model 3 also included other key features of an oscillatory network. These included mRNA abundance (m), production (α_m) and degradation rates (μ_m), protein abundance (p), production (α) and degradation rate (μ_p), along with the time-delays for auto-inhibition (τ_{auto}) and lateral inhibition (τ_{LI}) (Fig 5.8,G). All parameters used for this

model can be found in Chapter 2, Mathematical modelling.

The main question was: are there are any parameter sets for two coupled cells where with increasing degradation rate, cell-cell differences increase? The explorations using Model 3 were aimed to answer this question. The cell-cell concentration difference for any given degradation rate was calculated by $\Delta p^*(\mu) = |p_1^*(\mu) - p_2^*(\mu)|$. We wanted to determine how much the cell-cell expression difference has changed when degradation rate is increased by a factor $d_f > 1$. Therefore, during simulation, the model was run twice with each parameter set. In the first run, the degradation rate was μ and in the second run, degradation rate was altered to $d_f\mu$. Based on the two runs, an error value was calculated for each parameter set by the following equation

$$error = \Delta p^*(d_f\mu) - \Delta p^*(\mu). \tag{5.2}$$

Here, larger error values indicated larger cell-cell expression differences upon increasing protein degradation rate or destabilising the protein.

Model 3 included 10 parameters which made simulations much more complex than Models 1 and 2. Hence, the number of parameter values posed a challenge for exploring the parameter space as exploring all possible combinations required a large number of simulations. In fact, if 10 values were to be evaluated per parameter, at a speed of 1 simulation per second, determining the output for all combinations of parameters would require ~ 300 years. Worse yet, for exploring 20 values per parameter, the required time would increase to ~ 1 million years, which was by no means ideal. For a more efficient approach, an optimiser was used to search for the lowest error output from each simulation. Here, the MATLAB pattern search method was utilised (Chapter 2, Mathematical modelling).

For better visualisation of the extent of changes in the cell-cell expression difference, scatter plot of protein half-life versus $p_{0,LI}$ (determinant of coupling strength between two cells) was plotted (Fig 5.8,H). In this plot, each point was coloured by error. High error values that were indicative of bigger changes in cell-cell expression difference were predominantly found at lower $p_{0,LI}$, which reflect higher coupling strength. The largest error outputs were also focused but not restricted to higher starting half-lives. However, large error values still occurred at starting half-lives as low 5 minutes.

To understand how the steady state concentration (p^*) in cell 1 and cell 2 change with increasing μ, four parameter sets from figure Fig 5.8,H were run over a range of degradation factors (Fig 5.8,I). In all four parameter sets, Cell 1 and 2 transitioned from a common p^* to two distinct p^*, leading to a bifurcation. In short, Model 3 demonstrated that the increase in cell-cell difference by protein destabilisation is achieved via lateral inhibition.

5.3 Discussion

No previous work has addressed the single cell and tissue effects of altering an ultradian oscillator by direct manipulations of the protein turnover in a unified *in vivo* system. Reports using *in vitro* systems had demonstrated that global HES1 levels are sensitive to its stability and increase or decrease when the protein is stabilised (Chen et al., 2017) or destabilised (Kobayashi et al., 2015), respectively. But both these alterations dampened HES1 oscillations in bulked synchronised cells (Kobayashi et al., 2015; Chen et al., 2017). Due to a lack of insight into single cell protein dynamics, the relationship between these global level and dynamic observations was unclear. Here, I have used an *in vivo* model to investigate the effects of directed Her6 destabilisation in single cells and cell populations. This work reveals a novel, nuanced and multi-cellular response of a developmental system to destabilisation of an oscillator protein.

Similar to the report of HES1 destabilisation (Kobayashi et al., 2015), Her6 destabilisation in HVP also led to lowering of its expression levels in the majority of cells. But unexpectedly, some cells in the HVP population continued to express Her6 at HV (i.e. control) levels which increased Her6 heterogeneity in the HVP population. This type of nuanced changes in the population have been previously masked by techniques that average (Western blot, (Kobayashi et al., 2015; Chen et al., 2017)) or saturate signal from a large population of cells (Chromogenic in situ hybridisation, (Hirata et al., 2004)).

The main source of global heterogeneity were Her6-negative (Venus^{-}) cells and their numbers increased over time. Similar proportional reduction of Her6-expressing progenitors has been reported during normal hindbrain neurogenesis (Soto et al., 2020). Additionally, persistent repression of *HES1* expression by Notch inhibition with DAPT in mouse telencephalon dissociation cultures was accompanied with the upregulation of proneural genes, *Neurogenin 2 (Ngn2)* and *Delta-like 1 (Dll1)* (Shimojo et al., 2008). Similarly, neural differentiation was associated with HES1 downregulation and Achaete-Scute Complex-Like 1 (ASCL1) upregulation in acute dissociation cultures derived from mouse ventral telencephalon (Imayoshi et al., 2013). Therefore, HES1 down regulation can be associated with progression towards differentiation. Hence, given the expected role of Her6 as a regulator and marker of neural progenitors (also see Chapter 4, Discussion), I concluded that the reduction in the number of Her6-positive cells over time is most likely caused by cells downregulating Her6 as they move towards differentiation.

Relative to HV, Her6-positive (Venus^{+}) cells in HVP telencephalon were depleted slightly faster. Furthermore, while in both HV and HVP most tracked cells had a declining trend, the majority of HVP cells had lower relative trends. These findings suggested that Her6 downregulation occurs slightly prematurely in HVP, hence more rapidly depleting the Her6 expressing progenitor pool.

Interestingly, Her6 expression in the Her6-positive (Venus^{+}) population in HVP was also

more heterogeneous than in the Her6-positive population in HV. This was perhaps a reflection of increased single cell CV in HVP which, at least in part, was the result of more oscillators and higher fold-change of the oscillations. Based on my data, oscillations were not associated with a particular long-term trend in either HV or HVP. That is to say, they were not a specific trait associated with either Her6 maintenance or downregulation over time. However, relative to HV, oscillators were over-represented in HVP cells with stable or increasing Her6 long-term trends. One may assume that if the cells that are downregulating Her6 are moving towards differentiation, then the cells with stable or increasing Her6 are potentially involved in maintaining the progenitor pool. In HVP, where Her6 is depleted, it can be speculated that the Her6 oscillations in cells with maintained or increasing Her6, play a role in compensating for the lower Her6 levels by exposing the downstream genes to near normal pulses of Her6. However, the validation of such speculations requires extensive examination of the decoding mechanisms of oscillators by downstream targets.

Her6 destabilisation also affected the patterning of its expression at the tissue level. Neighbour analysis revealed that relative to HV, Venus expression was less correlated in neighbouring cells in HVP. This meant that in HVP, there was a larger difference of expression between neighbouring cells, resembling a "salt and pepper pattern" which is often characteristic of Notch-directed lateral inhibition in tissues (Bocci et al., 2020). Indeed, this HVP population phenotype was not reproduced by mathematical modelling that considered single cell intracellular dynamics alone. Instead, increasing cell-cell concentration difference or bifurcation between two cells was only achieved when Notch-like lateral inhibition was introduced, implying that the HVP traits are enabled by the presence of cell coupling. In Model 3 exploration, the biggest changes in cell-cell concentration were seen with high starting protein half-lives but could also be produced with starting half-lives of around 10 minutes, which is the estimated half-life of Her6 (Soto et al., 2020) (also see Chapter 4, Discussion). Therefore, I propose that Her6 expression in the zebrafish telencephalon is regulated by Notch.

At this time, the relationship between the single cell oscillatory and long term dynamics with cell-cell coupling in this system remain to be elucidated. Furthermore, the current mathematical approach is deterministic and only includes two cells. Future work will aim to extend this to a stochastic and multi-cellular model to better represent the tissue, similar to the modelling work by Biga et al. (2021) in the mouse spinal cord. Additionally, further experimental work will allow the model to be better parameterised specifically for Her6. These would enable the incorporation of the single cell oscillatory and long-term dynamics. Even though the underlying cause of the bifurcation between two cells remains to be experimentally assessed, it appears to involve an interplay between auto-inhibition and lateral inhibition as it could not be reproduced with lateral inhibition alone (data not shown).

5.4 Concluding remarks

This chapter provided an in depth comparative study of Her6 in HV with its destabilised form in HVP where single cells and cell populations were experimentally and mathematically explored. The single cell resolution of my experimental approach enabled me to reveal that while Her6 destabilisation reduced its levels as expected, it unexpectedly increased the Her6 expression heterogeneity in the global and Her6^{+} (Venus^{+}) populations. The high global heterogeneity in HVP was predominantly associated with high abundance of Her6^{-} cells which increased over time. In line with this, HVP single cells had slightly higher tendency for more drastic decline over time. On the other hand, the higher heterogeneity of Her6 expression in the Her6^{+} population in HVP was in part due to increased oscillatory behaviour and higher fold-changes. Higher Her6 heterogeneity in HVP was accompanied with changes in the pattern of its expression between neighbouring cells and imposed an inverse relationship, and hence higher differences between them. A mathematical modelling approach determined that the cause of this bifurcation between neighbouring cells is most likely cell-cell coupling and lateral inhibition.

I suspected that the HVP traits, such as more rapid decline in Her6 expression, higher abundance of Her6^{-} cells and larger expression difference between neighbouring cells could be indicative of premature depletion of the progenitor pool with implications in neural differentiation. Hence, the downstream phenotypic effects of Her6 destabilisation were examined and are presented in the following chapter.

Chapter 6

Assessing the downstream phenotypes of altering Her6 expression dynamics by its destabilisation

6.1 Background

In the early stages of zebrafish telencephalic development (∼14 Hours post fertilisation (hpf)), *shh* and *wnt8b* are respectively expressed at its ventral-most and dorsal-most regions (Danesin et al., 2009). The interplay between SHH and Wnt signalling pathways is mediated by Foxg1 which is expressed in the whole telencephalon in a ventral to dorsal gradient. Even though Foxg1 acts downstream of SHH signalling and is therefore a regulator of ventral fates, it also counteracts Wnt/β-Catenin signaling to prevent the expansion of dorsal fates (Danesin et al., 2009). The combined effect of these signalling centres plays a key role in Dorsoventral (DV) patterning of the telencephalon into the pallium (dorsal telencephalon) and sub-pallium (ventral telencephalon) that ultimately give rise to distinct neuronal identities distinguished by a distinct set of genes (Wilson, Rubenstein, 2000; Danesin et al., 2009).

Genes expressed in the pallium are predominantly involved in glutamatergic specification. For example, T-box transcription factors like *tbr2* and *tbr1* are expressed in the zebrafish pallium from ∼12 and 18hpf, respectively (Mione et al., 2001). Both of these transcription factors are involved in the genetic programme for development of glutamatergic cortical neurons in mice (Mihalas, Hevner, 2017) and may therefore be playing the same role in the zebrafish telencephalon as well. *Neurogenin 1 (Ngn1)* which is associated with glutamatergic fate in the zebrafish thalamus (Scholpp et al., 2009) is also present in the pallium (Yoshizawa et al., 2011; Miyake et al., 2017). Indeed, the vesicular glutamate transporter genes *vglut2.1* and *vglut2.2* that are terminal glutamatergic neuron markers (Higashijima et al., 2004) are also expressed in the dorsal telencephalon at least from 24hpf (Viktorin et al., 2009).

The sub-pallium expresses genes associated with the GABAergic fate. The terminal GABAergic neuron marker, *gad1*, encodes glutamic acid decarboxylase which is involved in Gamma-aminobutyric acid (GABA) synthesis. This gene is expressed in the zebrafish sub-pallium (Martin et al., 1998; Miyake et al., 2005). *Achaete-Scute Complex-Like 1 (Ascl1)* expression is also localised to the sub-pallium from ∼14hpf (Allende, Weinberg, 1994) and is thought to be involved in GABAergic determination. In support of this, Miyake et al. (2017) have shown that the reduction of *ascl1a* expression in 24hpf embryos caused by alteration of BMP signalling, was followed by a drop in *gad1* expression in 28hpf embryos to the detriment of GABAergic differentiation. *Ascl1* plays a similar role in specifying the ventral telencephalon in mice (Fode et al., 2000). In the sub-pallium, Distal-less-related Homeobox (*dlx*) genes are expressed in bigene pairs. *dlx1a/2a* expression is located closer to the ventricle while *dlx5a/6a* are located more laterally and throughout the sub-pallium which more closely matches *gad1* expression, consistent with their involvement in GABAergic specification, similar to their murine counterparts (MacDonald et al., 2010; Yu et al., 2011).

her6 is known to be involved in development of neuronal sub-types and regionalisation in the thalamus (part of the diencephalon) by promoting and inhibiting *ascl1* and *ngn1*, respectively. *her6* expression is focused in the rostral and prethalamic (rTh and PTh) regions where it promotes development of GABAergic neurons by inhibiting *ngn1*. *ngn1* inhibition permits the expression of *ascl1a* in these domains which later express the terminal GABAergic neuron markers, *gad1* and *gad2*. However, *ngn1* is freely expressed in the caudal thalamus (cTh) where *her6* is not present, specifying glutamatergic neurons. Indeed, morpholino Knock-down (KD) of *her6* leads to ectopic expression of *ngn1* across all thalamic regions, including the PTh, and the subsequent downregulation of *ascl1a*, *gad1* and *gad2* (Scholpp et al., 2009).

Similar inhibitory relationship between *her6* and *ngn1* has been described in the telencephalon where *her6* over expression suppressed *ngn1* expression in Wild type (WT) telencephalon (Yoshizawa et al., 2011). Dmrta2 is a doublesex and mab-3 related transcription factor that regulates neuronal differentiation in the zebrafish dorsal telencephalon. Its KD led to downregulation of *ngn1* in the pallium and the expansion of *her6* to this domain. The *ngn1* phenotype was rescued by injection of *her6* morpholino into dmrta2 knock-out mutants. Thus, the authors have suggested that Dmrta2 is an inhibitor of Her6 which in turn, inhibits *ngn1* (Yoshizawa et al., 2011). However, the dynamics of Her6 protein expression have neither been described nor directly targeted in the thalamus or the telencephalon. Therefore, it is not known whether these dynamics play a role in the relationship of Her6 with *ngn1* and *ascl1*, telencephalic regionalisation and determination of neuronal identity.

This is while the expression and dynamics of HES1, the murine counterpart of Her6, have been shown to have direct implications in neural differentiation and development in the nervous system. The phenotypic implications of drastic changes in HES1 expression such as upregulation, down regulation or abolishing its dynamics have been reported. For instance, in boundary cells like the Zona Limitans interthalamica (ZLI) and the isthmus, HES1 is expressed persistently and at high levels. This slows down cell proliferation and represses proneural Basic helix-loop-helix (bHLH) factors to block neural differentiation, allowing the boundary cells to compartmentalise the developing Central nervous system (CNS) and act as organising centres (Baek et al., 2006). It has been suggested that this behaviour is due to sustained and non-oscillatory expression of HES1 (Shimojo et al., 2008).

On the other hand, in non-boundary or compartmental cells like telencephalic neural progenitors, *Hes1* and HES1 expression is oscillatory. These dynamics drive the proneural factors like ASCL1, *Ngn2* and *Delta-like 1 (Dll1)* to oscillate and thereby prevents them from being sustained long enough to drive neural differentiation (Shimojo et al., 2008; Imayoshi et al., 2013). When HES1 expression was persistently repressed in mouse telencephalon dissociation cultures by inhibiting Notch signalling with a γ-secratase inhibitor

(DAPT), expression of *Ngn2* and *Dll1* were upregulated and exhibited more sustained rather than oscillatory expression. This was shown using reporters consisting of either *Ngn2* or *Dll1* promoters combined with Luciferase (Shimojo et al., 2008). Shimojo et al. (2008) also showed that cells with sustained expression of *Ngn2* and *Dll1* also expressed the early stage neuronal marker, TuJ1. These findings demonstrated that downregulation of HES1 enables neural differentiation (Shimojo et al., 2008).

Hes1 expression dynamics also contribute to brain morphogenesis. For instance, dampening *Hes1* oscillations in mice by removing its introns resulted in embryos with smaller brains than WT (Ochi et al., 2020). By quantifying Phospho-Histone H3 (Ph3) expression, the authors showed that these intron-less *Hes1* mutant embryos had slightly fewer mitotic cells in the ventral telencephalon than WT while the number of apoptotic cells detected with Caspase3 staining had increased. These observations could explain smaller brains in the mutant. However, intron-less *Hes1* also had lower levels of *Hes1* mRNA and HES1 protein relative to WT. To separate the effects of altering dynamics from levels, Ochi et al. (2020) used $Hes1^{+/-}$ (hemizygous) embryos that also had lower levels of *Hes1* mRNA and HES1 protein than WT. In the $Hes1^{+/-}$ embryos, the period of *Hes1* oscillations was the same as WT. Even though the amplitude of *Hes1* oscillations in $Hes1^{+/-}$ was lower than WT, it was higher than the amplitude in the intron-less *Hes1* when considered relative to the mean expression value. Furthermore, unlike the intron-less *Hes1*, $Hes1^{+/-}$ exhibited no significant defects in brain size, proliferation or apoptosis. Hence, these defects were specifically associated with *Hes1* dynamics (Ochi et al., 2020).

Less drastic shifts in the type of HES oscillations also impact neural development. For instance, in zebrafish hindbarin, a transition between noisy and aperiodic fluctuations to oscillatory expression of *her6* is critical in neural differentiation (Soto et al., 2020). Mutations in the *her6* miR-9 binding site (MBS) that hinder the binding of miR-9 to the *her6* 3' Untranslated region (UTR), prevented this transition in dynamics and resulted in down regulation of early neural commitment genes such as *neuroD4* and *elavl3*. Furthermore, this manipulation was also accompanied with failure of neural progenitors to down regulate Her6 which is another requirement for progression towards neural differentiation (Soto et al., 2020).

In the previous chapter (Chapter 5), I showed that destabilisation of Her6 in Her6-Venus-PEST (HVP) lowered its expression levels in most but not all cells, leading to increased Her6 heterogeneity and larger cell-cell differences relative to Her6-Venus (HV). These effects in HVP were in part associated with increased oscillations and higher fold change at single cell level. Furthermore, HVP cells were prone to more rapid down regulation of Her6. Based on the evidence in previous literature, I predicted that the HVP single cell and cell population traits have developmental consequences which I sought to reveal in this chapter based on the following aims:

1. Examination of telencephalon size and growth using *foxg1* expression;
2. Assessment of changes in cell proliferation;
3. Assessment of DV regionalisation in the telencephalon;
4. Quantitative comparison of expression levels of selected global and DV localised genes with Quantitative polymerase chain reaction (qPCR).

6.2 Results

6.2.1 Measurement of telencephalon size reveals potential alteration of telencephalon growth in HVP

It was established in Chapter 5 that Her6 expression and its dynamics are altered in HVP. To determined if this has a gross anatomical impact on the developing telencephalon, its size was measured during late stages of embryonic neurogenesis. For labelling the telencephalon, I relied on the expression of *foxg1* mRNA which is known to be expressed in the whole telencephalon except for the roof plate (Danesin et al., 2009).

For detection *foxg1* mRNA expression, I opted for using chromogenic In-situ hybridisation (ISH) as opposed to Fluorescent in-situ hybridisation (FISH). The reasoning behind this decision was two-fold. Firstly, ISH is sensitive enough to detect marked changes in the size of an expression domain. Secondly, chromogenic ISH staining is more high-throughput due to the ease of imaging which allows for more samples to be analysed. For these experiments, I examined three embryonic stages: 24 and 30hpf roughly corresponded to the mid and final point of the live imaging experiments. 48hpf was selected as a late-stage representing the telencephalon after the window of live imaging but before drastic morphological changes in the telencephalon that result in its final characteristic everted morphology (Folgueira et al., 2012) (described in Chapter 1).

Hence, chromogenic ISH against *foxg1* was carried out in 24, 30 and 48hpf HV and HVP embryos (Fig 6.1,A). For each condition, 20 embryos were imaged in both lateral and transversal orientations. The depth and length of the telencephalon was measured in the lateral orientation and its width in the transversal orientation (Fig 6.1,B). Telencephalon volume was estimated by multiplying these values as a proxy for its size and statistically analysed with 2way ANOVA.

Telencephalon size was variable in all conditions. At 24hpf, the telencephalon in HVP embryos tended to be smaller but the difference between HV and HVP was not statistically significant (P=0.2965). There was a bigger tendency for smaller telencephalon in HVP at 30hpf as the P value decreased, but this too was not significant (P=0.0806). By 48hpf, there was no tendency or significant difference between HV and HVP telencephalon sizes

(P>0.9999) (Fig 6.1,C). However, globally, both developmental stage (P<0.0001) and line (i.e HV vs HVP, P=0.0055) significantly contributed to variation in the data (Fig 6.1,C).

Next, I compared the change in telencephalon size (i.e. growth) between HV and HVP. In HV embryos, between 24 and 30hpf, telencephalon grew significantly larger (P=0.0052). But no significant change in size occurred between 30 and 48hpf (P=0.9950). However, in HVP, the telencephalon size increased significantly between 24 and 30hpf (P=0.0347) and also between 30 and 48hpf (P=0.0251) (Fig 6.1,D). In short, even though HVP telencephalon was slightly smaller than HV at 24 and 30hpf, it appeared to catch up by 48hpf, perhaps due to accelerated growth rate.

6.2.2 The mode of cell divisions may be altered in HVP while the quantity of proliferation is not affected

Her6 is predicted to be a regulator of actively proliferating neural progenitors. Therefore, I suspected that the changes in Her6 expression dynamics and the slight differences in telencephalon growth may be accompanied with changes in cell division. To examine this hypothesis, I first used Venus (i.e. Her6) expression from the single cells tracked from HV and HVP time-course pairs (spanning the developmental time between 20-30hpf) and grouped them by their cell division status. For this, two main assumptions were made: 1- The presence of detectable Her6 expression is a hallmark of progenitor state while Her6 down regulation is seen when cells move toward differentiation; 2- Termination of a single cell Venus track is predominantly caused by absence of detectable Venus (Her6) in that cell. Therefore, when a single Venus track terminated prior to the end of the time-course, it was deemed to be moving toward differentiation.

Using these assumptions, I categorised the divisions. Divisions where both daughter cells could be tracked until the end of the time-course were used as proxy for symmetric division where both daughter cells remained progenitors (Symmetric - Progenitor). Divisions that gave rise to one daughter that could be tracked to the end of the time course and one that could not, were classified as asymmetric where one daughter remained a progenitor while the other moved towards differentiation (Asymmetric). Lastly, divisions where neither daughter cell could be tracked to the end of the movie, were categorised as symmetric where both daughters moved towards differentiation (Symmetric - Neurogenic) (Fig 6.2,A).

Over all, three HV and HVP pairs had been imaged live and their single cells were tracked. However, one pair was imaged only for 6 hours and as a result, dividing tracks were not long enough to be reliably categorised based on these criteria. Therefore, single cell expression of Venus from only two pairs was examined. While the percentage of dividing tracks was different between experiments, it was comparable between HV and HVP within each experiment (Fig 6.2,B). In these dividing cells, the percentage of Symmetric-Neurogenic

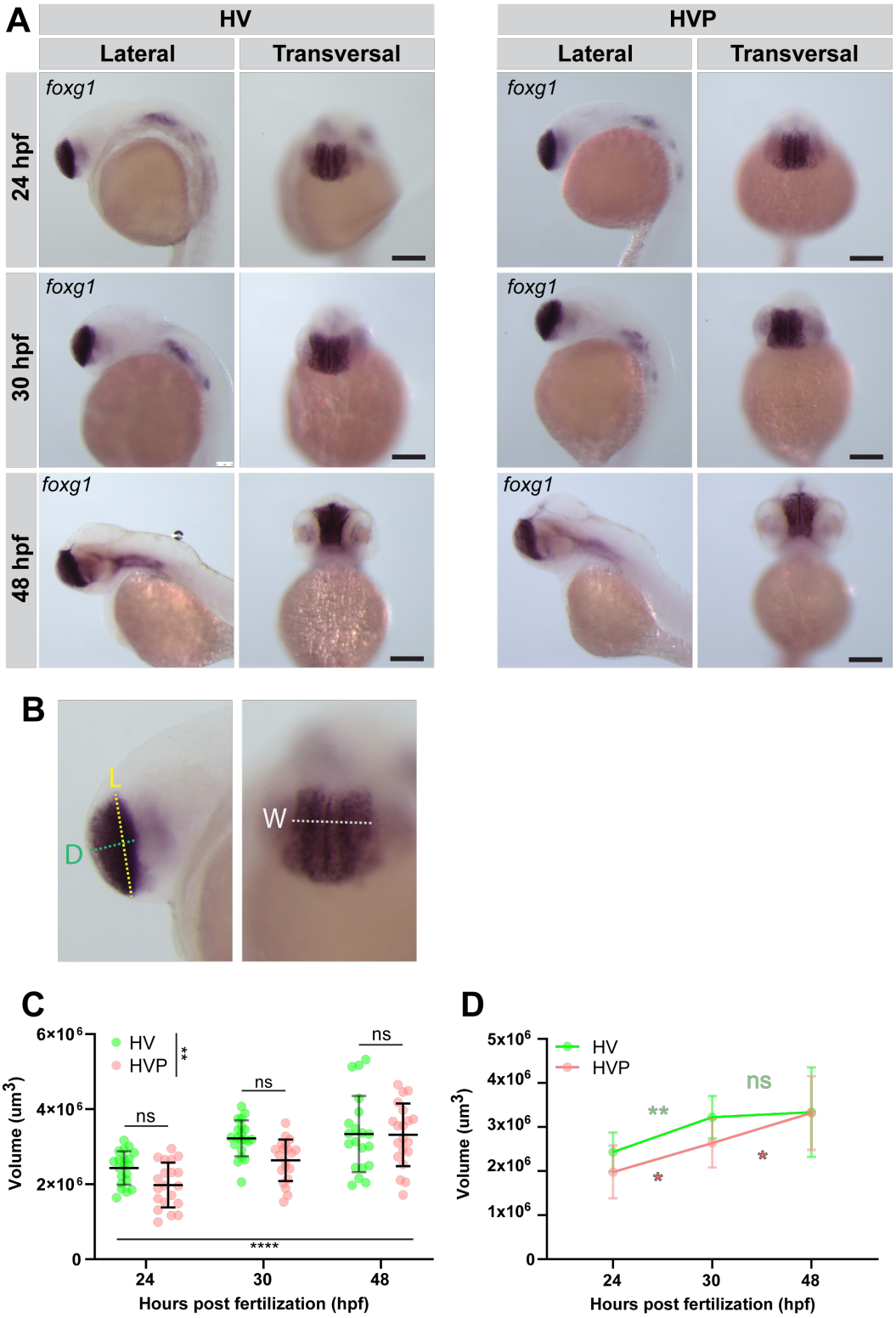

Figure 6.1: **Measuring telencephalon size using In-situ hybridisation against *foxg1*.** **(A)** In-situ hybridisation against *foxg1* in 24, 30 and 48hpf HV and HVP embryos. Scalebar=150µm. **(B)** Showing how telencephalon length, depth and width were measured based on *foxg1* staining. D: Depth, L: Length, W: Width. **(C)** Telencephalon volume was estimated by multiplying LxDxW measurements. HVP volumes at 24 and 30hpf were slightly lower than HV but not at 48hpf. None of these comparisons were statistically significant (ns). Globally, both developmental stage (****) and line to a lesser extent (**) were significant sources of variation in the data. **(D)** Shows a representation of telencephalon growth between 24 and 48hpf. HV telencephalon grew significantly larger between 24 and 30hpf (**). However, it did not grow further between 30 and 48hpf (ns). HVP telencephalon started at lower volume at 24hpf but also grew significantly by 30hpf (*). In HVP, telencephalon grew significantly also between 30 and 48hpf (*). 2way ANOVA with multiple comparisons, (ns): $P > 0.05$, (*): $P \leq 0.05$, (**): $P \leq 0.01$, (***): $P \leq 0.001$, (****): $P \leq 0.0001$.

.

divisions did not have a consistent trend between HV and HVP (Fig 6.2,C). However, the percentage of Symmetric-Progenitor divisions in HVP was lower than HV in both experiments (Fig 6.2,D). This is while the percentage of Asymmetric divisions was slightly higher in HVP in both experiments (Fig 6.2,E). In short, these observations implied that a decline in Symmetric-Progenitor divisions in HVP may contribute to the depletion of Her6 expressing cells while the slight increase in Asymmetric divisions may point to increased differentiation in HVP.

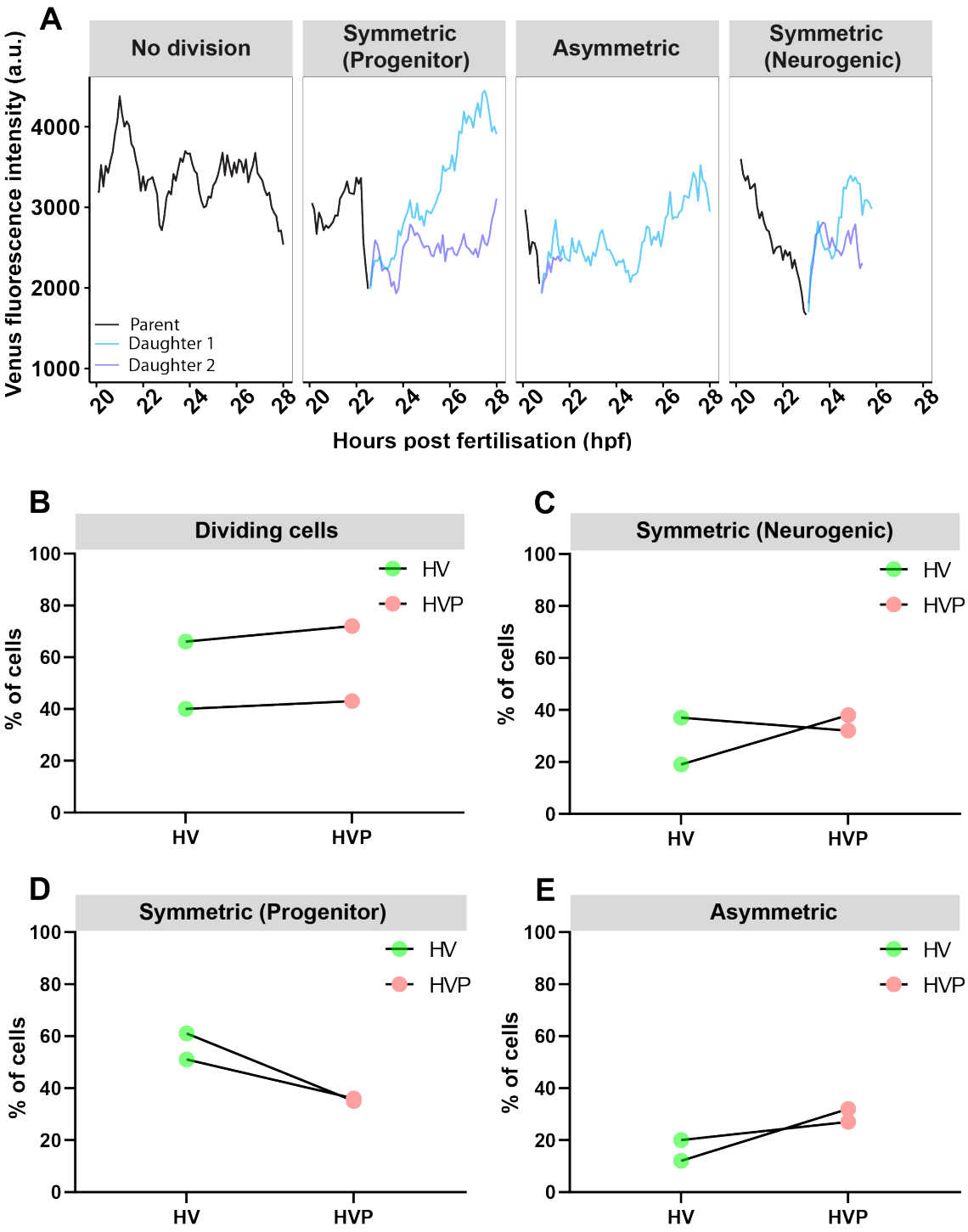

Figure 6.2: **Comparing mode of cell division between HV and HVP single tracked cells.** **(A)** Categorisation of single cell tracks based on division status in experiments 2 and 3. Cell divisions where both daughter cells could be tracked to the end of the time course were categorised as symmetric divisions that renew progenitors. Divisions where only one daughter cell could be followed to the end of the time course were categorised as asymmetric. Divisions where neither daughter cell could be tracked to the end of the time course were deemed as symmetric divisions that give rise to two differentiating cells. **(B)** The percentage of dividing cells is comparable between HV and HVP within each experiment (HV2-HVP2: 40-43%, HV3-HVP-3: 66-72%). **(B)** The percentage of symmetric (neurogenic) divisions relative to total number of divisions in each experiment was comparable between HV and HVP in experiment 2 but not 3 (HV2-HVP2: 37-32%, HV3-HVP-3: 19-38%). **(D)** The percentage of symmetric (progenitor) divisions relative to total number of divisions in HVP was consistently lower than HV in both experiments (HV2-HVP2: 51-36%, HV3-HVP-3: 61-35%). **(E)** The percentage of asymmetric divisions relative to total number of divisions in HVP was consistently higher than HV in both experiments (HV2-HVP2: 12-32%, HV3-HVP-3: 20-27%).

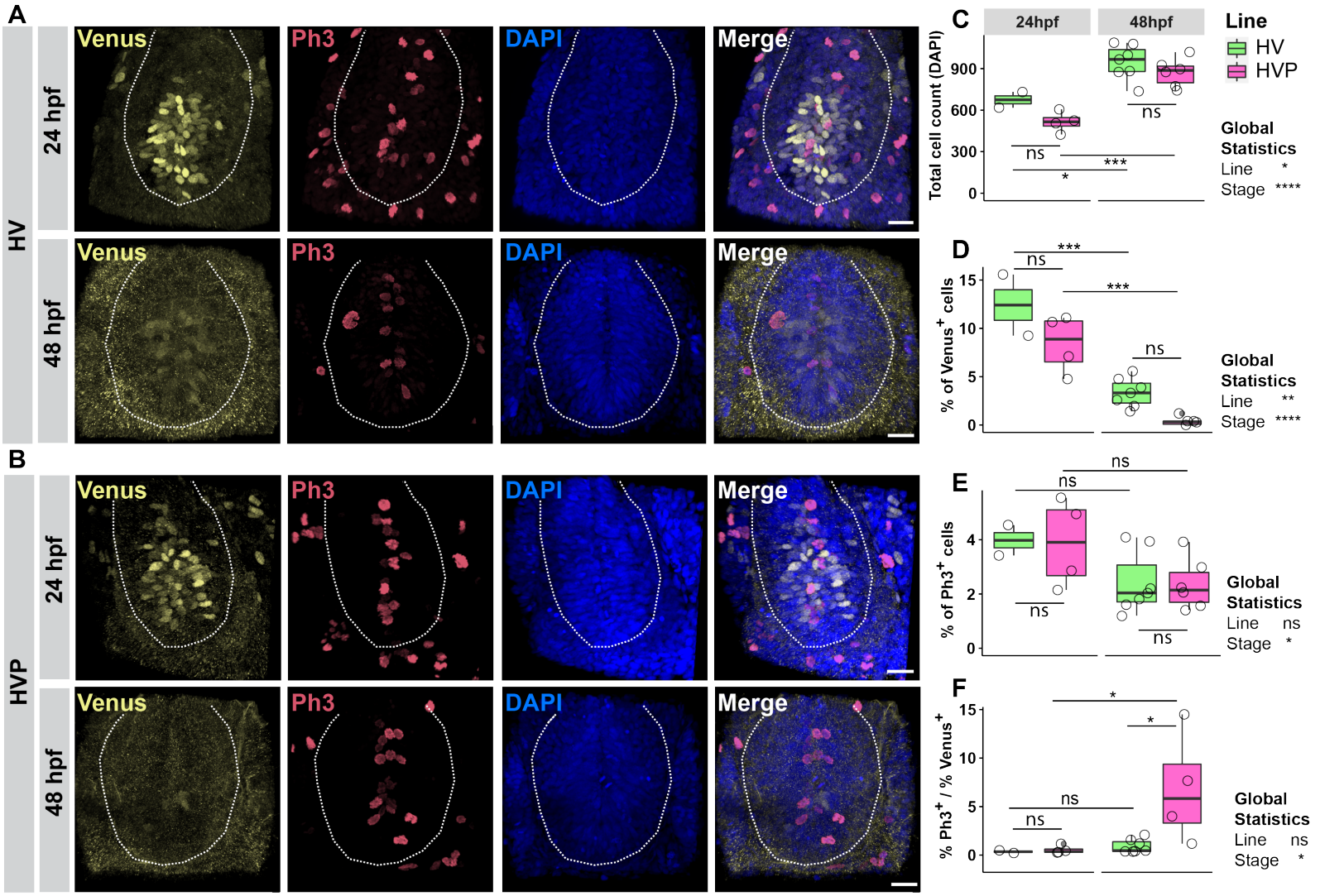

Figure 6.3: **Comparing the presence of mitotic cells in HV and HVP by Immunofluoresence against Venus and Ph3. Caption on the following page →**

Figure 6.3: **(A & B)** 3D reconstruction of z-stacks of the telencephalon in transversal view. Immunofluoresence labeling against Venus (labeling Her6) and Ph3 accompanied by DAPI staining in HV and HVP embryos at 24 and 48hpf. White dotted line shows the visible boundaries of the telencephalon. Venus was abundantly detected at 24hpf in HV and slightly less abundant in HVP. By 48hpf, the levels of Venus expression and the number of cells appeared reduced in HV and practically absent in HVP. Ph3 staining was focused at the midline in all conditions and declined slightly between 24 and 48hpf in HV and HVP but strongly present in both by 48hpf. Scalebar = 20µm. **(C)** The total number of cells (i.e. nuclei) detected based on DAPI signal within the boundaries of the telencephalon. At 24hpf, the number of cells in HVP (Median = 515) were slightly lower than HV (Median = 674) but this was not significant (ns). Between 24 and 48hpf, the number of cells increased significantly in HV (Median = 967) (*) and more so in HVP (Median = 886) (****). In comparison to 24hpf, total number of cells were more similar between HV and HVP at 48hpf (ns). Globally, both line (*) and to a greater extent, developmental stage (****) contributed significantly to variability in total number of cells in telencephalon. **(D)** Shows the percentage of Venus$^+$ cells in HV and HVP between 24 and 48hpf. At 24hpf, HVP embryos had tendency for lower percentage of Venus$^+$ cells (Median = 8.9%) than HV (Median = 12.4%) but this was not statistically significant (ns). This percentage declined significantly in HV and HVP by 48hpf (***). At 48hpf, HVP embryos retained tendency for lower percentage of Venus$^+$ cells (Median = 0.32%) than HV (Median = 3.3%) but this difference was not statistically significant (ns). Globally, both line (**) and to a greater extent, developmental stage (****) were significnat sources of variation in the percentage of Venus$^+$ cells. **(E)** Shows the percentage of Ph3$^+$ cells in HV and HVP between 24 and 48hpf. HV (Median = 4.0%) and HVP embryos (Median = 3.9%) had comparable percentage of Ph3$^+$ cells at 24 hpf (ns). This percentage declined in HV and HVP between 24 and 48hpf but the change was not significant (ns). At 48hpf, the percentage of Ph3$^+$ cells remained similar between HV (Median = 2.0%) and HVP (Median = 2.1%) (ns). Globally, developmental stage was a significant source of variation in the percentage of Ph3$^+$ cells (*) but line was not (ns).**(F)** Shows percentage of Ph3$^+$ cells relative to the percentage of Venus$^+$ cells. This ratio was comparable between HV (Median = 0.35) and HVP (0.37) (ns). Ratio of Ph3$^+$ cells to Venus$^+$ cells increased slightly but insignificantly in 48hpf HV (Median = 0.46) (ns) but drastically in 48hpf HVP (Median = 5.8) (*). At 48hpf, this ratio was significantly higher in HVP (*). Globally, developmental stage was a significant source of variation in the ratio of percentage of Ph3$^+$ cells to Venus$^+$ cells (*) but line was not (ns). 2way ANOVA with multiple comparisons, (ns): $P > 0.05$, (*): $P \leq 0.05$, (**): $P \leq 0.01$, (***): $P \leq 0.001$, (****): $P \leq 0.0001$.

The examination of divisions in single cell tracks was limited to the duration of live imaging. Furthermore, even though the criteria for categorising divisions were based on a sound hypothesis, their effectiveness was influenced by technical variability in single cell tracking. Therefore, to complement these observations with a more global assessment of cell division, I used Immunofluoresence (IF) to simultaneously visualise Venus, the mitosis marker Phospho-Histone H3 (Ph3) and cell nuclei with DAPI in HV and HVP embryos.

In 24hpf HV, Venus was expressed ventrally in the telencephalon which was consistent my previous observations (Chapters 3 and 5) and Ph3$^+$ (mitotically active) cells were predominantly localised at the midline. At 48hpf, the number and intensity of Venus expressing cells in HV was diminished and fewer cells appeared Ph3$^+$ at the midline (Fig 6.3,A). In 24hpf HVP, fewer cells were Venus$^+$ relative to 24hpf HV but there was no visually detectable difference in the presence of Ph3$^+$ cells. By 48hpf, very little Venus expression was detected in HVP while the expression of Ph3 persisted (Fig 6.3,B).

To quantify these observations, the Imaris spot function was used to automatically detect the majority of visible nuclei in the telencephalon using the DAPI signal. Venus$^+$ and Ph3$^+$ cells were determined by setting an intensity threshold based on signal intensity distribution in each individual embryo which was verified manually. 2way ANOVA was used to statistically assess the results. Relative to HV, the total number of cells detected in 24hpf HVP embryos tended to be lower, but this was not statistically significant

(P=0.4800). The total number of cells increased significantly at 48hpf in HV (P=0.0354) and HVP (P=0.0006) embryos. Even though at 48hpf, HVP embryos retained the slight insignificant tendency for fewer cells than HV, the total cell count at this stage was more similar between HV and HVP, reflected in the P value (P=0.7834). These observations were in line with the measurements of telencephalon size where there was a bigger difference between HV and HVP at 24hpf than at 48hpf (Fig 6.1,C&D). When the whole data was considered globally, line (HV or HVP) was a significant source of variation in the total number of cells (P=0.0489) but the contribution from stage (24 or 48hpf) was more significant (P<0.0001) (Fig 6.3,C).

As expected based on live imaging of HV and HVP embryos (Chapter 5), in 24hpf HVP embryos, lower proportion of cells were Venus$^+$ relative to HV but this difference was not statistically significant (P=0.2050). The percentage of Venus$^+$ cells decreased significantly at 48hpf in HV (P=0.003) and HVP (P=0.0001). At 48hpf, HVP embryos had proportionally fewer Venus$^+$ cells than HV but this difference was not statistically significant (P=0.1073). However, when the whole data was considered globally, there was a significant contribution from line to the variation in the percentage of Venus$^+$ cells (P=0.0044) but stage contributed more significantly (P<0.0001) (Fig 6.3,D).

There was no significant difference in the percentage of Ph3$^+$ cells between HV and HVP at 24hpf (P>0.9999). A smaller proportion of cells expressed Ph3 at 48hpf in both HV and HVP but this decline was not statistcally significant (P=0.5291 & P=0.3322, respectively). At 48hpf, there was no tendency or statistical difference in the percentage of Ph3$^+$ cells between HV and HVP (P>0.9999). Globally, there was no significant contribution from line to the variations in the percentage of Ph3$^+$ cells (P=0.9012) and the only source of variability was developmental stage (P<0.0001) (Fig 6.3,E).

Next, I calculated the proportion of Ph3$^+$ cells relative to Venus$^+$ cells. At 24hpf, the Ph3$^+$/Venus$^+$ ratio was less than 1 in both HV (Median = 0.35) and HVP (Median = 0.37) (P>0.9999), denoting that at this stage, Venus$^+$ cells were more abundant relative to the Ph3$^+$ cells. In HV, this ratio increased slightly but insignificantly at 48hpf (Median=0.46, P>0.9999). However, in 48hpf HVP, the Ph3$^+$/Venus$^+$ ratio was significantly higher than 24hpf HVP (Median=5.8, P=0.0442), denoting higher abundance of the Ph3$^+$ cells relative to Venus$^+$ cells. Hence, at 48hpf, the Ph3$^+$/Venus$^+$ ratio in HVP was significantly higher than HV (P=0.0308). At a global level, there was a tendency but no significant contribution from line to the variation in the Ph3$^+$/Venus$^+$ ratio (P=0.0635) but there was a significant contribution from developmental stage (P=0.0401) (Fig 6.3,F).

In summary, these observations suggested that despite the potential changes in the mode of division in Her6 expressing cells and the depletion of Her6 in HVP, cell proliferation was not globally depleted. Therefore, alternative mechanisms may allow the retention of proliferative ability and perhaps accelerate telencephalon growth between 24-48hpf.

6.2.3 Comparing regional organisation of the telencephalon in HV and HVP

In previous sections, I showed that relative to HV, growth rate of the telencephalon was slightly accelerated in HVP. This was accompanied by a potential increase in the proportion of Asymmetric divisions in Venus (Her6) positive cells in expense of Symmetric-Progenitor divisions. However, the overall quantity of proliferative cells did not appear to be altered in HVP. I suspected that the retention of proliferative cells may be due to expansion of dorsal and ventral fate determination markers, *ngn1* and *ascl1*, respectively, which have been proposed to be expressed in mitotically active cells in the embryonic thalamus (Schmidt et al., 2013). Therefore, I examined the organisation of the telencephalic domains.

Using Fluorescent in-situ hybridisation (FISH), I labeled *her6* mRNA expression domain along with the mRNAs of early post-mitotic differentiation marker *elavl3* (Fig 6.4,A), the ventral (sub-pallial) fate marker *ascl1a* (Fig 6.4,B) and the dorsal (pallial) fate marker *ngn1* (Fig 6.4,C) in 20, 24 and 28hpf HV and HVP embryos, corresponding to the starting, mid and end point stages of live imaging. All the markers tested were expressed in comparable positions between HV and HVP. Since the outcome was similar between the different stages, only 24hpf is presented here.

At 24hpf, *her6* mRNA was focused anteriorly in the medial region of ventral telencephalon but the size of its expression domain was smaller in HVP in comparison to HV (Fig 6.4,A-C). *elavl3* expression was seen more laterally in two lines surrounding but not limited to the *her6* expression domain. Relative to HV, *elavl3* expression appeared reduced in some HVP embryos analysed (Fig 6.4,A). *ascl1a* was expressed ventrally behind the *her6* domain (Fig 6.4,B) whereas *ngn1* was localised dorsally and above the *her6* expression domain. *ngn1* expression domain appeared expanded in some but not all HVP embryos (Fig 6.4,C).

For a quantitative analysis, the volume of each expression domain was measured with the surface tool on Imaris and statistically compared between HV and HVP using Mann-Whitney test. The *her6* expression domain in HVP was significantly smaller than HV (P=0.0286). The size of the *elavl3* domain in HVP was slightly smaller than HV but not statistically different (P=0.2000). The size of the *ascl1a* expression domain was highly variable in HV and HVP with a tendency to be smaller in HVP. But the difference in the size of the *ascl1* domain between HV and HVP was not statistically significant (P=0.6286). *ngn1* expression domain in HVP was also slightly but insignificantly smaller than HV (P=0.4857) (Fig 6.4,D).

It is important to note that due to lack of a suitable marker in this experiment, I was unable to measure the telencephalon size. Hence, none of the measurements were normalised to telencephalon size. I suspected that the tendency for smaller *elavl3, ascl1a* and *ngn1* expression domains in HVP was, at least in part, related to the tendency for smaller telen-

cephalon size in 24hpf HVP (Fig 6.1,C). Additionally, the quality of these staining was sub-optimal and there was a great deal of variation between embryos even within the same group (discussed further in Discussion). Therefore, I limited my conclusions to the positional relationship between the different domains and cautious suggestions. That is to say, I concluded that at least in 24hpf HVP, the organisation of the telencephalon and the size of the pallium and sub-pallium were *largely* unaffected and followed similar organisation predicted in WT (Fig 6.4,E, Also discussed in chapter 3).

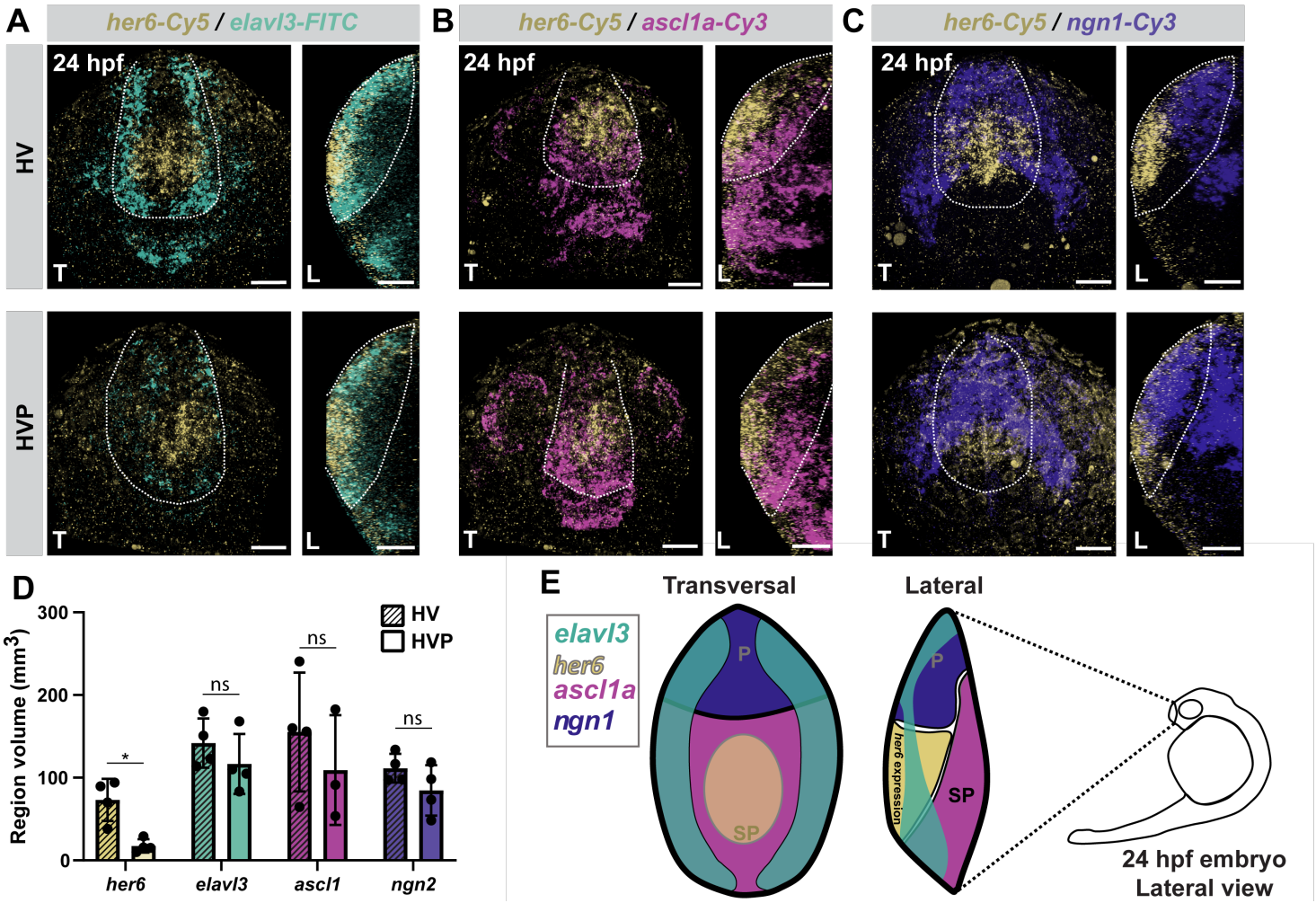

Figure 6.4: **Comparing telencephalon Dorsoventral organisation between HV and HVP with Fluorescent in-situ hybridisation (FISH).**
Caption on the following page →

Figure 6.4: **(A-C)** Maximum intensity projection of FISH in 24hpf HV and HVP embryos in transversal and lateral views. In all images, Dorsal is at the top and Vantral at the bottom. In lateral images, Anterior is to the left and Posterior to the right. **(A)** *her6* was expression was focused anteriorly in the medial region of the ventral telencephalon in HV and HVP. Its domain was smaller in HVP. *elavl3* was expressed more laterally along the DV axis of the telencephalon. *elavl3* domain also appeared diminished in HVP but not in all embryos. **(B)** *ascl1* was expressed posterior to *her6* in the ventral telencephalon. The size of the domain and its position was comparable between HV and HVP. **(C)** *ngn1* was expressed dorsally with respect to *her6* in the dorsal telencephalon. The size of the domain appeared expanded in some but not all HVP embryos and its position was comparable between HV and HVP. **(D)** Measurement of expression domain volume. *her6* domain in HVP (M=17.5mm^3, SD=±8.1) was significantly smaller than HV (M=73mm^3, SD=±25.5) (*). Tha *elavl3* domain in HVP (M=116.6mm^3, SD=±36.2) tended to be smaller than HV (M=141.9mm^3, SD=±29.9) (ns). Size of the *ascl1a* domain was variable in HV (M=155.2mm^3, SD=±71.9) and HVP (M=109.2mm^3, SD=±66.3) with a tendency to be smaller in HVP (ns). *ngn1* domain in HVP (M=84.7mm^3, SD=±30.5) also had a tendency to be smaller than HV (M=111.5mm^3, SD=±17.4) (ns). **(E)** Schematic diagram showing the organisation of dorsal (pallium) and ventral (sub-pallium) and their markers with respect to *her6* at 24hpf as seen in HV and HVP. Scalebar=40µm, T: Transversal, L: Lateral, P: Pallium, SP: Sub-pallium

6.2.4 Quantitative assessment of dorsal (pallial) and ventral (sub-pallial) telencephalon neural differentiation genes suggest increased neural differentiation in HVP

FISH was informative with respect to the positioning and size of the dorsal and ventral telencephalon. However, these measurements were not normalised relative to total telencephalon size. Furthermore, no conclusions could be made about levels of genes expression since FISH is based on signal saturation and therefore not quantitative. For a reliable quantitative assessment of gene expression at the mRNA level, Complementary DNA (cDNA) libraries were generated from dissected telencephalons of 24 and 48hpf HV and HVP embryos. Using Taqman reagents, the expression levels of several genes relevant in telencephalon development were assessed using Quantitative polymerase chain reaction (qPCR). For ease of visualising the statistical summaries, the comparisons between 24 and 48hpf are presented in figure 6.6 and the comparisons between HV and HVP are presented separately in figure 6.5. All statistics reported in this section are based on 2way ANOVA with multiple comparisons.

her6 expression at 24hpf HVP was slightly but insignificantly lower than HV (P=0.9988) (Fig 6.5,A). Its expression decreased between 24 and 48hpf in HV and HVP but the change was not statistically significant in either (P=0.1388 & P=0.4095, respectively) (Fig 6.6,A). At 48hpf, there was no strong tendency or statistical difference between HV and HVP (P=0.9999) (Fig 6.5,A). *elavl3* levels at 24hpf were similar between HV and HVP (P=0.9938) (Fig 6.5,B). At 48hpf, it was expressed at significantly lower levels in both HV and HVP (P<0.0001) (Fig 6.6,B) and there was no difference between HV and HVP (P=0.8463) Fig 6.5,B).

The telencephalon patterning gene *foxg1* was expressed at comparable levels between HV and HVP at 24hpf (P=0.9973) (Fig 6.5,C). Between 24 and 48hpf, its levels were significantly reduced in HV (P<0.0001) and to a lesser extent in HVP (P=0.0001) (Fig 6.6,C). Hence, at 48hpf, *foxg1* levels in HVP were significantly higher than HV (P=0.0065) (Fig 6.5,C). Expression levels of the cell cycle inhibitor *p27* at 24hpf were slightly higher in

HVP than HV but this was not significant (P=0.2173) (Fig 6.5,D). This genes was slightly but insignificantly upregulated between 24 and 48hpf in HV (P=0.2435) but did not change in HVP (P>0.9999) Fig 6.6,D). Therefore, at 48hpf, *p27* was expressed at comparable levels between HV and HVP (P>0.9999) (Fig 6.5,D).

Overall, this data indicated that between 24 and 48hpf, the expression of the neural progenitor, early post-mitotic neuron and early telencephalon patterning genes examined were depleted largely to the same extent in HV and HVP. Based on this, I hypothesised that differences in HV and HVP may lie in neuronal fate determination and terminally differentiated neurons. This hypothesis was addressed by quantifying the expression of genes associated with specific neuronal fates.

Four dorsally expressed genes associated with glutamatergic neuronal fates were examined. At 24hpf, *ngn1* expression in HVP was slightly lower than HV, but this was not statistically significant (P=0.1619) (Fig 6.5,E). Between 24 and 48hpf, its expression was significantly lowered in HV (P=0.0005) and to a lesser extent in HVP (P=0.0347) (Fig 6.6,E). By 48hpf, *ngn1* levels were comparable between HV and HVP (P>0.9999) (Fig 6.5,E). *emx3* levels at 24hpf HVP were slightly but insignificantly higher than HV (P=0.2108) (Fig 6.5,F). The expression of this genes strongly decreased between 24 and 48hpf in HV and HVP (P<0.0001) (Fig 6.6,F). At 48hpf, HVP embryos retained their mild tendency for higher *emx3* expression levels relative to HV, but this was not significant (P=0.0989) (Fig 6.5,F). Expression of *tbr1* was comparable between HV and HVP at 24hpf (P=0.9987) (Fig 6.5,G). It was slightly but insignificantly reduced between 24 and 48hpf in HV (P=0.6903) but to a lesser extent in HVP (P=0.9989) (Fig 6.6,G). At 48hpf, there was a small but insignificant tendency for higher *tbr1* expression in HVP in comparison to HV (P=0.5586) (Fig 6.5,G). At 24hpf, the expression of the terminal glutamatergic neural marker *vglut2a* in HVP was slightly but insignificantly higher than HV (P=0.4729) (Fig 6.5,H). At 48hpf, its expression was reduced in HV (P=0.0835) but not in HVP (P=0.9559) (Fig 6.6,H). This resulted in a significant difference in its levels between HV and HVP at 48hpf (P=0.0088) (Fig 6.5,H). Combined together, it appeared that the changes in Her6 expression and dynamics in HVP had a cumulative effect on pallial fates which was most pronounced in the terminally differentiated neurons.

Four genes expressed in the ventral telencephalon and related to GABAergic differentiation were also assessed. At 24hpf, *ascl1a* expression levels were comparable between HV and HVP (P>0.9999) (Fig 6.5,I). Between 24 and 48hpf, its levels were reduced significantly in both to a similar extent (P<0.0001) (Fig 6.6,I). Hence, *ascl1a* expression levels at 48hpf were the same between HV and HVP (P=0.9676). *dlx5a* levels were also comparable between HV and HVP at 24hpf (P=0.9988) (Fig 6.5,J). By 48hpf, the expression levels of this gene was slightly lower in HV (P=0.5382) but not in HVP (P>0.9999) (Fig 6.6,J). As a result, at 48hpf, *dlx5a* expression levels in HVP were slightly but insignificantly higher than HV (P=0.3501) (Fig 6.5,J). The expression of *gad* genes that are terminal GABAergic neu-

ron markers was also examined. At 24hpf, *gad1* was expressed at similar levels between HV and HVP (P>0.9999) (Fig 6.5,K). By 48hpf, its expression levels increased in both HV (P<0.0001) and HVP (P<0.0001) (Fig 6.6,K). At 48hpf, *gad1* levels in HVP were significantly higher than HV (P=0.0231) (Fig 6.5,K). *gad2* followed a pattern similar to *gad1*. It was expressed at comparable levels between HV and HVP at 24hpf (P=0.8174) (Fig 6.5,L). Between 24 and 48hpf, its expression levels increased significantly in HV (P=0.0427) and more drastically in HVP (P<0.0001) (Fig 6.6,L). By 48hpf, *gad2* expression levels in HVP were significantly higher than HV (P<0.0001) (Fig 6.5,L). In short, even though there was no drastic change in sub-pallial commitment in HVP (i.e. *ascl1* expression), there was a cumulative and drastic effect on terminally differentiated GABAergic neurons.

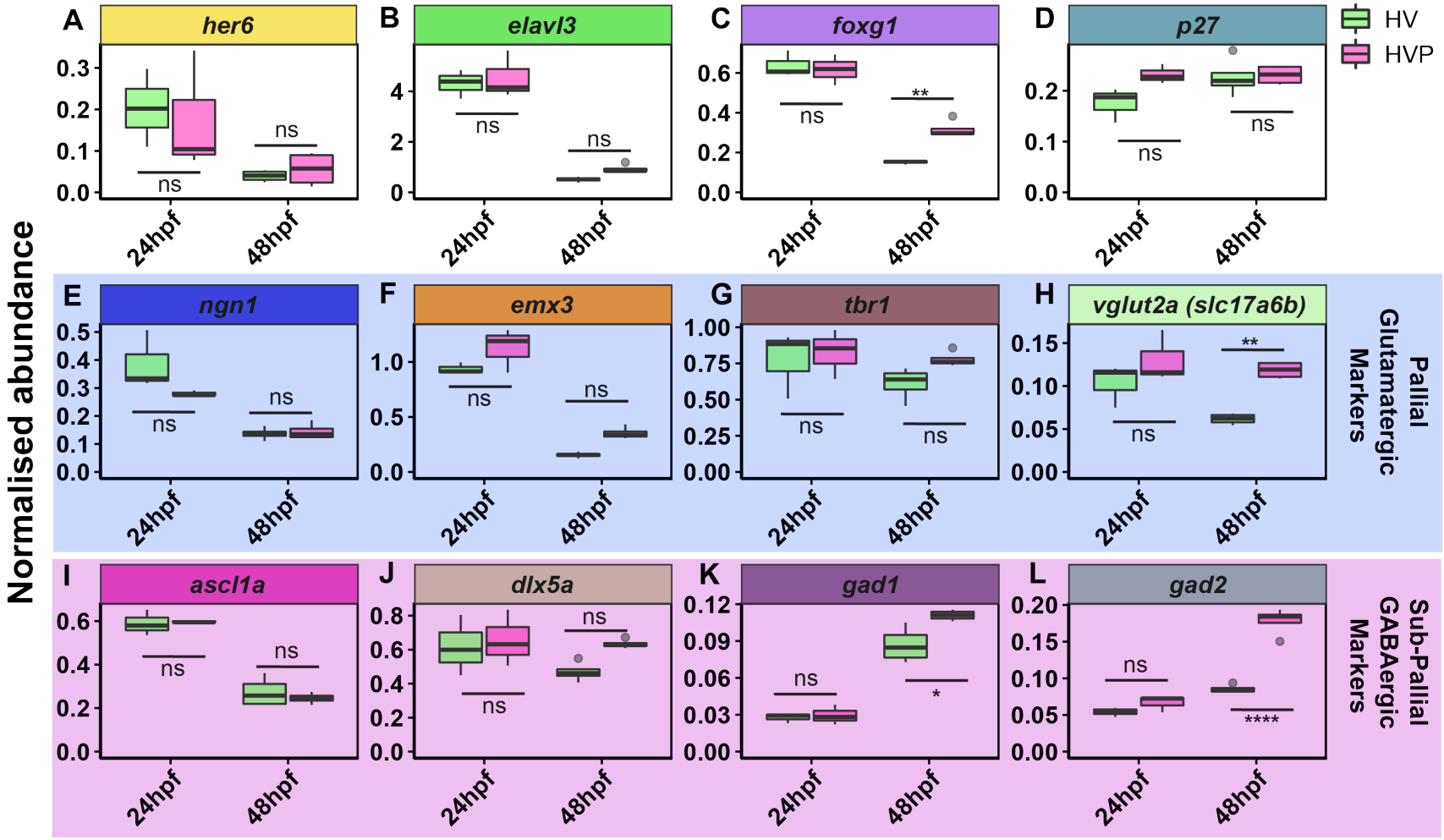

Figure 6.5: **Quantitative comparison of gene expression between HV and HVP at 24 and 48hpf. Caption on the following page →**

Figure 6.5: **(A)** At 24hpf, *her6* levels in HVP were slightly lower than HV (ns). At 48hpf, there was no tendency or difference in its levels between HV and HVP (ns). **(B)** At 24 and 48hpf, *elavl3* levels were not different between HV and HVP (ns). **(C)** At 24hpf, *foxg1* levels were comparable between HV and HVP (ns). At 48hpf, *foxg1* levels in HVP were significantly higher than HV (**). **(D)** At 24hpf, *p27* levels in HVP were slightly higher than HV (ns). At 48hpf, there was no tendency or difference in its levels between HV and HVP (ns). **(E)** At 24hpf, *ngn1* levels in HVP were slightly lower than HV (ns). At 48hpf, there was no tendency or difference in its levels between HV and HVP (ns). **(F)** At 24 and 48hpf, *emx3* levels in HVP were slightly higher than HV (ns). **(G)** At 24hpf, *tbr1* levels were comparable between HV and HVP (ns). At 48hpf, HVP had slight tendency for higher *tbr1* levels (ns). **(H)** At 24hpf, *vglut2a* levels in HVP were slightly higher than HV (ns). At 48hpf, its levels in HVP were significantly higher than HV (**). **(I)** At 24 and 48hpf, *ascl1a* levels were not different between HV and HVP (ns). **(J)** At 24 and more strongly at 48hpf, *dlx5a* levels in HVP were slightly higher than HV (ns). **(K)** At 24hpf, *gad1* levels were comparable in HV and HVP (ns). At 48hpf, its levels in HVP were significantly higher than HV (*). **(L)** At 24hpf, *gad2* levels in HVP were slightly higher than HV (ns). At 48hpf, its levels in HVP were significantly higher than HV (****). 2way ANOVA with multiple comparisons, (ns): $P > 0.05$, (*): $P \leq 0.05$, (**): $P \leq 0.01$, (***): $P \leq 0.001$, (****): $P \leq 0.0001$.

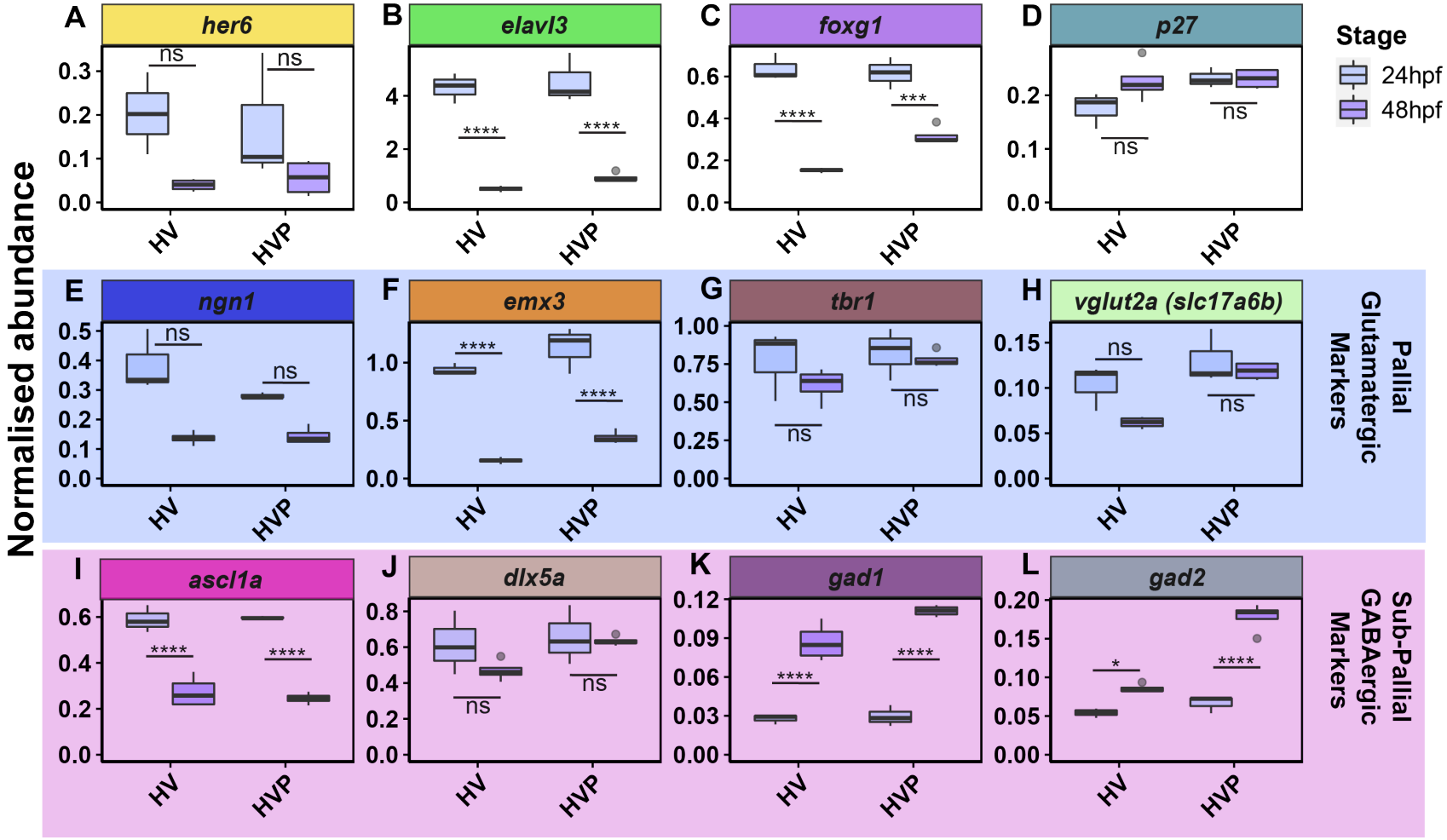

Figure 6.6: **Quantitative comparison of gene expression between 24 and 48hpf in HV and HVP. Caption on the following page →**

Figure 6.6: **(A)** *her6* levels decreased between 24 and 48hpf in HV and HVP but these changes were not statistically significant (ns). **(B)** *elavl3* levels at 48hpf were significantly lower than 24hpf in HV and HVP (****). **(C)** *foxg1* levels at 48hpf were significantly lower than 24hpf in HV (****) and to a slightly lesser extent in HVP (***). **(D)** *p27* levels at 48hpf were slightly but insignificantly higher than 24hpf in HV (ns) but not in HVP (ns). **(E)** *ngn1* levels at 48hpf were lower than 24hpf in HV and HVP but these differences were not statistically significant (ns). **(F)** *emx3* levels at 48hpf were significantly lower than 24hpf in HV and HVP (****). **(G)** *tbr1* levels at 48hpf were slightly but insignificantly lower than 24hpf in HV (ns) but not in HVP (ns). **(H)** *vglut2a* levels at 48hpf were slightly but insignificantly lower than 24hpf in HV (ns) but not in HVP (ns). **(I)** *ascl1a* levels at 48hpf were significantly lower than 24hpf in HV and HVP (****). **(J)** *dlx5a* levels at 48hpf were slightly but insignificantly lower than 24hpf in HV (ns) but not in HVP (ns). **(K)** *gad1* levels at 48hpf were significantly higher than 24hpf in HV and HVP (****). **(L)** *gad2* levels at 48hpf were significantly higher than 24hpf in HV (*) and more drastically in HVP (****). 2way ANOVA with multiple comparisons, (ns): $P > 0.05$, (*): $P \leq 0.05$, (**): $P \leq 0.01$, (***): $P \leq 0.001$, (****): $P \leq 0.0001$.

6.3 Discussion

Destabilisation of Her6 had marked effects on its expression and dynamics at single cell and population level (Chapter 5). HVP embryos are viable even as Homozygous (Hom) and survive to adulthood. Nonetheless, in this chapter, I have revealed that relative to HV, they have marked developmental changes in the telencephalon.

The HV telencephalon grew in size between 24 and 30hpf but then stabilised and did not change between 30 to 48hpf. This is while the HVP telencephalon was slightly smaller in earlier stages but grew steadily and reached the same size as HV at 48hpf. In hindsight, given the subtlety of the phenotype, perhaps FISH against *foxg1* would have provided less saturated signal and therefore, more precise volume measurements following confocal imaging. Nonetheless, this subtle change in growth rate could have been caused by alterations in proliferation, progression towards differentiation or increased apoptosis. Assessment of apoptosis between HV and HVP is missing from this work. However, I examined proliferation and differentiation, both of which were altered in HVP.

At a global level, proliferation was examined by IF against Ph3. It is important to note that determining the quantity of $Ph3^+$ cells in individual sub-regions of the telencephalon was beyond the scope of my experiment and was therefore not considered. Furthermore, the IF protocol used for Ph3 and Venus staining, damaged tissue integrity at 24hpf. As a result, the number of embryos analysed for this stage were low, especially in HV where only two embryos could be imaged, reducing the power of the analysis. But since the Venus IF output was comparable to snapshot live imaging of HV and HVP (chapter 5), the IF data was taken at face value.

The percentage of mitotically active ($Ph3^+$) and Her6 expressing ($Venus^+$) cells was reduced between 24 and 48hpf in both HV and HVP. In HV, the percentage of $Ph3^+$ cells in HV retained its ratio to Venus (Her6) at 24 and 48hpf but this was not the case in HVP. In HVP, by 48hpf, very little Her6 expression was detectable while cell proliferation was retained. This meant that even though Her6 expression was depleted at 48hpf HVP, the cells retained their proliferative ability and did not exit the cell cycle.

I hypothesised that this could be due to the expansion of fate determination markers that can maintain mitotic activity in cells (Schmidt et al., 2013). Using FISH, I showed that at least at 24hpf, expression of *ascl1* and *ngn1* had not expanded. Hence, they could not have maintained the levels of mitotically active cells.

However, this experiment had many shortcomings. Firstly, the quality of the staining was not optimal. The poor quality of staining may, at least in part, be associated to its large scale including three developmental stages for two lines. This posed a practical challenge and may have affected the duration of different steps in the protocol and the transitions between them. Secondly, the choice of Fast AiryScan microscopy which greatly enhanced imaging

speed also increased the resolution of imaging which did not result in smooth and uniform signal to examine expression pattern. Hence, in hindsight, Laser scanning microscopy (LSM) would have been a better choice. Last but not least, as both *ngn1* and *ascl1* probes were Digoxigenin (DIG) labelled, I did not combine them in the same staining combination which prevented me from making clear observations about the relationship between the two genes and how their domains may change with respect to on another. Lastly, in this experiment, 48hpf embryos in which the $Ph3^{+}$/$Venus^{+}$ was drastically different between HV and HVP were absent. Therefore, the hypothesis regarding potential changes in the size of *ngn1* and *ascl1* mRNA expression domains in HVP cannot be completely discarded. Alternatively, methods with single cell resolution such as Single molecule fluorescent in situ hybridisation (smFISH) can provide a much more detailed insight into the overlap between these different genes and how it may be altered at a cellular and tissue level.

Alternatively, the retention of proliferative ability may indicate compensation by other bHLH factor. Such compensation has been reported for mouse *Hes1*. While some earlier work claimed that *Hes1* deletion causes severe developmental defects (Ishibashi et al., 1995), later reports suggested that *Hes1* and *Hes5* knock-out mice ($Hes1^{-/-}$ and $Hes5^{-/-}$) develop normally (Hatakeyama et al., 2004). Although the cause of this discrepancy is unclear to me, both Ishibashi et al. (1995) and Hatakeyama et al. (2004) had reported upregulation of *Hes5* in $Hes1^{-/-}$ embryos (Ishibashi et al., 1995; Hatakeyama et al., 2004), suggesting that it was playing a compensatory role. Indeed in *Hes1*;*Hes5* double mutant, the structural integrity of the developing nervous system was defected, $nestin^{+}$ radial glial cells (progenitors) were depleted more rapidly than WT and proneural bHLH factors like *Delta-like 1 (Dll1)* and *Ascl1* were upregulated, pointing to premature differentiation. These double mutants also displayed a decreased abundance of $Ki67^{+}$ or mitotically active cells suggesting that *Hes* gene compensation also encompasses mitotic activity. These phenotypes were further exacerbated in the *Hes1*;*Hes3*;*Hes5* triple mutant (Hatakeyama et al., 2004).

Ochi et al. (2020) have also highlighted the importance of compensation in studying the mutant mouse embryos with intron-less *Hes1* with severely dampened oscillations. Except for slight upregulation of *Ascl1*, these embryos had no defects in expression of differentiation genes like TBR1 in the 6th cortical layer (dorsal telencephalon) or GAD65 in ventral telencephalon. However, the combination of intron-less *Hes1* mutant with $Hes5^{-/-}$, led to upregulation of neuronal genes like TUJ1 and TBR1, suggesting accelerated differentiation (Ochi et al., 2020). Interestingly, intron-less *Hes1* mutant in the *Hes3*;*Hes5* double mutant background no longer impacted cell death but still resulted in accelerated differentiation and microcephaly (Ochi et al., 2020).

My preliminary data from 20hpf embryos showed that *her9* (the other HES1 orthologue in zebrafish) was not widely expressed in the telencephalon in either HV or HVP while it was strongly expressed in the diencephalon, midbrain and hindbrain (Appendix 8.10).

Since at this stage, there was already a difference in Her6 expression between HV and HVP (Chapter 5), I conclude that *her9* is not playing a compensatory role at least at early stages. However, it is possible that *her9* or other *her* genes are ectopically expressed in the telencephalon at later stages in HVP to rescue cell proliferation. Indeed, Soto et al. (2020) have shown that *her9* is expressed in the telencephalon at 30-32hpf. Furthermore, the *Hes5* orthologues *her4.1* (Bai et al., 2010) and *her4.2* (Thisse et al., 2001) are both present in the developing telencephalon in partly overlapping domains with *her6* (based on my judgement). If these genes are partly compensating for Her6, it is likely that their removal would cause a reduction of mitotically active cells similar to reduction of $Ki67^{+}$ in *Hes1*;*Hes5* double mutant (Hatakeyama et al., 2004).

Even though compensation by other *her* genes may allow the retention of proliferative cells and recovery of telencephalon growth in HVP, it does not appear to alleviate all defects caused by Her6 destabilisation and its altered expression and dynamics. Ochi et al. (2020) reported only mild changes in expression of differentiation genes in the intronless *hes1* mutant as a result of compensation. However, altered Her6, alone, resulted in a small potential shift towards increased asymmetric divisions in expense of symmetric divisions that renew progenitors. This implied that while the quantity of mitotic cells is unaffected potentially due to compensation, the Her6 expressing cells may have altered mode of proliferation.

This determination of mode of division was based on hypothetical criteria that were prone to technical variability and therefore needed further verification. However, I was unable to do so based on the Ph3/Venus IF due to the nature of their expression. Ph3 labels cells in mitosis when nuclear membrane dissociates. Without the nuclear membrane, Her6 which is normally focused in the nucleus diffuses in the cytoplasm which makes its detection difficult in mitotic cells. Therefore, even though Ph3 was expressed within the Venus (i.e. Her6) expression domain, consistent with the role of Her6 as a progenitor regulator, their expression was not detected in the same cells. This posed a challenge in specifically determining the mitotic abilities of the $Venus^{+}$ cells based on IF. Especially, no information regarding the type of division could be extracted from snapshot expression of Ph3. Hence, Ph3 staining was not suitable to examine the potential changes in the mode of differentiation that was observed in single cell tracks.

Nonetheless, the reduction in Symmetric-Progenitor divisions in HVP could, at least partly, explain the more drastic depletion of $Her6^{+}$ cells in HVP which was observed by live imaging (chapter 5) and IF (Fig 6.2,A,B&D). Additionally, increased Asymmetric divisions in HVP could have been indicative of more differentiation events in HVP relative to HV. This was indeed consistent with the observation that the expression of genes associated with neural differentiation were altered in HVP.

The majority of genes that were examined by qPCR can represent a somewhat hierarchical gene network of patterning the telencephalon (*foxg1*), guiding stem-like neural progenitor

cells (*her6* expressing) to progenitors with specified fates (*ngn1* or *ascl1a* expressing) and then regulating young post-mitotic neurons (*elavl3* expressing) that move towards their specified fates (Schmidt et al., 2013). In the dorsal telencephalon, *emx3* expression is essential for glutamatergic specification. Morpholino KD of *emx3* downregulates *tbr1* (a post-mitotic marker of glutamatergic fates (Mione et al., 2001)) and the terminal glutamatergic marker *vglut2a* (Viktorin et al., 2009), but not *elavl3* of *foxg1*. In the ventral telencephalon, it is predicted that *dlx1a/2a*, *dlx5a/6a* and *gad1* represent the progression of GABAergic differentiation, downstream of *ascl1a* (MacDonald et al., 2010). Similar interactions between *Dlx1/2* and *Ascl1* have been described in sub-cortical (ventral telencephalic) specification of GABAergic neurons in mice (Yun et al., 2002).

foxg1 which is involved in telencephalon patterning (Danesin et al., 2009) was downregulated between 24 and 48hpf in both HV and HVP. But compared to 48hpf HV, its expression levels were significantly higher in HVP 48hpf. This was counterintuitive as *foxg1* has also been proposed as a progenitor marker in the telencephalon (Danesin et al., 2009). It is likely that my observation in HVP is related to *foxg1* function in ventral specification.

This gene is expressed in a gradient in the telencephalon with the highest levels of its expression focused ventrally (Toresson et al., 1998; Danesin et al., 2009; Viktorin et al., 2009; Kumamoto, Hanashima, 2017). Despite its expression in the whole telencephalon excluding only the roof plate (Jeong et al., 2007; Danesin et al., 2009), *foxg1* is more strongly associated with determination of ventral fates. As such, morpholino KD of *foxg1* leads to absence of ventral telencephalic markers like *dlx2* and expansion of dorsal markers like *emx3* (Danesin et al., 2009). Based on my observations, *her6* expression is more focused at the ventral telencephalon after 20hpf (Chapter 3).

Therefore, one may hypothesise that the ventral telencephalon is more severely affected in HVP, which could explain altered *foxg1* expression in 48hpf HVP. Based on the FISH observations, it appears that the patterning of the telencephalon and the organisation of its domains is largely unaffected at least at 24hpf. However, it is likely that the technical variability in this technique or the quantification method has masked changes in domain size and organisation. Furthermore, as mentioned earlier, I have not examined 48hpf embryos using FISH. Hence, I cannot exclude the possibility of telencephalic sub-regions having been affected.

Furthermore, qPCR technique lacks spatial information. Therefore, the changes in *foxg1* mRNA may be associated with the domain of its expression rather than its levels. The alternative methods that alleviate this issue have been discussed further below.

The genes associated with earlier stages of neuronal development like *ngn1*, *ascl1a* and *elavl3* were down regulated comparably in HV and HVP between 24 and 48hpf. Interestingly, despite the ventral focus of *her6* expression, its alterations in HVP affected the expression of late fate determination and terminal differentiation genes in both dorsal (pal-

lium) and ventral (sub-pallium) telencephalon. Genes involved in later stages of fate determination like *emx3* and *tbr1* (dorsal) and *dlx5a* (ventral) that were downregulated in HV between 24 and 48hpf, either downregulated less or not at all in HVP. This could be indicative of premature or prolonged period of fate determination and differentiation in HVP pallium and sub-pallium that could potentially lead to more neurons. However, having only examined two developmental stages for this experiment, I was unable to distinguish between premature or prolonged differentiation.

Surprisingly, *vglut2a* which is a terminal glutamatergic neuron marker and was expected to be upregulated between 24 and 48hpf in HV, followed the same trend as earlier genes. That is to say, its levels in 48hpf HV were lower than 24hpf HV while it did not drastically change in HVP between these two stages. Therefore, relative to HV, this gene had significantly stronger presence in HVP at 48hpf. This may be due to the sub-cellular localisation of *vglut2a* in synaptic vesicles (Takamori et al., 2001). Since extensive axonogenesis and tract formation takes place between 24 and 48hpf (Wilson et al., 1990; Ross et al., 1992), *vglut2a* expressing axonal terminals may be exiting the telencephalon which would appear as *vglut2a* down regulation. Therefore higher *vglut2a* levels in 48hpf HVP could be a result of either defected axon migration or more likely, increased differentiation. On the other hand, *gad* genes that are predicted to have cytoplasmic distribution, were upregulated in HV and HVP and were significantly more abundant in HVP ventral telencephalon.

p27 is involved in cell cycle exit and is important in healthy development of many organ systems including the CNS (Razavipour et al., 2020). At 24hpf, it was slightly higher in HVP than HV but this was not statistically significant. This gene was upregulated by 48hpf in HV to reach HVP levels which did not change between 24 and 48hpf. This observation implied that cells in HVP telencephalon may be less proliferative. This was not consistent with my Ph3 staining at 24hpf. The source of this variability may be the low number of 24hpf embryos that were imaged following Ph3 staining. Alternatively, understanding these results may require the examination of more genes associated with cell proliferation.

To validate the qPCR results and confirm any potential telencephalic defects, I collaborated with ***Robert Lea*** to carry out FISH against *emx3*, *tbr1*, *vglu2a* and *gad2* using probes gifted from the Houart lab. Unfortunately, there were some concerns about potential sample mix-up which lead me to decide against presenting this data in my thesis as due to time restraints, we were unable to repeat it.

It is, however, important to note that examining gene expression in tissue context using bulk RNA extraction and qPCR or whole mount FISH share major shortcomings. These shortcomings are limitations in the number of genes analysed, the lack of single cell resolution and complete loss of spatial information. Alternatively, more specialised methods that have been developed to include spatial information in transcriptomics can be used.

In recent years, there have been many advances in "Spatial transcriptomics" that aim to al-

leviate this issue (Reviewed and summarised by Longo et al. (2021)). These methods can be separated to two main groups: High-plex RNA imaging and Spatial barcoding (Longo et al., 2021). The High-plex RNA imaging methods always require pre-selection of the genes of interest. However, the limits of the number of genes that can be studied have been extended in recent studies. These studies utilise sequential Fluorescent in-situ hybridisation (seqFISH) which involves sequential probing of genes of interest with limited number of fluorophores which ultimately result in a temporal barcode for each gene (Shah et al., 2016). Shah et al. (2016) have successfully studied up to 249 genes per cell while Eng et al. (2019) have developed seqFISH+, increasing the gene limit to 10000. The single cell resolution of this technique is a clear advantage for spatial transcriptomics. However, the limitation is the requirement for selecting genes of interest and designing gene specific probes which hinders exploratory and unbiased transcriptomics.

Spatial barcoding on the other hand relies on RNA sequencing of fixed sections on a spatially barcoded flat surface (e.g. slide) which allows the preservation of tissue integrity and therefore spatial information (Ståhl et al., 2016; Chen et al., 2022). The dependence on sequencing as opposed to imaging, makes these methods more suitable for unbiased and exploratory transcriptomics and alleviates the optical challenges associated with limited number of fluorophores that can be used. However, the main shortcoming of the earlier versions of this method relative to the High-plex imaging was their low spatial resolution of between 55 to 100 μm which meant that the captured data was not from single cells (Ståhl et al., 2016; Longo et al., 2021). However, this has been greatly improved by development of nanoball-patterned arrays that can be used for larger surface area (such as sections from whole mouse embryos) and capture sequences with much better resolution (500-715 nm) (Chen et al., 2022).

In short, adoption of either one of these more advanced methods can provide a much more detailed understanding of the potential transcriptomic changes caused by altering Her6 expression dynamics without losing the spatial information of specific neuronal subpopulations. Furthermore, since Her6 is also present in many other developing tissues (Fig 1.10), implementing techniques such as nanoball-patterned arrays (Chen et al., 2022) may highlight not only changes in more genes, but also other developing regions of the CNS or organ systems, providing a much greater scope to studying the downstream effects of altered oscillatory dynamics than has ever been reported.

Despite these shortcomings, the indications of increased differentiation in HVP are in line with previous findings. Kobayashi et al. (2015) showed that HES1 can be destabilised by knocking down the Deubiquitinating enzyme (DUB) enzyme *Usp22*. To assess the developmental effects of this manipulation, they electoporated *Usp22* KD vectors along with nuclear GFP *in utero*, followed by IF to detect GFP in mutated cells in the embryonic brain. This alteration significantly increased the number of GFP^+ cells in intermediate zone and cortical plate, where differentiated neurons are found and decreased the number

of progenitors in ventricular zone and sub ventricular zone (Kobayashi et al., 2015). Furthermore, Manning et al. (2019) have shown that Notch inhibition in mouse spinal cord slice cultures pushed cells to be more oscillatory and more likely to differentiate (Manning et al., 2019). The mathematical work by Biga et al. (2021) also predicted that high cell-cell differences (resembling the HVP - Chapter 5) may be associated with higher probability of differentiation.

My focus in this chapter was on a limited time window of development, only comparing early (24hpf) and late (48hpf) primary neurogenesis. This prevented me from concluding if the difference between HV and HVP is in the timing or duration of differentiation (i.e. premature or prolonged/increased) and whether these changes have any lasting impact on the juvenile or adult brain. However, it is clear that while destabilisation of Her6 does not have a substantial effect on the quantity of proliferating cells, it may alter the mode of proliferation towards differentiation. Even though the data regarding mode of cell division is preliminary, it is consistent with more persistent and at times, higher expression levels of both glutamatergic and GABAergic differentiation genes. Such prolonged or increased differentiation may also contribute to the faster rate of telencephalon growth in HVP embryos.

6.4 Concluding remarks

Her6 destabilisation altered its single cell expression and dynamics as well as its behaviour in the cell population. In this chapter I provided evidence that these changes have effects beyond the single cell and the Her6 expressing population. HVP embryos had smaller telencephalons than HV at 24hpf but grew more rapidly and recovered this difference by 48hpf. I propose that this may be due to sustained proliferation (shown by Ph3 IF) and/or increased proliferation. The retention of normal (i.e. HV) levels of proliferation in HVP could be indicative of some level of compensation by other *her* genes. However, by performing a preliminary analysis of cell division in single cell Venus, I suggested that in HVP, the mode of proliferation in the Her6 expressing cells may have shifted away from self-renewal towards differentiation. In agreement, qPCR analysis of genes associated with neural differentiation in pallium and sub-pallium suggested prolonged or increased differentiation in HVP. Further work is required to determine whether these changes have lasting impact on the adult brain. Nonetheless, given the propensity of functional compensation between bHLH genes, the observation of detectable downstream phenotypes in HVP is a testament to the importance of Her6 expression and its dynamics in regulating telencephalic progenitors which was previously unknown.

Chapter 7

General discussion

7.1 General discussion

Her6 is one of the two zebrafish orthologues of HES1 (Pasini et al., 2001; Zhou et al., 2012), a well characterised mammalian ultradian oscillator (Shimojo et al., 2008; Kageyama et al., 2018; Marinopoulou et al., 2021). Given the conservation of the main functional domains of HES/Her proteins across species (Zhou et al., 2012), it was very likely that Her6 is also an oscillator and that its dynamics are relevant in its function. However, its expression dynamics, regulation and function during embryonic neurogenesis have not been extensively studied. This was predominantly due to the lack of suitable live imaging tools for Her6 which hindered the observation of its potentially periodic expression.

Previously, transgenic zebrafish were often generated by the introduction of DNA constructs under the regulation of known promoters or enhancers (Kimura et al., 2014). This was done by using tools such as Tol2 transposable elements (Kawakami, 2007; Ninov et al., 2012) or *I-SceI* meganuclease (Thermes et al., 2002; Delaune et al., 2012). These methods not only required some knowledge of specific regulatory elements for the gene of interest (Kimura et al., 2014), they also did not have the precision needed for direct modification of endogenous loci which was required for assessing the expression dynamics of Her6 in real-time.

As a result, studies involving *her6* were focused only on the mRNA and predominantly limited to descriptions of its expression domain during normal development (Thisse et al., 2001), its Knock-down (KD) or over expression. For instance, upon *her6* KD, expression of glutamatergic fate marker *ngn1* which is localised in the central thalamus, expanded to the whole thalamus. This was to the detriment of *ascl1* expression which drives GABAergic fates and inhibits glutamatergic fates in pre and rostral thalamus (Scholpp et al., 2009). Similarly, *her6* over-expression suppressed *ngn1* in the Wild type (WT) telencephalon (Yoshizawa et al., 2011). But these previous studies lacked any insight into the behaviour of the Her6 protein as a regulator of neural progenitors.

With the advent of CRISPR/Cas9 gene modification methods, precise targeting of endogenous genes also became possible in zebrafish (Kimura et al., 2014; Zhang et al., 2018). The generation of the Her6-Venus (HV) Knock-in (KI) line by Soto et al. (2020) provided the first opportunity for single cell resolution examination of Her6 protein in real time. In this thesis, I have shown that the CRISPR method utilised for generating this KI resulted in the aberrant incorporation of the CRISPR donor backbone followed by a partial duplication of Wild type (WT) *her6* sequence. Soto et al. (2020) had already shown that HV KI embryos develop normally and recapitulate WT *her6* expression. In this thesis, I have added to this previous knowledge by generating a detailed map of the HV KI locus. My findings show that the HV KI locus has all the correct components to express the designed fusion protein without being impeded by the genomic aberrations. These included the expected start and stop codons as well as the 3' untranslated region (UTR) which was incorporated in

the Right Homology arm (RHA). Overall, this highlighted the importance of the detailed characterisation of KI lines for their informed use.

In this thesis I have expanded the use of the HV model system to study Her6 expression dynamics in the telencephalon. I used a combination of cutting edge live imaging, single cell tracking and single cell resolution analysis of the Her6-expressing population to reveal that Her6 expression in the telencephalon is indeed dynamic. In 5-37% of cells, these Her6 dynamics were periodic (i.e. oscillatory) with a 1.7-2 hour periodicity and a median fold-change of 1.4. To assess the functional relevance of Her6 and its dynamics, I examined the Her6-Venus-PEST (HVP) KI line where Her6 was destabilised and therefore, was expected to have altered dynamics. The HVP KI also had genomic aberrations such as the incorporation of the donor backbone and an additional KI cassette. However, much like HV, I showed that the HVP fusion protein was also unaffected by these aberrations.

Single cell observations revealed that in HVP, Her6 expression levels fluctuated more than HV which was quantified by single cell Coefficient of Variation (CV). This increase in fluctuations could be attributed to at least two different single cell features. Firstly, Her6 was expressed in an oscillatory manner in 32.5-67.9% of HVP cells which was significantly higher than HV. In addition, even though the period of HVP oscillators was unaltered (2-2.1 hours), they exhibited significantly higher fold changes ($\sim$2). Secondly, regardless of oscillatory state, HVP cells were more prone to faster Her6 decline over time. Interestingly, these single cell behaviours were associated with an unexpected system response. In snapshot HVP analysis, fewer cells expressed Her6 (i.e. Venus) and its expression levels were lower in the population. Nonetheless, some cells retained HV (i.e. control) levels of Her6 expression which led to increased snapshot Her6 heterogeneity in the HVP telencephalic tissue. Additionally, in HVP, there were larger differences in expression of Her6 in neighbouring cells.

These tissue-level observations were counter-intuitive, as I had expected all cells to respond uniformly to ubiquitous Her6 destabilisation. To determine the cause of these population patterning observations in HVP, mathematical modelling was used. Modelling showed that the high cell-cell differences in HVP cannot be replicated in single cell models with or without auto-inhibition but only when cells are coupled by Notch-like lateral inhibition. Interestingly, when the optimiser for the two coupled cell model (Model 3) was run with lateral inhibition but without auto-inhibition, no parameter sets were found that could lead to increased cell-cell differences or bifurcation. This confirmed that both auto-inhibition and lateral inhibition are contributing to the HVP traits.

This finding challenged the previous reports regarding Notch regulation of *her6*. Hans et al. (2004) used a UAS-Gal4 system to mis-express *notch1a*-intracellular domain in embryos by crossing *hsp70::Gal4* to *UAS:myc-notch1a-intra*. They then examined the expression of *her* genes with In-situ hybridisation (ISH). They found that with constant presence of Notch intracellular domain (NICD), *her3* was downregulated, especially in

the mesencephalic/rhombencephalic domain. *her5* was also inhibited by this manipulation. However, *her6* expression was unaffected in the presence of *notch1a*-intracellular domain. This finding led to a widely accepted belief that *her6* is not regulated by Notch (Hans et al., 2004; Schmidt et al., 2013).

I suggest two possibilities for this discrepancy. One is the possibility that *her6* is regulated by Notch factors other than *notch1a*. For instance, *notch3* is also extensively expressed in the embryonic forebrain (Tseng et al., 2021). Secondly, it is likely that other signals regulate *her6* induction and expression in the telencephalon while Notch has a less significant role in induction but mediates cell coupling. In line with this, *Hes1* has been shown to be strongly activated by Sonic-Hedgehog (SHH) signalling in the mouse retina. When SHH was activated by addition of Smo agonist to post-natal mouse retina explants, *Hes1* expression (measured with RT-qPCR) was induced ∼20-fold relative to untreated explants (Wall et al., 2009). Additionally, when SHH was induced with constitutively active form of Smo in the presence of DAPT, a γ-secratase inhibitor that blocked Notch signal propagation, *Hes1* induction was unaffected. This showed that SHH regulation of *Hes1* was independent of Notch intracellular domain (NICD). Most interestingly, electroporation of active NICD did mildly but significantly induce *Hes1* expression relative to control explants but *Hes1* induction caused by constitutively active Smo was ∼10-folds higher than its activation by Notch (Wall et al., 2009). Hence, *Hes1* expression can be regulated by different signals with varying strength.

shh is indeed expressed in the ventral telencephalon during zebrafish embryonic development (Wilson, Rubenstein, 2000) and its role in mediating ventral fates through *foxg1* has been described (Danesin et al., 2009). Since Her6 expression is also ventrally focused, it is likely that similar to the mouse retina, *her6* expression in this domain is predominantly under SHH regulation but also influenced by Notch. Therefore, the findings of Hans et al. (2004) do not negate the possibility of Notch-mediated lateral inhibition in the telencephalon. Furthermore, Hans et al. (2004) only examined *her6* mRNA at the tissue level using ISH. Therefore, over-expression of NICD may have affected cell coupling and Her6 expression levels in single cells but this effect was not detected.

In short, my work has shifted the perception of Her6 as a non-canonical Her transcription factor that does not easily fit the common narrative of HES proteins as Notch effectors. Instead, I propose that Her6 is a more complex transcriptional regulator that is potentially controlled by a range of signalling inputs.

7.2 How does protein destabilisation affect intercellular communication?

The HES5 based mathematical model from Biga et al. (2021) predicted that increasing the cell's ability to repress HES5 expression in its neighbour (i.e. coupling strength) leads to stronger lateral inhibition and thereby higher expression level differences between neighbouring cells. They also suggested that this condition which gives rise to a "salt and pepper" like pattern of HES5 expression was also associated with higher probability of differentiation. The predictions of this model are consistent with my observations in HVP. However, a scenario where Her6 destabilisation directly alters coupling strength is not likely. But rather, it is more likely that this manipulation has imposed an indirect change on the strength of lateral inhibition. I propose that this is possible by shifting the balance between auto-inhibition and lateral inhibition.

In HV telencephalon, there is heterogeneity in Her6 (i.e. Venus) expression in the population but the difference between expression levels in neighbouring cells is not large (Fig 7.1,A). This is likely to be because auto-inhibition and lateral inhibition are balanced between cells. This is schematically shown in figure 7.1,B. More Her6 is expressed in the *right* cell which means that it more strongly inhibits expression in the *left* cell by lateral inhibition. But in the *right* cell, auto-inhibition keeps Her6 production in check, preventing its levels to overshoot (Fig 7.1,B). Over time, the *left* and *right* cells may switch their behaviour while maintaining their balance (Fig 7.1,C).

In HVP, however, due to destabilisation of Her6, its levels in the majority of cells are lower than HV as has been shown by others upon protein destabilisation (Kobayashi et al., 2015). Nonetheless, the cells are more heterogenous with bigger cell-cell differences (Fig 7.1,D). This may be because in this scenario, which is shown schematically in figure 7.1,E, when Her6 expression increases in the *right* cell, it is perhaps counteracted less effectively by auto-inhibition since the protein is short lived. This gives the unexpected outcome of strengthening the effect of lateral inhibition and lowering Her6 levels in the *left* cell faster than it can produce Her6 (Fig 7.1,E). Over time, this pattern can get re-enforced until the *left* cell is no longer expressing Her6 (Fig 7.1,F,Top). Alternatively, due to less effective auto-inhibition because of low Her6 levels as well as its instability, Her6 production may exceed Her6 degradation in the *left* cell, allowing it to impose stronger lateral inhibition on the *right* cell and shift their balance (Fig 7.1,F,Bottom).

Hence, one may hypothesise that in HV, auto-inhibition balances lateral inhibition and maintains two cells at high levels of expression, preventing lateral inhibition to bifurcate levels of protein concentration. While in HVP, with the drop in protein abundance caused by its destabilisation, auto-inhibition weakens and the effect of lateral inhibition strengthens, leading the cells to adopt distinct steady state concentrations or bifurcate. This could explain the similarities of HVP traits with some of the model predictions from Biga et al.

(2021) in a ”strongly coupled” scenario.

7.3 Insights into the function of Her6 oscillations

I believe that the shift in balance between auto-inhibition and lateral inhibition leads to more abundant and larger oscillations in HVP. However, the modelling presented in this thesis did not include any predictions about the dynamic states of single cells. Hence, the exact cause of this change and its relationship with auto- and lateral inhibition is not known. But my observations resemble the reports by Manning et al. (2019). They showed that in mouse spinal cord slice cultures, cells that moved unidirectionally away from the progenitor domain (i.e. moved towards differentiation) were more likely to be expressing HES5 in an oscillatory manner. Furthermore, these oscillations had larger fold-change in comparison to oscillations in progenitor cells. However, they showed that this increase in peak to trough ratio (fold-change) was due to the declining long-term trend in the differentiating cells and when the trend was removed, the fold-change was no longer higher than progenitors. Therefore, Manning et al. (2019) suggested that the combined effect of declining trend and the resulting increased fold-change is critical in differentiating cells.

Based on this observation, the propensity of Her6 levels to decline more rapidly in HVP cells could explain the increased fold-change which may be decoded by the cell as a transition signal towards fate determination and differentiation. This is consistent with the increased tendency for expression of differentiation genes in HVP. However, conclusion is in contrast to the model proposed by Shimojo et al. (2008) and Imayoshi et al. (2013) who associated *Hes1* expression and protein oscillations with maintenance of mouse telencephalic progenitors rather than transition towards differentiation. This may in part be because these reports have not extensively examined oscillatory fold-change or long-term trends in a tissue context. In summary, in the zebrafish telencephalon, the Her6 oscillatory state is more likely to be a signal for cells to leave the early progenitor state and move towards later stages in the developmental trajectory, similar to the findings of Soto et al. (2020) in zebrafish hindbrain.

However, the trend analysis showed that both HV and HVP oscillators exhibited a range of long term trends including declining, maintained or increasing Her6 levels. The cells with maintained or increasing Her6 trends over time represent only a small proportion of the whole population and only a small fraction of them ($\sim$17%) are oscillatory in HV control context. Therefore, I do not believe that Her6 oscillations play a significant role in these cells in HV. However, the proportion of oscillators in cells with maintained or upregulating Her6 was higher in HVP. Therefore, I also propose that increased proportion and fold-change of oscillators in HVP may have a secondary role which is complementary to its potential involvement with cell state transitions. It is likely that in this small population of cells, this shift in single cell dynamics also acts as a compensatory mechanism for

reduced levels of Her6 and its premature depletion. In theory, such compensation could minimise the effects of lower Her6 levels by enabling some cells to experience Her6 at HV (i.e. control) levels. This may be an advantageous bi-product of cell-cell coupling in developmental systems.

7.4 Expectations of *her6* mRNA behaviour in response to weakened auto-inhibition

If auto-inhibition is indeed becoming less effective upon Her6 destabilisation, one would expect upregulation of *her6* mRNA. However, using Fluorescent in-situ hybridisation (FISH) I showed that the domain of *her6* expression was significantly reduced in HVP and its levels were slightly reduced based on Quantitative polymerase chain reaction (qPCR) data. Even though this may appear to contradict the expectation, it has two potential explanations. Firstly, the result of both experiments can be attributed to fewer cells expressing *her6* as was seen for the protein. In these cells, *her6* mRNA levels may be similar to or higher than HV. This too resembles the observation of lower Her6 levels in the majority of HVP cells even though at a single cell level, some cells retained normal (HV) levels of Her6 expression. Hence, at an mRNA level, this could have been masked due to lack of single cell resolution in FISH and qPCR. This could be resolved by using techniques such as Single molecule fluorescent in situ hybridisation (smFISH) that allow quantitative assessment of mRNA expression in single cells.

Alternatively, the changes imposed on auto-inhibition by Her6 destabilisation may be reflected in gene expression or mRNA dynamics rather than their levels. That is to say, relieved auto-inhibition may lead to longer presence of the mRNA in the cell rather than increasing its levels. In line with this, HES1 destabilisation by knocking down the DUB enzyme Usp22 that targets ubiquitinated HES1, led to elongated and more variable period in *Hes1* oscillations in single cells. These measurements were made using *Hes1* promoter-Luciferase reporter which more closely represents *Hes1* gene expression dynamics (Kobayashi et al., 2015). The authors explained this by suggesting that HES1 destabilisation elongated the delay in auto-inhibition which slowed or dampened *Hes1* oscillations. One can speculate that in this scenario, with the elongation of the *Hes1* period, the duration of active transcription and HES1 translation may have also increased. This could potentially contribute to higher oscillatory fold-change at the protein level, similar to my observations in HVP. However, Kobayashi et al. (2015) did not describe single cell protein oscillations making the verification of this hypothesis difficult. Alternatively, they reported dampened HES1 protein oscillations in synchronised bulk cells in response to serum stimulation and measured by Western blot (Kobayashi et al., 2015). In theory, this observation could be explained by strengthened effect of lateral inhibition due to less effective or delayed auto-inhibition which perhaps leads to more out of phase or anti-phase

oscillations that could make the population appear uniform.

In short, my work suggests that Her6 destabilisation may affect the strength of auto-inhibition. However, confirming this interaction requires more quantitative examination of mRNA expression and dynamics at the single cell level.

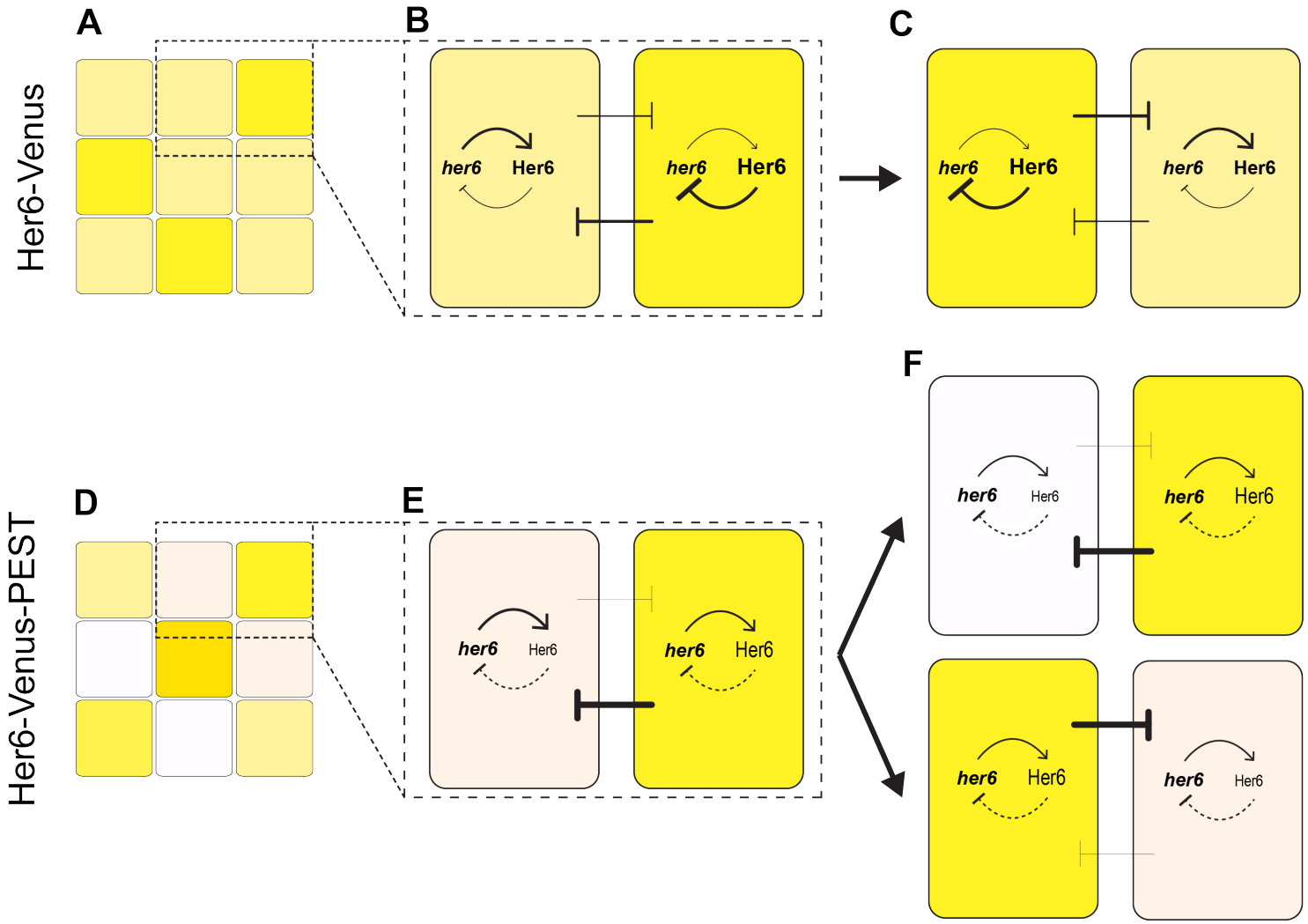

Figure 7.1: **Hypothetical model describing auto-inhibition and lateral inhibition in HV and HVP. Caption on the following page →**

Figure 7.1: **(A)** Schematic representation of Her6 (i.e. Venus) expressing population in HV where cells tend to have more similar levels. **(B)** Schematic representation of two cells outlined from (A). The *right* cell expresses more Her6 and exerts stronger lateral inhibition on the *left* cell. However it also more likely to auto-inhibit *her6* which will keep Her6 production in check. **(C)** Over time, these interations may lead the cells to alternate between slightly different levels. **(D)** Schematic representation of Her6 (i.e. Venus) expressing population in HVP where cells tend to have larger differences in levels and are more heterogenous.**(E)** Schematic representation of two cells outlined from (D). The *right* cell expresses more Her6 and exerts stronger lateral inhibition on the *left* cell. Due to protein destabilisation, auto-inhibition of *her6* may be less effective and cannot keep Her6 production in check. Hence, the effects of lateral inhibition are more pronounced and push *left* cell to lower levels of expression. **(F)** Top: A scenario where lateral inhibition switches off expression of *left* cell while *right* cell remains. Bottom: A scenario where the *left* cell can stochastically recover its levels due to low auto-inhibition and the resulting high production of Her6 which shifts the balance of the two cells.

7.5 Future work to examine the interpretation of the data

These interpretation of the data can be tested experimentally by targeting Her6 levels and/or Notch signalling. For targeting Her6 levels, the hemizygous (deleting one copy of the gene of interest) approach also used by Ochi et al. (2020) to examine the effect of *Hes1* levels versus dynamics could be suitable. This approach is expected to alters protein levels without greatly impeding other parts of the oscillatory network. If the change in levels in HVP is the primary effect that weakens auto-inhibition and strengthens the effect of coupling in the tissue, then hemizygous HV fish ($HV^{+/-}$) that have lower Her6 levels would phenocopy the HVP traits. Alternatively, $HV^{+/-}$ may have more or less drastic phenotype than HVP. In this case, I would conclude that the primary effect of Her6 destabilisation that gives rise to HVP traits is on the dynamics and that the change in levels in HVP is a secondary effect. Experimental inhibition of Notch in either of these outcomes along with its inhibition in HV and HVP could further verify the role of lateral inhibition in this system.

In a theoretical scenario, if $HV^{+/-}$ replicates HVP phenotypes, I would conclude that the altered Her6 levels are the primary effect of Her6 destabilisation which results in less effective auto-inhibition and stronger lateral inhibition. Therefore, in both HVP and $HV^{+/-}$, Notch inhibition would make the expression between neighbouring cells more uniform and perhaps resemble HV but with lower Her6 levels. This may also reduce the proportion of oscillators and expression of differentiation genes. On the other hand, in this scenarios, Notch inhibition in HV would not impose a drastic effect.

7.6 Limitations

The work presented in this thesis is not without limitations. For instance, unlike the reports by Manning et al. (2019), I have not been able to directly associate different Her6 dynamic behaviours with specific cell states. Further work is required to better understand the relationship between long-term trend, oscillatory/dynamic state and cell state transitions. For this purpose, two main areas require further improvements. First is to overcome

the technical challenges associated with live imaging that hindered capturing long time-courses and detecting cell state transitions. Second area to be further developed is the spatial understanding of cell movement in the telencephalon from progenitors to neurons accompanied by spatial mapping of single cell Her6 dynamics.

Another limitation to consider is that the work in my thesis did not examine much of the complexity of telencephalic development which is orchestrated by many signaling networks including Wnt/β-catenin, Bone morphogenic protein (BMP), Hedgehog (Hh) and Fibroblast growth factor signaling (FGF) pathways (Wilson, Houart, 2004; Miyake et al., 2005; Danesin et al., 2009). Furthermore, organisation of the telencephalon and the neuronal composition in its sub-regions is influenced by neuronal migration like the glutamatergic neurons generated in the dorsal telencephalon that migrate ventrally (Mione et al., 2008). Such cell movements were also not examined in this thesis.

7.7 Concluding remarks

My work is the first to highlight the role of Her6 as an important early progenitor regulator and describe its expression dynamics in the zebrafish telencephalon. Altering these dynamics by Her6 destabilisation did not cause detectable changes in the organisation of the telencephalon and global cell proliferation which in part, may be due to compensation by other factors. However, altered Her6 dynamics did cause developmental consequences such as accelerated telencephalic growth and prolonged or increased neural differentiation. Hence, this thesis highlighted the importance of Her6 while also revealing the robustness of the regulatory network. I propose that this robustness is firstly a result of coupling between cells that enables them to respond to manipulations collectively and secondly due to compensation by other factors. But the latter remains to be shown.

The work of Mione et al. (2008) and Furlan et al. (2017) have shown that embryonic neurons are indeed relevant in the adult zebrafish brain. Hence, the characterisation of potential long-term impact of altering Her6 dynamics presents an exciting avenue for the continuation of my work.

Bibliography

Akazawa Chihiro, Sasai Yoshiki, Nakanishi Shigetada, Kageyama Ryoichiro. Molecular characterization of a rat negative regulator with a basic helix-loop-helix structure predominantly expressed in the developing nervous system. // Journal of Biological Chemistry. 1992. 267, 30. 21879–21885.

Allende Miguel L, Weinberg Eric S. The expression pattern of two zebrafish achaete-scute homolog (ash) genes is altered in the embryonic brain of the cyclops mutant // Developmental biology. 1994. 166, 2. 509–530.

Artavanis-Tsakonas Spyros, Rand Matthew D, Lake Robert J. Notch signaling: cell fate control and signal integration in development // Science. 1999. 284, 5415. 770–776.

Aulehla Alexander, Wiegraebe Winfried, Baubet Valerie, Wahl Matthias B, Deng Chuxia, Taketo Makoto, Lewandoski Mark, Pourquié Olivier. A β-catenin gradient links the clock and wavefront systems in mouse embryo segmentation // Nature cell biology. 2008. 10, 2. 186–193.

Ay Ahmet, Knierer Stephan, Sperlea Adriana, Holland Jack, Özbudak Ertuğrul M. Short-lived Her proteins drive robust synchronized oscillations in the zebrafish segmentation clock // Development. 2013. 140, 15. 3244–3253.

Bae Young-Ki, Shimizu Takashi, Hibi Masahiko. Patterning of proneuronal and inter-proneuronal domains by hairy-and enhancer of split-related genes in zebrafish neuroectoderm // Development. 2006. 133, 8. 1609–1609.

Baek Joung Hee, Hatakeyama Jun, Sakamoto Susumu, Ohtsuka Toshiyuki, Kageyama Ryoichiro. Persistent and high levels of Hes1 expression regulate boundary formation in the developing central nervous system // Development. 2006. 133, 13. 2467–2476.

Bai Haipeng, Liu Lijun, An Ke, Lu Xiaochan, Harrison Michael, Zhao Yanqiu, Yan Ruibin, Lu Zhijie, Li Song, Lin Shuo, others . CRISPR/Cas9-mediated precise genome modification by a long ssDNA template in zebrafish // BMC genomics. 2020. 21, 1. 1–12.

Bai Ting, Seebald Jamie L, Kim Kyu-Eui, Ding Hong-Mei, Szeto Daniel P, Chang Henry C. Disruption of zebrafish cyclin G-associated kinase (GAK) function impairs the expression of Notch-dependent genes during neurogenesis and causes defects in neuronal development // BMC Developmental Biology. 2010. 10, 1. 1–17.

Barth Katrin Anukampa, Wilson Stephen W. Expression of zebrafish nk2. 2 is influenced by sonic hedgehog/vertebrate hedgehog-1 and demarcates a zone of neuronal differentiation in the embryonic forebrain // Development. 1995. 121, 6. 1755–1768.

Bessho Yasumasa, Hirata Hiromi, Masamizu Yoshito, Kageyama Ryoichiro. Periodic repression by the bHLH factor Hes7 is an essential mechanism for the somite segmentation clock // Genes & development. 2003. 17, 12. 1451–1456.

Bessho Yasumasa, Miyoshi Goichi, Sakata Ryoichi, Kageyama Ryoichiro. Hes7: a bHLH-type repressor gene regulated by Notch and expressed in the presomitic mesoderm // Genes to Cells. 2001. 6, 2. 175–185.

Bhat Kavita Purnanda, Truax Agnieszka Dorota, Greer Susanna Fletcher. Phosphorylation and ubiquitination of degron proximal residues are essential for class II transactivator (CIITA) transactivation and major histocompatibility class II expression // Journal of Biological Chemistry. 2010. 285, 34. 25893–25903.

Bierkamp Christiane, Campos-Ortega JoséA. A zebrafish homologue of the Drosophila neurogenic gene Notch and its pattern of transcription during early embryogenesis // Mechanisms of development. 1993. 43, 2-3. 87–100.

Biga Veronica, Hawley Joshua, Soto Ximena, Johns Emma, Han Daniel, Bennett Hayley, Adamson Antony D, Kursawe Jochen, Glendinning Paul, Manning Cerys S, others . A dynamic, spatially periodic, micro-pattern of HES5 underlies neurogenesis in the mouse spinal cord // Molecular systems biology. 2021. 17, 5. e9902.

Blader Patrick, Fischer Nadine, Gradwohl Gerard, Guillemont F, Strahle U. The activity of neurogenin1 is controlled by local cues in the zebrafish embryo // Development. 1997. 124, 22. 4557–4569.

Blader Patrick, Plessy Charles, Strähle Uwe. Multiple regulatory elements with spatially and temporally distinct activities control neurogenin1 expression in primary neurons of the zebrafish embryo // Mechanisms of development. 2003. 120, 2. 211–218.

Boareto Marcelo. Patterning via local cell-cell interactions in developing systems // Developmental Biology. 2020. 460, 1. 77–85.

Bocci Federico, Onuchic José Nelson, Jolly Mohit Kumar. Understanding the principles of pattern formation driven by notch signaling by integrating experiments and theoretical models // Frontiers in Physiology. 2020. 929.

Bonev Boyan, Pisco Angela, Papalopulu Nancy. MicroRNA-9 reveals regional diversity of neural progenitors along the anterior-posterior axis // Developmental cell. 2011. 20, 1. 19–32.

Bonev Boyan, Stanley Peter, Papalopulu Nancy. MicroRNA-9 modulates Hes1 ultradian oscillations by forming a double-negative feedback loop // Cell reports. 2012. 2, 1. 10–18.

Burton Joshua, Manning Cerys S, Rattray Magnus, Papalopulu Nancy, Kursawe Jochen. Inferring kinetic parameters of oscillatory gene regulation from single cell time-series data // Journal of the Royal Society Interface. 2021. 18, 182. 20210393.

Cabrera Carlos V. Lateral inhibition and cell fate during neurogenesis in Drosophila: the interactions between scute, Notch and Delta // Development. 1990. 109, 3. 733–742.

Castella Paul, Sawai Shoji, Nakao Keiko, Wagner John A, Caudy Michael. HES-1 repression of differentiation and proliferation in PC12 cells: role for the helix 3-helix 4 domain in transcription repression // Molecular and cellular biology. 2000. 20, 16. 6170–6183.

Chen Ao, Liao Sha, Cheng Mengnan, Ma Kailong, Wu Liang, Lai Yiwei, Qiu Xiaojie, Yang Jin, Xu Jiangshan, Hao Shijie, others . Spatiotemporal transcriptomic atlas of mouse organogenesis using DNA nanoball-patterned arrays // Cell. 2022. 185, 10. 1777–1792.

Chen Fangfang, Zhang Chunxiao, Wu Haonan, Ma Yue, Luo Xiaomin, Gong Xinqi, Jiang Fan, Gui Yaoting, Zhang Hui, Lu Fei. The E3 ubiquitin ligase SCFFBXL14 complex stimulates neuronal differentiation by targeting the Notch signaling factor HES1 for proteolysis // Journal of Biological Chemistry. 2017. 292, 49. 20100–20112.

Chen Herbert, Thiagalingam Arunthathi, Chopra Hemi, Borges Michael W, Feder John N, Nelkin Barry D, Baylin Stephen B, Ball Douglas W. Conservation of the Drosophila lateral inhibition pathway in human lung cancer: a hairy-related protein (HES-1) directly represses achaete-scute homolog-1 expression // Proceedings of the National Academy of Sciences. 1997. 94, 10. 5355–5360.

Cole LK, Ross LS. Apoptosis in the developing zebrafish embryo // Developmental biology. 2001. 240, 1. 123–142.

Collery Ross F, Link Brian A. Dynamic smad-mediated BMP signaling revealed through transgenic zebrafish // Developmental Dynamics. 2011. 240, 3. 712–722.

Collier Joanne R, Monk Nicholas AM, Maini Philip K, Lewis Julian H. Pattern formation by lateral inhibition with feedback: a mathematical model of delta-notch intercellular signalling // Journal of theoretical Biology. 1996. 183, 4. 429–446.

Coolen Marion, Thieffry Denis, Drivenes Øyvind, Becker Thomas S, Bally-Cuif Laure. miR-9 controls the timing of neurogenesis through the direct inhibition of antagonistic factors // Developmental cell. 2012. 22, 5. 1052–1064.

Danesin Catherine, Peres João N, Johansson Marie, Snowden Victoria, Cording Amy, Papalopulu Nancy, Houart Corinne. Integration of telencephalic Wnt and hedgehog signaling center activities by Foxg1 // Developmental cell. 2009. 16, 4. 576–587.

De Decker Matthias, Lavaert Marieke, Roels Juliette, Tilleman Laurentijn, Vandekerckhove Bart, Leclercq Georges, Van Nieuwerburgh Filip, Van Vlierberghe Pieter, Taghon Tom. HES1 and HES4 have non-redundant roles downstream of Notch during early human T-cell development // Haematologica. 2021. 106, 1. 130.

Delaune Emilie A, François Paul, Shih Nathan P, Amacher Sharon L. Single-cell-resolution imaging of the impact of Notch signaling and mitosis on segmentation clock dynamics // Developmental cell. 2012. 23, 5. 995–1005.

Dirian Lara, Galant Sonya, Coolen Marion, Chen Wenbiao, Bedu Sébastien, Houart Corinne, Bally-Cuif Laure, Foucher Isabelle. Spatial regionalization and heterochrony in the formation of adult pallial neural stem cells // Developmental cell. 2014. 30, 2. 123–136.

Dong Zhiqiang, Yang Nan, Yeo Sang-Yeob, Chitnis Ajay, Guo Su. Intralineage directional Notch signaling regulates self-renewal and differentiation of asymmetrically dividing radial glia // Neuron. 2012. 74, 1. 65–78.

Dörrbaum Aline R, Kochen Lisa, Langer Julian D, Schuman Erin M. Local and global influences on protein turnover in neurons and glia // Elife. 2018. 7. e34202.

Durisic Nela, Laparra-Cuervo Lara, Sandoval-Álvarez Ángel, Borbely Joseph Steven, Lakadamyali Melike. Single-molecule evaluation of fluorescent protein photoactivation efficiency using an in vivo nanotemplate // Nature methods. 2014. 11, 2. 156–162.

Easter Jr Stephen S, Burrill John, Marcus Riva C, Ross Linda S, Taylor Jeremy SH, Wilson Stephen W. Initial tract formation in the vertebrate brain // Progress in brain research. 1994. 102. 79–93.

Eng Chee-Huat Linus, Lawson Michael, Zhu Qian, Dries Ruben, Koulena Noushin, Takei Yodai, Yun Jina, Cronin Christopher, Karp Christoph, Yuan Guo-Cheng, others . Transcriptome-scale super-resolved imaging in tissues by RNA seqFISH+ // Nature. 2019. 568, 7751. 235–239.

Fang Xiaoguang, Zhou Wenchao, Wu Qiulian, Huang Zhi, Shi Yu, Yang Kailin, Chen Cong, Xie Qi, Mack Stephen C, Wang Xiuxing, others . Deubiquitinase USP13 maintains glioblastoma stem cells by antagonizing FBXL14-mediated Myc ubiquitination // Journal of Experimental Medicine. 2017. 214, 1. 245–267.

Fekany Kimberly, Yamanaka Yojiro, Leung TinChung, Sirotkin Howard I, Topczewski Jacek, Gates Michael A, Hibi Masahiko, Renucci Armand, Stemple Derek, Radbill Andy, others . The zebrafish bozozok locus encodes Dharma, a homeodomain protein essential for induction of gastrula organizer and dorsoanterior embryonic structures // Development. 1999. 126, 7. 1427–1438.

Fekany-Lee Kimberly, Gonzalez Encina, Miller-Bertoglio Valarie, Solnica-Krezel Lilianna. The homeobox gene bozozok promotes anterior neuroectoderm formation in zebrafish through negative regulation of BMP2/4 and Wnt pathways // Development. 2000. 127, 11. 2333–2345.

Fernández Virginia, Llinares-Benadero Cristina, Borrell Víctor. Cerebral cortex expansion and folding: what have we learned? // The EMBO journal. 2016. 35, 10. 1021–1044.

Fisher Alfred L, Ohsako Shunji, Caudy Michael. The WRPW motif of the hairy-related basic helix-loop-helix repressor proteins acts as a 4-amino-acid transcription repression and protein-protein interaction domain // Molecular and cellular biology. 1996. 16, 6. 2670–2677.

Fode Carol, Ma Qiufu, Casarosa Simona, Ang Siew-Lan, Anderson David J, Guillemot François. A role for neural determination genes in specifying the dorsoventral identity of telencephalic neurons // Genes & development. 2000. 14, 1. 67–80.

Folgueira Mónica, Bayley Philippa, Navratilova Pavla, Becker Thomas S, Wilson Stephen W, Clarke Jonathan DW. Morphogenesis underlying the development of the everted teleost telencephalon // Neural development. 2012. 7, 1. 1–14.

Furlan Giacomo, Cuccioli Valentina, Vuillemin Nelly, Dirian Lara, Muntasell Anna Janue, Coolen Marion, Dray Nicolas, Bedu Sébastien, Houart Corinne, Beaurepaire Emmanuel, others . Life-long neurogenic activity of individual neural stem cells and continuous growth establish an outside-in architecture in the teleost pallium // Current Biology. 2017. 27, 21. 3288–3301.

Geling Andrea, Itoh Motoyuki, Tallafuß Alexandra, Chapouton Prisca, Tannhäuser Birgit, Kuwada John Y, Chitnis Ajay B, Bally-Cuif Laure. bHLH transcription factor Her5 links patterning to regional inhibition of neurogenesis at the midbrain-hindbrain boundary // Development. 2003. 130, 8. 1591–1604.

Ghoda LDWT, Daalen Wetters T van, Macrae M, Ascherman D, Coffino P. Prevention of rapid intracellular degradation of ODC by a carboxyl-terminal truncation // Science. 1989. 243, 4897. 1493–1495.

Ghoda Lucy, Phillips MA, Bass KE, Wang CC, Coffino P. Trypanosome ornithine decarboxylase is stable because it lacks sequences found in the carboxyl terminus of the mouse enzyme which target the latter for intracellular degradation. // Journal of Biological Chemistry. 1990. 265, 20. 11823–11826.

Gong Zhen, Liu Jianyun, Xie Xin, Xu Xiaoyuan, Wu Ping, Li Huimin, Wang Yaqin, Li Weidong, Xiong Jianjun. Identification of potential target genes of USP22 via ChIP-seq and RNA-seq analysis in HeLa cells // Genetics and molecular biology. 2018. 41. 488–495.

Grbavec Diane, Stifani Stefano. Molecular interaction between TLE1 and the carboxyl-terminal domain of HES-1 containing the WRPW motif // Biochemical and biophysical research communications. 1996. 223, 3. 701–705.

Gurskaya Nadya G, Verkhusha Vladislav V, Shcheglov Alexander S, Staroverov Dmitry B, Chepurnykh Tatyana V, Fradkov Arkady F, Lukyanov Sergey, Lukyanov Konstantin A.

Engineering of a monomeric green-to-red photoactivatable fluorescent protein induced by blue light // Nature biotechnology. 2006. 24, 4. 461–465.

Hagmann Michael, Bruggmann Rémy, Xue Lei, Georgiev Oleg, Schaffner Walter, Rungger Duri, Spaniol Philipp, Gerster Thomas. Homologous recombination and DNA-end joining reactions in zygotes and early embryos of zebrafish (Danio rerio) and Drosophila melanogaster // Biological chemistry. 1998. 379, 6. 673–682.

Hans Stefan, Scheer Nico, Riedl Iris, Weizsäcker Elisabeth v, Blader Patrick, Campos-Ortega José A. her3, a zebrafish member of the hairy-E (spl) family, is repressed by Notch signalling // Development. 2004. 131, 12. 2957–2969.

Hartenstein Volker, Wodarz Andreas. Initial neurogenesis in Drosophila // Wiley Interdisciplinary Reviews: Developmental Biology. 2013. 2, 5. 701–721.

Hashimoto Hisashi, Itoh Motoyuki, Yamanaka Yojiro, Yamashita Susumu, Shimizu Takashi, Solnica-Krezel Lilianna, Hibi Masahiko, Hirano Toshio. Zebrafish Dkk1 functions in forebrain specification and axial mesendoderm formation // Developmental biology. 2000. 217, 1. 138–152.

Hatakeyama Jun, Bessho Yasumasa, Katoh Kazuo, Ookawara Shigeo, Fujioka Makio, Guillemot François, Kageyama Ryoichiro. Hes genes regulate size, shape and histogenesis of the nervous system by control of the timing of neural stem cell differentiation // Development. 2004. 131, 22. 5539–5550.

Hershko Avram, Ciechanover Aaron. The ubiquitin system // Annual review of biochemistry. 1998. 67, 1. 425–479.

Higashijima Shin-Ichi, Mandel Gail, Fetcho Joseph R. Distribution of prospective glutamatergic, glycinergic, and GABAergic neurons in embryonic and larval zebrafish // Journal of Comparative Neurology. 2004. 480, 1. 1–18.

Hirata Hiromi, Bessho Yasumasa, Kokubu Hiroshi, Masamizu Yoshito, Yamada Shuichi, Lewis Julian, Kageyama Ryoichiro. Instability of Hes7 protein is crucial for the somite segmentation clock // Nature genetics. 2004. 36, 7. 750–754.

Hirata Hiromi, Yoshiura Shigeki, Ohtsuka Toshiyuki, Bessho Yasumasa, Harada Takahiro, Yoshikawa Kenichi, Kageyama Ryoichiro. Oscillatory expression of the bHLH factor Hes1 regulated by a negative feedback loop // Science. 2002. 298, 5594. 840–843.

Holley Scott A, Geisler Robert, Nüsslein-Volhard Christiane. Control of her1 expression during zebrafish somitogenesis by a delta-dependent oscillator and an independent wavefront activity // Genes & development. 2000. 14, 13. 1678–1690.

Horikawa Kazuki, Ishimatsu Kana, Yoshimoto Eiichi, Kondo Shigeru, Takeda Hiroyuki. Noise-resistant and synchronized oscillation of the segmentation clock // Nature. 2006. 441, 7094. 719–723.

Horwitz KB, Costlow ME, McGuire W Ll. MCF-7: a human breast cancer cell line with estrogen, androgen, progesterone, and glucocorticoid receptors // Steroids. 1975. 26, 6. 785–795.

Hou Damon, Cenciarelli Cristina, Jensen Jane P, Nguygen HB, Weissman Allan M. Activation-dependent ubiquitination of a T cell antigen receptor subunit on multiple intracellular lysines. // Journal of Biological Chemistry. 1994. 269, 19. 14244–14247.

Houart Corinne, Caneparo Luca, Heisenberg Carl-Philipp, Barth K Anukampa, Take-Uchi Masaya, Wilson Stephen W. Establishment of the telencephalon during gastrulation by local antagonism of Wnt signaling // Neuron. 2002. 35, 2. 255–265.

Howe Kerstin, Clark Matthew D, Torroja Carlos F, Torrance James, Berthelot Camille, Muffato Matthieu, Collins John E, Humphray Sean, McLaren Karen, Matthews Lucy, others . The zebrafish reference genome sequence and its relationship to the human genome // Nature. 2013. 496, 7446. 498–503.

Huang Sui. Non-genetic heterogeneity of cells in development: more than just noise // Development. 2009. 136, 23. 3853–3862.

Huesa Gema, ANADO RAMO N, FOLGUEIRA MO NICA, YA JULIA N. Evolution of the pallium in fishes // perspective. 2009. 1016. 61–76.

Imayoshi Itaru, Ishidate Fumiyoshi, Kageyama Ryoichiro. Real-time imaging of bHLH transcription factors reveals their dynamic control in the multipotency and fate choice of neural stem cells // Frontiers in Cellular Neuroscience. 2015. 9. 288.

Imayoshi Itaru, Isomura Akihiro, Harima Yukiko, Kawaguchi Kyogo, Kori Hiroshi, Miyachi Hitoshi, Fujiwara Takahiro, Ishidate Fumiyoshi, Kageyama Ryoichiro. Oscillatory control of factors determining multipotency and fate in mouse neural progenitors // Science. 2013. 342, 6163. 1203–1208.

Imayoshi Itaru, Kageyama Ryoichiro. Oscillatory control of bHLH factors in neural progenitors // Trends in neurosciences. 2014. 37, 10. 531–538.

Imayoshi Itaru, Shimogori Tomomi, Ohtsuka Toshiyuki, Kageyama Ryoichiro. Hes genes and neurogenin regulate non-neural versus neural fate specification in the dorsal telencephalic midline // Development. 2008. 135, 15. 2531–2541.

Ishibashi Makoto, Ang Siew-Lan, Shiota Kohei, Nakanishi Shigetada, Kageyama Ryoichiro, Guillemot Francois. Targeted disruption of mammalian hairy and Enhancer of split homolog-1 (HES-1) leads to up-regulation of neural helix-loop-helix factors, premature neurogenesis, and severe neural tube defects. // Genes & development. 1995. 9, 24. 3136–3148.

Isomura Akihiro, Kageyama Ryoichiro. Ultradian oscillations and pulses: coordinating cellular responses and cell fate decisions // Development. 2014. 141, 19. 3627–3636.

Isomura Akihiro, Ogushi Fumiko, Kori Hiroshi, Kageyama Ryoichiro. Optogenetic perturbation and bioluminescence imaging to analyze cell-to-cell transfer of oscillatory information // Genes & development. 2017. 31, 5. 524–535.

Jarriault Sophie, Brou Christel, Logeat Frédérique, Schroeter Eric H, Kopan Raphael, Israel Alain. Signalling downstream of activated mammalian Notch // Nature. 1995. 377, 6547. 355–358.

Jeffery Jessie, Neyt Christine, Moore Wade, Paterson Scott, Bower Neil I, Chenevix-Trench Georgia, Verkade Heather, Hogan Benjamin M, Khanna Kum Kum. Cep55 regulates embryonic growth and development by promoting Akt stability in zebrafish // The FASEB Journal. 2015. 29, 5. 1999–2009.

Jeong Jae-Yeon, Einhorn Zev, Mathur Priya, Chen Lishan, Lee Susie, Kawakami Koichi, Guo Su. Patterning the zebrafish diencephalon by the conserved zinc-finger protein Fezl // Development. 2007. 134, 1. 127–136.

Jesenberger Veronika, Jentsch Stefan. Deadly encounter: ubiquitin meets apoptosis // Nature Reviews Molecular Cell Biology. 2002. 3, 2. 112–121.

Jiang Yun-Jin, Aerne Birgit L, Smithers Lucy, Haddon Catherine, Ish-Horowicz David, Lewis Julian. Notch signalling and the synchronization of the somite segmentation clock // Nature. 2000. 408, 6811. 475–479.

Johnson Jane E, Birren Susan J, Saito Tetsuichiro, Anderson David J. DNA binding and transcriptional regulatory activity of mammalian achaete-scute homologous (MASH) proteins revealed by interaction with a muscle-specific enhancer. // Proceedings of the National Academy of Sciences. 1992. 89, 8. 3596–3600.

Kageyama Ryoichiro, Nakanishi Shigetada. Helix-loop-helix factors in growth and differentiation of the vertebrate nervous system // Current opinion in genetics & development. 1997. 7, 5. 659–665.

Kageyama Ryoichiro, Ohtsuka Toshiyuki, Kobayashi Taeko. The Hes gene family: repressors and oscillators that orchestrate embryogenesis // Development. 2007. 134, 7. 1243–1251.

Kageyama Ryoichiro, Shimojo Hiromi, Isomura Akihiro. Oscillatory control of notch signaling in development // Molecular Mechanisms of Notch Signaling. 2018. 265–277.

Kang Seon Ah, Seol Jae Hong, Kim Jaesang. The conserved WRPW motif of Hes6 mediates proteasomal degradation // Biochemical and biophysical research communications. 2005. 332, 1. 33–36.

Kao Shih-Han, Wang Wen-Lung, Chen Chi-Yuan, Chang Yih-Leong, Wu Yi-Ying, Wang Yi-Ting, Wang Shu-Ping, Nesvizhskii Alexey I, Chen Yu-Ju, Hong Tse-Ming, others . Analysis of protein stability by the cycloheximide chase assay // Bio-protocol. 2015. 5, 1.

Katoh Masuko, Katoh Masaru. Integrative genomic analyses on HES/HEY family: Notch-independent HES1, HES3 transcription in undifferentiated ES cells, and Notch-dependent HES1, HES5, HEY1, HEY2, HEYL transcription in fetal tissues, adult tissues, or cancer // International journal of oncology. 2007. 31, 2. 461–466.

Kawakami Koichi. Tol2: a versatile gene transfer vector in vertebrates // Genome biology. 2007. 8, 1. 1–10.

Kesavan Gokul, Chekuru Avinash, Machate Anja, Brand Michael. CRISPR/Cas9-mediated zebrafish knock-in as a novel strategy to study midbrain-hindbrain boundary development // Frontiers in neuroanatomy. 2017. 11. 52.

Keskin Sevdenur, Devakanmalai Gnanapackiam S, Kwon Soo Bin, Vu Ha T, Hong Qiyuan, Lee Yin Yeng, Soltani Mohammad, Singh Abhyudai, Ay Ahmet, Özbudak Ertuğrul M. Noise in the vertebrate segmentation clock is boosted by time delays but tamed by notch signaling // Cell reports. 2018. 23, 7. 2175–2185.

Kim Cheol-Hee, Ueshima Emiko, Muraoka Osamu, Tanaka Hidekazu, Yeo Sang-Yeob, Huh Tae-Lin, Miki Naomasa. Zebrafish elav/HuC homologue as a very early neuronal marker // Neuroscience letters. 1996. 216, 2. 109–112.

Kimmel Charles B, Ballard William W, Kimmel Seth R, Ullmann Bonnie, Schilling Thomas F. Stages of embryonic development of the zebrafish // Developmental dynamics. 1995. 203, 3. 253–310.

Kimura Yukiko, Hisano Yu, Kawahara Atsuo, Higashijima Shin-ichi. Efficient generation of knock-in transgenic zebrafish carrying reporter/driver genes by CRISPR/Cas9-mediated genome engineering // Scientific reports. 2014. 4, 1. 1–7.

King Randall W, Deshaies Raymond J, Peters Jan-Michael, Kirschner Marc W. How proteolysis drives the cell cycle // Science. 1996. 274, 5293. 1652–1659.

Kobayashi Taeko, Iwamoto Yumiko, Takashima Kazuhiro, Isomura Akihiro, Kosodo Yoichi, Kawakami Koichi, Nishioka Tomoki, Kaibuchi Kozo, Kageyama Ryoichiro. Deubiquitinating enzymes regulate Hes1 stability and neuronal differentiation. 2015. 2411–2423.

Kobayashi Taeko, Kageyama Ryoichiro. Expression dynamics and functions of Hes factors in development and diseases // Current topics in developmental biology. 2014. 110. 263–283.

Kobayashi Taeko, Mizuno Hiroaki, Imayoshi Itaru, Furusawa Chikara, Shirahige Katsuhiko, Kageyama Ryoichiro. The cyclic gene Hes1 contributes to diverse differentiation responses of embryonic stem cells // Genes & development. 2009. 23, 16. 1870–1875.

Kozol Robert A, Abrams Alexander J, James David M, Buglo Elena, Yan Qing, Dallman Julia E. Function over form: modeling groups of inherited neurological conditions in zebrafish // Frontiers in molecular neuroscience. 2016. 9. 55.

Kumamoto Takuma, Hanashima Carina. Evolutionary conservation and conversion of Foxg1 function in brain development // Development, growth & differentiation. 2017. 59, 4. 258–269.

Laje Rodrigo, Agostino Patricia V, Golombek Diego A. The times of our lives: interaction among different biological periodicities // Frontiers in integrative neuroscience. 2018. 12. 10.

Lea Robert, Bonev Boyan, Dubaissi Eamon, Vize Peter D, Papalopulu Nancy. Multicolor fluorescent in situ mRNA hybridization (FISH) on whole mounts and sections // Xenopus Protocols. 2012. 431–444.

Levine Joe H, Lin Yihan, Elowitz Michael B. Functional roles of pulsing in genetic circuits // Science. 2013. 342, 6163. 1193–1200.

Lewis Julian, Hanisch Anja, Holder Maxine. Notch signaling, the segmentation clock, and the patterning of vertebrate somites // Journal of biology. 2009. 8, 4. 1–7.

Li Xianqiang, Zhao Xiaoning, Fang Yu, Jiang Xin, Duong Tommy, Fan Connie, Huang Chiao-Chain, Kain Steven R. Generation of destabilized green fluorescent protein as a transcription reporter // Journal of Biological Chemistry. 1998. 273, 52. 34970–34975.

Liu Jingang, Gong Lu, Chang Changqing, Liu Cong, Peng Jinrong, Chen Jun. Development of novel visual-plus quantitative analysis systems for studying DNA double-strand break repairs in zebrafish // Journal of Genetics and Genomics. 2012. 39, 9. 489–502.

Longo Sophia K, Guo Margaret G, Ji Andrew L, Khavari Paul A. Integrating single-cell and spatial transcriptomics to elucidate intercellular tissue dynamics // Nature Reviews Genetics. 2021. 22, 10. 627–644.

MacDonald Ryan B, Debiais-Thibaud Mélanie, Talbot Jared Coffin, Ekker Marc. The relationship between dlx and gad1 expression indicates highly conserved genetic pathways in the zebrafish forebrain // Developmental Dynamics. 2010. 239, 8. 2298–2306.

Macdonald Rachel, Xu Qiling, Barth K Anukampa, Mikkola Ingvild, Holder Nigel, Fjose Anders, Krauss Stefan, Wilson Stephen W. Regulatory gene expression boundaries demarcate sites of neuronal differentiation in the embryonic zebrafish forebrain // Neuron. 1994. 13, 5. 1039–1053.

Manning Cerys S, Biga Veronica, Boyd James, Kursawe Jochen, Ymisson Bodvar, Spiller David G, Sanderson Christopher M, Galla Tobias, Rattray Magnus, Papalopulu Nancy. Quantitative single-cell live imaging links HES5 dynamics with cell-state and fate in murine neurogenesis // Nature communications. 2019. 10, 1. 1–19.

Marinopoulou Elli, Biga Veronica, Sabherwal Nitin, Miller Anzy, Desai Jayni, Adamson Antony D, Papalopulu Nancy. HES1 protein oscillations are necessary for neural stem cells to exit from quiescence // Iscience. 2021. 24, 10. 103198.

Martin Stella C, Heinrich Gerhard, Sandell Julie H. Sequence and expression of glutamic acid decarboxylase isoforms in the developing zebrafish // Journal of Comparative Neurology. 1998. 396, 2. 253–266.

Matsuda Mitsuhiro, Hayashi Hanako, Garcia-Ojalvo Jordi, Yoshioka-Kobayashi Kumiko, Kageyama Ryoichiro, Yamanaka Yoshihiro, Ikeya Makoto, Toguchida Junya, Alev Cantas, Ebisuya Miki. Species-specific segmentation clock periods are due to differential biochemical reaction speeds // Science. 2020. 369, 6510. 1450–1455.

McIntosh Rebecca, Norris Joseph, Clarke Jon D, Alexandre Paula. Spatial distribution and characterization of non-apical progenitors in the zebrafish embryo central nervous system // Open biology. 2017. 7, 2. 160312.

Mendieta-Serrano Mario A, Schnabel Denhi, Lomelí Hilda, Salas-Vidal Enrique. Cell proliferation patterns in early zebrafish development // The Anatomical Record. 2013. 296, 5. 759–773.

Mevissen Tycho ET, Komander David. Mechanisms of deubiquitinase specificity and regulation // Annual review of biochemistry. 2017. 86. 159–192.

Mihalas AB, Hevner RF. Control of neuronal development by T-box genes in the brain // Current Topics in Developmental Biology. 2017. 122. 279–312.

Mione Marina, Baldessari Danila, Deflorian Gianluca, Nappo Gilda, Santoriello Cristina. How neuronal migration contributes to the morphogenesis of the CNS: insights from the zebrafish // Developmental neuroscience. 2008. 30, 1-3. 65–81.

Mione Marina, Shanmugalingam Shantha, Kimelman David, Griffin Kevin. Overlapping expression of zebrafish T-brain-1 and eomesodermin during forebrain development // Mechanisms of development. 2001. 100, 1. 93–97.

Miyake Ayumi, Mekata Yoko, Fujibayashi Hidenori, Nakanishi Kazuya, Konishi Morichika, Itoh Nobuyuki. Brorin is required for neurogenesis, gliogenesis, and commissural axon guidance in the zebrafish forebrain // PloS one. 2017. 12, 4. e0176036.

Miyake Ayumi, Nakayama Yoshiaki, Konishi Morichika, Itoh Nobuyuki. Fgf19 regulated by Hh signaling is required for zebrafish forebrain development // Developmental biology. 2005. 288, 1. 259–275.

Monk Nicholas AM. Oscillatory expression of Hes1, p53, and NF-κB driven by transcriptional time delays // Current biology. 2003. 13, 16. 1409–1413.

Mueller Thomas, Dong Zhiqiang, Berberoglu Michael A, Guo Su. The dorsal pallium in zebrafish, Danio rerio (Cyprinidae, Teleostei) // Brain research. 2011. 1381. 95–105.

Mueller Thomas, Wullimann Mario F. Anatomy of neurogenesis in the early zebrafish brain // Developmental Brain Research. 2003. 140, 1. 137–155.

Müller Patrick, Rogers Katherine W, Jordan Ben M, Lee Joon S, Robson Drew, Ramanathan Sharad, Schier Alexander F. Differential diffusivity of Nodal and Lefty underlies a reaction-diffusion patterning system // Science. 2012. 336, 6082. 721–724.

Nakamura Yuki, Sakakibara Shin-ichi, Miyata Takaki, Ogawa Masaharu, Shimazaki Takuya, Weiss Samuel, Kageyama Ryoichiro, Okano Hideyuki. The bHLH gene hes1 as a repressor of the neuronal commitment of CNS stem cells // Journal of Neuroscience. 2000. 20, 1. 283–293.

Nieuwkoop Pieter Dirk. Activation and organization of the central nervous system in amphibians. Part I. Induction and activation // Journal of Experimental Zoology. 1952. 120, 1. 1–31.

Nijman Sebastian MB, Luna-Vargas Mark PA, Velds Arno, Brummelkamp Thijn R, Dirac Annette MG, Sixma Titia K, Bernards René. A genomic and functional inventory of deubiquitinating enzymes // Cell. 2005. 123, 5. 773–786.

Ninov Nikolay, Borius Maxim, Stainier Didier YR. Different levels of Notch signaling regulate quiescence, renewal and differentiation in pancreatic endocrine progenitors // Development. 2012. 139, 9. 1557–1567.

Oates Andrew C, Ho Robert K. Hairy/E (spl)-related (Her) genes are central components of the segmentation oscillator and display redundancy with the Delta/Notch signaling pathway in the formation of anterior segmental boundaries in the zebrafish // Development. 2002. 129, 12. 2929–2946.

Ochi Shohei, Imaizumi Yui, Shimojo Hiromi, Miyachi Hitoshi, Kageyama Ryoichiro. Oscillatory expression of Hes1 regulates cell proliferation and neuronal differentiation in the embryonic brain // Development. 2020. 147, 4. dev182204.

Ohtsuka Toshiyuki, Ishibashi Makoto, Gradwohl Gérald, Nakanishi Shigetada, Guillemot François, Kageyama Ryoichiro. Hes1 and Hes5 as notch effectors in mammalian neuronal differentiation // The EMBO journal. 1999. 18, 8. 2196–2207.

Oishi Katsutaka, Miyazaki Koyomi, Kadota Koji, Kikuno Reiko, Nagase Takahiro, Atsumi Gen-ichi, Ohkura Naoki, Azama Takashi, Mesaki Miho, Yukimasa Shima, others . Genome-wide expression analysis of mouse liver reveals CLOCK-regulated circadian output genes // Journal of Biological Chemistry. 2003. 278, 42. 41519–41527.

Özbudak Ertuğrul M, Lewis Julian. Notch signalling synchronizes the zebrafish segmentation clock but is not needed to create somite boundaries // PLoS genetics. 2008. 4, 2. e15.

Papan Cyrus, Campos-Ortega José A. On the formation of the neural keel and neural tube in the zebrafishDanio (Brachydanio) rerio // Roux's archives of developmental biology. 1994. 203, 4. 178–186.

Park Hae-Chul, Mehta Amit, Richardson Joanna S, Appel Bruce. olig2 is required for zebrafish primary motor neuron and oligodendrocyte development // Developmental biology. 2002. 248, 2. 356–368.

Pasini Andrea, Henrique Domingos, Wilkinson David G. The zebrafish Hairy/Enhancer-of-split-related gene her6 is segmentally expressed during the early development of hindbrain and somites // Mechanisms of development. 2001. 100, 2. 317–321.

Patrick Gentry N, Zhou Pengbo, Kwon Young T, Howley Peter M, Tsai Li-Huei. p35, the neuronal-specific activator of cyclin-dependent kinase 5 (Cdk5) is degraded by the ubiquitin-proteasome pathway // Journal of Biological Chemistry. 1998. 273, 37. 24057–24064.

Patterson George H, Lippincott-Schwartz Jennifer. A photoactivatable GFP for selective photolabeling of proteins and cells // Science. 2002. 297, 5588. 1873–1877.

Phillips Nick E, Manning Cerys, Papalopulu Nancy, Rattray Magnus. Identifying stochastic oscillations in single-cell live imaging time series using Gaussian processes // PLoS computational biology. 2017. 13, 5. e1005479.

Phillips Nick E, Manning Cerys S, Pettini Tom, Biga Veronica, Marinopoulou Elli, Stanley Peter, Boyd James, Bagnall James, Paszek Pawel, Spiller David G, others . Stochasticity in the miR-9/Hes1 oscillatory network can account for clonal heterogeneity in the timing of differentiation // Elife. 2016. 5. e16118.

Plachta Nicolas, Bollenbach Tobias, Pease Shirley, Fraser Scott E, Pantazis Periklis. Oct4 kinetics predict cell lineage patterning in the early mammalian embryo // Nature cell biology. 2011. 13, 2. 117–123.

Rafferty Sara A, Quinn T Alexander. A beginner's guide to understanding and implementing the genetic modification of zebrafish // Progress in biophysics and molecular biology. 2018. 138. 3–19.

Ravid Tommer, Hochstrasser Mark. Diversity of degradation signals in the ubiquitin–proteasome system // Nature reviews Molecular cell biology. 2008. 9, 9. 679–689.

Razavipour Seyedeh Fatemeh, Harikumar Kuzhuvelil B, Slingerland Joyce M. p27 as a transcriptional regulator: new roles in development and cancer // Cancer research. 2020. 80, 17. 3451–3458.

Rechsteiner Martin, Rogers Scott W. PEST sequences and regulation by proteolysis // Trends in biochemical sciences. 1996. 21, 7. 267–271.

Reyes Rosario, Haendel Melissa, Grant Deanna, Melancon Ellie, Eisen Judith S. Slow degeneration of zebrafish Rohon-Beard neurons during programmed cell death // Developmental dynamics: an official publication of the American Association of Anatomists. 2004. 229, 1. 30–41.

Rogers Katherine W, Bläßle Alexander, Schier Alexander F, Müller Patrick. Measuring protein stability in living zebrafish embryos using fluorescence decay after photoconversion (FDAP) // JoVE (Journal of Visualized Experiments). 2015. 95. e52266.

Rogers Scott, Wells Rodney, Rechsteiner Martin. Amino acid sequences common to rapidly degraded proteins: the PEST hypothesis // Science. 1986. 234, 4774. 364–368.

Rohde Laurel A, Bercowsky-Rama Arianne, Negrete Jose, Valentin Guillaume, Naganathan Sundar Ram, Desai Ravi A, Strnad Petr, Soroldoni Daniele, Jülicher Frank, Oates Andrew C. Cell-autonomous generation of the wave pattern within the vertebrate segmentation clock // bioRxiv. 2021.

Ross Linda S, Parrett T, Easter SS. Axonogenesis and morphogenesis in the embryonic zebrafish brain // Journal of Neuroscience. 1992. 12, 2. 467–482.

Sabherwal Nitin, Rowntree Andrew, Marinopoulou Elli, Pettini Tom, Hourihane Sean, Thomas Riba, Soto Ximena, Kursawe Jochen, Papalopulu Nancy. Differential phase register of Hes1 oscillations with mitoses underlies cell-cycle heterogeneity in ER+ breast cancer cells // Proceedings of the National Academy of Sciences. 2021. 118, 45.

Sakai Catalina, Ijaz Sundas, Hoffman Ellen J. Zebrafish models of neurodevelopmental disorders: past, present, and future // Frontiers in molecular neuroscience. 2018. 294.

Santillán Moises. On the use of the Hill functions in mathematical models of gene regulatory networks // Mathematical Modelling of Natural Phenomena. 2008. 3, 2. 85–97.

Sasai Yoshiki, Kageyama Ryoichiro, Tagawa Yoshiaki, Shigemoto Ryuichi, Nakanishi Shigetada. Two mammalian helix-loop-helix factors structurally related to Drosophila hairy and Enhancer of split. // Genes & development. 1992. 6, 12b. 2620–2634.

Sassen Wiebke A, Köster Reinhard W. A molecular toolbox for genetic manipulation of zebrafish // Advances in Genomics and Genetics. 2015. 5. 151.

Schimke Robert T, Doyle Darrell. Control of enzyme levels in animal tissues // Annual review of biochemistry. 1970. 39, 1. 929–976.

Schmidt Rebecca, Strähle Uwe, Scholpp Steffen. Neurogenesis in zebrafish–from embryo to adult // Neural development. 2013. 8, 1. 1–13.

Scholpp Steffen, Delogu Alessio, Gilthorpe Jonathan, Peukert Daniela, Schindler Simone, Lumsden Andrew. Her6 regulates the neurogenetic gradient and neuronal identity in the thalamus // Proceedings of the National Academy of Sciences. 2009. 106, 47. 19895–19900.

Shah Sheel, Lubeck Eric, Zhou Wen, Cai Long. In situ transcription profiling of single cells reveals spatial organization of cells in the mouse hippocampus // Neuron. 2016. 92, 2. 342–357.

Shankaran Sunita S, Sieger Dirk, Schröter Christian, Czepe Carmen, Pauly Marie-Christin, Laplante Mary A, Becker Thomas S, Oates Andrew C, Gajewski Martin. Completing the set of h/E (spl) cyclic genes in zebrafish: her12 and her15 reveal novel modes of expression and contribute to the segmentation clock // Developmental biology. 2007. 304, 2. 615–632.

Shimojo Hiromi, Isomura Akihiro, Ohtsuka Toshiyuki, Kori Hiroshi, Miyachi Hitoshi, Kageyama Ryoichiro. Oscillatory control of Delta-like1 in cell interactions regulates dynamic gene expression and tissue morphogenesis // Genes & development. 2016. 30, 1. 102–116.

Shimojo Hiromi, Ohtsuka Toshiyuki, Kageyama Ryoichiro. Oscillations in notch signaling regulate maintenance of neural progenitors // Neuron. 2008. 58, 1. 52–64.

Sieger Dirk, Tautz Diethard, Gajewski Martin. her11 is involved in the somitogenesis clock in zebrafish // Development genes and evolution. 2004. 214, 8. 393–406.

Sokalingam Sriram, Raghunathan Govindan, Soundrarajan Nagasundarapandian, Lee Sun-Gu. A study on the effect of surface lysine to arginine mutagenesis on protein stability and structure using green fluorescent protein // PloS one. 2012. 7, 7. e40410.

Soroldoni Daniele, Jörg David J, Morelli Luis G, Richmond David L, Schindelin Johannes, Jülicher Frank, Oates Andrew C. A Doppler effect in embryonic pattern formation // Science. 2014. 345, 6193. 222–225.

Soto Ximena, Biga Veronica, Kursawe Jochen, Lea Robert, Doostdar Parnian, Thomas Riba, Papalopulu Nancy. Dynamic properties of noise and Her6 levels are optimized by miR-9, allowing the decoding of the Her6 oscillator // The EMBO journal. 2020. 39, 12. e103558.

Ståhl Patrik L, Salmén Fredrik, Vickovic Sanja, Lundmark Anna, Navarro José Fernández, Magnusson Jens, Giacomello Stefania, Asp Michaela, Westholm Jakub O, Huss Mikael, others . Visualization and analysis of gene expression in tissue sections by spatial transcriptomics // Science. 2016. 353, 6294. 78–82.

Stringer Daniel K, Piper Robert C. Terminating protein ubiquitination: Hasta la vista, ubiquitin // Cell Cycle. 2011. 10, 18. 3067–3071.

Takamori Shigeo, Rhee Jeong Seop, Rosenmund Christian, Jahn Reinhard. Identification of differentiation-associated brain-specific phosphate transporter as a second vesicular glutamate transporter (VGLUT2) // Journal of Neuroscience. 2001. 21, 22. RC182–RC182.

Takebayashi Koichi, Sasai Yoshiki, Sakai Yuka, Watanabe Tomomasa, Nakanishi Shigetada, Kageyama Ryoichiro. Structure, chromosomal locus, and promoter analysis of the gene encoding the mouse helix-loop-helix factor HES-1. Negative autoregulation

through the multiple N box elements. // Journal of Biological Chemistry. 1994. 269, 7. 5150–5156.

Tan Siok-Lay, Ohtsuka Toshiyuki, González Aitor, Kageyama Ryoichiro. Micro RNA 9 regulates neural stem cell differentiation by controlling H es1 expression dynamics in the developing brain // Genes to cells. 2012. 17, 12. 952–961.

Thermes Violette, Grabher Clemens, Ristoratore Filomena, Bourrat Franck, Choulika André, Wittbrodt Jochen, Joly Jean-Stéphane. I-SceI meganuclease mediates highly efficient transgenesis in fish // Mechanisms of development. 2002. 118, 1-2. 91–98.

Thisse B, Pflumio S, Fürthauer M, Loppin B, Heyer V, Degrave A, Woehl R, Lux A, Steffan T, Charbonnier XQ, others . Expression of the zebrafish genome during embryogenesis // ZFIN direct data submission. 2001.

Thisse B, Thisse C. Fast release clones: a high throughput expression analysis // ZFIN direct data submission. 2004. 2004.

Thisse C. High throughput expression analysis of ZF-models consortium clones. ZFIN Direct Data Submission // http://zfin. org. 2005.

Toresson Håkan, Martinez-Barbera Juan Pedro, Bardsley Anne, Caubit Xavier, Krauss S. Conservation of BF-1 expression in amphioxus and zebrafish suggests evolutionary ancestry of anterior cell types that contribute to the vertebrate telencephalon // Development genes and evolution. 1998. 208, 8. 431–439.

Treier Mathias, Staszewski Lena M, Bohmann Dirk. Ubiquitin-dependent c-Jun degradation in vivo is mediated by the δ domain // Cell. 1994. 78, 5. 787–798.

Tseng Wei-Chia, Johnson Escauriza Ana J, Tsai-Morris Chon-Hwa, Feldman Benjamin, Dale Ryan K, Wassif Christopher A, Porter Forbes D. The role of Niemann–Pick type C2 in zebrafish embryonic development // Development. 2021. 148, 7. dev194258.

Turner Katherine J, Hawkins Thomas A, Henriques Pedro M, Valdivia Leonardo E, Bianco Isaac H, Wilson Stephen W, Folgueira Mónica. A structural atlas of the developing zebrafish telencephalon based on spatially-restricted transgene expression // bioRxiv. 2022.

Uriu Koichiro. Genetic oscillators in development // Development, Growth & Differentiation. 2016. 58, 1. 16–30.

Varshavsky Alexander. The N-end rule: functions, mysteries, uses // Proceedings of the National Academy of Sciences. 1996. 93, 22. 12142–12149.

Viktorin Gudrun, Chiuchitu Christina, Rissler Michael, Varga Zoltán M, Westerfield Monte. Emx3 is required for the differentiation of dorsal telencephalic neurons // Developmental dynamics: an official publication of the American Association of Anatomists. 2009. 238, 8. 1984–1998.

Viñas-Castells Rosa, Beltran Manuel, Valls Gabriela, Gómez Irene, García José Miguel, Montserrat-Sentís Bàrbara, Baulida Josep, Bonilla Félix, De Herreros Antonio García, Díaz Víctor M. The Hypoxia-controlled FBXL14 Ubiquitin Ligase Targets SNAIL1 for Proteasome Degradation 2 // Journal of biological chemistry. 2010. 285, 6. 3794–3805.

Wall Dana S, Mears Alan J, McNeill Brian, Mazerolle Chantal, Thurig Sherry, Wang Yaping, Kageyama Ryoichiro, Wallace Valerie A. Progenitor cell proliferation in the retina is dependent on Notch-independent Sonic hedgehog/Hes1 activity // The Journal of cell biology. 2009. 184, 1. 101–112.

Wang Siyuan, Moffitt Jeffrey R, Dempsey Graham T, Xie X Sunney, Zhuang Xiaowei. Characterization and development of photoactivatable fluorescent proteins for single-molecule–based superresolution imaging // Proceedings of the National Academy of Sciences. 2014. 111, 23. 8452–8457.

Wang Xue, Chen Xianjun, Yang Yi. Spatiotemporal control of gene expression by a light-switchable transgene system // Nature methods. 2012. 9, 3. 266–269.

Wang Yong, Chen Keping, Yao Qin, Zheng Xiaodong, Yang Zhe. Phylogenetic analysis of zebrafish basic helix-loop-helix transcription factors // Journal of molecular evolution. 2009. 68, 6. 629–640.

Weiss James N. The Hill equation revisited: uses and misuses // The FASEB Journal. 1997. 11, 11. 835–841.

Wertz Ingrid E, O'rourke Karen M, Zhou Honglin, Eby Michael, Aravind L, Seshagiri Somasekar, Wu Ping, Wiesmann Christian, Baker Rohan, Boone David L, others . De-ubiquitination and ubiquitin ligase domains of A20 downregulate NF-κB signalling // Nature. 2004. 430, 7000. 694–699.

Westerich Kim J, Chandrasekaran Karthik S, Gross-Thebing Theresa, Kueck Nadine, Raz Erez, Rentmeister Andrea. Bioorthogonal mRNA labeling at the poly (A) tail for imaging localization and dynamics in live zebrafish embryos // Chemical science. 2020. 11, 11. 3089–3095.

Whiteside Simon T, Ernst Mary K, LeBail Odile, Laurent-Winter Christine, Rice Nancy, Israël Alain. N-and C-terminal sequences control degradation of MAD3/I kappa B alpha in response to inducers of NF-kappa B activity // Molecular and cellular biology. 1995. 15, 10. 5339–5345.

Wierson Wesley A, Welker Jordan M, Almeida Maira P, Mann Carla M, Webster Dennis A, Torrie Melanie E, Weiss Trevor J, Kambakam Sekhar, Vollbrecht Macy K, Lan Merrina, others . Efficient targeted integration directed by short homology in zebrafish and mammalian cells // Elife. 2020. 9. e53968.

Wilson Stephen W, Houart Corinne. Early steps in the development of the forebrain // Developmental cell. 2004. 6, 2. 167–181.

Wilson Stephen W, Ross Linda S, Parrett TIMOTHY, Easter SS. The development of a simple scaffold of axon tracts in the brain of the embryonic zebrafish, Brachydanio rerio // Development. 1990. 108, 1. 121–145.

Wilson Stephen W, Rubenstein John LR. Induction and dorsoventral patterning of the telencephalon // Neuron. 2000. 28, 3. 641–651.

Wu Gang, Anafi Ron C, Hughes Michael E, Kornacker Karl, Hogenesch John B. MetaCycle: an integrated R package to evaluate periodicity in large scale data // Bioinformatics. 2016. 32, 21. 3351–3353.

Wullimann Mario F. Secondary neurogenesis and telencephalic organization in zebrafish and mice: a brief review // Integrative zoology. 2009. 4, 1. 123–133.

Xu Guoqiang, Jaffrey Samie R. Proteomic identification of protein ubiquitination events // Biotechnology and Genetic Engineering Reviews. 2013. 29, 1. 73–109.

Xu H, Li C, Zeng Q, Agrawal I, Zhu X, Gong Z. Genome-wide identification of suitable zebrafish Danio rerio reference genes for normalization of gene expression data by RT-qPCR // Journal of Fish Biology. 2016. 88, 6. 2095–2110.

Yang Yaoming, Duguay David, Bédard Nathalie, Rachalski Adeline, Baquiran Gerardo, Na Chan Hyun, Fahrenkrug Jan, Storch Kai-Florian, Peng Junmin, Wing Simon S, others . Regulation of behavioral circadian rhythms and clock protein PER1 by the deubiquitinating enzyme USP2 // Biology open. 2012. 1, 8. 789–801.

Yeo Sang-Yeob, Kim MinJung, Kim Hyung-Seok, Huh Tae-Lin, Chitnis Ajay B. Fluorescent protein expression driven by her4 regulatory elements reveals the spatiotemporal pattern of Notch signaling in the nervous system of zebrafish embryos // Developmental biology. 2007. 301, 2. 555–567.

Yoshizawa Akio, Nakahara Yoshinari, Izawa Toshiaki, Ishitani Tohru, Tsutsumi Makiko, Kuroiwa Atsushi, Itoh Motoyuki, Kikuchi Yutaka. Zebrafish Dmrta2 regulates neurogenesis in the telencephalon // Genes to Cells. 2011. 16, 11. 1097–1109.

Yu Man, Xi Yanwei, Pollack Jacob, Debiais-Thibaud Mélanie, MacDonald Ryan B, Ekker Marc. Activity of dlx5a/dlx6a regulatory elements during zebrafish GABAergic neuron development // International journal of developmental neuroscience. 2011. 29, 7. 681–691.

Yun Kyuson, Fischman Seth, Johnson Jane, Angelis Martin Hrabe de, Weinmaster Gerry, Rubenstein John LR. Modulation of the notch signaling by Mash1 and Dlx1/2 regulates sequential specification and differentiation of progenitor cell types in the subcortical telencephalon // Development. 2002. 129, 21. 5029–5040.

Zhang Lijuan, Gurskaya Nadya G, Merzlyak Ekaterina M, Staroverov Dmitry B, Mudrik Nikolay N, Samarkina Olga N, Vinokurov Leonid M, Lukyanov Sergey, Lukyanov Kon-

stantin A. Method for real-time monitoring of protein degradation at the single cell level // Biotechniques. 2007. 42, 4. 446–450.

Zhang Yibo, Zhang Zhiwei, Ge Wei. An efficient platform for generating somatic point mutations with germline transmission in the zebrafish by CRISPR/Cas9-mediated gene editing // Journal of Biological Chemistry. 2018. 293, 17. 6611–6622.

Zhou Mi, Yan Jun, Ma Zhaowu, Zhou Yang, Abbood Nibras Najm, Liu Jianfeng, Su Li, Jia Haibo, Guo An-Yuan. Comparative and evolutionary analysis of the HES/HEY gene family reveal exon/intron loss and teleost specific duplication events // PloS one. 2012. 7, 7. e40649.

Zhou Pengbo. Determining protein half-lives // Signal Transduction Protocols. 2004. 67–77.

github . GitHub. 2020.

Chapter 8

Appendices

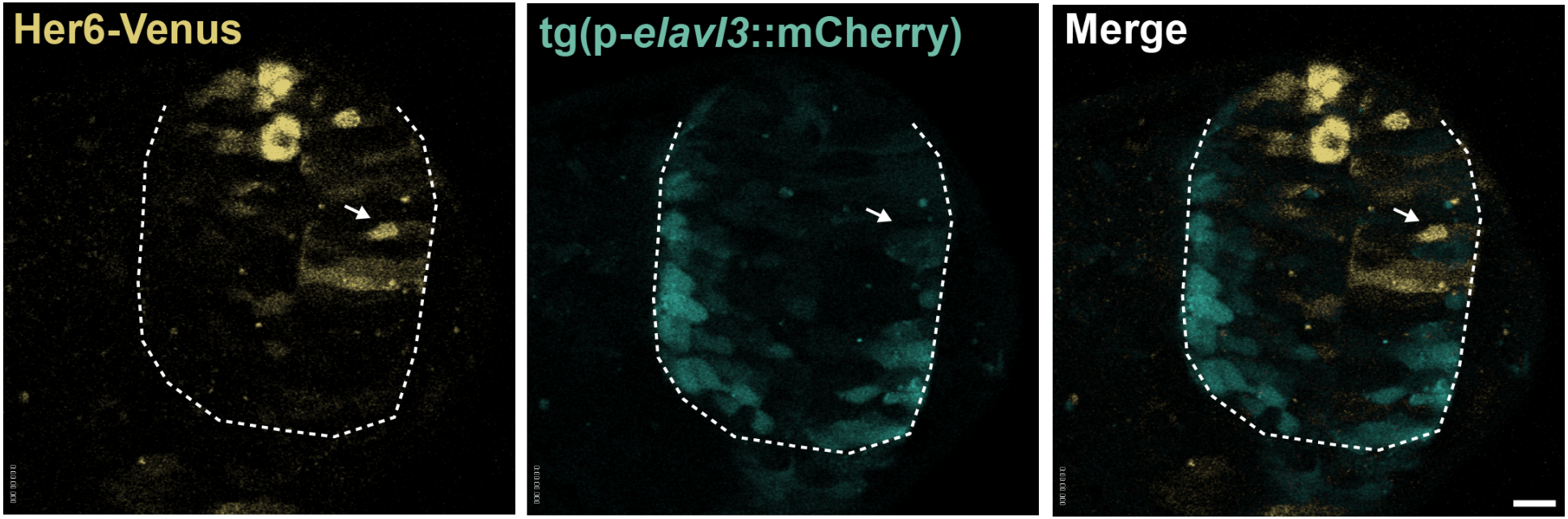

Figure 8.1: **Her6 and Elavl3 expression do not overlap at the single cell level. This Appendix is related to figure 3.1.** Snapshot of a single Z-plane from HV:tg(p*elavl3*::mCherry) double line. Dotted line demarcates the visible boundaries of the telencephalon. Her6 and *elavl3* are not expressed in the same cells. The Her6-Venus expressing cell shown by arrow is adjacent to cells with faint *elavl3* expression but does not express *elavl3* itself. Scalebar = 15µm

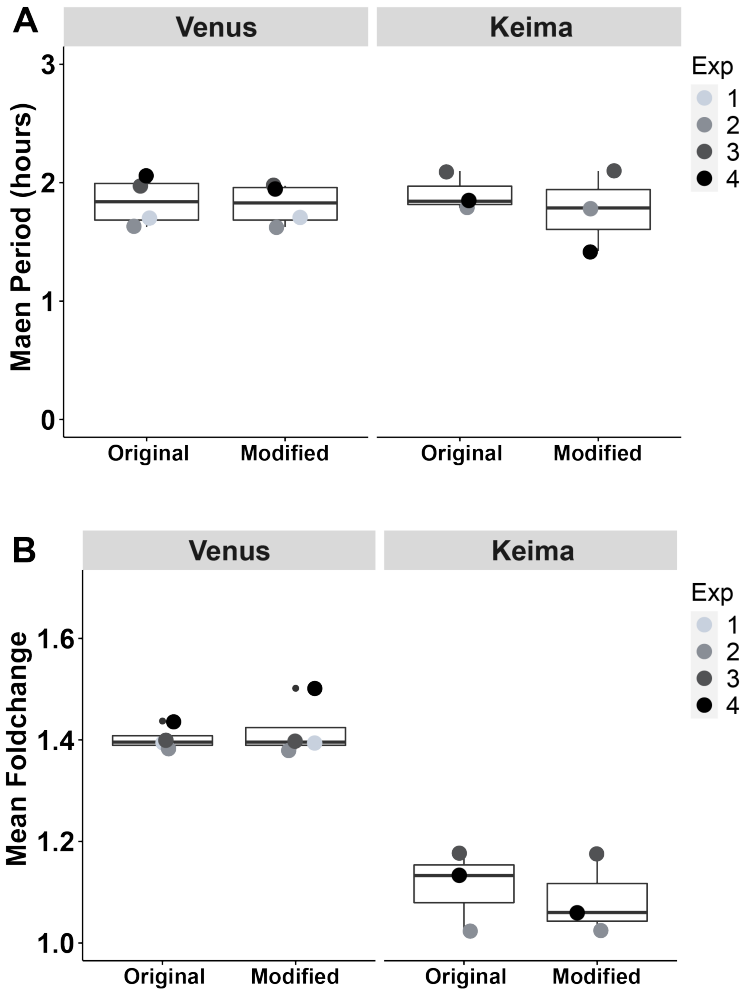

Figure 8.2: **The modifications of single cell track length and paired analysis do not affect period and fold-change of oscillators. This Appendix is related to figure 3.10.** In "Original", all experiments were analysed for the full duration of the original time-course (Exp1 = 6 hours, Exp2 = 8 hours, Exp3 = 10 hours, Exp4 = 12 hours). In "Modified", exp4 was truncated to 8 hours and analysed as a pair with an experimental embryo from exp2. **(A)** These modifications did not alter the estimations of oscillatory period (Venus Median = 1.8 hours in both Original and Modified, Keima Median = 1.8 hours in both Original and Modified. **(B)** The modifications also did not alter the mean fold-change estimates (Venus Median = 1.39 in both Original and Modified, Keima Median Original= 1.13, Keima Median Modified= 1.06.

.

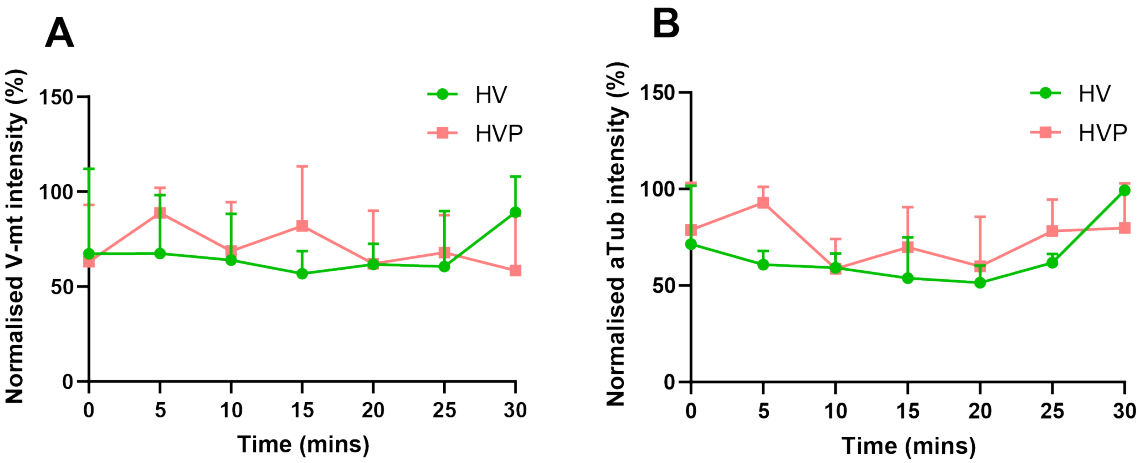

Figure 8.3: **Venus-Myc tag (V-mt) and α-Tub during Cycloheximide (CHX) chase in embryos measured by Western Blot. This Appendix is related to figure 4.7.** Time refers to duration of CHX treatment. HV and HVP data represent means of 3 and 4 biological repeats, respectively. For each repeat, the values were normalised to the maximum value. **(A)** V-mt was used as an injection control. Its levels did not show a declining trend in HV or HVP over 30 minutes of exposure to CHX suggesting that its expression is not likely to be affected by CHX in this time-scale. **(B)** α-Tub was used as a loading control. Its levels declined slightly between 0-20 minutes in HV but recovered between 20-30. In HVP, it declined slightly only between 5-10 minutes. The lack of consistency between HV and HVP suggests that the variations are due to loading rather than caused by CHX.

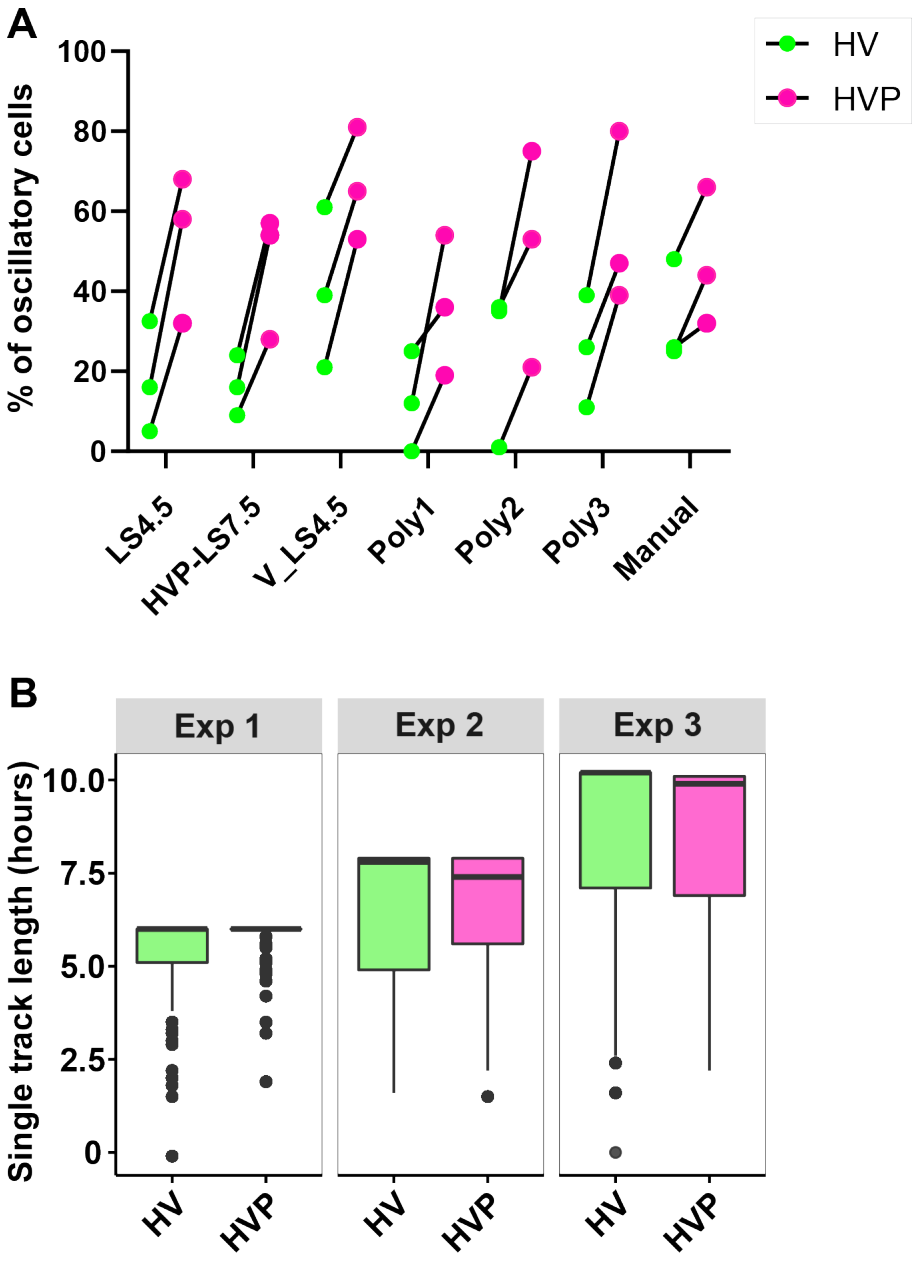

Figure 8.4: **The higher percentage of oscillators in HVP is not an artefact of analysis method or single cell track length. This Appendix is related to figure 5.3. (A)** The single cell tracks from paired HV and HVP experiments were analysed with the computational pipeline (Phillips et al., 2017; Soto et al., 2020) using a range of parameters for removing the long-term trend of Her6 expression or detrending. Even though the resulting absolute values of the percentage of oscillatory cells were variable between different detrending methods, the trend between HV and HVP was always consistent in all methods and all 3 experiments: More cells passed as oscillatory in HVP. LS: Lengthscale (hours). It refers to the length/period of fluctuations that are considered as long-term. LS4.5: Lengthscale 4.5 hours (this was the detrending parameter used for all data in the main text), HVP-LS7.5: HV was detrended with lengthscale of 4.5 while HVP was detrended with 7.5 hours. V_LS4.5: Venus intensity was not normalised with Keima and detrended with 4.5 hour lengthscale. Poly1-3: Detrending was done by a polynomial trend factor 1-3. Manual: Oscillators and non-oscillators where determined manually. If at least 2 periodic peaks were observed in the signal, it was classified as an oscillator. **(B)** Since track length was shown to affect the percentage of oscillators, I checked track lengths in all experiments between HV and HVP to ensure the increased percentage of oscillators is not due to longer tracks. In all 3 paired experiments, HV and HVP were comparable with each other and in correlation with the length of the movie. Experiments 1,2 & 3 were 6, 8 and 12 hours, respectively.

.

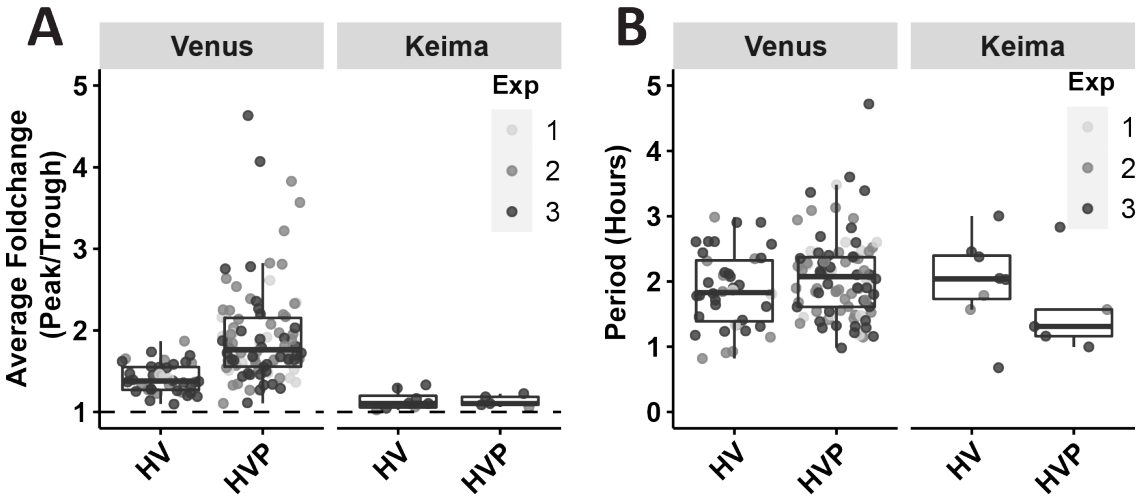

Figure 8.5: **Single cell distribution of average fold-change and period in cells that pass as oscillators. This Appendix is related to figure 5.3. (A)** The distribution of fold-change in all Venus and Keima single cell traces that passed as oscillators in HV and HVP. Medians: HV-Venus=1.37, HVP-Venus=1.76, HV-Keima=1.1, HVP-Keima=1.1. **(B)** The distribution of period in all Venus and Keima single cell traces that passed as oscillators in HV and HVP. Medians: HV-Venus=1.82, HVP-Venus=2.07, HV-Keima=2.04, HVP-Keima=1.31. **(C & D)** Contribution of all 3 experiments to the relative trend analysis in Venus and Keima from HV and HVP. Relative trend is the last value in a single cell track divided by the first value in the same track. Relative trends at 1 indicate steady expression over time.

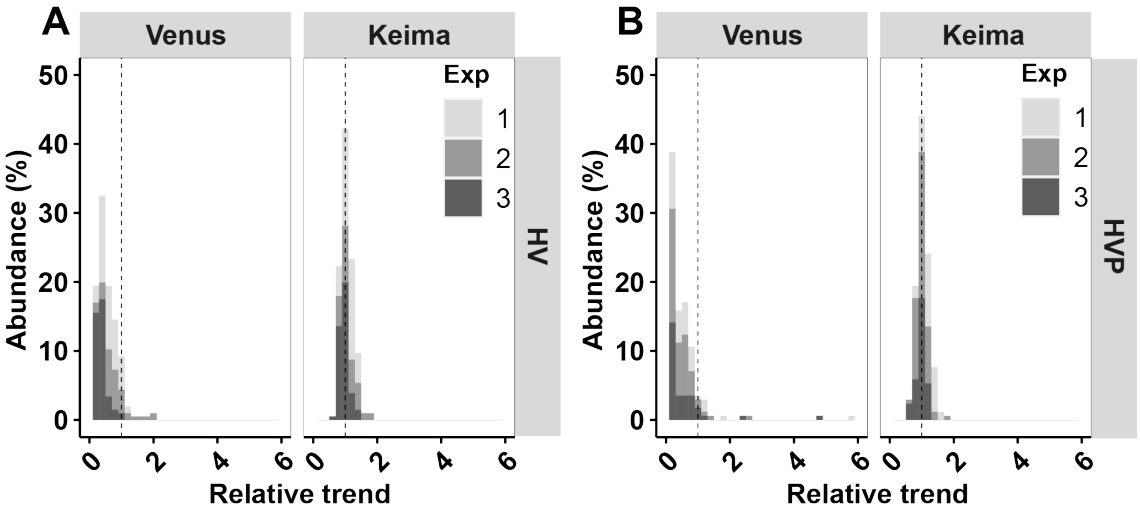

Figure 8.6: **The contribution of different experiments to trend analysis. This Appendix is related to figure 5.4. (A & B)** Contribution of all 3 experiments to the relative trend analysis in Venus and Keima from HV and HVP. Relative trend is the last value in a single cell track divided by the first value in the same track. Relative trends at 1 indicate steady expression over time.

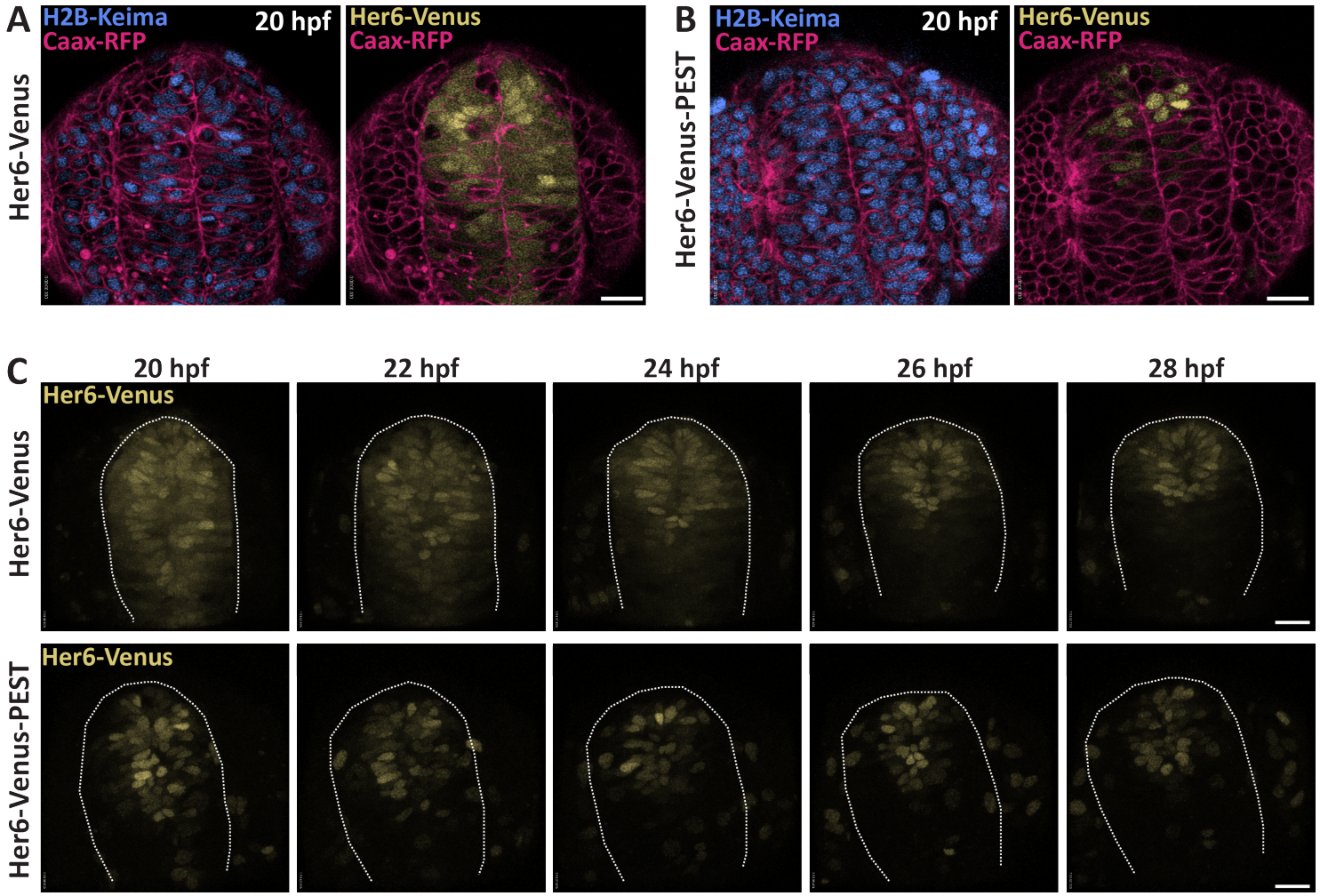

Figure 8.7: **Additional images of Venus expression in HV and HVP from experiment 2 in a transversal view. This Appendix is related to figure 5.5. (A) & (B)** Transverse snapshots of a single Z-plane from the HV and HVP telencephalons at 20hpf which highlights the heterogeneity in Her6-Venus expression. **(C)** 3D reconstruction of transversal view of the telencephalon. Shows the raw and unadjusted levels of Venus expression in the pair of HV and HVP embryos from experiment 2. Scalebar = 20µm

.

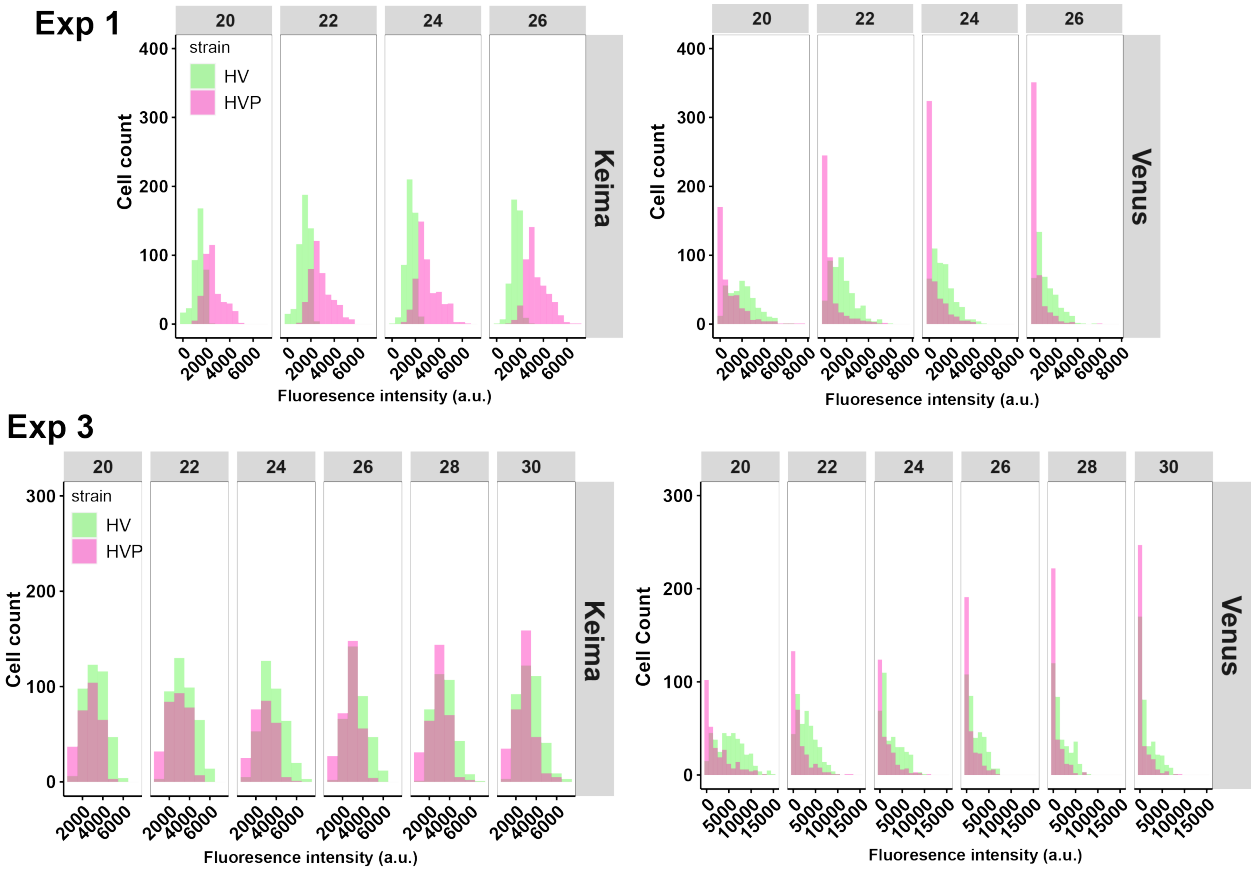

Figure 8.8: **Intensity distribution of Venus and Keima expression in HV and HVP (Experiments 1 and 3). This Appendix is related to figure 5.5**. In both experiments, Keima and Venus intensity values in HV and HVP from all detected telencephalic cells were plotted in overlapping histograms. Distribution of Keima intensities in both HV and HVP populations were close to normal. The width of the distribution differed correlating with the quality of injection. In 20hpf HV, Venus intensities were normally distributed. Over time, the distribution shifted towards lower values, peaking close to 0. In 20hpf HVP, the distribution of Venus intensities was shifted to the left with high count of cells with intensity values close to 0. The left-ward shift became more pronounced over time and higher intensities were depleted.

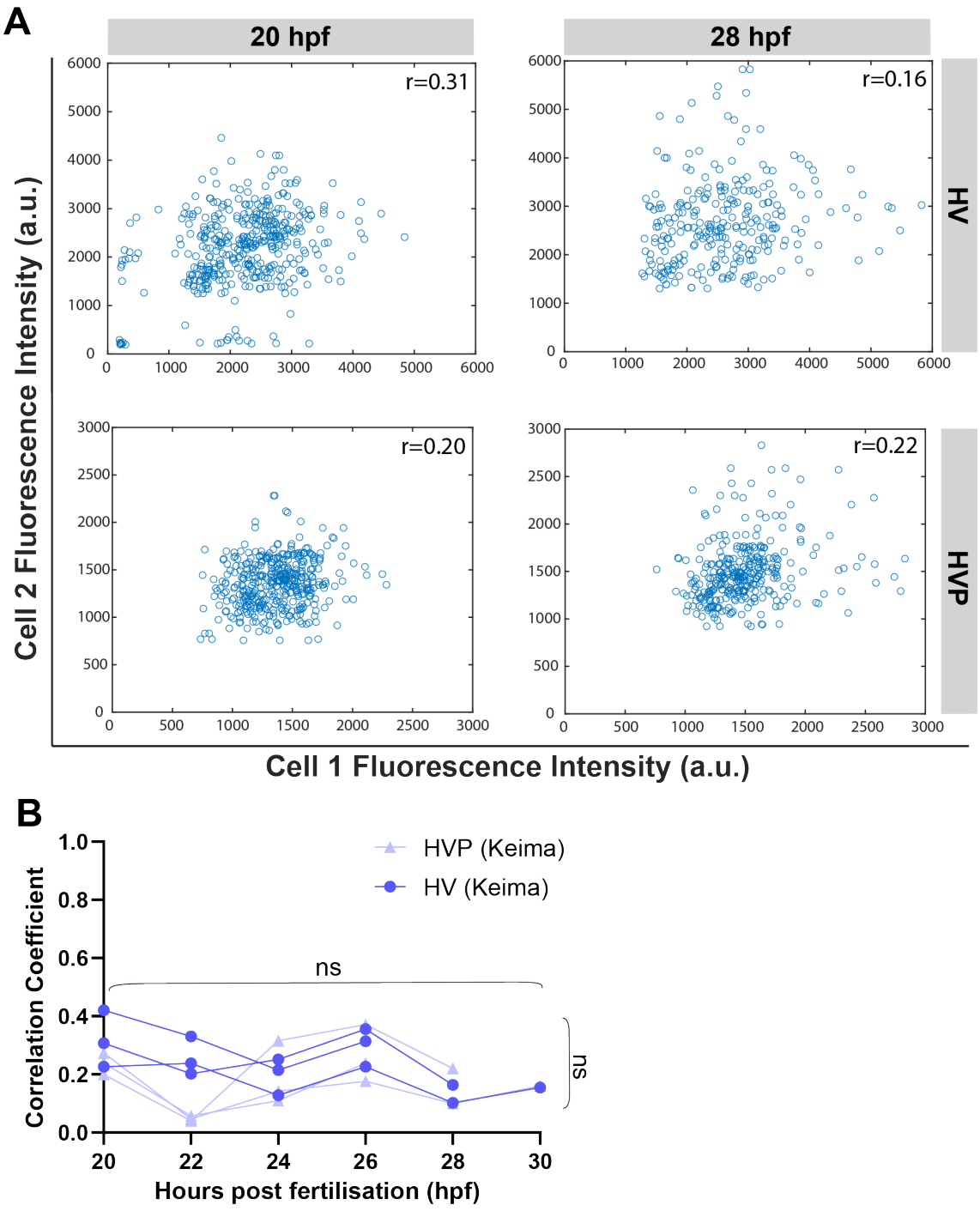

Figure 8.9: **Keima intensities in neighbouring cells have no distinct relationship in HV or HVP. This Appendix is related to figure 5.7. (A)** Example time points from experiment 2. For each cell, the closest neighbour was identified and the intensity levels of Keima were plotted as paired sets with Keima intensity of a selected cell (cell 1) on the x-axis and its neighbouring cell (cell 2) on the y-axis. In both HV and HVP, data points appeared scattered randomly and there was no distinct relationship between cell 1 and cell 2 intensities, giving rise to a weak correlation at 20hpf (HV: r=0.31, HVP: r=0.20). These correlations did not change drastically by 28hpf (HV: r=0.16, HVP: r=0.22). **(B)** The correlation coefficient for Keima between neighbouring cells (based on analysis in A) is comparable between HV and HVP. Neither strain (HV vs HVP) or time had any significant contribution to the variability in Keima correlation coefficient (Mixed-effects analysis, P=0.2511 and P=0.1008 respectively).

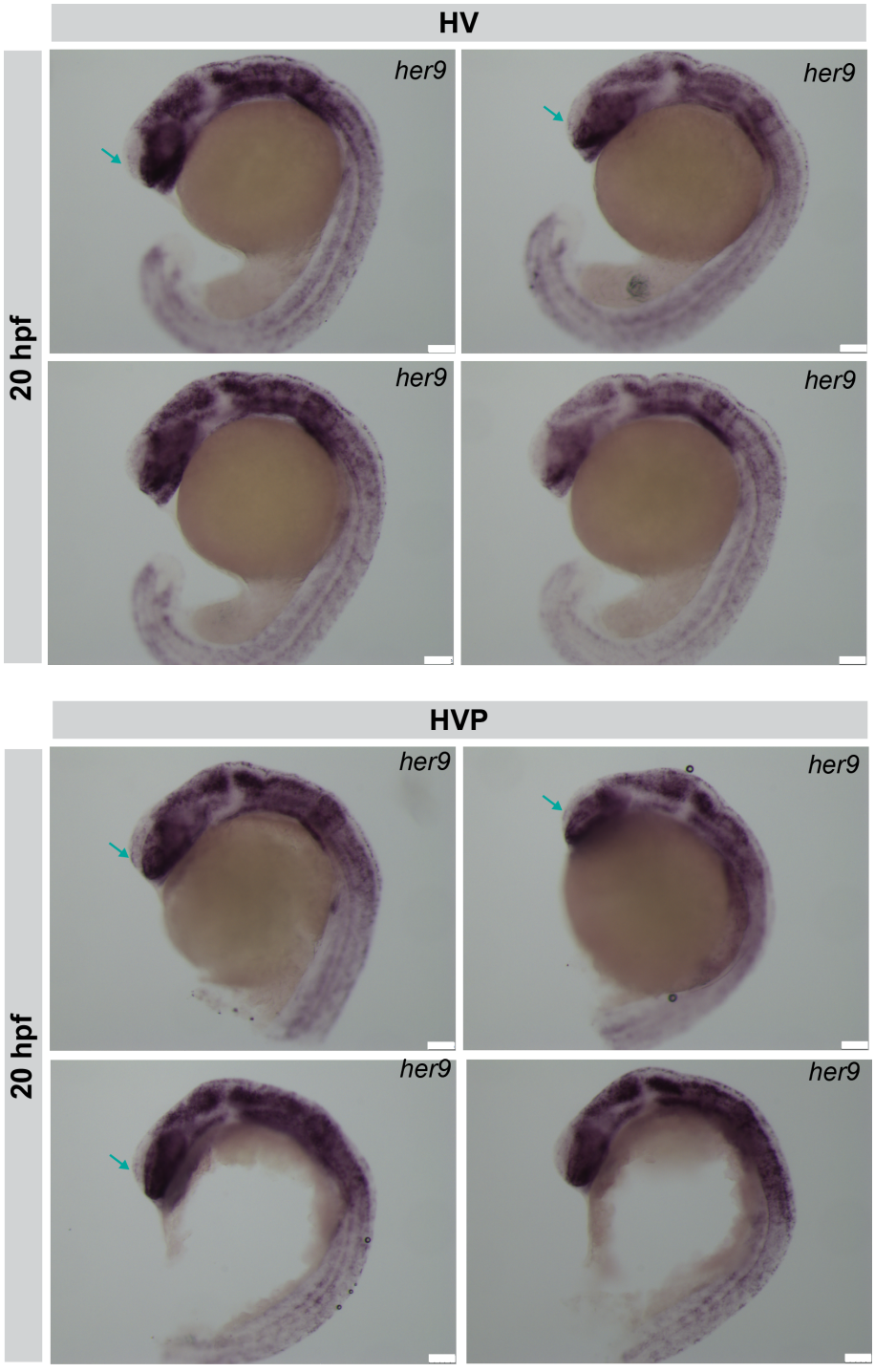

Figure 8.10: **The 20hpf telencephalon has little to no *her9* expression. This figure is related to the Discussion in Chapter 6. (A)** In-situ hybridisation (ISH) against *her9* in 20hpf HV and HVP embryos. There is little to no expression of *her9* in the telencephalon. The green arrow shows sites where little *her9* expression may be present which is seen in both HV and HVP embryos. More quantitative assessment of *her9* expression is required to verify this finding. Scalebar = 75µm

.